Print ISSN 0033-9008
Online ISSN 1880-1765

QUARTERLY REPORT of RTRI

Nov. 2025 Vol. 66 No. 4

CONTENTS

[H] Human factors
[I] Infrastructure
[N] Natural hazards
[O] Operations
[R] Rolling stock
[T] Technical system integration and interaction

RAILWAY TECHNICAL RESEARCH INSTITUTE

QUARTERLY REPORT of RTRI

Print ISSN 0033-9008
Online ISSN 1880-1765

November 2025 Vol. 66 No. 4

CONTENTS

PAPERS

SUMMARIES

[H] Human factors
[I] Infrastructure
[N] Natural hazards
[O] Operations
[R] Rolling stock
[T] Technical system integration and interaction

Method for Proposing Countermeasures against Ground Vibrations along Railway Lines Based on Numerical Simulation

Masanori NOYORI
Geology Laboratory, Disaster Prevention Technology Division

Hidefumi YOKOYAMA
Disaster Prevention Technology Division (Former)

This paper introduces a new method for proposing measures to reduce train-induced ground vibration, which considers three primary factors: source, structure, and ground. In this method, the primary factor is first extracted by using a numerical simulation consisting of a running train, tracks, supporting structures and the ground. Second, candidate countermeasures targeting the primary factor are selected from a provided list. Thirdly, the vibration reduction of each countermeasure is evaluated quantitatively. Finally, based on results a countermeasure is selected.

Key words**:** *train-induced ground vibrations, countermeasures, numerical simulation, primary factor extraction, vibration characteristics of viaducts, propagation characteristics of ground*

1. Introduction

Train-induced ground vibrations sometimes cause environmental problems. Countermeasures to reduce vibrations may be implemented depending on their magnitude. Many studies have examined countermeasures targeting vehicles, tracks, supporting structures and the ground [1], [2]. Table 1 lists countermeasures against train-induced ground vibrations taken from the literature. In general, candidate countermeasures are selected from a list such as Table 1. Countermeasures are then selected on the basis of the results of an evaluation of their vibration reduction effect. However, the selection of countermeasures and the evaluation results of vibration reduction effects often depend on previous cases or practical experience. As a result, there are cases where countermeasures have been implemented without clear evidence that the expected vibration reduction effect has been achieved. This points to a need for a method for selecting countermeasures according to target site conditions that does not rely on practical experience.

Numerical simulation of train-induced ground vibrations, consisting of a running train, tracks, supporting structures and the ground (hereinafter referred to as the "train-induced ground vibration simulation") have been carried out in recent years due to advancements in computing power [4]. Numerical simulation allows us to estimate the vibration reduction effect of the countermeasures targeting vehicles, tracks, supporting structures, and the ground based on the vibration generation and propagation mechanism. Another advantage is its ability to estimate things that are difficult to actually measure, such as excitation force from running trains to tracks and transfer function from viaducts to the ground.

This paper aims to develop a method that minimizes reliance on previous cases or practical experience for proposing countermeasures. In this paper, we investigated a method for proposing countermeasures that were designed to reduce the primary factors of a large ground vibration (hereinafter referred to as the "primary factor"). Furthermore, we investigated a method for primary factor extraction in this process. In these investigations, we used a numerical simulation that has already been researched, consisting of a running train, tracks, supporting structures, and the ground [4].

2. Overview of target site and measurement of train-induced ground vibrations

Figure 1 shows a cross section of a target site. Measurements of the train-induced ground vibrations and surveys of soil properties of the surface ground were carried out at the target site. The target site is located in a cantilever-type rigid-frame viaduct section, double tracks, and three spans. The viaducts have foundations with piles, which are 4 m in length, and have no underground beams. The measurements of the train-induced ground vibrations were carried out by using vibration meters (VM-52, Lion Co., Ltd.) and data recorders (LX-110, TEAC Co.). The sampling frequency was 3 kHz. Measurement target components of the vibration were one vertical and two horizontal components. The two horizontal components consisted of one parallel to the tracks and the other orthogonal to the tracks. The two measurement points for the ground vibrations were located at a distance of 1.0 and 10.0 m from the center line of the track (hereinafter referred to as the "1.0 m point" and the "10.0 m point," respectively). The measurements were carried out while trains were running on the track nearest where the vibration meters were installed.

S-wave velocity profiles of the surface ground were estimated using surface wave exploration [6] and array microtremor observation [7]. These results were then used for the ground model in the numerical simulations in Chapter 3.

3. Numerical simulations

Figure 2 shows the general idea of train-induced ground vibration simulation [4]. This method calculates train-induced ground vibrations using a combination of two models: a coupled vibration analysis model of a running train, tracks and supporting structures; and a three-dimensional vibration analysis of supporting structures and the ground.

The coupled vibration analysis was conducted to calculate the moving excitation forces using a dynamic interaction analysis method between mobile objects and supporting structures based on a substructure method [8]. A numerical simulation model of the coupled vibration analysis was created using a two-dimensional finite

Table 1 List of countermeasures against train-induced ground vibrations (Addition to [3])

Section	Methodology	Technique	Explanation	
Vehicle	Axle load reduction	Vehicle weight reduction	Measure to reduce the source of static and dynamic excitation force. Reflected in the design of high-speed trains. Mainly reducing the weight of car body.	
Track	Track-supporting spring constant reduction	Resilient rail pad, vibration isolating rail fastening system	Reduce the spring constant under the rail.	
		Sleeper with resilient under sleeper pad	Install elastic material under sleepers. Practical application as a measure for ballast tracks on high speed train.	
		Ballast mat	Install elastic mats under ballast. Practical application as a measure for ballast tracks on high speed train.	
		Solid bed track with resilient sleeper	Support the sleepers with resilient under sleeper pad and fix them to roadbed. Practical application on new conventional lines. Trial installation on high speed train.	
		Floating track	Supporting the entire slab including track using elastic support devices. Measures mainly for tunnel sections of new conventional lines.	
	Reduction of track irregularities	Track maintenance, rail replacement, rail grinding	To reduce the source of dynamic excitation force, reduce track irregularities through track maintenance, rail replacement, rail grinding, etc.	
	High rigidity	Track stiffening	Measures by increasing the bending stiffness of track in track direction. Upgrading rails (heavy rails), fastening existing sleepers with steel materials in the track direction (sleeper fastening work), etc.	
	Weight increasing	Additional sleepers	Increase the number of sleepers per unit length by narrowing sleeper spacing.	
		Heavier sleepers	Increase weight of sleepers.	
	Roadbed improvement	EPS Block	Lay expanded polystyrene (EPS) blocks under track.	
		3D reinforcement material	Cover the subgrade of the track with 3D reinforcement material.	
		Roadbed improvement	Strengthen roadbed under sleepers by grouting, by constructing piles using improved soil, etc.	
Supporting structure	Increased rigidity of parts		Increase the rigidity of structural parts such as columns and beams, or expand foundations, etc.	
	Edge reinforcement of viaduct		Reinforce the edges of cantilever-type rigid-frame viaduct. Practical application in high speed railway with cantilever-type rigid-frame viaduct sections.	
	Damper		Reduce vibrations by installing dampers on structures.	
	TMD (Tuned Mass Damper)		A device that combines a weight, spring, and damper to absorb vibrations of a specific frequency. A device that is tuned to the natural frequency of the target structure is called a TMD.	
	Active control, Hybrid control		Control the vibration of a structure using an external excitation device and a controller. The combination of TMD and active control is called hybrid control.	
Ground	Trench	Trench	Dig trenches between the vibration source and the target.	The vibrations are cut off within the ground, which is the propagation path, reducing the vibrations transmitted to the target.
	Underground barrier	Sheet pile	Construct steel sheet pile wall between the vibration source and the target.	
		Concrete	Construct concrete wall between the vibration source and the target.	
		PC Wall-Piles	Construct vibration barrier with hollow PC piles (with a cross section of approximately 70 cm × 70 cm) between the vibration source and the target.	
		Polyurethane foam	Construct vibration barrier with polyurethane foam blocks between the vibration source and the target. It is also possible to construct barrier using in-situ foaming.	
		Improved soil	Construct walls between the vibration source and the target using improved soil made of a mixture of cement, water, and soil.	
		Others	Underground barriers with other materials such as recycled rubber.	
	Ground improvement	Ground improvement	Improve the ground around the vibration source or between the vibration source and the target. Suppresses vibrations at or around the vibration source.	

element method (Fig. 3). The supporting structures were modeled on five double-track, three-span, rigid-frame cantilever type viaducts, based on the design standards and the standard design drawings. The vehicles were assumed to be standard Shinkansen high-speed train vehicles, and their dynamic characteristics were modeled based on a previous study [9]. The vehicle models had eight cars due to simulation scale constraints. The dynamic characteristics of tracks were modeled based on Ref. [10]. Onsite observed values were used for track irregularities.

A three-dimensional vibration analysis was conducted using a dynamic interaction analysis method based on a substructure method [11]. Models of the supporting structures were made using a three-dimensional finite element method (Fig. 4). Models of the ground were made using a thin layer method. Details of the train-induced ground vibration simulation method are given in Ref. [5].

Figure 5 shows 1/3 octave band spectra at the 10.0 m point for the simulation results and the observation records. Figure 5 also shows the standard deviation of the observation record. The observed train-induced ground vibrations in this paper were averaged from five observation records induced by trains running on the track where the vibration meters were installed. The train speed difference was within a range of +/− 6% from the average train speed. The 1/3 octave band spectra in this paper, including Fig. 5, are shown after being normalized by the observation record at the 16 Hz frequency band. As shown in Fig. 5, the 1/3 octave band spectra of the simulation results generally agree with the observation records for frequency bands of 31.5 Hz or less. In addition, the 1/3 octave band spectra of the simulation results and the observation records have peaks within the frequency bands from 16 to 20 Hz. Furthermore, it can be seen that the overall vibration levels in the simulation results and the observation records are determined by peaks in the 16-20Hz frequency bands. Therefore, investigations in the following chapters center on the method for primary factor extraction focusing on the frequency bands from 16 to 20 Hz.

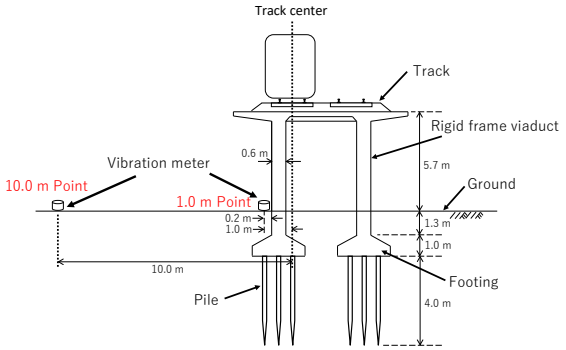

Fig. 1 Cross section of target site and measurement instrument arrangement of train-induced ground vibration [5]

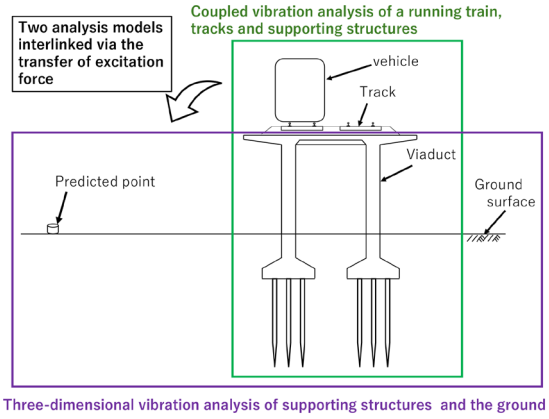

Fig. 2 General idea of train-induced ground vibration simulation [4]

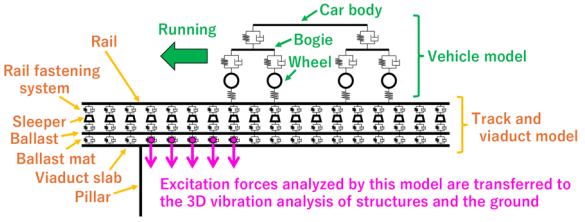

Fig. 3 Analysis model of the coupled vibration of a running train, tracks, and supporting structures [5]

4. Method of primary factor extraction for large ground vibration

It is considered that observed train-induced ground vibrations are multiplied products of characteristics of vibration source, vibration characteristics of viaducts, and propagation characteristics of the ground. Additionally, when train-induced ground vibrations in a specific location are large, they are considered to be caused by one or more of these three characteristics. However, it is difficult to observe these three characteristics individually. Therefore, we investigated the primary factor extraction method for large ground vibration. This method involves individually evaluating the characteristics of the vibration source, the vibration characteristics of viaducts, and

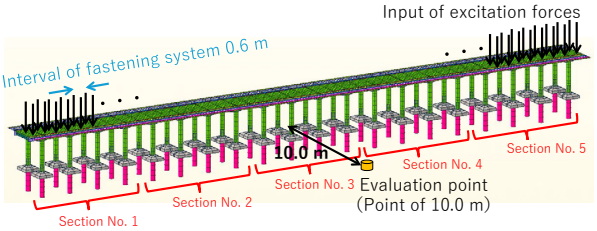

Fig. 4 Analysis model of the three-dimensional vibration of supporting structures and the ground. Modeling of five set viaducts [5].

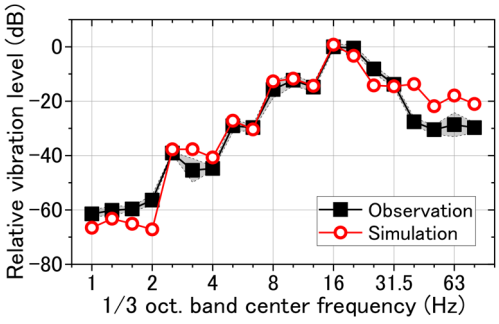

Fig. 5 Comparison between vibration acceleration level of the observation and that of the simulation at the 10.0 m point from the track center. The grey shaded areas show the standard deviation of the observations [5].

the propagation characteristics of the ground using numerical simulation.

4.1 Investigation of the method for primary factor extraction of large ground vibration

In this chapter, focusing on the frequency bands from 16 to 20 Hz, which showed peaks in the simulation results and the observations. The primary factor extraction method was investigated. The investigation was carried out using the 10.0 m point shown in Fig. 1, as an example. The investigation used the numerical simulations described in Chapter 3 and Medium Responses [12], which were calculated using layered ground models.

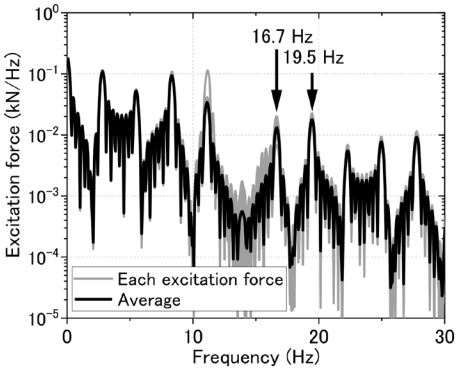

Fig. 6 Characteristics of vibration source [5]

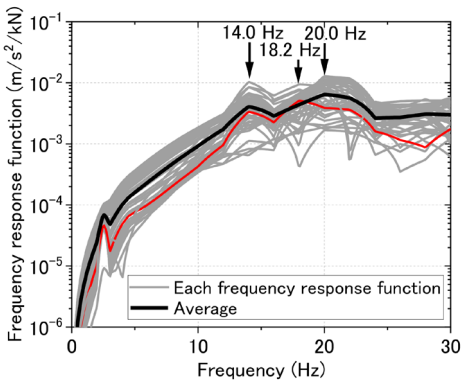

Fig. 7 Vibration characteristics of viaducts. Red line represents a frequency response function that peaks at the frequency of 18.2 Hz [5].

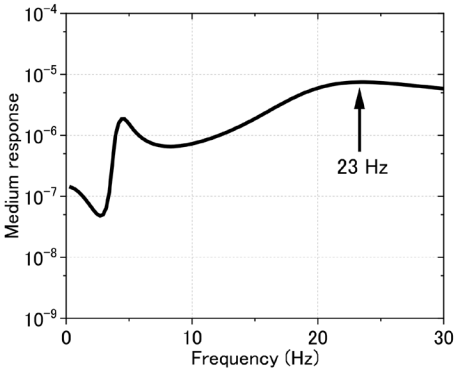

Fig. 8 Propagation characteristics of the ground [5]

The characteristics of the vibration source were evaluated using the moving excitation forces in each point below the rail fastening systems and their average. Each moving excitation force was calculated by a coupled vibration analysis and is the force between the ballast and the viaduct slabs.

The vibration characteristics of viaducts were evaluated using acceleration frequency response functions in each point below the rail fastening systems and their average. Each frequency response function was calculated by the three-dimensional vibration analysis. The input points of each frequency response function are the viaduct slab points directly below each rail fastening system and the output points of each frequency response function are the 1.0 m point shown in Fig. 1.

The propagation characteristics of the ground were defined as the Medium Responses of the fundamental mode Rayleigh wave.

Figures 6, 7, and 8 show the characteristics of the vibration source, the vibration characteristics of viaducts, and the propagation characteristics of the ground, respectively. As shown in Fig. 6, the vibration source has peaks at the frequencies of 16.7 and 19.5 Hz which are induced by repeated passes of axle [13] within the bands of interest. These peaks correspond to the peaks of 1/3 octave band spectrum at the frequency bands from 16 to 20 Hz. However, the peak values at 16.7 and 19.5 Hz are lower than those at other frequencies, such as 2.8, 8.4 or 11.1 Hz. Therefore, it is unlikely that the large ground vibrations at the frequency bands from 16 to 20 Hz were directly caused by the large excitation forces at the frequencies.

As shown in Fig. 7, there is a trend in the vibration characteristics of viaducts in which the amplitude increases along with frequency, with peaks occurring at 14.0 and 20.0 Hz. Furthermore, there are peaks at 18.2 Hz depending on the excitation points. It is possible that these peaks directly cause the large ground vibration at the frequencies from 16 to 20 Hz .

Figure 8 shows a trend in the propagation characteristics of the ground in which the amplitude increases along with frequency, with peaks occurring at around 23 Hz. With reference to the characteristic value around 23 Hz, the values are approximately 0.8 times around 20 Hz and are approximately 0.3 times around 16 Hz. Therefore, it is considered that the large ground vibrations at the frequencies of 20 Hz are affected by these characteristics. However, the characteristics have little effect on the large ground vibration at the frequencies of 16 Hz. Furthermore, the peak at the frequency around 23 Hz is gentle. It is considered that the influence on the large ground vibration at the frequency bands from 16 to 20 Hz is small compared with the vibration characteristics of viaducts.

These investigations suggest that the large ground vibrations in the frequency bands from 16 to 20 Hz are mostly caused by the vibration characteristics of viaducts. The influences of the characteristics of the vibration source and the propagation characteristics of the ground on the large ground vibrations are small. To investigate the vibration characteristics of viaducts as the cause of large ground vibration and to identify which parts of the viaduct primarily contribute to them, the vibration modes of the viaducts were examined at the frequencies where peaks existed: 14.0, 18.2, and 20.0 Hz. The vibration modes of the viaducts were evaluated using the model of the three-dimensional vibration analysis when the viaduct slab was excited in the vertical direction. The excitation points were the center of the slab surrounded by beams (hereinafter referred to as the "center slab"), the slab on a pillar, and the edge of the slab in the rail direction (hereinafter referred to as the "slab edge"), shown in Fig. 9. The excitation points in the rail orthogonal direction are left and right rail points, and the two points were excited at the same

time. The evaluation of the vibration modes of the viaducts was carried out using a method of modal testing [14].

Figure 10 shows the results of the modal testing with excitation point on the center slab, as shown in Fig. 9. Figure 10 describes the deformations of representative points of the model. At frequency of 14.0 Hz, the deformation at the slab edge was the largest. At frequencies of 18.2 and 20.0 Hz, the deformations at the center slab were the largest. Therefore, the large ground vibration at the frequency bands from 16 to 20 Hz in the vibration characteristics of viaducts is likely caused by the vibrations of the slab edge and the center slab.

4.2 Investigating validity of extracted primary factors of large ground vibration

In the previous section, the vibrations from the slab edge and the center slab were extracted as the primary factors in frequency bands from 16 to 20 Hz. This section investigates the validity of the extracted results. If the primary factors extracted from the previous section are the real primary factors, then changing the property or the structural form of the parts of the primary factors is considered to change the train-induced ground vibrations at the evaluation point and at the target frequency. Therefore, this assumption was verified by comparing the train-induced ground vibrations before and after the property or the structural form of the parts were changed using the numerical simulation consisting of a running train, tracks, supporting structures, and the ground.

As shown in Table 1, the measures include increased component rigidity, edge reinforcement and damper as countermeasures targeting the viaduct. This section presents the analysis models of the countermeasures which changed the properties or the structural form of the viaduct.

The model in which slab edges of adjacent viaducts were rigidly connected to each other was made for the slab edge (hereinafter referred to as the "rigidly connected model"). The model in which the cross-sectional stiffness of the center slabs was increased by a factor of five was made for the center slabs (hereinafter referred to as the "five times stiffness model"). In the five times stiffness model, the Young's modulus of the center slabs was set to five times the original value. Note that there is a previous study of a countermeasure that inhibits the vibration of the slab edges in the rigid frame viaducts, by Hara et al. [15]. Furthermore, there is a previous study of a method to enhance the stiffness of the center slabs, by Nihei et al. [16]. The models for this investigation were built considering the countermeasures from these previous studies. The excitation conditions for the rigidly connected model and the five times stiffness model, were the same as in the reproduction analysis in Chapter 3.

Figure 11 shows the simulation results. We now focus on the variation of the train-induced ground vibrations before and after changing the physical property or the structural form of the parts. The result of the rigidly connected model changed in the frequency bands from 10 to 40 Hz including the target frequency bands from 16 to 20 Hz. This result indicates that large ground vibration in the frequency bands from 16 to 20 Hz is caused by slab edge vibrations. Additionally, because the result of the five times stiffness model changed in the frequency bands from 16 to 40 Hz including the target frequency bands from 16 to 20 Hz, the result also indicates that the large ground vibration in the frequency bands from 16 to 20 Hz is caused by the vibrations of the center slabs.

Thus, by evaluating each of the three characteristics, namely, the characteristics of vibration source, the vibration characteristics of viaducts, and the propagation characteristics of the ground, the primary factors could be extracted from the target frequency bands. In the next chapter, a method for proposing the countermeasures to reduce vibration is investigated, using the primary factors extracted in this chapter.

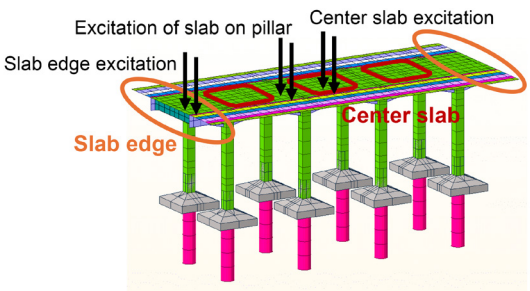

Fig. 9 Excitation points used by investigations of primary factor extraction of large ground vibration [5]

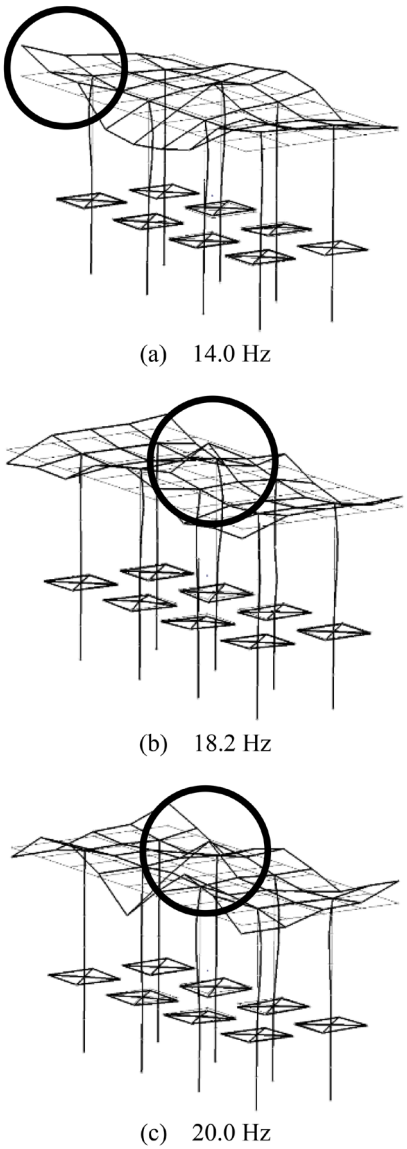

Fig. 10 Results of the model testing with excitation point on the center slab. ○ symbols represent the maximum deformation points [5].

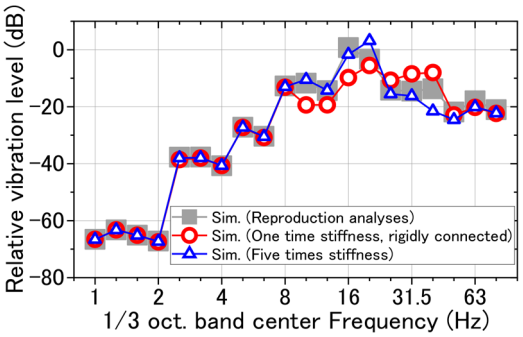

Fig. 11 Simulation results calculated by the model that changed the property or the structural form of the parts. Evaluation point is the 10.0 m point from the track center [5].

5. Method for proposing countermeasures to reduce vibration based on primary factors extraction of the large ground vibration

As shown in Fig. 11, the vibration variation at the frequency bands from 16 to 20 Hz is indicated before and after changing the properties or the structural form of the parts, as discussed in the previous chapter. As shown in Fig. 11, the results of the rigidly connected model at the frequency bands from 10 to 20 Hz were lower than in the reproduction analysis when comparing the vibration levels before and after changing the properties or the structural form of the parts. Therefore, the method by which the slab edges of adjacent viaducts were rigidly connected to each other is considered as a potential countermeasure at the frequency bands from 16 to 20 Hz. However, the results of the rigidly connected model at the frequency bands from 25 to 40 Hz were larger than the results of the reproduction analysis. One possible explanation is that the countermeasure of rigidly connecting the slab edges of adjacent viaducts made the entire structure more rigid.

However, the results of the five times stiffness model at the frequency band of 20 Hz were larger than the results of the reproduction analysis. Therefore, increasing the center slab stiffness by a factor of five cannot be considered as a potential countermeasure for the frequency bands 16 to 20 Hz. This result shows that even when primary factors are extracted it is difficult to determine which countermeasures will be counterproductive or not.

In the light of this result, we investigated a method that could be used to propose countermeasures based on primary factors that would also be able to take into account in cases where the ground vibration was increased due to the first countermeasures based on the primary factors. First, the primary factors of the model were identified by reevaluating the characteristics of vibration source, the vibration characteristics of viaducts, and the propagation characteristics of the ground after the first countermeasures were implemented. Secondly, a model was made after second countermeasure, which inhibited the vibrations of the reextracted primary factors. Then, the ground vibrations calculated by numerical simulation using the model were compared with those of the model after the first countermeasure. In this chapter, we investigated the case where the center slab stiffening was used as a countermeasure based on the primary factors extracted from the previous chapter as an example. In this case the ground vibrations increased with the first countermeasures at the frequency band of 20 Hz. The countermeasures to reduce vibrations are proposed using Table 1.

Figure 12 shows the ratio of acceleration frequency response functions of the five times stiffness model to that of the reproduction analysis model. The excitation points are the slab center, the slab on a pillar and the slab edge shown in Fig. 9. The response output points are located at the 10.0 m point shown in Fig. 1. These investigations were carried out using results from the case where the excitation points in the rail orthogonal direction were excited simultaneously on the left and right rail points. The results of Fig. 12 can be interpreted as a combination of the vibration characteristics of viaducts and the propagation characteristics of the ground. Figure 12 also shows the frequency through the bands of 20 and 25 Hz of the 1/3 Octave band spectrum. The ratios at the frequency around 15 to 21 Hz in Fig. 12 are larger than 1 in the case where the slab edges of the model were excited. From this result, it is considered that the primary factor behind the amplified vibration 20 Hz frequency band is the stiffened center slab, which facilitates vibration transmission. These results indicate that the large ground vibration of the five times stiffness model in the 20 Hz frequency band is caused by slab edge vibrations. This suggests that a potential countermeasure in the 16 to 20 Hz frequency band, could be a combination of the method used to rigidly connect the slab edges of adjacent viaducts to each other and the method for increasing the stiffness of the center slabs by a factor of five.

Figure 11 shows that there is no remarkable increase in vibrations for the five times stiffness model in the 25 Hz frequency band. Figure 12 shows that the ratios at frequencies around 24 Hz are greater than 1 either when the slab center or the slab on a pillar of the model is excited. Conversely, the ratios at frequencies greater than or equal to 26 Hz are less than 1. The frequency through the band of 25 Hz of the 1/3 Octave band spectrum is between 22.4 and 28.2 Hz, so that the increasing and decreasing parts of vibrations cancel each other out within the band. Consequently, the amount of variation in the 25 Hz band is considered to be small.

Figure 13 shows the simulation results of the model in which the stiffness of the center slabs was increased five times, and slab edges of adjacent viaducts were rigidly connected to each other (hereinafter referred to as the “five times stiffness plus rigidly connected model”). Figure 13 also shows the results of the reproduction analysis and the simulation results of the rigidly connected model (in Fig. 13, one time stiffness, rigidly connected), which are shown in Fig. 11. As shown in Fig. 13, the simulation results of five times stiffness plus rigidly connected model (in Fig. 13, five times stiffness, rigidly connected) in the 16 to 20 Hz frequency band are smaller than those of the simulation results of the rigidly connected model. Additionally, the simulation results of five times stiffness plus rigidly connected model show a suppression of the trend where the simulation results of the rigidly connected model in the 25 to 40 Hz frequency band are larger than the results of the reproduction analysis.

These investigations confirmed that reevaluating the characteristics of the first countermeasures and taking measures to address the factors in those countermeasures that cause the reverse effect of increasing ground vibrations, it is possible to propose new countermeasures that avoid this counterproductive effect.

Finally, the investigations in this paper were organized into a flowchart showing the method for proposing countermeasures based on the extracted primary factors (see Fig. 14). The first step in this flowchart is to measure the train-induced ground vibration at the target location. The measurement results are then used to determine whether countermeasures are needed. A reproduction analysis is carried out if countermeasures are necessary. Based on the analysis results, the characteristics of vibration source, the vibration characteristics of viaducts, and the propagation characteristics of the

ground are evaluated individually. Secondly, the primary factors are extracted from the three characteristics. The countermeasures are determined based on these factors. Here, in the case where the extracted primary factors are the characteristics of vibration source, it is necessary to determine whether they are due to the vehicles or the tracks. This can be achieved through an analysis of the measurement results of the train-induced vibrations, the investigated vehicle and track data, or the simulation results. In the case where the extracted primary factors are the vibration characteristics of viaducts, it is necessary to identify the viaduct parts that cause the large ground vibration, by using the model testing, and so on. Thirdly, the vibration reduction effects of the countermeasures are calculated using numerical simulation. If the calculated vibration reduction effects meet the required vibration reduction level, the countermeasures are proposed for implementation. If the calculated vibration reduction effects do not meet the required vibration reduction level, new primary factors are extracted by reevaluating the characteristics of the first countermeasure model. Thus, investigating the countermeasures of the train-induced ground vibrations based on the extracted primary factors makes it possible to propose countermeasures suitable for the target location.

This paper focuses on the vibration characteristics of viaducts as the primary factors of the large ground vibration. It also investigates countermeasures of the train-induced ground vibrations based on these characteristics. As other primary factors of the large ground vibration, it is possible that the vibrations of tracks and the vibrations of combination of vehicles and tracks in the characteristics of vibration source, and the peaks of transfer function and the vibrations of combination of viaducts and the ground in the propagation characteristics of the ground are extracted. Countermeasures can be investigated following the flowchart in Fig. 14 even if these factors are extracted.

When using the flowchart in Fig. 14, countermeasures corresponding to each primary factor can be proposed with Table 1 as a reference. Modeling the countermeasures shown in Table 1 for numerical simulation, can be achieved by changing the properties or structural form of the parts in a similar way to what was done for the investigation in this chapter. It should be noted that it is important to research target countermeasures before carrying them out because research and development conditions and the vibration reducing effect may differ for each countermeasure.

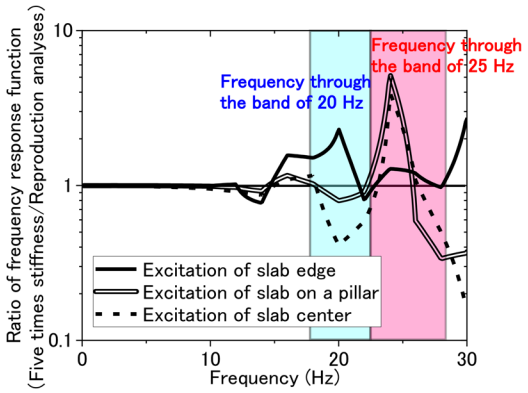

Fig. 12 Ratios of frequency response functions of the five times stiffness model and the reproduction analyses model. Excitation points are slab edge, slab on a pillar, or slab center. Output point is the 10.0 m point from the track center [5].

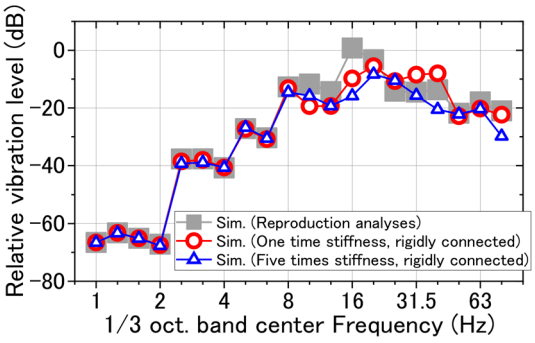

Fig. 13 Simulation results calculated by the five times stiffness + rigidly connected model. Evaluation point is the 10.0 m point from the track center [5].

6. Conclusions

This paper papered on investigations conducted to build a method for proposing ground vibration reducing countermeasures that significantly reduces reliance on previous cases or practical experience. To this end, we investigated a method for proposing countermeasures designed to reduce the primary factors of large ground vibrations. Furthermore, we investigated a method for extracting large ground vibration primary factors in this process. The results showed that the countermeasures with large vibration reduction effects, which inhibit the amplification of vibration, could be proposed through primary factor extraction and investigation of countermeasures based on the extracted primary factors. Additionally, we developed a flowchart to apply the method for proposing countermeasures based on extracted primary factors. The list of the countermeasures for train-induced ground vibrations published in the literature was also shown.

The findings obtained from extracting the primary factors of large ground vibrations and investigating a method for proposing countermeasures based on these factors, are as follows:

- Based on the results of numerical simulations, the primary factors of large ground vibrations can be extracted from the target frequency bands by individually evaluating the characteristics of vibration source, the vibration characteristics of viaducts, and the propagation characteristics of the ground.
- It was indicated that there may be cases in which ground vibrations increase despite the proposed countermeasures being based on the primary factors of large ground vibration.
- By reevaluating the characteristics of the first countermeasures and taking measures to address the factors in those countermeasures that cause the reverse effect of increasing ground vibrations, it is possible to propose new countermeasures that avoid this counterproductive effect.

References

[1] Yoshioka, O., "Reduction measures for train-induced ground vibrations," *The Journal of the Acoustical Society of Japan*, Vol. 55, No. 6, pp. 455-460, 1999 (in Japanese).

[2] Institute of Noise Control Engineering, Japan, *Chiiki no kankyo shindo*. Gihodo Syuppan, pp. 187-193, 2001 (in Japanese).

[3] Ashiya, K. and Yokoyama, H., "Present State of Research and Development of Measures to reduce Ground Vibration," *RTRI*

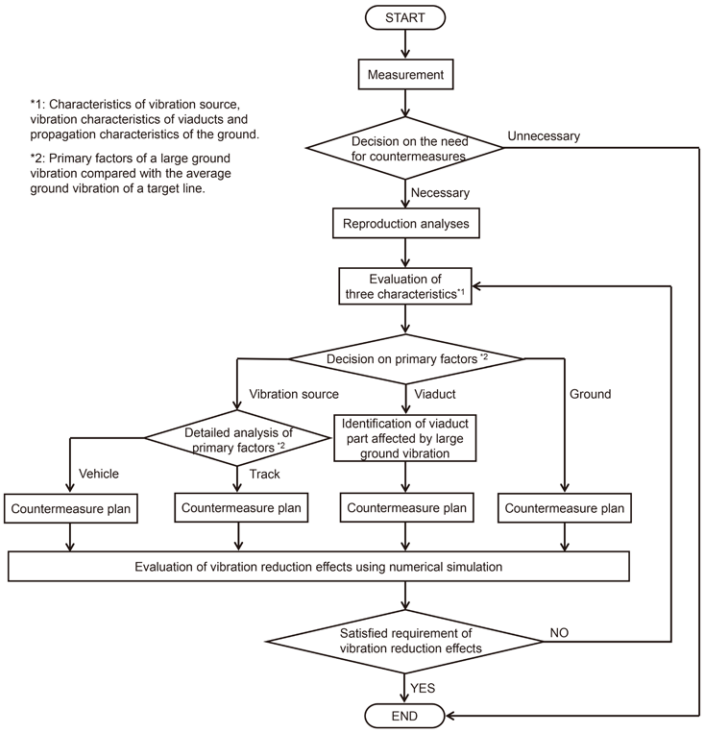

Fig. 14 Flowchart of method for proposing countermeasures based on extracted primary factors [5]

Report, Vol. 16, No. 12, pp. 55-58, 2002 (in Japanese).

[4] Yokoyama, H., Izumi, Y. and Watanabe, T., "A Numerical Simulation Method for Ground and Building Vibration Based on Three Dimensional Dynamic Analysis," *QR of RTRI*, Vol. 57, No. 2, pp. 151-157, 2016.

[5] Noyori, M. and Yokoyama, H., "SUGGESTION METHOD OF COUNTERMEASURES OF TRAIN-INDUCED GROUND VIBRATION USING NUMERICAL SIMULATION," *Japanese Journal of JSCE*, Vol. 79, No. 2, 22-00197, 2023 (in Japanese).

[6] Ashiya, K., Yoshioka, O. and Yokoyama, H., "Estimation of phase velocities of multiple modes by inversion of frequency-wavenumber spectrum and its application to train-induced ground vibrations," *BUTSURI-TANSA*, Vol. 52, No. 3, pp. 214-226, 1999 (in Japanese).

[7] Tsuno, S. and Kudo, K., "Valuation for practical use of S-wave velocity structure determined by the spatial autocorrelation method applied for microtremors," *J. Struct. Constr. Eng., AIJ*, No. 596, pp. 17-24, 2005 (in Japanese).

[8] Yabe, A., "Development of dynamic interaction analysis method between mobile and structure using substructure method," *The 61st JSCE Annual Meeting Proceedings*, I-424, pp. 845-846, 2006 (in Japanese).

[9] Kato, S., Kamohara, A., Yokoyama, H. and Iwata, Y., "Influence of Variation in Track Support Rigidity Around Overbridges on Ground Vibration," *QR of RTRI*, Vol. 55, No. 4, pp. 241-248, 2014.

[10] Suda, Y., Nagato, A., Tokuoka, K. and Miura, A., *Atarashii senro –Kido no kozo to kanri-*, Japan Railway Civil Engineering Association, 1997 (in Japanese).

[11] Japan Society of Civil Engineers, *Dotekikaisekitotaishinsekkei Vol.2 Dotekikaisekinohoho*, Gihodosyuppan, pp. 111-161, 1989 (in Japanese).

[12] Harkrider, D. G., "Surface waves in multilayered elastic media. I. Rayleigh and Love waves from buried sources in a multilayered elastic half-space," *Bull. Seism. Soc. Am*., Vol. 54, No. 2, pp. 627-679, 1964.

[13] Yoshioka, O. and Ashiya, K., "Effects of Mass and Axle Arrangement of Rolling Stock on Train-Induced Ground Vibrations," *RTRI REPORT*, Vol. 3, No. 8, pp. 33-40, 1989 (in Japanese).

[14] Nagamatsu, A., *Introduction to Model Analysis*, Coronasha, 1993 (in Japanese).

[15] Hara, T., Yoshioka, O., Kanda, H., Funabashi, H., Negishi, H., Fujino, Y. and Yoshida. K., "Development of a new method to reduce Shinkansen-induced wayside vibrations applicable to rigid frame bridges: Bridge-end reinforcing method," *Proceedings of JSCE*, No. 766/I-68, pp. 325-338, 2004 (in Japanese).

[16] Nihei, T., Kasakura, R., Kuroiwa, T., Maehara, S. and Okamoto, M., "The development of the method to retrofit a slab of a rigid frame viaduct with ultra high performance fiber reinforced concrete plate," *Proceedings of the Concrete Structure Scenarios, JSMS*, Vol. 14, pp. 453-460, 2014 (in Japanese).

Authors

Masanori NOYORI
Senior Researcher, Geology Laboratory, Disaster Prevention Technology Division
Research Areas: Train-induced Ground Vibration

Hidefumi YOKOYAMA, Dr.Eng.
Senior Chief Researcher, Disaster Prevention Technology Division (Former)
Research Areas: Train-induced Ground Vibration

Method for Evaluating Crashworthiness of Railway Vehicles Based on Correlation with Injury Severity of Passengers Occupying Longitudinal Seats

Kazuma NAKAI
Ergonomics Laboratory, Human Science Division
Tomohiro OKINO
Vehicle & Bogie Parts Strength Laboratory, Vehicle Technology Division (Former)
Shota ENAMI
Ergonomics Laboratory, Human Science Division
Keisuke NAGATA
Vehicle & Bogie Parts Strength Laboratory, Vehicle Technology Division

Improving safety for train passengers in the event of a collision is a priority. To this end, this paper proposes safety indexes. The severity of injury for these indexes was estimated for a level crossing accident using numerical simulation. We compared the correlation between the severity of injury of a human model and the safety index of vehicles, which is the integral of deceleration waveforms, mean deceleration waveforms and maximum deceleration waveforms. It was found that the integral of deceleration values had the highest correlation with the injury values. We therefore propose using the integral of deceleration as a method for evaluating crashworthiness design.

***Key words*:** *railway level crossing accident, crashworthiness, longitudinal seat*

1. Introduction

In Japan, design standards for railcar body structures do not take into account collision accidents, and do not specify indexes for evaluating collision safety. Design standards for the collision safety of railcar bodies are specified however, in European countries and the United States. For example, in European countries, the average deceleration that occurs inside the car during a collision is used as an index, assuming several accident scenarios including a train-to-train collision (collision speed of 36 km/h) [1]. In the United States, the maximum deceleration that occurs inside the car during a train-to-train collision (collision speed of 48 km/h) is used as an index [2]. Each of these indexes has its own limit value. The assumed accident scenarios and the evaluation indexes vary depending on the railway systems and past accident cases in each country.

On closer investigation, it was found that out of all train accidents in Japan, train-to-train collisions are rare [3] compared to train-automobile collisions at level crossings that are the most common type of accident. Therefore, in Japan, collision with automobile should be a priority. Although there have been studies on the crashworthiness of car body structures in Japan [4]-[7], these have focused on examining the vehicle's impact absorbing structure and reproducing the phenomenon through the analysis of collision tests. Consequently, there is limited knowledge that can be used to establish design standards.

In this report, we performed an injury analysis of passengers seated on longitudinal seats, in different conditions of varying train collision speed and collision position of trains. This analysis was based on the result of a statistical survey of major level crossing accidents that have occurred in Japan in the past. We also estimated the severity of head injuries in secondary collisions with a bench-end partition installed at the end of longitudinal seats (it has been confirmed that the risk of head injury is high in a secondary collision with bench-end partitions [3]). In addition, we present crashworthiness evaluation indexes and limit values for car body structures appropriate to the situation in Japan, by comparing the correlation between the "integral of deceleration" suggested by Okino et al. [8] for passengers seated on rotating reclining seats, and the Western "mean deceleration" and "maximum deceleration" indexes, which estimate injury levels. There have been no reports that have evaluated the safety of passenger compartments for passengers seated on longitudinal seats using Western indexes under various conditions that assume actual level crossing accidents and that have verified the validity of the evaluation indexes for car body structures using the degree of injury to passengers as a criterion. Therefore, verification results from this study will contribute to the establishment of design standards for the crashworthiness of railway vehicles in Japan.

2. Assessment of passenger compartment safety under various level crossing accident conditions

In this report, we carried out a safety evaluation by combining "level crossing accident analysis" and "passenger injury analysis" using numerical analysis. In the former numerical analysis, a train mathematical model was collided with a large dump truck mathematical model under various conditions, and the impact deceleration waveform generated in the train model was calculated. In the latter numerical analysis, a passenger model was seated in a longitudinal seat model, and the deceleration waveform obtained from the level crossing accident analysis was input to an interior equipment model including the longitudinal seat model to reproduce the interior situation of a train at the time of an accident.

For the "level crossing accident analysis" we used the model constructed by Okino et al. [9]. The analysis model consists of a train model with a standard stainless steel body structure and a large dump truck model (Fig. 1). Using this analysis model, the impact deceleration waveform (relative to the train travel direction) of the train passenger compartment when colliding with a dump truck was calculated using the input parameters of the train collision speed, left and right collision positions, collision angle, top and bottom collision positions and cargo mass. From these waveforms, the "mean deceleration" in accordance with European standards [1], the "maximum deceleration" in accordance with US standards [2], and

the "integral of deceleration" proposed by Okino et al. [8] were calculated as evaluation indexes for the vehicle body structure.

For the "passenger injury analysis," we used a passenger injury analysis model [10] that we developed to estimate the injury level of passengers seated in longitudinal seats. This analysis model is composed of a human dummy model that imitates a passenger (a rigid model of the ES-2 dummy developed in the automotive industry to evaluate side impacts on the body) and a model of the longitudinal seats and bench-end partition installed at the ends of seats that are actually used in trains (Fig. 2). This model can output the level of head injury at the time of impact by inputting the cabin's impact deceleration waveform obtained from the above-mentioned "level crossing accident analysis." Figure 2 shows an example of a dummy model sitting in the third seat from the bench-end partition, colliding with the partition and falling down.

By comparing the four evaluation indexes obtained from the "level crossing accident analysis" (two types of mean deceleration, maximum deceleration, and integral of deceleration) with the head injury severity obtained from the "passenger injury analysis," we investigated evaluation indexes that were highly correlated with passenger injury severity.

2.1 Conditions and evaluation indexes for railroad crossing accident analysis

A total of 37 level crossing accident analysis scenarios were performed by combining the following factors: vehicle collision speed, collision position in the horizontal direction, collision angle, collision position in the vertical direction, and cargo mass (Table 1). As shown in Fig. 1, under the basic condition of Case 1-1, the horizontal collision position was set so that the centerline of the carbody was aligned with the center of the dump truck's load. The collision angle was set so that the vehicle and the dump truck were positioned at right angles to each other in the direction of travel. The vertical collision position was set so that the bottom of the underframe was 355 mm lower than the bed bottom of the dump truck (the reference height). The cargo mass was 11,000 kg. Cases 1-2 to 1-5 represent condition groups with different horizontal collision positions. Cases 2-1 to 2-4 represent condition groups with different collision angles, Cases 3-1 to 3-3 represent condition groups with different vertical collision positions, and Cases 4-1 to 4-5 represent condition groups with different cargo masses.

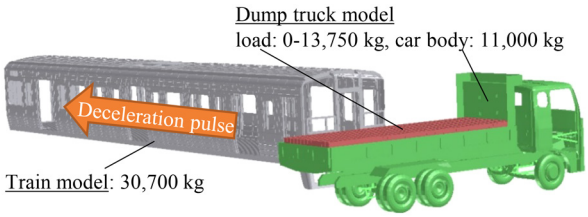

Fig. 1 Train model and dump truck model

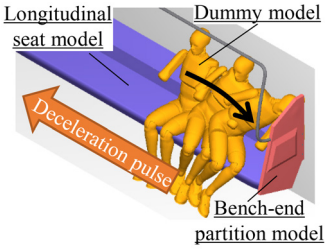

Fig. 2 Dummy model and longitudinal seat model

The collision speeds were set to five conditions: 20 km/h, 30 km/h, 40 km/h, 54 km/h, and 60 km/h. 54 km/h corresponds to the average estimated collision speed of serious accidents at level crossings occurred in Japan between FY1987 and FY2010 [11]. The horizontal collision positions were set to the following five conditions: the center of the load, the center of gravity of the entire dump truck including the load, the center of gravity of the dump truck cabin, the rear end of the load of the dump truck (overlap condition where half the width of the train body overlaps), and a position 750 mm rearward from the rear end of the load (overlap condition where 1/4 the width of the train body overlaps). The collision angle was defined as positive when the dump truck cab rotated towards the train, with the center of the load acting as the axis of rotation. The condition where the train and dump truck were perpendicular to each other was set to 0 degrees. And five conditions were set to ±5 degrees and ±10 degrees including this. Four vertical collision positions were set: the reference height, a position where the dump truck was 177 mm lower than the reference height, a position where the dump truck was 354 mm lower than the reference height (condition where the center height of the train's floor structure and the main frame of the dump truck's loading platform are aligned), and a position where the dump truck was 512 mm lower than the reference height (condition where the height of the underside of the train's floor structure and the underside of the dump truck's load are aligned). Six cargo mass conditions were set: 0 kg, 2,750 kg, 5,500 kg, 8,250 kg, 11,000 kg, and 13,750 kg (assuming a 25% overload).

To incorporate the effects of passenger position within the train, three locations within the cabin were evaluated for each scenario: the front, center, and rear. A total of 111 deceleration waveforms were output and four evaluation indexes were calculated from each waveform: two types of "mean deceleration," "maximum deceleration," and "integral of deceleration." The two types of "mean deceleration" are indexes [1] that are the maximum value of the moving average of the deceleration waveform over 30 ms and 120 ms sections, hereafter referred to as "mean deceleration_30 ms" and "mean deceleration_120 ms" respectively. Additionally, "maximum deceleration" is an index [2] that is the maximum value of the deceleration waveform processed through a 50 Hz low-pass filter. The "integral of deceleration value" is the single integral of the deceleration waveform up to the time t_{imp}, at which point the double integral of the deceleration waveform becomes equal to the distance between the initial seating position of the dummy and the bench-end partition (see Fig. 3, seat 1: 277 mm, seat 2: 690 mm, seat 3: 1,150 mm, seat 4: 1,610 mm). In other words, t_{imp} corresponds to the estimated time until the passenger collides with the partition for a second time (secondary collision).

2.2 Conditions and injury index for passenger injury analysis

To evaluate the effect of a passenger's initial seating position on injury levels during a secondary collision with the bench-end partition, we created a scenario in which one dummy model was seated in seats 1 to 4 relative to the partition (Fig. 3). The seat width for one person was set to 460 mm, and the center of the seat was positioned at the center of the head. However, for the first seat condition, the dummy model was too large to be seated in the center of the seat width, so it was seated 47 mm away from the center and the partition. By inputting the 111 deceleration waveforms described in the previous section for each of these seating conditions, a total of 444 conditions were analyzed.

The head injury level and head speed in the direction of train

Table 1 Analysis conditions of level crossing accident

Analysis condition	Collision speed [km/h]	Collision position in horizontal direction	Collision angle [degree]	Collision position in vertical direction	Cargo mass [kg]
Case1-1_20 km/h	20	Center of load	0	Reference position	11,000
Case1-1_30 km/h	30	Center of load	0	Reference position	11,000
Case1-1_40 km/h	40	Center of load	0	Reference position	11,000
Case1-1_54 km/h	54	Center of load	0	Reference position	11,000
Case1-1_60 km/h	60	Center of load	0	Reference position	11,000
Case1-2_40 km/h	40	Center of gravity of dump truck	0	Reference position	11,000
Case1-3_40 km/h	40	Center of gravity of cabin	0	Reference position	11,000
Case1-4_40 km/h	40	1/2 lap	0	Reference position	11,000
Case1-5_40 km/h	40	1/4 lap	0	Reference position	11,000
Case2-1_40 km/h	40	Center of load	+5	Reference position	11,000
Case2-2_40 km/h	40	Center of load	−5	Reference position	11,000
Case2-3_40 km/h	40	Center of load	+10	Reference position	11,000
Case2-4_40 km/h	40	Center of load	−10	Reference position	11,000
Case3-1_40 km/h	40	Center of load	0	Reference position -177 mm	11,000
Case3-2_40 km/h	40	Center of load	0	Reference position -354 mm	11,000
Case3-3_40 km/h	40	Center of load	0	Reference position -512 mm	11,000
Case4-1_40 km/h	40	Center of load	0	Reference position	0
Case4-2_40 km/h	40	Center of load	0	Reference position	2,750
Case4-3_40 km/h	40	Center of load	0	Reference position	5,500
Case4-4_40 km/h	40	Center of load	0	Reference position	8,250
Case4-5_40 km/h	40	Center of load	0	Reference position	13,750
Case1-2_54 km/h	54	Center of gravity of dump truck	0	Reference position	11,000
Case1-3_54 km/h	54	Center of gravity of cabin	0	Reference position	11,000
Case1-4_54 km/h	54	1/2 lap	0	Reference position	11,000
Case1-5_54 km/h	54	1/4 lap	0	Reference position	11,000
Case2-1_54 km/h	54	Center of load	+5	Reference position	11,000
Case2-2_54 km/h	54	Center of load	−5	Reference position	11,000
Case2-3_54 km/h	54	Center of load	+10	Reference position	11,000
Case2-4_54 km/h	54	Center of load	−10	Reference position	11,000
Case3-1_54 km/h	54	Center of load	0	Reference position -177 mm	11,000
Case3-2_54 km/h	54	Center of load	0	Reference position -354 mm	11,000
Case3-3_54 km/h	54	Center of load	0	Reference position -512 mm	11,000
Case4-1_54 km/h	54	Center of load	0	Reference position	0
Case4-2_54 km/h	54	Center of load	0	Reference position	2,750
Case4-3_54 km/h	54	Center of load	0	Reference position	5,500
Case4-4_54 km/h	54	Center of load	0	Reference position	8,250
Case4-5_54 km/h	54	Center of load	0	Reference position	13,750

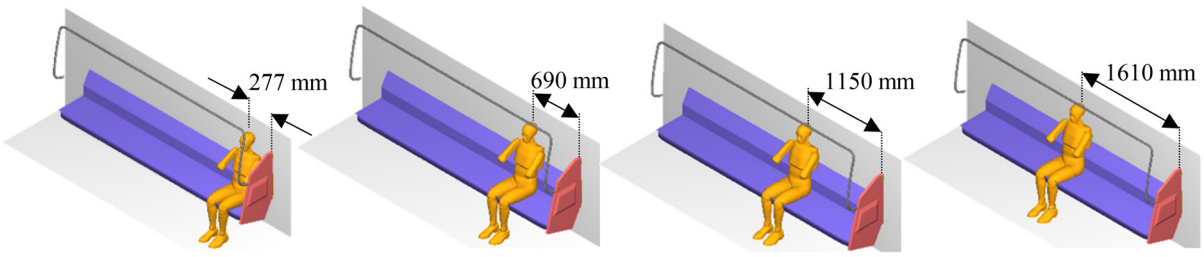

(a) Ps1 (b) Ps2 (c) Ps3 (d) Ps4

Fig. 3 Condition of initial seating position

travel at the time of the secondary collision with the partition (secondary impact velocity) were calculated using the dummy model. The head injury level was calculated using the Head Performance Criterion (hereinafter referred to as HIC, as it is calculated in the

same way as the Head Injury Criterion, which is an index of head injury from the front direction) specified in the Safety Standards [12]. The higher the value, the higher the risk of injury. The limit value is set at 1000. HIC was calculated from the resultant acceleration of the dummy head in three translational directions using eq. (1). In this report, injury severity was evaluated using HIC and its limit value of 1000.

$$HIC = \left\{ (t_2 - t_1) \left[\frac{\int_{t_1}^{t_2} a(t)\,dt}{(t_2 - t_1)} \right]^{2.5} \right\}_{max} \quad (1)$$

$|t_1 - t_2| \leq 36$ms, a(t): Head translational 3-axis resultant acceleration [G]

3. Results of passenger injury analysis and evaluation indexes

Of the total 444 conditions, 375 conditions (1st seat: 81 conditions, 2nd seat: 111 conditions, 3rd seat: 111 conditions, 4th seat: 72 conditions) were confirmed to cause the head to undergo a secondary collision with the bench-end partition. Of these, 75 conditions were confirmed to cause the HIC to fall below 50 (5% of the limit value of 1000). In this report, we evaluated 300 conditions (1st seat: 62 conditions, 2nd seat: 111 conditions, 3rd seat: 87 conditions, 4th seat: 40 conditions) in which secondary impact behavior was confirmed and the HIC was 50 or higher.

3.1 Evaluation based on deceleration integral value

Figure 4 shows the relationship between the "deceleration integral value" and HIC for each initial seating position, as shown in Section 2.1, along with the limit value. In the first seating condition, the limit value was significantly lower than the limit value in all seating conditions. In the fourth seat, the limit value was exceeded in only one condition, while in the second seat, the limit value was exceeded in 77 conditions and in the third seat, the limit value was exceeded in 31 conditions. Within the range of accident scenarios considered in this study, the risk of head injury was higher in the second and third seats than in the first and fourth seats, with the second seat tending to be the highest. In general, it was confirmed that the HIC tended to increase as the deceleration integral value increased in all seating conditions, but in the second seat, it was confirmed that once the deceleration integral value exceeded approximately 5 m/s, the HIC did not increase any further and tended

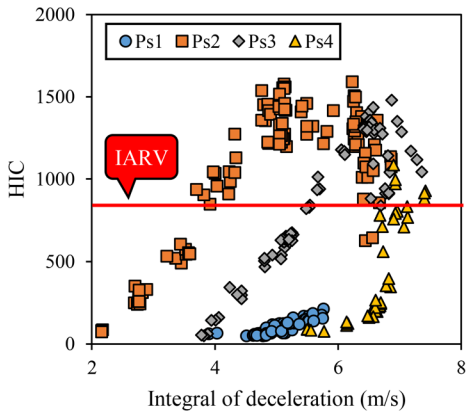

Fig. 4 Comparison of HIC and integral of deceleration by the seating position

to decrease. It is thought that this is due to the dummy's head straddling the upper part of the bench-end partition immediately after the secondary impact. Because the behavior of the dummy affecting the HIC differs when the dummy is and isn't straddling (described in detail in Section 4.1), section 3.2 examined the evaluation indexes for the car body structure in the non-straddling condition.

3.2 Study of evaluation indexes for vehicle body structure

In the second and third seat conditions, where the risk of head injury was high, the coefficients of determination were calculated using a linear approximation of four vehicle structure indexes, namely "integral of deceleration," "mean deceleration at 30 ms" and "mean deceleration at 120 ms" in the European standard, and "maximum deceleration" in the US standard, and the HIC (an indicator of injury severity). And the correlation between these indexes and the HIC was compared (Fig. 5). For these comparisons, 78 conditions were used for the second seat, excluding the conditions in which the straddling behavior described in the previous section was observed from the 111 conditions in which the HIC was 50 or more, and 87 conditions in which the HIC was 50 or more were used for the third seat.

Comparing the coefficients of determination for the four indexes and HIC (Fig. 5(e)), the coefficients of determination for "integral of deceleration" and "mean deceleration at 120 ms" were similarly high in the second seat condition, and the coefficient of determination for "integral of deceleration" was the highest in the third seat condition. This indicates that under the seating conditions in question, the "integral of deceleration value" is an index that has a higher correlation with the degree of injury to passengers than the "mean deceleration" and "maximum deceleration."

4. Discussion

4.1 Considerations regarding seating conditions for the second seat

In the second seating condition, where the risk of head injury was the highest, the HIC tended to decrease when the "deceleration integral" exceeded approximately 5 m/s (Fig. 4). Previous sled tests (tests in which the "passenger injury analysis" performed in this report was performed using actual in-car equipment and dummies) confirmed that the HIC increases as the secondary impact velocity of the head increases [13]. Therefore, the secondary impact velocity and "deceleration integral" in the second seating condition were compared (Fig. 6). As shown in this figure, there was no tendency for the secondary impact velocity to decrease when the deceleration integral was 5 m/s or more, so it can be concluded that the decrease in HIC is not caused by a decrease in the secondary impact velocity.

Comparing the "deceleration integral" and the dummy behavior as shown in Fig. 7, when the "deceleration integral" increased, the dummy's falling toward the bench-end partition side was reduced, and the head was confirmed to straddle the upper part of the partition immediately after the secondary impact. Specifically, as shown on the right side of Fig. 7, when the head hits the partition at a height of approximately 1.2 m or more from the floor, the head moves over the partition to the right side of the figure immediately after the secondary impact. This behavior reduces the impact acceleration generated at the head during the secondary impact, resulting in a lower HIC. This phenomenon has also been confirmed in sled tests [3].

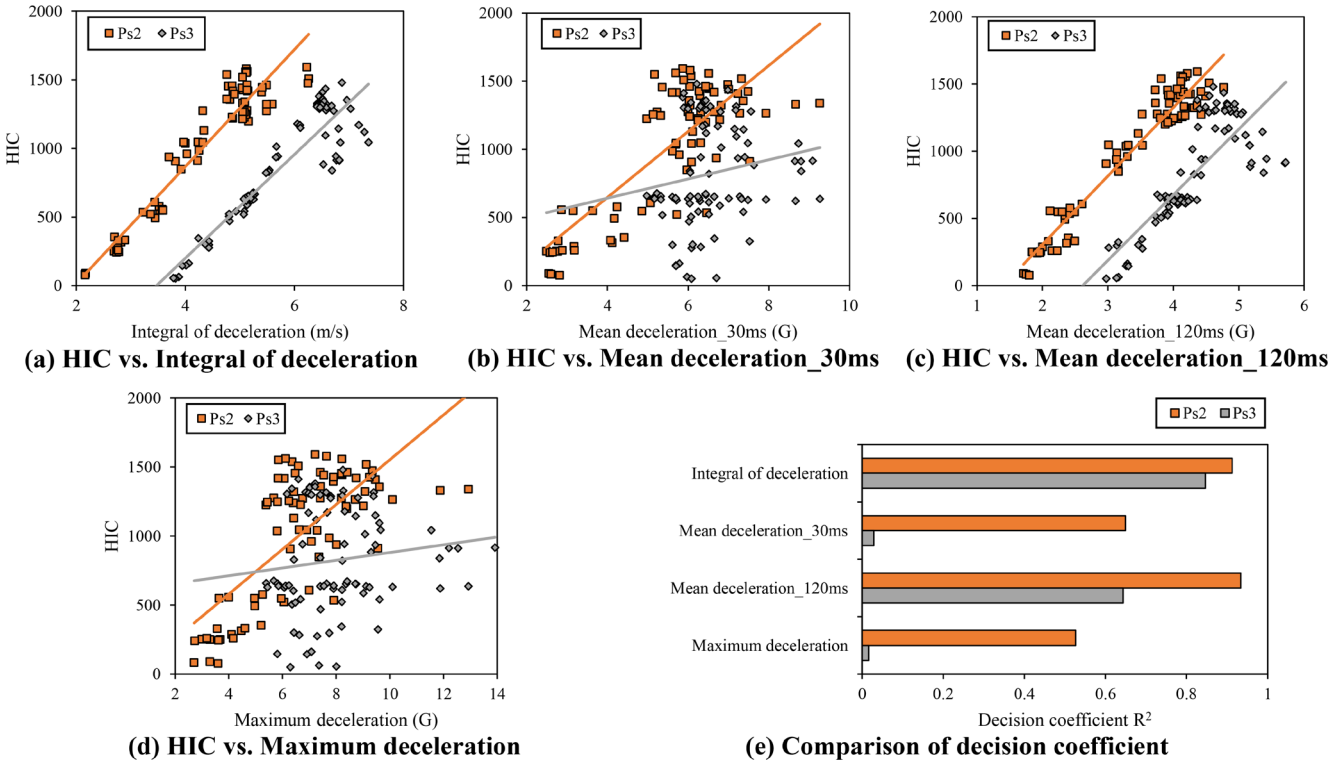

(a) HIC vs. Integral of deceleration (b) HIC vs. Mean deceleration_30ms (c) HIC vs. Mean deceleration_120ms

(d) HIC vs. Maximum deceleration (e) Comparison of decision coefficient

Fig. 5 Comparison of correlation between HIC and safety evaluation indexes at Ps2 and Ps3

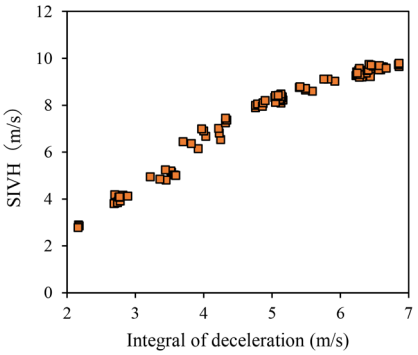

Fig. 6 Comparison of SIVH and Integral of deceleration at Ps2

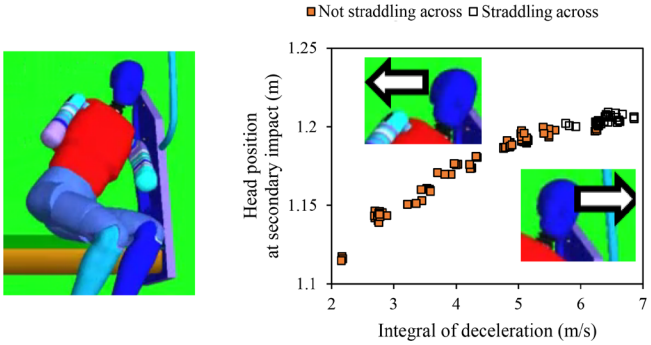

Fig. 7 Head position from the floor at secondary impact vs. integral of deceleration

4.2 A study on the correlation between vehicle body structure evaluation indexes and injury severity

In the previous chapter, we clarified that the "integral of deceleration" was highly correlated with the degree of injury to passengers in the second and third seat conditions, which have a high risk of head injury. To investigate this further, we calculated the coefficient of determination by linearly approximating the "integral of deceleration," "mean deceleration," and "maximum deceleration," which are evaluation indexes of the car body structure, as well as the secondary impact velocity. We then compared the correlation (Fig. 8). For the second seat condition, data from 78 conditions in which the head did not straddle the bench-end partition, as described in the previous section, was used. Figure 8(a) shows that the secondary impact velocity increases as the "integral of deceleration" increases. As confirmed in Section 3.1, the risk of injury is highest in the second seat and the secondary impact velocity was also high. Furthermore, the coefficient of determination for the "integral of deceleration" was high for both seating conditions (Fig. 8(e)), indicating that the secondary impact velocity, which affects the HIC, is highly correlated with the "integral of deceleration." From the above, the high correlation between the "integral of deceleration" and the HIC is largely influenced by the secondary impact velocity.

4.3 Proposal of evaluation index and limit value for vehicle body structure

Considering the analysis results and discussion, the "deceleration integral" is considered to be the most suitable crashworthiness evaluation index for the design of the vehicle body structure among the indexes compared this time, because it has a high correlation with passenger injury levels and contains information on seating positions on longitudinal seats, i.e. the time until the secondary impact. When using the "deceleration integral" as an evaluation index

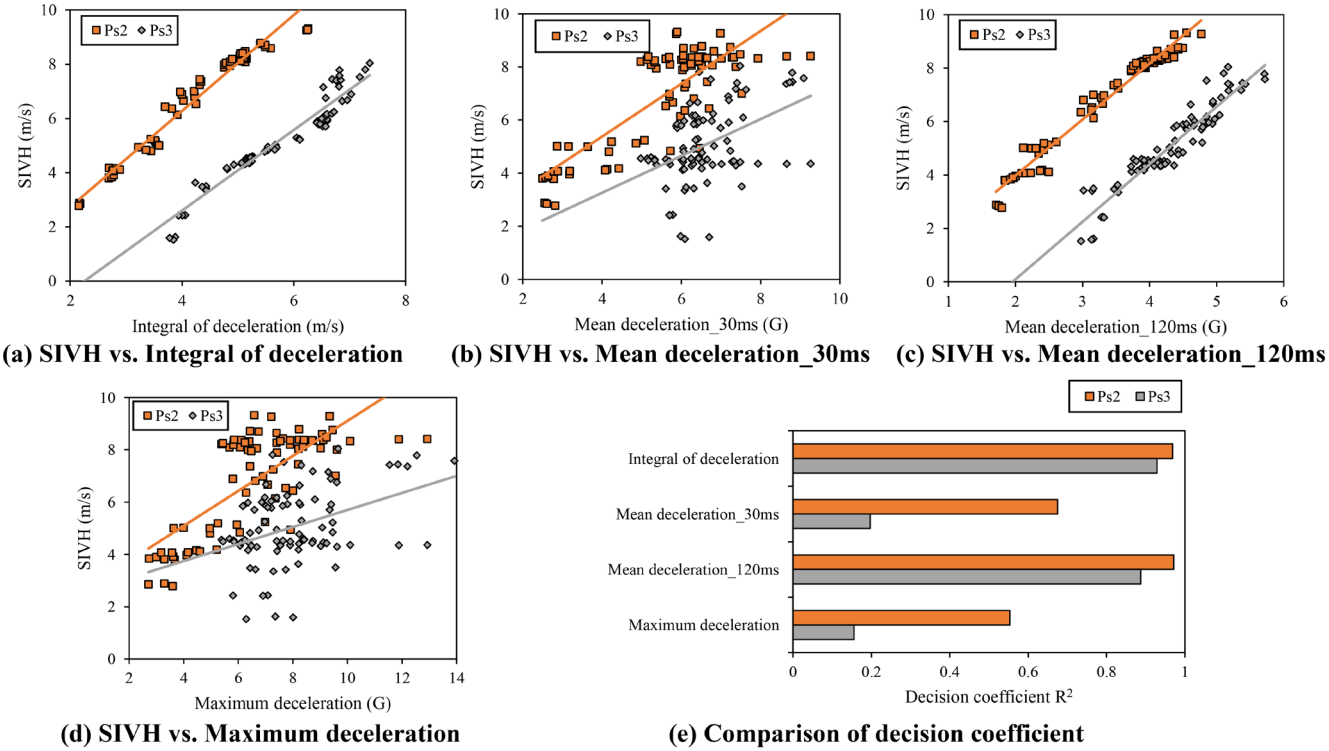

(a) SIVH vs. Integral of deceleration (b) SIVH vs. Mean deceleration_30ms (c) SIVH vs. Mean deceleration_120ms

(d) SIVH vs. Maximum deceleration (e) Comparison of decision coefficient

Fig. 8 Comparison of correlation between SIVH and safety evaluation indexes at Ps2 and Ps3

for the vehicle body structure, a positive correlation was observed between the "deceleration integral" and the HIC. Therefore, in order to improve crashworthiness, it is desirable for the "deceleration integral" to be low in the vehicle body during a collision. In addition, since it was confirmed that the seating condition of the second seat has a higher risk of head injury than other seating conditions, it is desirable to target this seating condition. From the above, referring to the results of the seating condition of the second seat shown in Fig. 5(a), it is recommended that the limit value for the "deceleration integral" to ensure safety (hereinafter, the vehicle body structure limit value) is set at approximately 4.0 m/s or less, taking into account the injury level limit value of 1000 for the HIC (Fig. 9(a)).

In Japan, where there are no evaluation standards, the "integrated deceleration value" is optimal. However, with the aim of global standardization, such as the ISO standardization of crash safety evaluation standards, the "120 ms mean deceleration" which is used in the European standard has a good correlation with injury severity, so it was also considered appropriate to select this as the domestic evaluation index. However, the limit value of 5.0 G [1] for vehicle body structures based on this index far exceeds the injury severity limit value of HIC as shown in Fig. 9(b). Therefore, when using it to evaluate vehicle body structures with longitudinal seats in Japan, it is recommended to use a value of approximately 3.0 G or less, taking the injury severity limit value of 1000 into account.

We have presented an evaluation index and its limit value for vehicle body structures that align with the actual situation in Japan, but the severity of injury depends on the interior fittings that are hit in the secondary impact. There are various types of bench-end partitions at the ends of longitudinal seats, and in this report, we used one of the plate-type partitions that has been widely adopted in Japan in recent years. The high correlation between the "integral of deceleration" and injury level is due to the fact that the integral of deceleration has been confirmed to be highly correlated with the secondary impact velocity. Therefore, it is expected that the correlation with

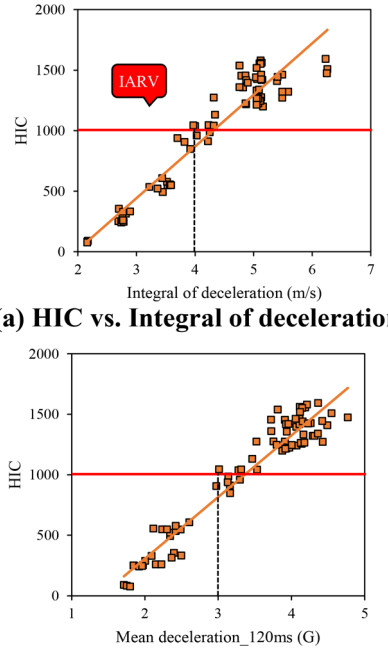

(a) HIC vs. Integral of deceleration

(b) HIC vs. Mean deceleration_120ms

Fig. 9 Comparison of correlation between HIC and safety indexes at Ps2

injury level will be high even if the partition is of a different plate type. On the other hand, the limit value of the recommended body structure may differ depending on the type of partition (integral of deceleration 4.0 m/s, mean deceleration of 3.0 G over 120 ms). It is expected that the limit value of this evaluation index can be increased by reducing the injury level by changing the partition design. Therefore, the limit value presented in this report is considered

to be a strict value (a safe assumption when considering the injury level).

4.4 Future study

The results of this report are based on the assumption that impact deceleration occurs only in the direction of train travel, and that a dummy seated alone on a longitudinal seat experiences a secondary collision with the bench-end partition. In reality, train behavior is not limited to the direction of travel, and is also affected by the pitching of the railway vehicle. However, this situation cannot be reproduced in sled testing, and the accuracy of the analysis cannot be ensured, so this is not included in the analysis conditions. In addition, the analysis accuracy of the behavior and injury level of the dummy model and partition model during a secondary impact was confirmed by comparing with tests using actual in-car equipment such as partitions [10], but the accuracy when applied to an actual accident could not be confirmed. This is because detailed information such as "the location and degree of injury to passengers," "the in-car equipment causing the injury," and "the seating position at the time of the accident" in the event of a railway crossing accident has not been made public at present.

Although an analysis was conducted under limited conditions for a situation where multiple dummies were seated on a longitudinal seat, an increase in chest injury values due to secondary collisions with other dummies was observed [14]. However, there are many combinations of the number of dummies seated on the longitudinal seat and the seating positions, and the ES-2 dummy can only evaluate one side of the chest at a time, so the combinations are even more diverse. In addition, since the physique of the ES-2 dummy is larger than that of Japanese people, it is difficult to reproduce a 100% sitting rate in a natural posture on the longitudinal seat, and some ingenuity is required in setting the analysis conditions. For this reason, the evaluation of multiple passengers is considered a future issue.

5. Conclusions

In order to improve the safety of passengers in longitudinal seats during train accidents, we investigated a crashworthiness evaluation method suited to the actual situation in Japan that can be used in the design of car body structures that take crashworthiness into account. We performed crash analyses under various level crossing accident conditions, referring to past accidents that have occurred in Japan. As a result, we proposed the integral value of the car body deceleration as an evaluation index, with the integral time being the time t_{imp} calculated from the distance between the dummy initial position and the bench-end partition, which showed the highest correlation with the degree of head injury of passengers seated in longitudinal seats. In addition, we proposed a limit value of 4.0 m/s or less for the second seating condition when using this index. We also showed that the 120 ms mean deceleration, which is the evaluation index of the European standard, could be a candidate for the evaluation index, with a view to global commonality, such as the future establishment of ISO crashworthiness evaluation standards. In the future, we plan to use the proposed evaluation index to propose specific car body structures and in-car equipment measures. When determining crashworthiness assessment indexes and their limit values in Japan, it is necessary to hold discussions among relevant government ministries, railway operators, rolling stock manufacturers, and other relevant stakeholders, and we believe that the knowledge gained in this report will be useful at that time.

This report is a reprint of the content published in the Transactions of the Japan Society of Mechanical Engineers in 2021 [15] with some omissions and modifications.

References

[1] CEN, *EN15227 2020 Railway applications –Crashworthiness requirements for rail vehicles*, 2020.

[2] Federal Railroad Administration, *49 CFR Part 238 Passenger equipment safety standards*, 2011.

[3] Nakai, K. and Enami, S., "Experimental validation of effect on reducing the severity of injury to rail passengers occupying longitudinal seats using handrails in the event of collision," *Transactions of the JSME*, Vol. 85, No. 878, 2019 (in Japanese), DOI: 10.1299/transjsme.19-00093.

[4] Marunaka, T., Taguchi, M., Kishida, K., Kumamoto, H. and Yoshikawa, T., "Rail vehicle design for crashworthiness (1st report, Development of carbody structure for high energy absorption and calculation method for crashworthiness)," *Transactions of the Japan Society of Mechanical Engineers*, Series A, Vol. 67, No. 664, pp. 72-78, 2001 (in Japanese).

[5] Marunaka, T., Taguchi, M., Kimura, T., Kishida, K., Kumamoto, H. and Yoshikawa, T., "Rail vehicle design for crashworthiness (2nd report, Carbody crash test and crash behavior by numerical calculation)," *Transactions of the Japan Society of Mechanical Engineers*, Series A, Vol. 68, No. 666, pp. 163-168, 2002 (in Japanese).

[6] Kimura, S., Mochida, T., Kawasaki, T., Nakamura, H. and Yamaguchi, T., "Evaluation of energy absorption of crashworthy structure for railway's rolling stock (Numerical simulation using damage-mechanics model)," *Transactions of the Japan Society of Mechanical Engineers*, Series A, Vol. 78, No, 793, pp. 98-112, 2012 (in Japanese).

[7] Hamajima, T. and Terumichi, Y., "Train set motion analysis in large displacement in consideration of plastic deformation of a coupler," *Transactions of the Japan Society of Mechanical Engineers*, Series C, Vol. 79, No. 806, pp. 497-507, 2013 (in Japanese).

[8] Okino, T., Nagata, K., Horikawa, K. and Kobayashi, H., "Evaluation method for crashworthiness of railway vehicles based on the correlation with the degree of passenger injury," *Transactions of the JSME*, Vol. 86, No. 881, 2020 (in Japanese), DOI: 10.1299/transjsme.19-00249.

[9] Okino, T., Nagata, K., Sato, H., Horikawa, K. and Kobayashi, H., "Evaluation of effect of various collision conditions on safety of occupants in the event of level crossing accident," *Transactions of the JSME*, Vol. 85, No. 869, 2019 (in Japanese), DOI: 10.1299/transjsme.18-00270.

[10] Nakai, K., Suzuki, D., Enami, S., Okino, T. and Takano, J., "An estimation of the severity of passenger injuries seated on a longitudinal seat in a train accident and measures to mitigate it by using numerical simulation," *RTRI report*, Vol. 33, No. 1, pp. 29-34, 2019 (in Japanese).

[11] Okino, T., Yamamoto, M., Takano, J. and Ujita, Y., "Crashworthiness evaluation for train carbody in the event of level crossing accident by driver's injury indexes," *Proceedings of the 19th Jointed Railway Technology Symposium 2012*, No. 12-79, pp. 557-560, 2012 (in Japanese).

[12] Ministry of Land, Infrastructure, Transport and Tourism, *Announcement details appendix 24: Technical standard for the*

occupant protection device in the event of a lateral collision, The new safety standard of the road transport vehicle, pp. 769-811, 2009 (in Japanese).
[13] Nakai, K., Suzuki, D., Enami, S., Okino, T., Takano, J. and Palacin, R., "An Estimation of behaviour and severity of injury to rail passengers occupying longitudinal seats in the event of collision," *Proceedings of IRCOBI Conference 2015*, pp. 315-326, 2015.
[14] Omino, K., Nakai, K., Shiroto, H. and Suzuki, D., "Simulation of behavior of passengers aboard commuter train in the event of level crossing accident," *RTRI report*, Vol. 26, No. 1, pp. 21-26, 2012 (in Japanese).
[15] Nakai, K., Enami, S., Okino, T. and Nagata, K., "Evaluation method for crashworthiness of railway vehicles based on the correlation with the injury severity of passengers occupying longitudinal seats," *Transactions of the JSME*, Vol. 87, No. 903, 2021 (in Japanese), DOI: 10.1299/transjsme.21-00181.

Authors

Kazuma NAKAI, Dr.Eng.
Senior Chief Researcher, Head of Ergonomics Laboratory, Human Science Division
Research Areas: Interior Passive Safety, Human Dynamics, Ergonomics

Shota ENAMI
Senior Researcher, Ergonomics Laboratory, Human Science Division
Research Areas: Interior Passive Safety, Ergonomics

Tomohiro OKINO, Ph.D.
Senior Chief Researcher, Head of Vehicle & Bogie Parts Strength Laboratory, Vehicle Technology Division (Former)
Research Areas: Crashworthiness, Carbody Strength

Keisuke NAGATA
Senior Researcher, Vehicle & Bogie Parts Strength Laboratory, Vehicle Technology Division
Research Areas: Crashworthiness, Carbody Strength

Shake Table Test and Numerical Simulation on Verification for Seismic Stability of Railway Embankments Taking into Account Damage Process

Ryuichi IBUKI **Tatsuya DOI** **Jun IZAWA**
Soil Dynamics and Earthquake Engineering Laboratory, Center for Railway Earthquake Engineering Research

Kentaro UEMURA **Sokkheang SRENG**
Nippon Koei Co., Ltd.

This study aims to validate a seismic performance verification method for embankments that accounts for the damage process up to sliding failure. A centrifuge shake table test was conducted to observe the damage process during shaking. Results showed that sliding failure occurred as soon as shear strain at the toe of the slope exceeded the limit value of Damage level 3. Furthermore, the FEM using the GHE-S model combined with the multi-shear spring model successfully reproduced the damage process. These findings confirm the applicability of the proposed analysis method for both safety and reparability assessments of embankments.

Key words**:** *embankment, seismic design, damage process, centrifuge shake table test*

1. Introduction

In the seismic design of embankments in the Japanese railway field, the settlement of an embankment calculated using Newmark's sliding block method (Newmark [1]) (hereinafter referred to as "Newmark method"), which assumes arc slip failure, is often used as a verification index for reparability (Railway Technical Research Institute [2, 3]) (hereinafter referred to as "the earth structure design standard" and "the seismic design standard"). This is because the Newmark method can easily calculate some reasonable sliding displacement. In general, it is supposed to verify reparability instead of safety because reparability verification is stricter than safety. Furthermore, many studies have been conducted to improve the accuracy of the Newmark method, for example, as described in Sarma [4].

On the other hand, because the Newmark method assumes rigid-plastic arc slip failure, it does not always accurately reproduce the damage process of embankments up to the point of sliding failure. This makes it difficult to properly evaluate seismic performance. For instance, Fujiwara et al. [5] compared the observed seismic displacement of railway embankments during the 2011 off the Pacific coast of Tohoku Earthquake with the settlement calculated using the Newmark method. As a result, although 13 embankments were actually undamaged, settlements exceeding 200 mm were calculated for five of them, which is generally regarded as the threshold for minor damage in the seismic design standard. They also cited the following factors as contributing to this discrepancy: errors in the setting of geotechnical material properties and input seismic acceleration, the influence of soft supporting ground, and differences in failure modes. In particular, the difference in failure mode is that the Newmark method assumes sliding failure, whereas the actual phenomenon is often limited to damage that does not lead to sliding failure, such as settlement, slope bulging, and cracking. In other words, the safety factor of the extreme balance method based on arc slip failure, which is assumed in the Newmark method, cannot evaluate this damage process leading up to sliding failure.

Based on the above background, we carried out centrifuge shake table tests to clarify the seismic damage process of embankments (e.g., Izawa et al. [6]). As a result, from digital images captured after each shaking, it was clarified that shear strain was concentrated at the toe of the slope and the sliding plane was formed from there as the damage process leading to sliding failure. It was also confirmed that the strain level at which sliding failure occurs can be explained by the damage level specified by the deformation characteristics of the embankment material, as shown in Fig. 1. In addition, a seismic safety performance verification method using shear strain at a toe of a slope was proposed that can take into account the damage process (hereinafter referred to as the "proposed verification method"). However, in the test, sinusoidal waves were input, and these tests results were observed based on image analysis using digital images captured before and after shakings. The damage process during earthquakes is not fully clarified.

In this study, we attempted to observe the damage process of embankments during earthquakes in the centrifugal acceleration field and to confirm the validity of the proposed verification method. In addition, a seismic response value calculation method using Finite Element Method (FEM) analysis was also discussed to estimate shear strain necessary for the safety verification in the proposed verification method. At this time, we combined the multiple shear spring model with the GHE-S model, which is often used in a ground response analysis in the Japanese railway field, in order to keep the calculations from becoming too complicated for practical seismic design. Finally, the results of the test and the FEM analysis were compared to validate the proposed verification method and the applicability of the calculation method using FEM analysis.

2. Centrifuge Shake table test

A centrifuge shake table test was carried out to clarify the damage process of an embankment with steep slope gradient during earthquakes. A beam type centrifuge with a diameter of 5.2 m and a shake table of the Nippon Koei Co. LTD. (Sreng et al. [7]) were used in this study. In particular, the damage process was observed in detail by capturing high-speed, high-resolution digital images of the embankment not only before and after shaking, but also during shaking. This test was carried out at a centrifugal acceleration field of 50 G. Hereafter, all values are expressed in prototype scale unless stated otherwise.

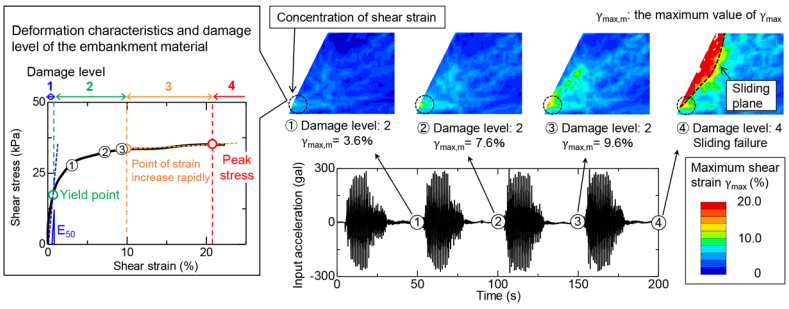

Fig. 1 Seismic damage process leading to sliding failure in previous study [6]

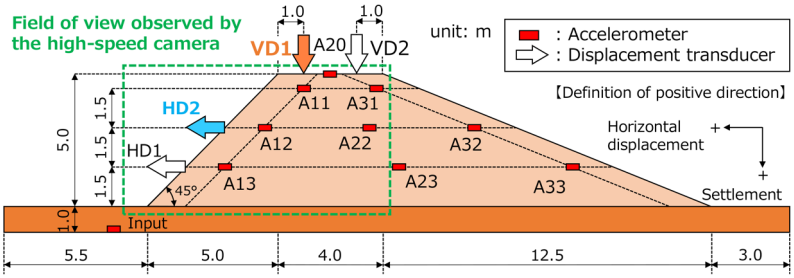

Fig. 2 Schematic view of model embankment

Table 1 Physical properties of Edosaki sand

Soil particle density	: G_s	2.68
Mean grain size	: D_{50}	0.34 mm
Effective grain size	: D_{10}	0.15 mm
Uniformity coefficient	: U_c	2.6
Coefficient of curvature	: U'_c	1.00
Fine content	: F_c	4.4%
Optimum water content	: w_{opt}	14.6%
Maximum dry density	: ρ_{dmax}	1.707 g/cm^3

Table 2 Physical and Mechanical properties of Edosaki sand (Dc = 95%)

Dry density	: ρ_d	1.622 g/cm^3
Degree of compaction	: D_c	95%
Compression index	: C_c	0.055
Consolidation yield stress	: P_c	318.1 kPa
Cohesion	: c	9.5 kPa
Internal friction angle	: φ	32.5 deg.

2.1 Outline of the test

Figure 2 shows the schematic view of the model embankment, together with an arrangement of sensors. The slope of the left side embankment was set to be 1:1.0, which is steep enough to induce a sliding failure during shakings, since the purpose of this study is to capture the damage process of embankments leading to sliding failure. The slope of the other side was 1:2.5 so as not to cause a sliding failure. The embankment height was set to 5 m.

The embankment material used was Edosaki sand with a degree of compaction (Dc) of 95%. The physical and mechanical properties of the embankment material are shown in Tables 1 and 2. Figure 3 shows the shear stress-shear strain relationship obtained from a monotonic loading test performed on the embankment material. This test was carried out using a hollow torsional shear testing machine under a confining pressure of 50 kPa. Additionally, a proposed definition of damage levels and limit value are shown. The shear strain at the point of the maximum shear stress (τ_{max} = 48 kPa), which can be defined as the failure of the embankment material, is 7.5% (hereinafter referred to as "γ_{fail}"). This value is equivalent to the limit value γ_{cr3} of Damage level 3. Damage level 2, associated with γ_{cr2}, can be also defined as the point where the shear stress begins to increase linearly toward the failure point (γ_{fail}, τ_{max}). For the sake of convenience, this is defined as the point at which shear strain reaches approximately half of γ_{fail}. The limit value γ_{cr1}, associated with Damage level 1, shows the undamaged region, and is set at the point where shear stress reaches half of τ_{max} (24 kPa), which corresponds to the elastic region E_{50}. In this scheme, Damage level 1 signifies no damage, Damage level 2 denotes minor damage, Damage level 3 suggests relatively severe damage, and Damage level 4 is equivalent to failure. Since these limit values are defined in terms of strain, they can be considered as valid for both at a centrifugal acceleration field and 1 G field. Furthermore, these limit values were also examined under higher confining pressures of 100 kPa and 150 kPa. In the embankment material used, it was confirmed that the limit values could be set at approximately the same strain level without being affected by confining pressure.

In capturing digital images during shaking at a centrifugal acceleration field of 50 G, it is necessary that a camera possesses the ability to withstand forces equivalent to 50 times its own weight. A high frame rate is also necessary since an elapsed time is 1/50 during the tests. There are several constraints, such as lens selection to ensure an adequate field of view within confined spaces, as well as appropriate lighting arrangements. In addition, when capturing images at high-speed, it is desirable to fix a camera on a shake table to maintain a constant positional relationship between the model embankment and that camera. Hence, as in a previous study (Ibuki et al. [8]), a high-speed camera was fixed to the shake table as shown in Fig. 4 to capture digital images of an embankment during shaking. The camera speed was set to 100 frames per second, allowing for the acquisition of images at intervals of 0.5 seconds in a 50 G centrifugal acceleration field (equivalent to 0.01 second intervals in the model scale). An image analysis technique was applied to these images to calculate displacements and strain distribution of the embankment during shaking, thereby a seismic damage process of the embankment was observed in detail. In the image analysis, the mesh was approximately 250 mm by 250 mm (equivalent to 5 mm by 5 mm in the prototype scale). In addition, it was confirmed that the calculated displacement and the displacement measured with a sensor were generally in agreement.

The input acceleration wave was the Spectrum I ground motion as indicated in the seismic design standard. Although the acceleration amplitude was not accurately reproduced, the characteristics of Spectrum I were generally reproduced.

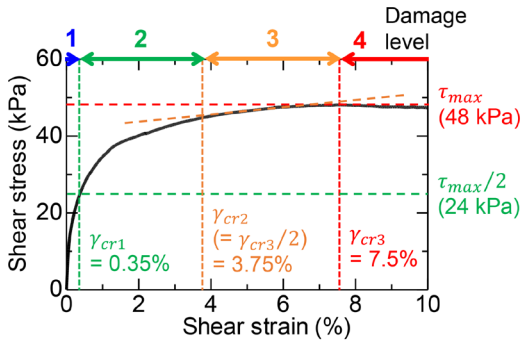

Fig. 3 Shear stress-strain relationship of Edosaki sand and proposed damage level

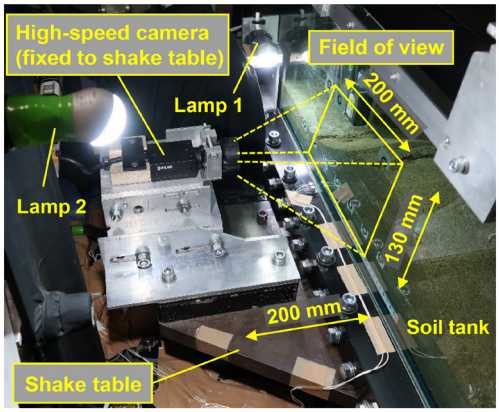

Fig. 4 Location of high-speed camera

2.2 Test Results

Figure 5 shows time histories of the maximum shear strain at the toe of the slope calculated from the image analysis using digital images captured between 5 and 30 seconds, together with horizontal displacement HD2, vertical displacement VD1 and the input acceleration. The timing of image capture is plotted in time history of the input acceleration. Furthermore, the strain distributions obtained from image analysis at ① ~ ④ are shown in Fig. 6. It was confirmed that the horizontal displacement obtained from the image analysis increased rapidly at around 29 seconds, and the model embankment experienced sliding failure as shown in Fig. 7. Additionally, the maximum shear strain at the toe of the slope increased rapidly at around 21 seconds. As illustrated in Fig. 6, the shear strain is concentrated at the toe of the slope during shaking. In particular, after 19.1 seconds, the strain is concentrated near the sliding plane as shown in Fig. 7, which is a so-called potential sliding plane. The red dotted line in Fig. 5 is the limit value of Damage level 3 (7.5%), defined from the deformation characteristics of the embankment material shown in Fig. 3. Similar to the damage process observed in the previous study (Izawa et al. [6]), when the maximum shear strain at the toe of the slope exceeds the limit value of Damage level 3 and reaches Damage level 4, the toe of the slope locally leads to shear failure and progressive failure begins, resulting in overall sliding failure. In addition, Fig. 8 shows that the volumetric strain tends to expand in the surface layer of the embankment and slightly compress in the central part. However, the magnitude of the compressive volumetric strain is only about 1%. Therefore, if compaction is sufficient and uniform, it is unlikely that the volume change will occur in the center of the embankment.

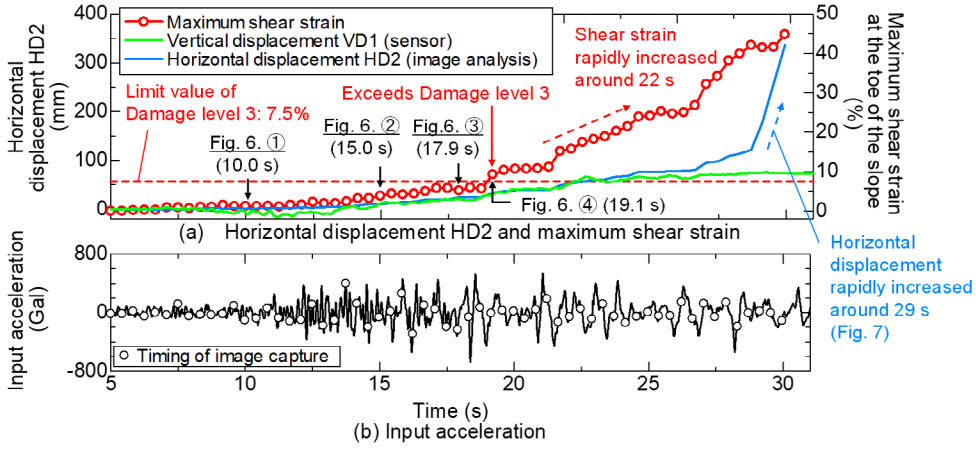

Fig. 5 Time histories of maximum shear strain at the toe of the slope and displacements

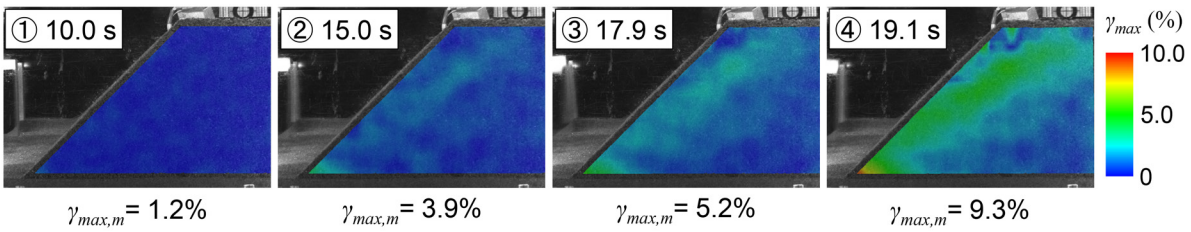

Fig. 6 Maximum shear strain distribution obtained from image analysis

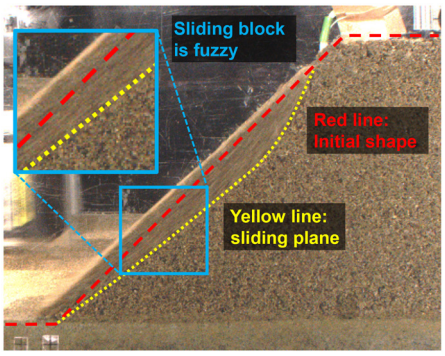

Fig. 7 Moment sliding failure occurs

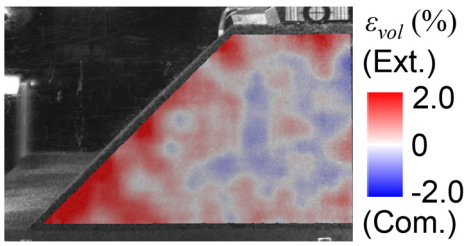

Fig. 8 Volumetric strain distribution

3. Seismic response value evaluation

The above test results indicate that an embankment with a steep slope may lead to sliding failure during earthquakes. Thus, safety verification against sliding failure is required in the seismic performance verification. Since the occurrence of sliding failure could be judged by whether or not shear strain at the toe of a slope reaches Damage level 3 of an embankment material, a seismic response value calculation method is necessary for safety verification that can evaluate shear strain accumulated at the toe of a slope. Therefore, a method based on parameters obtained from seismic design was discussed with a practical method in mind.

3.1 Outline of the numerical simulation

Here, as a practical response value calculation method, the effectiveness of the Finite Element Method (FEM) was verified. In the FEM analysis, a constitutive model was used, which was combined with the GHE-S model (Nogami et. al. [9]), a nonlinear model of a ground that is standard in the seismic design of the Japanese railways, and the multiple shear spring model (Towhata and Ishihara [10]). In this model, a number of shear springs applied to the GHE-S model take into account a region of shear stress - axial differential stress relationship and shear strain - axial differential strain relationship. For example, using two shear springs allows evaluation of shear behavior at $\theta = 45°$ and 135°. Furthermore, by using four shear springs, θ = 22.5°, 67.5°, 112.5°, and 157.5° can be evaluated. In this study, the shear behavior was evaluated at 5-degree intervals by setting 18 shear springs. When carrying out dynamic analysis using the GHE-S model, the GHE parameters are generally set by fitting shear stiffness - strain relationship obtained from dynamic shear tests. On the other hand, in this calculation of an embankment, here, it is necessary to properly evaluate the shear behavior of an embankment material up to around Damage level 3 to 4 (about 10% strain) in order to perform safety verification. Therefore, the GHE parameters were set to match the region corresponding to Damage level 3 of the embankment material used, as shown in Fig. 9 and Table 3(b). The historical damping was set by fitting the historical damping-shear strain relationship up to the 1% shear strain level. However, it was confirmed that the historical damping did not significantly affect the analytical results of the embankment. The analysis parameters used in the study are listed in Table 3(a). Here, the reference strain γ_r is calculated from the shear strength τ_f and the initial shear stiffness G_0 as $\gamma_r = \tau_f / G_0$. The shear strength parameters were set as well, as shown in Table 3, for the central part of the embankment, while for the slope surface, the cohesion was reduced considering the drying of the embankment material. In addition, joint elements were placed between the surface layer of the embankment and the supporting ground, because the toe of the slope was observed to slide toward the front of the slope during shaking.

In this calculation, first, an embankment was analyzed under self-weight as an elastic body with uniform shear stiffness. The

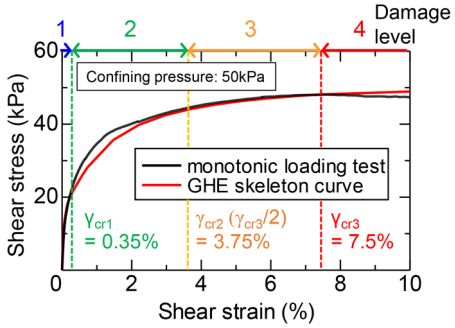

Fig. 9 GHE skeleton curve calibrated to monotonic loading test

Table 3 Analytical parameters

(a) physical properties

		Embankment	Supporting ground
Unit volume weight	: γ	16.9 kN/m^3	18.0 kN/m^3
Poisson ratio	: ν	0.499	0.499
Initial stress stiffness	: G_0	10,179 kN/m^2 *	165,306 kN/m^2
Cohesion	: c	3.0 kPa (Surface) 9.5 kPa (Central part)	-
Internal friction angle	: φ	32.5 deg.	-

*When the confining pressure is 1 kPa.

(b) GHE parameters

C1(0)	1.0
C2(0)	0.2
C1(∞)	0.11
C2(∞)	1.0
α	0.986
β	1.38

shear stiffness was set based on confining pressure near the center of the embankment (50 kPa). Secondly, the shear stiffness G_0 was modified to be expressed as in equation (1), which takes into account the dependence of each element on confining pressure σ_m obtained from the self-weight analysis.

$$G_0 = 10{,}179\,\sigma_m^{0.5} \quad (1)$$

Finally, dynamic analysis was carried out taking over the stress state obtained by nonlinear self-weight analysis using the shear stiffness considering the dependence on confining pressure.

3.2 Numerical simulation results and discussions

Figure 10 shows time histories of the settlement, horizontal displacement, and maximum shear strain at the toe of the slope calculated using FEM. It can be seen that the results reproduce an increasing trend in the test. Since the FE model does not take into account the deformation after shear failure, the behavior after sliding failure (around 29 seconds) is not consistent with the test. However, the maximum shear strain at the toe of the slope reaches Damage level 3 in around 16 seconds. Thus, it can be judged from the analysis result that the embankment might lead to sliding failure. Comparing the timing when the toe of the slope reaches Damage level 3 between the test and the analysis, although the analysis reaches Damage level 3 a little earlier, the timings are generally in agreement. In addition, Fig. 11 shows the distributions of the maximum shear strain after 10, 15, 16, and 20 seconds. As in the test, the damage process was adequately reproduced. Altogether, the shear strain was concentrated at the toe of the slope and the potential sliding plane.

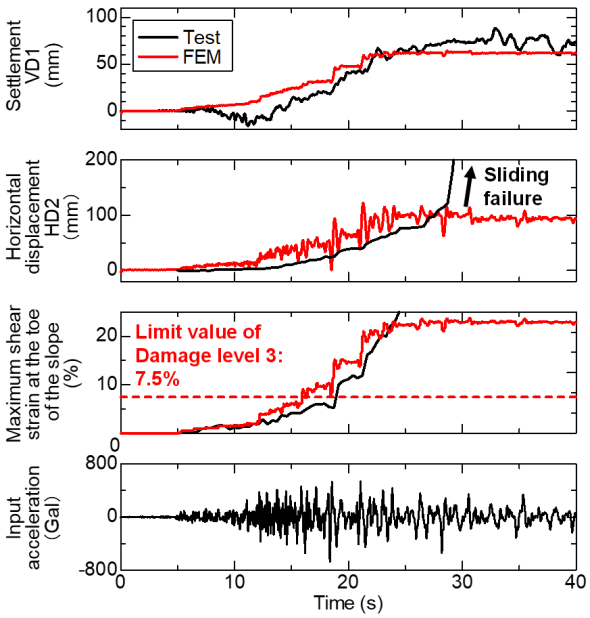

Fig. 10 Time histories obtained from the FEM analysis and the test results

In the proposed verification method, safety against sliding failure is evaluated based on whether the shear strain at the toe of the embankment, where deformation is concentrated, exceeds the limit value of Damage level 3 (γ_{fail}) of the embankment material. The FEM employed in this study not only reproduces the damage process leading up to sliding failure, but also enables precise calculation of time history of shear strain at the toe of the slope. Therefore, the proposed FEM is considered applicable as a seismic response value calculation method for verifying safety against sliding failure. Furthermore, based on the settlement at the embankment crest obtained from the FEM analysis, it is also considered possible to assess the reparability of the embankment. Although the present model does not account for volumetric strain, good agreement between test and analysis is partly attributed to the fact that volumetric strain was negligible in the test. Given that railway embankments are typically subjected to sufficient compaction, the proposed model is also considered applicable for evaluating reparability.

4. Conclusions

This study aimed to validate the proposed performance verification method for embankments that can take into account the seismic damage process up to sliding failure. A centrifuge model test was carried out to observe detailed damage process during shaking, and a seismic response value calculation method was proposed using a finite element method. The following findings were obtained:

1) A measurement system capable of high-speed, high-resolution imaging during shaking in a centrifuge acceleration field was developed. By conducting deformation analysis using digital images, it became possible to observe the seismic damage process of the embankment during shaking.
2) When the shear strain at the toe of the slope exceeded the limit value of Damage level 3 (γ_{fail}), as defined by the shear stress–shear strain relationship of the embankment material, a sliding plane developed, leading to sliding failure. This observation supports the validity of the proposed performance verification method.
3) To reproduce the test results, a two-dimensional dynamic FEM was proposed by combining the GHE-S model with the multiple shear spring model. By fitting the model parameters to align with the shear stress–strain relationship around Damage level 3 obtained from the laboratory test, it was confirmed that the proposed model can accurately capture the embankment response up to the onset of sliding failure. This confirms the applicability of the proposed calculation method for verifying the seismic safety of embankments against sliding failure.

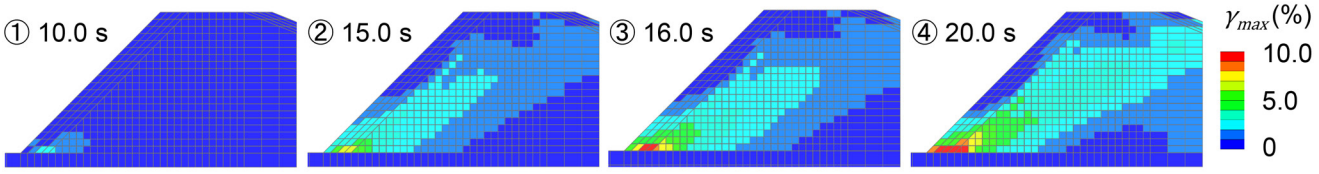

Fig. 11 Calculated distribution of maximum shear strain

References

[1] Newmark, N. M., "Effects of earthquakes on dams and embankments," *Geotechnique*, Vol. 15, No. 2, pp. 139-160, 1965.

[2] Railway Technical Research Institute. *The Design Standards for Railway Structures and Commentary (Earth Structure)*, Supervised by Ministry of Land, Infrastructure and Transportation, Maruzen, 2009 (in Japanese).

[3] Railway Technical Research Institute, *The Design Standards for Railway Structures and Commentary (Seismic Design)*, Supervised by Ministry of Land, Infrastructure and Transportation, Maruzen, 2012 (in Japanese).

[4] Sarma, S. K., "Seismic Stability of Earth Dams and Embankments," *Geotechnique*, Vol. 25, No. 4, pp. 743-761, 1975.

[5] Fujiwara, T., Nakamura. H., Taniguchi, Y., Takasaki, H. and Kaneda, J., "A study about factors which caused railway embankment damages by circular slip analysis," *Journal of Japanese Society of Civil Engineering A1*, Vol. 71, No. 4, pp. I_87-94, 2015 (in Japanese).

[6] Izawa, J., Doi, T., Suzuki, A. and Kojima, K., "Seismic Design of Embankments in Consideration of Damage Process during Earthquakes," *Quarterly Report of RTRI*, Vol. 63, No. 1, pp. 56-63, 2022.

[7] Sreng, S., Okochi, Y., Kobayashi, K., Tanaka, H., Sugiyama, H., Kusaka, T., Miki, H. and Makino, M., "Centrifuge model tests of embankment with a new liquefaction countermeasure by ground improvement considering constraint effect," *6th International Conference on Earthquake Geotechnical Engineering*, 2015.

[8] Ibuki, R., Uemura, K., Doi, T., Izawa, J. and Sreng, S., "High speed observation on damage process of embankments during earthquakes in a centrifugal acceleration field," *10th Physical Modelling in Geotechnics*, pp. 912-915, 2022.

[9] Nogami, Y., Murono., Y. and Morikawa, H., "Nonlinear hysteresis model taking into account S-shaped hysteresis loop and its standard parameters," *Proceedings of 15th World Conference on Earthquake Engineering*, 2012.

[10] Towhata, I., Ishihara, K., "Modelling soil behavior under principal stress axes rotation," *5th International Conference on Numerical Methods in Geomechanics*, pp. 523-530, 1985.

Authors

Ryuichi IBUKI
Senior Researcher, Soil Dynamics and Earthquake Engineering Laboratory, Center for Railway Earthquake Engineering Research
Research Areas: Seismic Behavior of Earth Structures

Tatsuya DOI, Ph.D.
Senior Researcher, Soil Dynamics and Earthquake Engineering Laboratory, Center for Railway Earthquake Engineering Research
Research Areas: Seismic Behavior of Structures and Earth Structures

Jun IZAWA, Ph.D.
Senior Chief Researcher, Head of Soil Dynamics and Earthquake Engineering Laboratory, Center for Railway Earthquake Engineering Research
Research Areas: Soil Liquefaction, Seismic Behavior of Surface Ground, Seismic Behavior of Earth Structures

Kentaro UEMURA, Dr.Eng.
Researcher, NIPPON KOEI CO., LTD., Geotechnical Experiment Group, Testing & Experiment Center, Research and Development Center
Research Areas: Geotechnical Experiment, Soft Soils and Liquefaction, Seismic Resistance of Retaining Wall, Soil Improvement

Sokkheang SRENG, Dr.Eng.
Chief Specialist, NIPPON KOEI CO., LTD., Geotechnical Experiment Group, Testing & Experiment Center, Research and Development Center
Research Areas: Geotechnical Experiment, Shear Strength of Coarse-grain Material, Soft Soils and Liquefaction, Seismic Resistance of Embankments

Method for Verifying the Restorability of Railway Viaducts Using Recovery Time After an Earthquake as a Verification Index

Kimitoshi SAKAI **Kazunori WADA**
Structural Dynamics and Response Control Laboratory, Center for Railway Earthquake Engineering Research

Akihiro TOYOOKA
Center for Railway Earthquake Engineering Research

We have proposed a method for evaluating the restorability of railway structures. In the proposed method, all earthquake motions expected within a structure's design service life are used as the design of earthquakes. In addition, the recovery time after an earthquake, which is directly related to early recovery, is used as the verification index. We also propose a more practical method of expressing structural conditions with the same recovery time as a nomogram by performing calculations under various conditions in advance. The proposed method allows us to construct structures that are easy to recover in the same procedure as the conventional seismic design, and it is expected to shorten the recovery time after an earthquake.

Key words**:** *seismic design, restorability evaluation method, recovery time after an earthquake, railway structure*

1. Introduction

In addition to ensuring safety, infrastructure facilities developed as foundational structures for industrial and residential areas are required to ensure restorability during earthquakes. For example, railway structures need to "maintain in a state where they can be restored functionally in a short period of time by limiting damage to within a certain range determined by difficulty of structural repair in response to expected seismic action" [1]. One approach to confirming the restorability of these structures is to verify that the recovery period and expenses are within a reasonable range when subjected to multiple seismic motions expected during their useful lives, considering initial costs and earthquake loss costs [2]. Various facilities have undergone examinations that consider the total cost [3-5], and there are cases where this has been introduced into seismic design [6]. We previously proposed a design method for minimizing the total cost of railway RC piers [7].

Following the trends described above, the restorability of railway structures after seismic damage is, in principle, verified according to the concept [1]. On the other hand, there have been moderate earthquakes in recent years, such as the 2018 Northern Osaka Earthquake, the 2021 Earthquake off the Coast of Fukushima Prefecture, and the Northwestern Chiba Earthquake. Although structural damage in these earthquakes was limited, determining the extent of damage and undertaking post-earthquake restoration work took time. Issues regarding the early resumption of operations and post-earthquake restoration have been highlighted [8]. Methods to address such issues may include cost-based restorability verification and the explicit calculation of the post-earthquake recovery time, which can be used as an indicator for structural design. From this perspective, we previously calculated the relationship between the damage level caused by the earthquake and the recovery time required for various railway structures. We then prepared a database [9],which makes it relatively easy to calculate the recovery time for each structure after an earthquake. However, implementing these methods requires specialized design techniques and knowledge, as well as relevant information such as the probability of earthquakes and the concept of loss costs. Analytical techniques for large-scale numerical calculations are also necessary. Therefore, similar to when calculating the total cost of a structure, it is expected that implementing this method in practice will be difficult.

In this paper, we propose a method for verifying the restorability of railway structures [10]. In Section 2, we propose a verification method for railway structure restorability in which the recovery time is used as the verification index. We propose a basic procedure and present a display method called a restorability verification nomogram. This nomogram enables implementation in practical designs. In Section 3, we perform trial calculations to verify the restorability of reinforced concrete (RC) rigid-frame viaducts. In Section 4, we evaluate and validate the restorability verification nomogram for the structure that was subject to trial calculations in Section 3.

2. Proposal of restorability verification method with recovery time as a verification index

2.1 Proposal of restorability verification method

First, we propose a method for verifying the restorability of railway structures using post-earthquake recovery time as the verification index. Figure 1 shows the proposed verification procedure. The general flow process involves setting the required performance and design earthquake motion, calculating the response value of the structure and verifying its performance of the structure. This process is equivalent to the seismic design procedure of normal railway structures [1]. Meanwhile, the design method proposed here has several features.

The "post-earthquake recovery time" is set as the required performance of the structure. This directly addresses the issue of post-earthquake recovery time, which has become a serious concern in recent medium- to large-scale earthquakes.

To correspond to the above-mentioned verification index, the design earthquake motion must be set as "multiple earthquake motions with a wide range of characteristics expected at the construction location." These seismic actions are represented by a set of waveforms, and its occurrence probabilities [11] are represented by

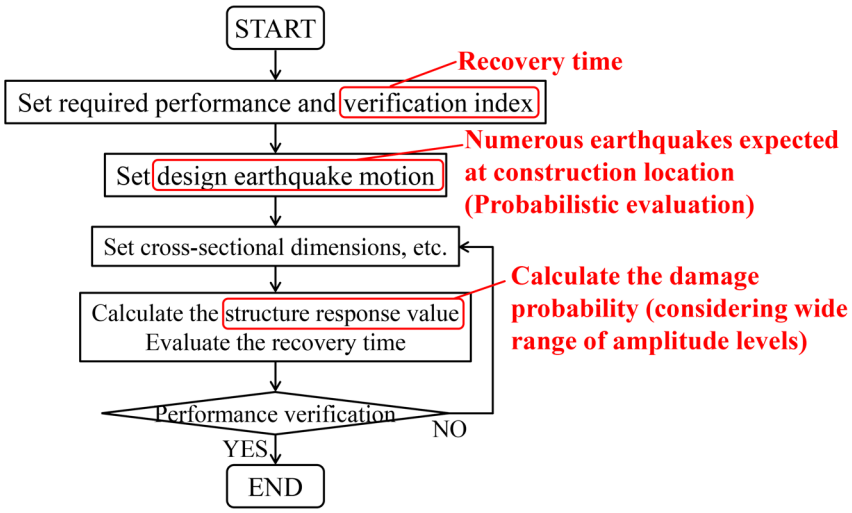

Fig. 1 Proposed restorability verification procedure

the results of probabilistic earthquake risk analysis [12, 13].

The method used to calculate the response value of the structure is based on the method used for normal seismic design. It should be noted that the current seismic design of railway structures aims to accurately evaluate the response to L2 earthquake motion. The structures are modeled to respond relatively safely to earthquake motions with smaller amplitudes than an L2 earthquake, such as the L1 earthquake and other earthquakes. However, the restorability verification method proposed in this paper requires calculating the appropriate earthquake response values for small- and medium-sized earthquakes. Therefore, it can effectively adopt a structural modeling method and response value calculation method that considers such aspects [14].

Finally, the recovery time of the structure is evaluated. This requires setting a recovery time that corresponds to the response value of the structure. However, the time required for recovery can naturally vary greatly depending on the part of the structure that is damaged and the degree of damage. Recovery is known to vary greatly depending on circumstances, such as the structural type and surrounding environment. Therefore, the recovery time must be appropriately evaluated in accordance with the earthquake response value and the situation at the location. We previously conducted a basic examination of the relationship between earthquake response value and recovery time under standard railway structure conditions [9]. The results of this examination are used in the following calculations.

The above procedure enables us to calculate the expected recovery time for a group of earthquake motions. In this procedure, the design earthquake motion is set as multiple earthquake motions acting on the structure at the target location. We plan to verify the performance by determining if it meets the required recovery time. Meanwhile, performance verification is conducted using the following equation, which is based on the limit state design method - the standard design method for railway structures.

$$\gamma_i \cdot \frac{I_{RD}}{I_{LD}} \leq 1.0 \qquad (1)$$

where I_{RD}, I_{LD}, and γ_i represent the design response value (expected recovery time), design limit value (required recovery time), and structural factor (1.0 in this study), respectively.

2.2 Restorability verification nomogram

The proposed method requires a large amount of work to set the design earthquake motion, calculate the response value, and verify the performance. Consequently, implementing this method for all structures in actual designs is difficult. Therefore, we propose a more practical method.

To verify practical restorability, it is necessary to simplify each stage of work, and the strength demand spectra [1] used in the seismic design of railway structures can then be a useful reference here. Therefore, we propose a method to evaluate the recovery time under a wide range of conditions in advance, similar to the strength demand spectra. We display this as a restorability verification nomogram. Figure 2 presents the calculation procedure for the restorability verification nomogram. An overview of each step is given below.

Step 1: Set the target location. Then, evaluate the design earthquake motion at the location. This involves considering multiple earthquake motions with a wide range of characteristics expected at construction location. This is expressed as a group of earthquake motions and their respective probabilities.

Step 2: Calculate the response value of the structure against the design earthquake motion. First, build a group of structure models with different yield seismic coefficients $k_{hy.}$ for conditions with T_{eq} and μ. Conduct a dynamic analysis on this structure by inputting the earthquake motion waveforms at the target point. Then, calculate the response ductility factor and occurrence probability of the degree of damage for each structure.

Step 3: Evaluate the recovery time corresponding to the damage obtained in Step 2. Then, multiply it by the occurrence probability to evaluate the expected recovery time.

Step 4: Set the required performance of the structure (target recovery time). Then, determine the structure that satisfies the required performance based on the relationship of the expected recovery time obtained in Step 3. The structure is a combination of T_{eq}, μ, $k_{hy.}$

Step 5: Repeat Steps 2-4 by varying the T_{eq} and μ. Using these results, connect the conditions that result in the same recovery time. This will display the combination of the structure's vibration characteristics that satisfies a certain recovery time via a nomogram.

This procedure displays the same dimensions corresponding to

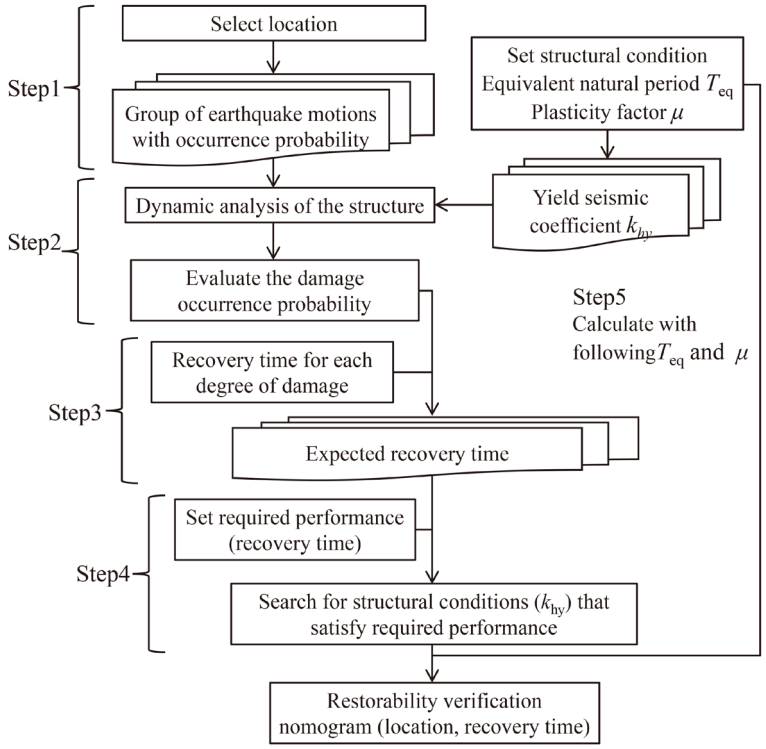

Fig. 2 Nomogram calculation procedure for restorability verification

the strength demand spectra for a location and recovery time. The calculation conditions for creating the above restorability verification nomogram are compared with those based on the fundamental method proposed in the previous section. In addition, research has confirmed that appropriate earthquake response values and damage occurrence probabilities can be calculated for railway bridges and viaducts, even if the entire structure is replaced with an equivalent single-degree-of-freedom (SDOF) system [15]. Thus, an analysis model can be used to obtain equivalent results for both. Moreover, the restorability verification nomogram displays the characteristics of the structure based on the recovery time. Therefore, it can be used for any required performance and recovery time. The proposed restorability verification nomogram uses the same seismic action as the fundamental method described in Section 2.1. The same results are obtained for the structural response value and recovery time. This suggests that the work required for verification has been considerably reduced and that an appropriate restorability verification has been achieved.

In Step 2, the "recovery time according to each earthquake response value of the structure" needs to be calculated. Since this varies considerably depending on the damaged part and the surrounding environment, multiple nomograms need to be prepared as required. Further study is needed on how to create and display a simple nomogram that considers this aspect appropriately. In this paper, however, we plan to estimate a nomogram using the relationship between earthquake response values and recovery time under standard conditions [9].

2.3 Design procedure using restorability verification nomogram

This restorability verification nomogram simplifies the determination of the seismic yield coefficient demand according to various conditions, such as the earthquake seismicity of the construction location, the vibration characteristics of structure, deformation performance, damaged areas, ease of restoration, and required performance. We summarize the restorability verification procedure for a structure using the restorability verification nomogram. Figure 3 shows the specific flow process. The differences from the basic restorability verification method proposed in Section 2.1 (Fig. 1) are listed below.

- In "design earthquake motion setting," the basic method uses a group of earthquake motions with occurrence probabilities for each region. However, in our examination, we select a restorability verification nomogram based on various conditions.
- In the "structure response value calculation and recovery

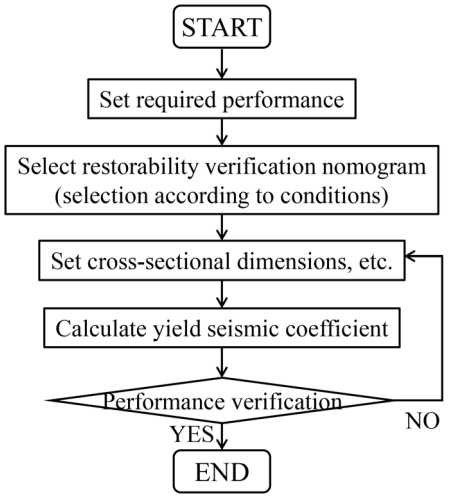

Fig. 3 Restorability verification procedure for structures using restorability verification nomogram

time evaluation," the basic method uses each waveform to evaluate the response value, damage level, and recovery time. However, in our examination, we calculate the structure's yield seismic coefficient k_{hy} is from the results of the push-over analysis.

- In the "performance verification," the basic method uses Eq. (1) to verify the recovery time. However, our study confirmed that k_{hy} of the target structure is equal to or greater than the required yield seismic coefficient calculated by the restorability verification nomogram.

As previously described, an advanced preparation of the restorability verification nomogram based on various conditions enables verification using recovery time as the verification index because its function is similar to performance verification using the strength demand spectra. Therefore, this method is considered a design procedure that can be applied to practical designs. The validity of these results is confirmed in Section 4.

3. Restorability verification of structures based on the proposed method

3.1 Setting required performance and verification index

We verify the effectiveness of the proposed method by applying the basic procedure of the restorability verification method to an actual railway structure. The ground conditions shown in Fig. 4 are used as prerequisites for the calculations. The target structure is a rigid-frame viaduct, which has a height of 12.2 m from the ground to the track. The outcome of this method varies depending on the seismicity of the assumed area. Therefore, a construction location needs to be set. For this study, the Sendai area was selected as the location. We set a cross-section to meet the required recovery time at this location.

The proposed method set the "expected post-earthquake recovery time" as the required performance of the structure. In this case, the expected recovery time is set to five days. Although there is room for debate on how to set this value, the average recovery time is five days according to trial calculations conducted in major regions across the country for multiple structures designed according to current railway standards (rigid viaducts with pile foundations, where the upper structure yields first). Therefore, we adopted this value in our study, considering the perspective of code calibration. This recovery time of five days corresponds to the design limit value I_{LD} in Eq. (1).

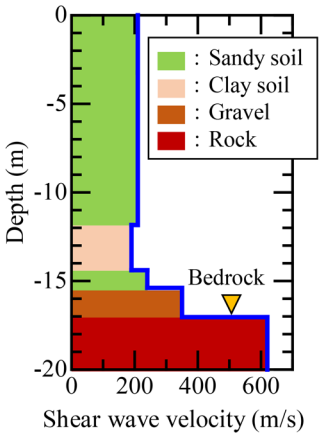

Fig. 4 Ground condition

3.2 Setting the design earthquake motion

In the proposed method, the earthquake occurrence probability and design earthquake motion are set based on the construction location. For this trial calculation, we conducted a probabilistic earthquake hazard analysis in the Sendai area, which was set as the location. The return period for the calculation is set to 100 years, which corresponds to the design working life [1] of the structure. The specific implementation procedure of the earthquake hazard analysis and the information used are based on reference [13], which includes the calculation method for the earthquake motion waveform group described later. Figure 5 shows the final evaluation results of the earthquake occurrence probability.

This result was used as the basis for synthesizing the group of earthquake motions by occurrence probability. For this examination, we divided the amplitude into 15 levels with 100 Gal increments from 100 to 1,500 Gal ("Gal" refers to cm/s^2). Twenty waves were evaluated for each amplitude level for a total of 300 waves. Figure 6 presents an example of the final calculated waveform. Naturally, the magnitude M_w and epicenter distance R assumed for each earthquake motion waveform differ, affecting not only the amplitude but also the time and frequency characteristics. A group of earthquake motion waveforms is set as the design earthquake motion.

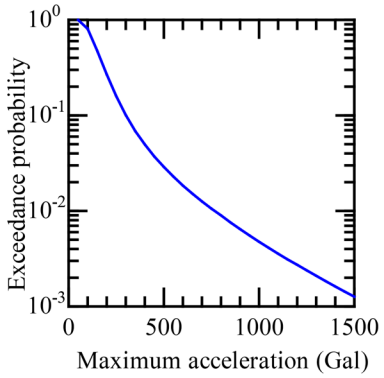

Fig. 5 Evaluation results of earthquake occurrence probability (Sendai area)

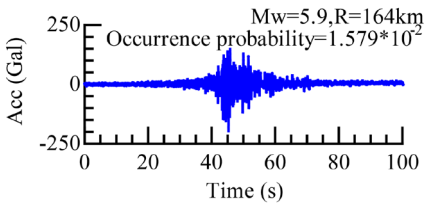

(a) Maximum acceleration of 200 Gal

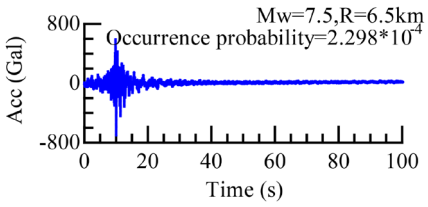

(b) Maximum acceleration of 700 Gal

Fig. 6 Calculation results of the group of earthquake motions with occurrence probability (Sendai area).

3.3 Structure response value calculation and recovery time evaluation

The dimensions and sectional reinforcement of the rigid-frame viaduct were determined based on the various conditions at the construction site. The cross-section was designed to satisfy the verification of restorability using our proposed method, as well as normal structural safety. Finally, we set the structure dimensions and section reinforcement shown in Fig. 7. Note that only the columns and piles are shown for the cross-sectional reinforcement for subsequent discussions. We created a model to calculate the earthquake response value of this structure. The model is created using two-dimensional beam and spring elements in accordance with various design standards for railway structures [1]. The elastic and nonlinear characteristics of each element are modeled in accordance with railway standards. Figure 8 shows the results of a push-over analysis perpendicular to the track. This analysis reveals the structure's equivalent natural period is T_{eq} = 1.14 s and its yield seismic intensity is k_{hy} = 0.33. We note that points Y, M, and N in this figure are damage control points used to evaluate the number of days required for structural restoration.

A nonlinear dynamic analysis that uses the detailed model of the structure can be conducted to calculate the response value. However, we replaced this model with an equivalent SDOF system, considering the number of seismic waves used [1, 14, 15]. We conducted a dynamic analysis by comprehensively inputting all 300 earthquake motion waveforms calculated in the previous section into the analysis model of this structure. Then, we calculated the response value for each waveform. Figure 9 shows the results of organizing the relationship between the response ductility factor of the structure and exceedance probability from the maximum response displacement of each waveform. This figure shows the control points (μ_y, μ_m) of each form of damage obtained by the push-over analysis of the target structure. However, in our examination of structures and earthquake motions, there was no response that exceeded μ_n, which corresponds to the collapse of the structure.

We calculated the recovery time of the structure based on the relationship with the standard recovery time corresponding to the structure type and degree of damage that we described in a previous study [9]. As shown in Table 1, the maximum response displacement of the structure and corresponding number of days to recovery were set to the damage level for the rigid-frame viaduct. The details of the calculation conditions and method for recovery time are based on reference [9]. The damage level of the structure is the same as the definition of seismic design for railway structures [1]. We assume ideal conditions for the surrounding environment of the structure, including sufficient workspace and the ability to bring materials and equipment in and from the side road. The expected recovery time of the structure is calculated by combining the relationship between the structural response and recovery time with the occurrence probability of each degree of damage shown in Fig. 9. The results showed that the expected recovery time of the target structure was 3.0 days. This corresponds to the design response value I_{RD} in Eq. (1).

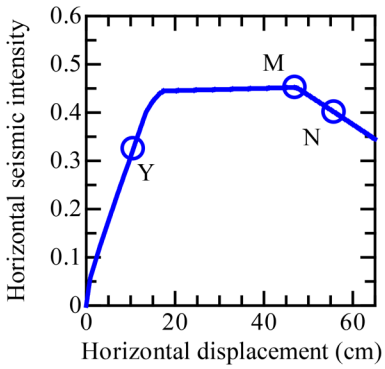

Fig. 8 Load-displacement relationship of entire structure

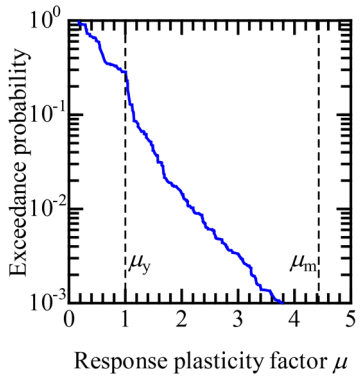

Fig. 9 Damage occurrence probability of structure

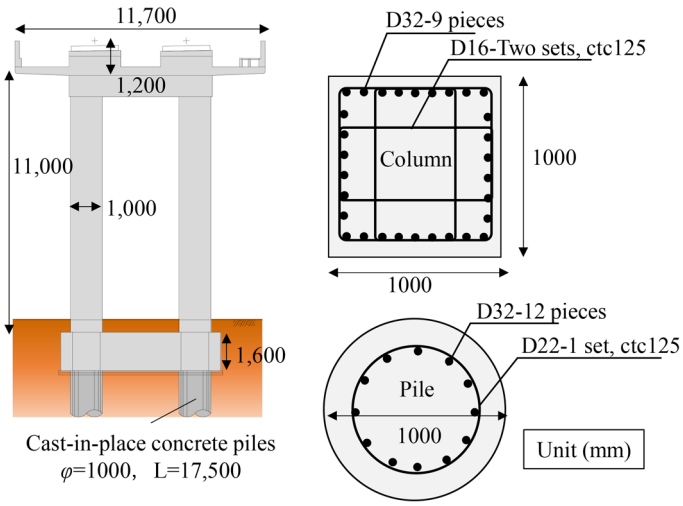

Fig. 7 Set structure dimensions and reinforcement of columns and pile sections

Table 1 Relationship between degree of damage and recovery time

Damage level	Response ductility factor μ	Recovery time (days)
1	$0 \leqq \mu < \mu_y$	1
2	$\mu_y \leqq \mu < \mu_m$	8
3	$\mu_m \leqq \mu < \mu_n$	23
4	$\mu_n \leqq \mu$	28

3.4 Performance verification of the structure

We verified the restorability of the structure using Eq. (1). Assuming the structural factor $\gamma_I = 1.0$, using the expected required performance and recovery time from the study in the previous section, the value is obtained by the following equation.

$$\gamma_i \cdot I_{RD} / I_{LD} = 1.0 \cdot 3.0 / 5 = 0.60 \leq 1.0 \quad (2)$$

This indicates that the structure shown in Fig. 7 satisfies the performance requirements. However, if Eq. (2) were to fail to meet the performance requirements, then the structural cross-section would be reviewed, as shown in Fig. 1. The recovery time would then be calculated using the same procedure.

We confirmed that using the proposed method to evaluate the design earthquake motion, calculate the response value, and conduct the performance verification enabled us to design a structure that satisfied the required recovery time at the relevant location.

4. Restorability verification of structures using the restorability verification nomogram

We confirm the effectiveness of using the nomogram for the structure in this section. The target examination area is set as the Sendai area, and the target recovery time is set to "5 days."

The equivalent natural period of the structure was set to T_{eq} = 0.5 s, and a response analysis was conducted under conditions where the M-point ductility factor (μ_m) and the yield seismic coefficient (k_{hy}) were both changed. Then, we used the same procedure as in the previous section to calculate the expected recovery time of each structure using. Figure 10 shows the results. It is now conceivable to use the N-point ductility ratio, which defines damage level 4, as a structural parameter for estimating recovery time. However, in designing railway structures, structural details are focused on ensuring safety against Level 2 (L2) seismic motions, which are the largest anticipated ground motions at a given site. In this study, the N-point ductility ratio is not included as a parameter since the damage level 4 will not be reached under the design seismic motion. In the seismic design of railway structures, events with an extremely low probability exceeding the L2 level are usually addressed within the framework of "resilience against catastrophic events."

As shown in Fig. 10, the expected recovery time decreases as the k_{hy} of the structure increases. Furthermore, the recovery time shows low sensitivity to μ_m when the ductility factor μ_m of the structure is 2 or greater. Figure 9 shows that this can be attributed to the relatively small probability of a structure suffering major damage. In terms of the recovery time, information on the yield seismic coefficient becomes more important when μ exceeds 1. This figure can be used to easily calculate the k_{hy} of a structure with the target performance of a recovery time of five days. For example, if μ_m = 1, then a yield seismic coefficient k_{hy} approximately 0.6 satisfies the recovery time of five days.

A similar examination was conducted for various T_{eq} values. Figure 11 shows the relationship between T_{eq} and k_{hy} resulting in a recovery time of five days for each ductility factor μ_m. This is the restorability verification nomogram proposed in Section 2.

As shown in Fig.11, the restorability verification nomogram can be used to easily determine the combination of T_{eq}, k_{hy}, and μ_m of a structure that satisfies the required recovery time in the region (five days in this case). If the k_{hy} of a structure is equal to or greater than the vertical axis of the nomogram, then the expected recovery time of that structure will be five days or less. Therefore, the vertical axis of the nomogram is labeled "yield seismic coefficient demand" referring to the yield seismic coefficient required to achieve a recovery time of a certain length or less. In addition, the restorability

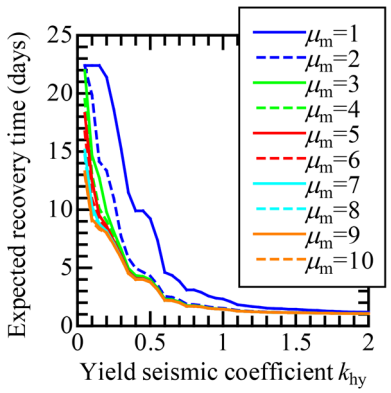

Fig. 10 Recovery time calculation results (T_{eq} = 0.5 s)

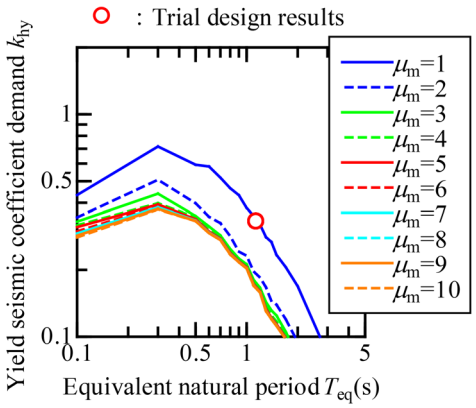

Fig. 11 Restorability verification nomogram calculation results (Sendai area: recovery time is 5 days)

verification nomogram calculated in this examination showed that the demand of the yield seismic coefficient is high for structures with $\mu_m = 1$. However, the demand is similar for structures with $\mu_m \geq 2$. Figure 10 shows that differences in damage and deformation performance do not significantly affect the recovery time of structures undergoing large deformation.

Furthermore, Fig. 11 shows the restorability verification nomogram, which lots the conditions of the structure with the trial design from Section 3 ($T_{eq} = 1.14$ s, $k_{hy} = 0.33$) as a red circle. The M-point ductility factor of the structure is $\mu_m = 4.43$, However, according to the nomogram, the yield seismic coefficient of the structure is slightly larger than the yield seismic coefficient demand. Therefore, the restorability verification nomogram can be used to appropriately verify the performance design of the structure section. It can be said that the proposed nomogram can be used in the general design procedure when a recovery time is considered as the verification index.

5. Conclusion

In this paper, we proposed a method for verifying the restorability of railway structures that uses the post-earthquake recovery time as the verification index. The results of our study were as follows:

- The proposed method uses "multiple earthquake motions with a wide range of assumed characteristics during the design working life" as the design earthquake motion, and the "recovery time" as the verification index. Recovery time is directly related to the speed of restoration after an earthquake. This allows for the seismic design of structures that consider the issue of recovery time.
- A trial design of a rigid-frame viaduct was conducted using the proposed method. The results indicate that the method allows for the seismic design of structures with recovery time as a direct verification index. However, since multiple dynamic analyses and damage evaluations are required each time the specifications of the structure change, this method of restorability verification during seismic design requires a large amount of effort.
- A more practical design method was proposed by conducting calculations under various conditions in advance and displaying the structural conditions resulting in the same recovery time in a nomogram. Additionally, trial calculations for the above-mentioned rigid-frame viaduct showed that the performance of structures can be verified using this restorability verification nomogram. This method can be used to design structures that can be easily restored using the same procedure as conventional seismic design.

The developed method can be used to design new structures that are easier to restore. Furthermore, identifying the parts and members of existing structures that require restoration in advance enables the implementation of targeted inspections and measures, ultimately shortening the post-earthquake recovery time. Additionally, evaluating existing structures based on their future service life can help determine the appropriate level of measures, set the same performance requirements, and optimize the priority of measures for special structures that require more time to recover.

However, it should be noted that this examination has limitations. First, it is based on a proposed method. Second, it uses trial calculations based on limited conditions, such as regions and structures. Moreover, recovery time for damaged structures can vary considerably depending on various conditions. While trial calculations in this examination consider the uncertainty and variance of earthquake occurrence and motion through probabilistic earthquake hazard analysis, they ignore the uncertainty and variance of structural response values and recovery time. Resolving these issues requires a more in-depth examination. This includes improving the evaluation of recovery time associated with structural damage, correcting the restorability verification nomogram according to the structural characteristics, and considering structural responses uncertainty. Furthermore, standardizing the nomogram requires future evaluations under a wide range of conditions.

Acknowledgment

This work was financially supported by the Japanese Ministry of Land, Infrastructure, Transport and Tourism. We would like to express our gratitude to those involved here.

References

[1] Railway Technical Research Institute, *Design Standards for Railway Structures and Commentary (Seismic Design)*, Maruzen co., Ltd, Tokyo, 2012 (in Japanese).

[2] Earthquake Engineering Committee, Earthquake Standards Subcommittee, Japan Society of Civil Engineers, "New Level 1 Concept for Seismic Performance-Based Design of Civil Engineering Structures (Draft)," *Committee activity report*, 2003 (in Japanese).

[3] Ohsumi, M. and Unjoh, S., "A study on the determination of earthquake resistance requirements for civil engineering structures based on total cost," *Civil engineering journal*, Vol. 41, No. 10, pp. 50-55, 1999 (in Japanese).

[4] Ichii, K., "A proposal and a trial of the seismic design based on total cost (gravity type quay wall case)," *The earthquake engineering symposium proceeding*, Vol. 11, pp. 2371-2376, 2002 (in Japanese).

[5] Abe, J., Sugimoto, H. and Watanabe, T., "A study on calculation of seismic design forces for structures considering their seismic risks," *Journal of the Japan Society of Civil Engineers.* Ser. A1, Vol. 63, No. 4, pp. 780-794, 2007 (in Japanese).

[6] Japan water works association, *Guidelines and explanations for earthquake-resistant construction methods for water facilities*, 2022 (in Japanese).

[7] Sakai, K., Murono, Y., Sato, T. and Sawada, S., "A new seismic design method for railway structures considering total cost," *Journal of the Japan Society of Civil Engineers.* Ser. A1, Vol. 68, No. 2, pp. 248-264, 2012 (in Japanese).

[8] Ministry of Land, Infrastructure, Transport and Tourism, *Holding of a Liaison Conference on Response to the Resumption of Operations after the Northern Osaka Earthquake*, https://www.mlit.go.jp/common/001240621.pdf, (accessed on 2024.5.6) (in Japanese).

[9] Nanami, K., Wada, K. and Sakai, K., "Estimation of post-earthquake restoration duration for various structures in railway according to damage level," *Journal of the Japan Society of Civil Engineers.*, Vol. 79, No. 13, 22-13037, 2023 (in Japanese).

[10] Sakai, K., Wada, K. and Toyooka, A., "Proposal of Restorability Evaluation Method for Railway Structures Using the Recovery Time After an Earthquake," *Journal of Japan Association for Earthquake Engineering*, Vol. 24, No. 4, pp. 96-108, 2024.

[11] Cornell, C. A., "Engineering Seismic Risk Analysis," *Bulletin*

of the seismological society of America, Vol. 58, No. 5, pp. 1583-1606, 1968.
[12] Annaka, T., Kagawa, T., Ishikawa, Y., Ejiri, J. and Nishioka, T., "A method for designing earthquake motion waveforms suitable for stochastic hazards for the assessment of expected loss," *Proc. 28th JSCE Earthquake Engineering Symposium*, 2005 (in Japanese).
[13] Sakai, K. and Murono, Y., "Evaluation of earthquake ground motion equipped with probability of its occurrence based on the seismic hazard analysis," *RTRI REPORT*, Vol. 24, No. 5, pp. 11-16, 2010 (in Japanese).
[14] Nanami, K. and Sakai, K., "An improved skeleton curve of railway bridges for equivalent single-degree-of-freedom system," *Journal of the Japan Society of Civil Engineers.* Ser. A1, Vol. 78, No. 4, pp. I_266-I_274, 2022 (in Japanese).
[15] Murono, Y. and Sato, T., "Applicability of non-linear response spectrum for verification of seismic performance of structure," *JSCE journal of Earthquake Engineering*., Vol. 29, pp. 520-528, 2007 (in Japanese).

Authors

Kimitoshi SAKAI, Dr.Eng.
Senior Chief Researcher, Head of Structural Dynamics and Response Control Laboratory, Center for Railway Earthquake Engineering Research
Research Areas: Earthquake Engineering, Seismic Design of Railway Structure

Kazunori WADA
Senior Researcher, Structural Dynamics and Response Control Laboratory, Center for Railway Earthquake Engineering Research
Research Areas: Earthquake Engineering, Seismic Design of Railway Structure

Akihiro TOYOOKA, Dr.Eng.
Director, Head of Center for Railway Earthquake Engineering Research
Research Areas: Earthquake Engineering, Seismic Design of Railway Structure

A Method for Constructing Geosynthetics-Reinforced Soil Retaining Wall with Rigid Facing Using Lightweight Embedded Formwork Applicable to Narrow Spaces

Yuki KURAKAMI
Foundation & Geotechnical Engineering Laboratory, Structure Technology Division
(Currently Computational Mechanics, Railway Dynamics Division)

Susumu NAKAJIMA
Foundation & Geotechnical Engineering Laboratory, Structure Technology Division

Takeharu KONAMI
OKASAN LIVIC Co.,LTD.

Yoshio YAMASHITA
Enbine Company

This paper presents a construction method for geosynthetic-reinforced soil retaining walls with rigid facing that can be used in narrow spaces. We developed settlement-following components to prevent backfill settlement from causing formwork deformation when formwork and backfill are connected. The proposed method uses these components in combination with lightweight embedded formwork to simultaneously construct the formwork and reinforced-backfill from the rear side, eliminating the need for scaffolding. A trial construction was conducted to verify the feasibility of the proposed method. Results confirmed settlement-following components functioned properly in a retaining wall with a height of 2.4 m. Considering the allowable sliding displacement of the components, the maximum height of this method is estimated to be approximately 4.0 m.

Key words**:** *reinforced soil retaining walls, geogrid arrangement, RC facing construction method, full-scale test construction*

1. Introduction

The geosynthetics-reinforced soil retaining wall with a rigid facing (RRR method), (hereinafter referred to as the "reinforced soil retaining wall") has been widely used in railway construction. Proper construction of the rigidly integrated wall facing is critical. After constructing the reinforced-backfill, scaffolding is typically erected on the front side to build the wall facing. Construction projects such as continuous grade separation and double-track often take place in narrow areas adjacent to operating railway lines, roads, and residential areas. In such cases, there is insufficient space to erect scaffolding, which makes constructing the wall facing of the reinforced soil retaining wall difficult.

To address this issue, we developed a construction method that enables wall facing to be built from the rear side (i.e., from the backfill side), eliminating the need for scaffolding. This paper discusses the issues associated with the conventional wall construction method and outlines the proposed rear-side construction method in Chapter 2. Chapter 3 discusses the feasibility of the proposed method based on test construction. Chapter 4 describes the applicable height range for the method.

2. Conventional wall construction method and proposed rear-side construction method

2.1 Issues with conventional wall construction method

Figure 1 shows the conventional construction procedure for geosynthetics-reinforced soil retaining walls [1]. The procedure is as follows, consisting of step 1 through step 4. Step 1: Construct the foundation. Step 2: Place geogrid reinforcement wrapped with temporary holding (such as gravel bags or welded steel fabric) and then construct the reinforced-backfill using the holding effect of the temporary holding at the wall facing and the geogrid (Fig.1(a)). Step 3: After the backfill has settled, erect scaffolding in front of the retaining wall. Step 4: Construct the wall facing (Fig. 1(b)). Since the wall facing is constructed step by step, it is not affected by the deformation of the backfill. Note that scaffolding is required not only for formwork installation but also for formwork removal.

The structure of the wall facing is shown in Fig. 2. The formwork is welded to the L-steel through the separator. The L-steel is then welded to the steel for fixing external formwork on the backfill side. As a result, the formwork is supported from the backfill side via the L-steel.

The conventional procedure of installing the formwork after constructing the reinforced-backfill cannot be applied in rear-side construction without scaffolding. Constructing the formwork from the rear-side allows construction to proceed without scaffolding. However, it is necessary to build the reinforced-backfill and the formwork simultaneously. Using the current fixing method, if the reinforced-backfill and the formwork are constructed simultaneously without any countermeasures, the formwork may deform through the L-steel when the backfill settles, as shown in Fig. 3.

In addition to plywood formwork, the RRR-B method uses precast concrete panels that do not require demolding. This aims to shorten the construction period and reduce the amount of labor required for concrete work. The standard specifications for precast concrete panels for the RRR-B method are as follows: each panel weighs 584 kg and measures 2,000 mm in width, 1,008 mm in

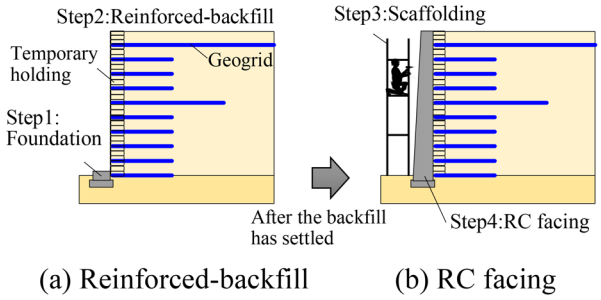

Fig. 1 Conventional construction procedure for reinforced soil retaining wall

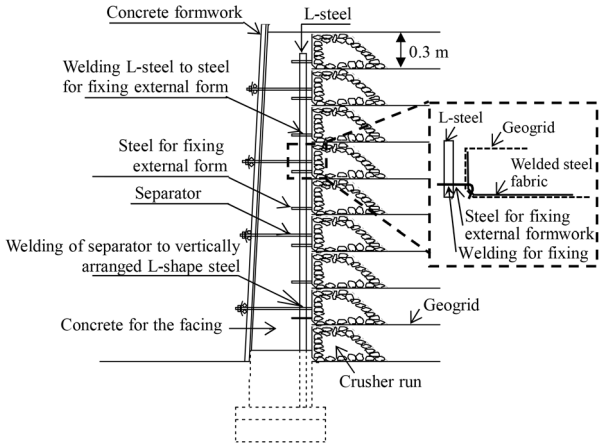

Fig. 2 Structure of wall facing [1]

height, and 125 mm in thickness. This necessitates the use of a large crane during construction. The advantage of using precast concrete panels for the RRR-B method is that they serve as both formwork and part of the structure simultaneously.

2.2 Rear-side construction method

We proposed a construction method for geosynthetics-reinforced soil retaining walls with a rigid facing that is suitable for narrow spaces. We developed components that can accommodate the settlement of backfill (hereafter referred to as "settlement-following components"), to prevent settlement from causing deformation of the formwork when it is connected to the backfill.

2.2.1 Rear-side construction using lightweight embedded formwork

Construction work in narrow areas adjacent to operating railway lines, roads, or residential buildings has issues related to the construction space. This makes securing the necessary working area and bringing in large construction machinery difficult. As mentioned above, the precast concrete panels used in the RRR-B method require a large crane for installation and scaffolding for placement.

Therefore, we considered using lightweight embedded formwork [2] as the formwork for the rear-side construction. The lightweight, embedded formwork is a residual formwork made of concrete that does not require demolding. The concrete mix design has a maximum coarse aggregate dimension of 15 mm and a design standard strength of 36 N/mm^2. The standard specifications of the lightweight embedded formwork are as shown in Fig. 4. It is light-

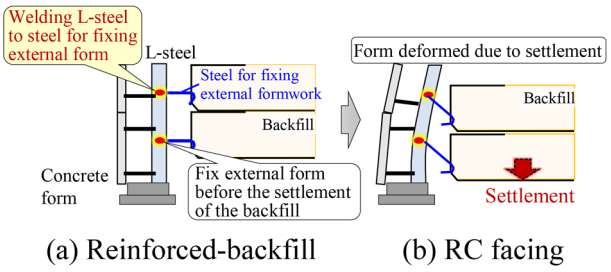

Fig. 3 Issues with simultaneous construction using the conventional fixing method

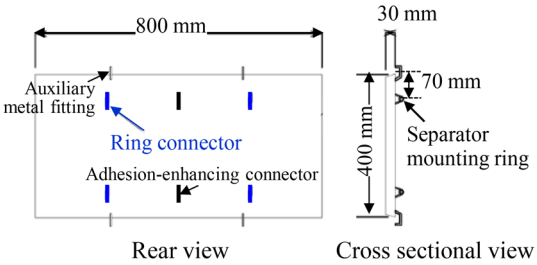

Fig. 4 Lightweight embedded formwork

weight, with width of 800 mm, height of 400 mm, thickness of 30 mm, and weight of 20 kg per panel. It can be installed from the rear-side while being lifted with a small backhoe. In addition to ring connectors for connecting separators, adhesion strengthening connectors are attached to the rear-side of the lightweight embedded formwork to prevent it from falling off when in service. The attached adhesion-reinforcing connectors have been confirmed to have sufficient pull-out strength (adhesion strength).

Figure 5 shows the procedure for rear-side construction using lightweight embedded formwork. Step 1: Construct the foundation. Step 2: The lightweight embedded formwork is erected simultaneously with the construction of the reinforced-backfill. Step 3: After completion of reinforced-backfill and formwork construction, and when the reinforced-backfill has settled, concrete is placed to anchor the wall to the reinforced-backfill.

2.2.2 Development of settlement-following components

In rear-side construction, the reinforced-backfill and formwork must be constructed simultaneously. Therefore, we investigated a solution that enables this. During construction, the loads acting on the formwork are wind loads and lateral pressure from concrete placement, both of which act horizontally. When the reinforced-backfill and formwork are constructed simultaneously, in addition to the horizontal loads mentioned above, the formwork is also affected by settlement and bulging of the backfill that occur during construction, as shown in Fig. 3. It should be noted that settlement of the reinforced-backfill increases progressively with backfill placement, while the bulging tends to stabilize after the layer is compacted. For further details, refer to Reference 3.

In other words, applying horizontal restraint after constructing the first backfill layer can prevent bulging from significantly affecting the formwork and accommodate the deformation of the backfill. However, in the vertical direction, a sliding mechanism is necessary to accommodate the settlement of the backfill. Considering these factors, we developed a settlement-following component that is fixed horizontally to the L-steel but can slide vertically. This compo-

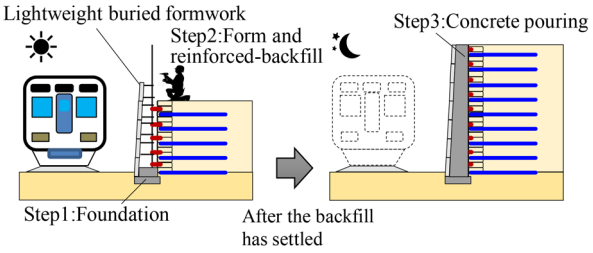

Fig. 5 Rear-side construction procedure using lightweight embedded formwork

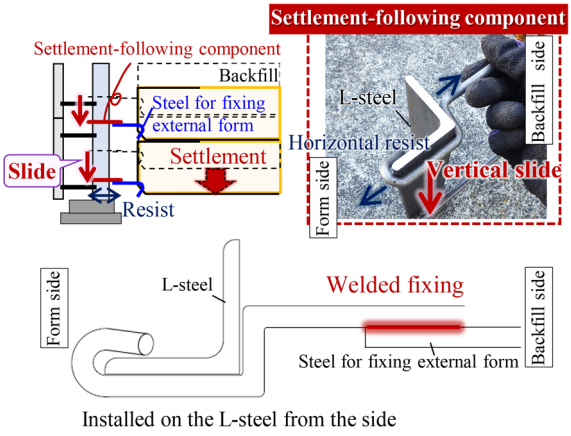

Fig. 6 Settlement-following components enabling simultaneous construction

nent is shown in Fig. 6. This component can easily be installed on the side of the L-steel and connected to a commonly used steel for fixing external form by welding. Installing the settlement-following component suppresses the displacement of the wall surface. It resists wind loads acting on the formwork during construction and lateral pressure during concrete placement. Furthermore, by sliding along the L-steel, the component can adapt to the settlement of the backfill. This allows the formwork and backfill to be constructed simultaneously. The settlement-following component is installed at the tip of the steel for fixing external form after the first backfill layer is constructed and is then fixed in the horizontal direction.

The settlement-following component is made of separator steel wire with a tensile strength of 540 N/mm² or higher (equivalent to or exceeds JIS G 3532 standard for ordinary steel wire SWM-P) and has a diameter of 6.9 mm. As shown in Fig.6, the tip of the component is twisted into a hook shape and bent to follow the contour of the L-steel. The bent portion is 25 mm in length, which is half the width of the L-steel's flange. This configuration allows the component to resist horizontal loads such as lateral pressure during concrete placement, while enabling it to slide vertically along the L-steel.

3. Test construction

We confirmed the feasibility of the back-construction method using lightweight embedded formwork and settlement-following components through test construction.

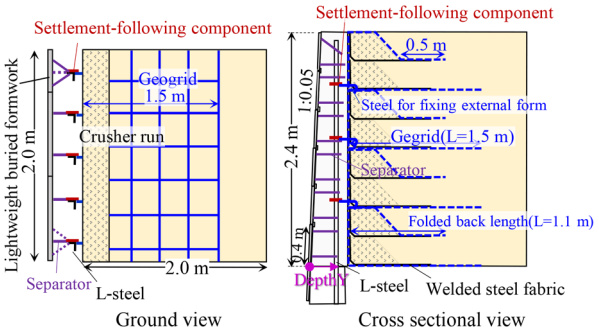

Fig. 7 Overview of test structure

3.1 Overview of the test construction

Figure 7 shows a schematic diagram of the test specimen constructed for the test. The specimen measured 2.4 m in height, 2.0 m in width, and 2.0 m in depth. The lightweight embedded formwork was arranged in a staggered pattern.

The backfill material used was crusher run (C-40), compacted in 0.15 m thick layers to achieve a compaction degree of Dc = 90% (E-c method). The standard vertical spacing of geogrid reinforcement in reinforced soil retaining walls using the RRR method is 0.3 m. However, in this test construction, in addition to investigating the wall construction method, the influence of vertical geogrid reinforcement spacing on the stability of the retaining wall was also examined. Therefore, the vertical spacing was experimentally increased to 0.6 m—twice the standard spacing—and the geogrid reinforcement length was set to the minimum design length of 1.5 m. It has been confirmed [3] that even with the increased spacing of 0.6 m, construction stability remains approximately equivalent to that of the standard 0.3 m spacing. For further details, see Reference 3. Since one layer of geogrid reinforcement was installed for every two layers of welded steel fabric, the reinforcement in the folded-back sections wrapped around both welded steel fabrics together and embedded in the backfill. This resulted in a structure where the upper and lower welded steel fabrics act as one. The steels for fixing external formwork were installed at the same vertical intervals as the geogrid reinforcement (i.e., every 0.6 m). These fixings were equipped with settlement-tolerant members. Normally, these steels for fixing external formwork are placed at 0.3 m intervals to align with each layer of welded wire fabric. However, in this test construction, they were installed at 0.6 m intervals—half the usual frequency.

Figure 8 shows the construction procedure and the test construction. The procedure was as follows: (1) During the initial foundation work, L-steel was erected (Step 1 in Fig. 8). (2) A lightweight embedded formwork was then installed, and separators were welded and fixed to the L-steel (Step 2 in Fig. 8). (3) After constructing one layer of reinforced-backfill, settlement-following components were installed onto the L-steel, and the steels for fixing external formwork were welded together with the settlement-following components (Step3 in Fig. 8 and Fig. 6). Once the lightweight embedded formwork and the reinforced-backfill were completed, concrete was placed into the formwork (Step4 in Fig. 8).

During the construction of the reinforced-backfill, measurement items were taken the displacement in the depth direction of each level of the lightweight embedded formwork, the amount of bulging and settlement of the reinforced-backfill, and the stress of the separator member and steels for fixing external formwork. The displacement of the lightweight embedded formwork was measured

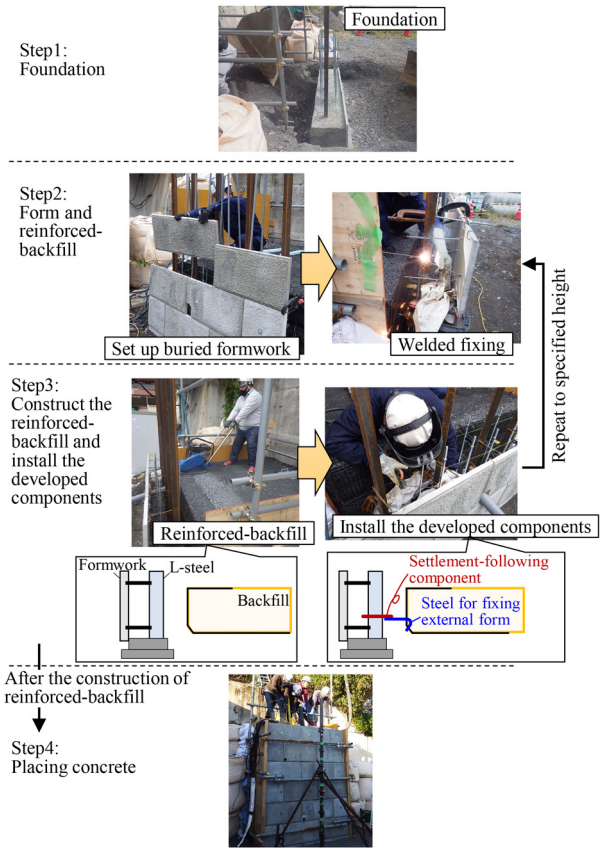

Fig. 8 Construction procedure and scenes from test construction

using an optical range finder. The bulging and settlement of the reinforced-backfill were measured by placing targets on the welded wire fabric at vertical intervals of 0.3 m. Strain gauges were installed on the separators and steels for fixing the external formwork in order to measure stress on these members.

During concrete placement, displacement gauges were installed along the center row of the lightweight embedded formwork at each level to measure time-dependent displacement in the depth direction. Earth pressure cells were installed on the lightweight embedded formwork at each level to monitor the lateral pressure exerted on the formwork during concrete placement.

3.2 Results of the test construction

3.2.1 Deformation during construction of the wall

Figure 9 shows both the measured settlement of the backfill and the displacement of the formwork. Figure 9(a) shows the amount of settlement, which was obtained by placing targets at the boundaries of each backfill layer immediately after compaction and surveying them after the completion of the backfill construction. Figure 9(b) shows the displacement of the formwork, measured at the center of each formwork level. The displacement in the depth direction was evaluated relative to the initial position at the time of formwork installation. Displacement toward the front (facing) side is defined as negative, while displacement toward the rear (backfill) side is defined as positive.

From the results shown in Fig. 9, it is verified below whether the settlement-following components functioned effectively against

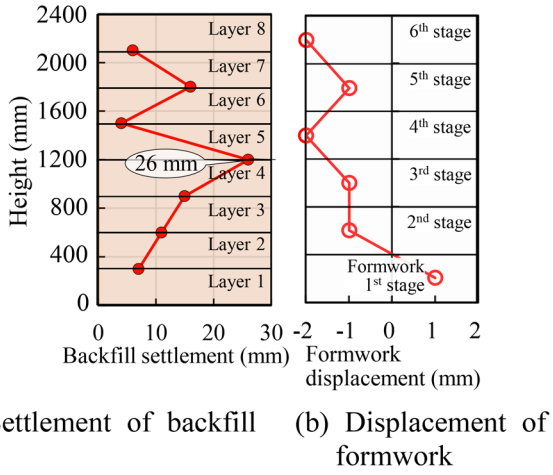

(a) Settlement of backfill (b) Displacement of formwork

Fig. 9 Confirmation of effectiveness of settlement-following components

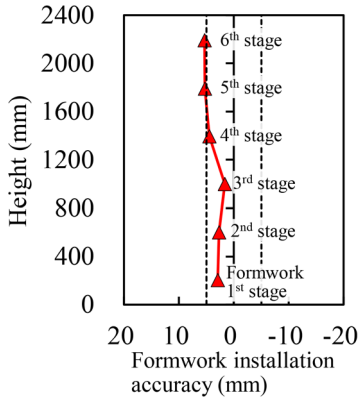

Fig. 10 Installation accuracy of formwork

the settlement of the backfill induced by rolling compaction during backfill construction. If the settlement-following components do not function properly against the settlement of the backfill, the formwork is expected to undergo displacement in the depth direction as the backfill settles, as illustrated in Fig. 3. However, as shown in Fig. 9, the backfill experienced a maximum settlement of 26 mm, while the deformation of the formwork was limited to less than 2 mm. This result indicates that the settlement-following components effectively accommodated the settlement of the backfill. These findings confirm the feasibility of constructing the reinforced-backfill and lightweight embedded formwork simultaneously through the use of settlement-following components.

Figure 10 shows the depth wise installation accuracy of the lightweight embedded formwork after the reinforced-backfill is complete. The installation accuracy in Fig. 1 was evaluated as the deviation from the design slope of the wall (1:0.05). The installation accuracy of the formwork was defined as positive on the front side and negative on the back side.

Although there are no explicit standards for formwork installation in railway structures, the black dashed line in the figure indicates a reference tolerance of ±5 mm from the designed position. The variation was kept within about ±5 mm, confirming that the lightweight embedded formwork was installed with adequate precision. For reference, the specified by the Ministry of Land, Infrastructure, Transport and Tourism (MLIT) [4]'s control criteria for retaining wall construction allow for a tolerance of ±0.03H (72 mm)

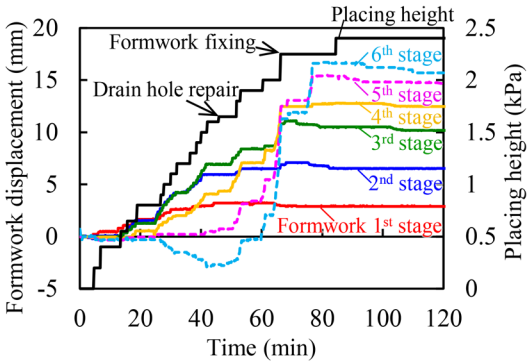

Fig. 11 Formwork displacement during concrete placement

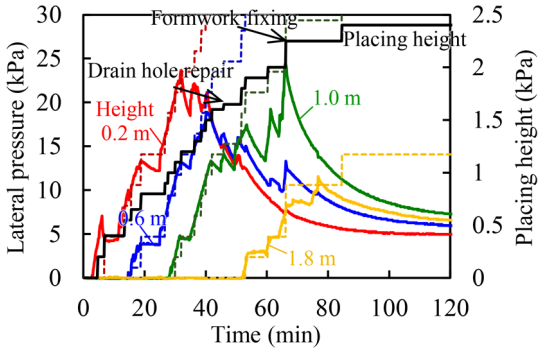

Fig. 12 Lateral pressure during concrete placement

and within ±300 mm. This indicates that there are no issues with regard to these standards. Furthermore, the finishing tolerance for retaining walls in actual railway engineering practice is typically around ±20 mm, a criterion that the present installation meets.

3.2.2 Concrete placement

The concrete mix was designed with an ordinary Portland cement and 20 mm coarse aggregate. It has a nominal compressive strength of 21 N/mm², a maximum water-cement ratio of 60%, and a slump of 21 cm. The concrete was placed at an approximate rate of 2.4 m/h. The ambient temperature during placement was 19°C.

Figure 11 shows the time history of the displacement of the lightweight embedded formwork during concrete placement. The displacement is plotted as the incremental change from the initial value just before placement. Outward bulging of the formwork is defined as positive. At a placement height of 1.65 m, a gap was observed between the drainage hole located at 1.8 m and the formwork. As a result, the placement was halted temporarily for approximately 3 minutes, while the gap was repaired with mortar putty.

A sudden increase in displacement was observed during placement at a height of 2.0 to 2.25 m in the fifth and sixth stages of the lightweight embedded formwork. Placement was suspended again (for about 8 minutes), and the formwork was temporarily restrained to prevent it from displacing any further outward.

The maximum displacement (bulging) of the lightweight embedded formwork was 17.3 mm. This satisfies the ±20 mm tolerance that is commonly used as a finishing standard for retaining walls. According to the current specifications, placing settlement-following components and steels for fixing external formwork at 0.3 m intervals is considered to enhance the restraining effect and reduce formwork displacement. Indeed, past construction records have confirmed that safe execution without the need for repairs can be achieved by placing the steels for fixing external formwork at 0.3 m intervals. However, in this test construction, the settlement-following components and fixing steels were installed at 0.6 m intervals, in accordance with the vertical spacing of the geogrid reinforcement. Nevertheless, to further reduce formwork displacement during concrete placement, it is necessary to adopt the 0.3 m interval as specified in the current design standards.

Figure 12 shows the time history of the time-dependent lateral pressure acting on the lightweight embedded formwork during concrete placement. The figure also includes the lateral design pressure corresponding to each earth pressure gauge installation height. which is represented by an equivalent hydrostatic pressure assuming a unit weight of 23.5 kN/m³ and a lateral pressure coefficient of 1.0 which is shown by dashed lines. Attention is focused on the earth pressure gauge installed at the lowest position (0.2 m height), where the lateral pressure is expected to be the greatest. The maximum value was recorded when the concrete placement height reached approximately 1.2 m, and the increasing trend of the lateral pressure at that point was found to be comparable to the hydrostatic pressure indicated by the dashed line. Furthermore, based on the gauges installed at 0.6 m and 1.0 m, it was observed that the lateral pressure equivalent to hydrostatic pressure only acted up to a placement height of around 1.5 m. Beyond this value, even as the placement progressed, no further increase in lateral pressure was observed. These results suggest that the design of components can be based on a pressure distribution model. In this model, hydrostatic pressure acts up to a concrete height of 1.5 m. After that, the lateral pressure remains constant. This model is based on the distribution presented in the Standard Specifications for Concrete [5]. The maximum stresses measured in the separator and the steels for fixing external formwork were 78 N/mm² and 86 N/mm², respectively—both sufficiently lower than the tensile strength of 540 N/mm².

4. Settlement of backfill and applicable height of settlement-following components

4.1 Sliding displacement of settlement-following components

Using settlement-following components allows for the simultaneous construction of the reinforced-backfill and formwork. However, it should be noted that these components are designed to accommodate the settlement and compression of the backfill body itself. They are not intended to respond to consolidation settlement of the underlying ground.

The settlement-following components slide vertically along L-shaped steel sections to follow the settlement of the backfill. However, the separators for formwork are welded and fixed to the L-shaped steel. Figure 13 shows an example of the positional relationship between a separator and a settlement-following component. The ring connector used to attach the separator is installed 70 mm inward from the end of the formwork (Fig. 4). Depending on the positional relationship, the separator and the settlement-following component may interfere with each other. Since the separator can be welded at a slight angle if necessary, it is possible to ensure a clearance of at least 80 mm between the separator and the settlement-following component. Taking the construction tolerances and the weld leg length into account, the sliding allowance of the settlement-following component is approximately 70 mm when such clearance is ensured.

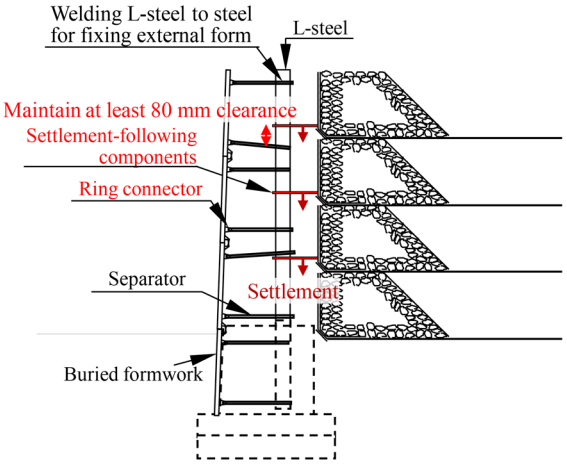

Fig. 13 Positional relationship between separator and settlement-following component

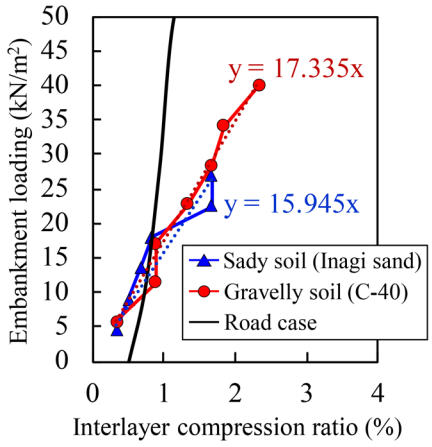

Fig. 14 Compression ratio of backfill

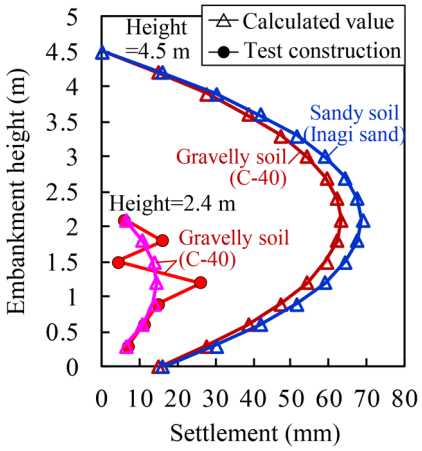

Fig. 15 Relationship between backfill height and settlement of each layer

4.2 Interlayer compression ratio and settlement of backfill

Figure 14 shows the relationship between the average interlayer compression ratio and the applied overburden load of the backfill observed in the test construction. In this test, crusher-run gravel (C-40) was used as the gravelly soil, and Inagi sand, which was compacted to a degree of compaction (D_c) of 90% using the E-c method, with a compacted layer thickness of 0.3 m , was used as the sandy soil [3]. For reference, the results from a highway project (hereinafter referred to as the "road case") are also shown [6] and [7]. Although there was some variability between the sandy and gravelly soil, both exhibited an increasing trend in compression ratio with increasing overburden load. This is consistent with observations from the road case. Notably, the interlayer compression ratio was higher in the test construction than in the road case under increasing load. This difference is considered to be due to variations in the thickness of the compacted layers.

In the road case, the compacted layer thickness was 0.6 m. In the test construction, it was reduced to 0.3 m for sandy soil and 0.15 m for gravelly soil to achieve the target compaction degree of D_c = 90%. Although sandy soil is generally more compressible than gravelly soil, both types of soil showed similar trends in this test. This is believed to be partly due to the thinner, more compacted layers used in the test construction.

Figure 15 illustrates the relationship between the backfill height and the settlement for each layer of backfill. For the case with a backfill height of 2.4 m, the measured settlement shown in the figure is the residual settlement obtained by surveying during the construction test. The calculated settlement values were derived from the results in Fig. 14 (gravelly soil) to estimate the total backfill settlement.

Although some variability in the test at heights of 1.2 m and 1.5 m, the results generally followed the same trend as the calculated values. The greatest amount of settlement was found in the mid-height layers. This is because the layer equipped with settlement-following components experiences not only its own settlement, but also the cumulative effect of compression settlement in the underlying layers. A similar trend was also observed in the road case.

4.3 Applicable height of settlement-following components

When the allowable sliding amount of the settlement-following component is set to 70 mm, the system can accommodate backfill settlement of up to 70 mm. As shown in Fig. 13, the maximum settlement of the backfill is 70 mm at a retaining wall height of approximately 4.5 m for both sandy and gravelly soils. However, considering the variation between calculated and measured values, the applicable wall height is currently set at approximately 4.0 m, which corresponds to an estimated settlement of about 53 mm.

Furthermore, according to surveys of actual reinforced soil retaining wall construction, about 45% of cases involve wall heights of less than 5 m [8]. Therefore, this component is expected to be applicable to a relatively large number of practical construction projects.

5. Conclusions

In this study, a construction method was developed for building retaining walls from the rear side to eliminate the need for scaffolding. The feasibility of the method was verified through test construction, and the applicable wall height was evaluated. The key findings are as follows:

1. A rear-side construction method for reinforced soil retaining

walls suitable for narrow construction sites was proposed. By combining the newly developed settlement-following components with lightweight embedded formwork that does not require removal, simultaneous construction of the formwork and reinforced-backfill from the rear side is possible, thereby eliminating the need for scaffolding.

2. Test construction verified the feasibility of the proposed method. For a retaining wall with a height of 2.4 m, it was confirmed that the settlement-following components effectively responded to backfill settlement.
3. Considering the allowable sliding distance of the settlement-following components, the applicable height for this construction method is estimated to be approximately 4.0 m.

Furthermore, details regarding the rear-side construction method that combines settlement-following components with lightweight embedded formwork—including component specifications, construction procedures, and key considerations during construction—are now provided in the revised editions of the RRR Method Design and Construction Manual [9], Materials Manual [10], and Cost Estimation Manual [11], which were published in October and November 2024.

References

[1] Association of RRR Construction System, "*Manual for the design and construction of RRR Geosynthetic-Reinforced Soil structures*," 2021.

[2] Konami, T., Yamashita, Y. and Sugiura, M., "Construction technology for concrete retaining walls using Remaining form," Proceedings of the *77th Annual Meeting of the Japan Society of Civil Engineers*, VI-724, 2022 (in Japanese).

[3] Kurakami, Y., Takagi, S., Nakashima, S., Konami, T. and Yamashita, Y., "Effect of geogrid arrangement and rigid facing construction method on stability during construction of geosynthetics-reinforced soil retaining walls," Proceedings of the *38th Symposium on Geosynthetics*, Vol. 38, pp. 122-129, 2023 (in Japanese).

[4] Ministry of Land, Infrastructure, Transport and Tourism (MLIT), "*Standard for Construction Management and Specification Values (Draft)* ," March 2023 Edition, 2023 (in Japanese).

[5] Japan Society of Civil Engineers (JSCE), "*Standard Specifications for Concrete Structures – Construction*," 2017 (in Japanese).

[6] Abe, H., Himeno, H., Morishita, H. and Kawasaki, H., "Compressibility behavior of high embankments using gravelly soil," Proceedings of the *57th Annual Conference of the Japan Society of Civil Engineers*, III-815, 2002 (in Japanese).

[7] Tanifuji, Y., Kawashima, M. and Yamauchi, S., "Compression settlement behavior of thick-layer compacted embankments on expressways – Long-term changes over five years after commencement of service," *Journal of the Hokkaido Branch, Japan Society of Civil Engineers*, No. 66, 2009 (in Japanese).

[8] Association of RRR Construction System, "*RRR Construction System Newsletter*," Vol. 48, 2021 (in Japanese).

[9] Association of RRR Construction System, "*Materials Manual for the RRR-B Method (Rigid-Facing Reinforced Soil Retaining Wall Method)* ," Revised October 2024 (in Japanese).

[10] Association of RRR Construction System, "*Standard Cost Estimation Manual for the RRR-B Method (Rigid-Facing Reinforced Soil Retaining Wall Method)* ," Revised November 2024 (in Japanese).

[11] Association of RRR Construction System, "*Materials Manual for Reinforced Backfill Method using the RRR Construction System*," Revised November 2024 (in Japanese).

Authors

Yuki KURAKAMI, Ph.D.
Senior Researcher, Foundation & Geotechnical Engineering Laboratory, Structure Technology Division (Former)
Research Areas: Geotechnical Engineering

Takeharu KONAMI
OKASAN LIVIC Co.,LTD.

Susumu NAKAJIMA, Ph.D.
Senior Chief Researcher, Head of Foundation & Geotechnical Engineering Laboratory, Structure Technology Division
Research Areas: Geotechnical Engineering

Yoshio YAMASHITA
Enbine Company

Vibration Test Method for Connectors of Overhead Contact Line Based on OCL Vibration Analysis

Takuya OHARA
Current Collection Maintenance Laboratory, Power Supply Technology Division

Chikara YAMASHITA
Current Collection Maintenance Laboratory, Power Supply Technology Division (Former)

Electrical connectors connecting contact wires and messenger wires are sometimes subject to fatigue-failure due to vibration caused by train passage. It is therefore desirable to establish a method for evaluating the fatigue resistance of the connectors. Therefore, the authors proposed a test method consisting of two types of vibration test that take into account the two fatigue factors of the connectors: the relative displacement of the contact wire and their resonance. The test conditions were determined by analyzing overhead contact line vibration using an OCL-pantograph simulation. Furthermore, the authors carried out vibration tests on real connectors and confirmed that the test results were consistent with the actual failure status of the connectors.

Key words: *connectors of overhead contact line, copper strand wire, fatigue test, OCL relative displacement, resonance*

1. Introduction

An overhead contact line (OCL) connector (Fig. 1; henceforth, "connector") is a metal fitting that electrically connects OCL wires and eliminates the potential difference in order to prevent unnecessary current from flowing through the wires and metal fittings. The conducting wires that constitute the connector are made of easily bent wires such as soft copper stranded wires. These wires are subject to fatigue-failure due to OCL vibrations from passing trains. This has been a long-standing issue when using connectors.

Fatigue durability evaluations of OCL fittings, including connectors, have been conducted in accordance with the vibration test specified in the Japanese Industrial Standards (JIS) [1, 2]. However, the JIS vibration test is mainly defined as a confirmation test for the loosening of bolts, and fatigue-failure has occurred in the field even in connectors that have passed the test. The vibration conditions have also not been changed since their establishment in the former Japanese National Railways Standards in 1968. Consequently, there has been demand for a new test method that appropriately evaluates the fatigue durability of connectors.

To this end, the authors proposed two types of test method that focus on the fatigue modes of connectors, namely, a vertical vibration test and horizontal vibration test. The vibration conditions for these tests were set based on the results of OCL vibration analysis. In this paper, the authors use M-T connectors that connect the contact wire to the messenger wire in a simple catenary as an example in order to explain the specific test method. In the following text, "dropper" is referred to as "hanger," which is abbreviated as "H."

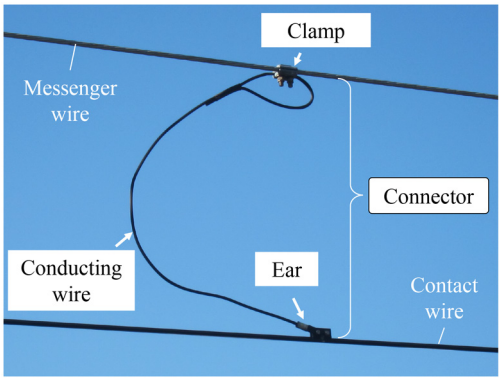

Fig. 1 Connector of overhead contact line

2. Test types

The fatigue modes of connectors in the field need to be considered in order to determine which vibration test method is suitable. Figure 2 shows an example of the vertical vibration waveform of an OCL and two types of connector fatigue modes reported in past research [3]. The maximum strain in the M-T connector shown in Fig. 2 occurs at the ear of the conducting wire in each mode.

The first fatigue mode is fatigue caused by deformation of the conducting wire due to the difference in vertical vibration displacement between the wires connected by the connector ("OCL relative displacement"). This mainly occurs at the moment when the pantograph passes. Figure 3 shows the results of the measurement of the vertical vibration displacement of an OCL on a certain line and the structural analysis results of the conducting wire strain when a connector is attached to that OCL [3]). The agreement between the OCL relative displacement and the strain waveform indicates that the relative displacement has a large effect on the fatigue of the conducting wire.

The second fatigue mode is fatigue caused by the deformation of the conducting wire due to the resonance of the connector. Connector resonance occurs when the OCL vibrates horizontally due to residual vibration of the OCL after a train passes, or when a viaduct or catenary pole vibrates, and the frequency of this vibration matches the natural frequency of the connector. The conducting wires are subjected to a large number of bending strains when resonance occurs. This may lead to fatigue-failure in a short period of time.

In the present study, the authors proposed two types of vibration test corresponding to each fatigue mode as follows:

(1) Vertical vibration test (corresponding to fatigue caused by

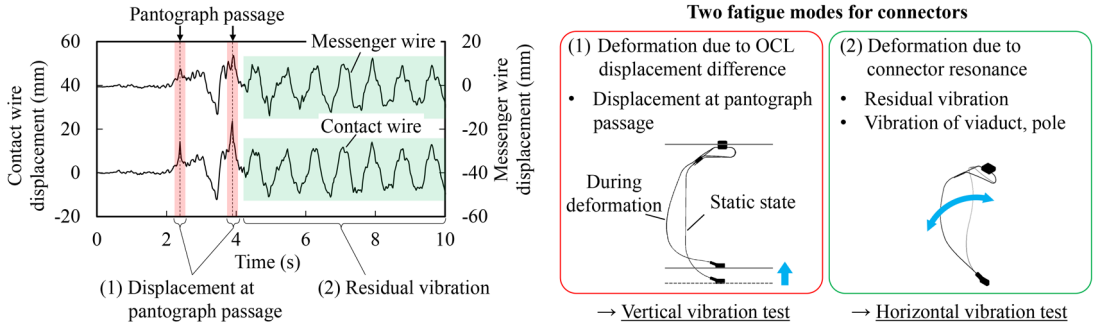

Fig. 2 Two types of connector fatigue mode and corresponding vibration test method

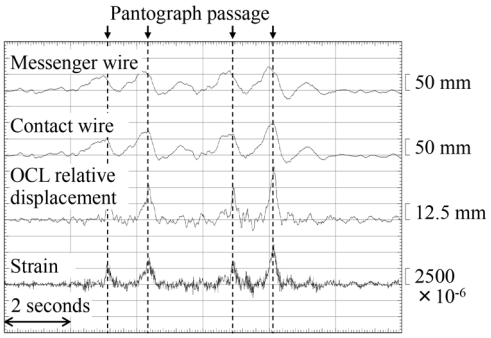

Fig. 3 OCL vibration waveform and connector estimated strain waveform [3]

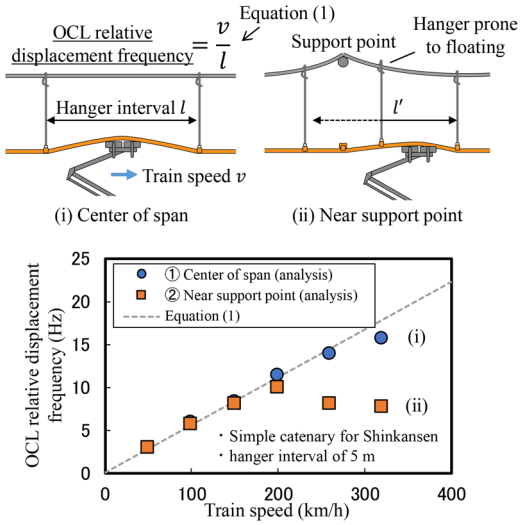

Fig. 4 Relationship between train speed and OCL relative displacement frequency

OCL relative displacement)

Fatigue durability is evaluated for the case where the messenger wire side of the connector is fixed, and the contact wire side is repeatedly pushed up in the vertical direction.

(2) Horizontal vibration test (corresponding to fatigue caused by connector resonance)

Fatigue durability is evaluated with consideration given to the primary vibration mode of the M-T connector when the connector is subjected to horizontal (sleeper direction) vibration.

Note that "fatigue durability" here refers to the whether the conducting wire fails after each test. The evaluation concept and specific test method are described in the following sections.

3. OCL vibration analysis

In this section, the authors show the results of OCL vibration frequency and amplitude analysis. This vibration is the basis for the vibration conditions for the vertical and horizontal vibration tests.

3.1 OCL relative displacement

The frequency of OCL relative displacement is expressed by the equation consisting of train speed v and hanger interval l, that is, v/l, as shown in Eq. (1) in Fig. 4 [4]. The graph in Fig. 4 compares the above equation with the analysis results of the vibration frequency of a simple catenary for Shinkansen. The equation and results were roughly in agreement at the center of the span ((i) in the graph in Fig. 4). However, a hanger tends to float relative to the messenger wire near the support points of a simple OCL. This results in the tendency of the hanger interval effectively increasing and the frequency of the OCL relative displacement becoming lower ((ii) in the graph in Fig. 4).

Past research [3] has indicated that the amplitude of the OCL relative displacement also varied depending on the position within the span. Figure 5 shows the relationship between the position within the span and the OCL relative displacement amplitude and frequency for a simple Shinkansen catenary. In contrast to the frequency, the amplitude of the OCL relative displacement had an increasing tendency near the support point. This was because the messenger wire was fixed at the support point, which resulted in a smaller messenger wire vibration displacement, and a larger difference in vibration displacement between the contact wire and messenger wire. Therefore, the OCL relative displacement frequency and amplitude vary depending on the position within the span. This in turn suggests that the vibration conditions for the vertical vibration test must be set for each position where the connector is attached.

Figure. 6 shows the results of calculating the OCL relative displacement frequency and amplitude for a simple catenary for Shinkansen line currently used in Japan by OCL/pantograph simulation. Section 5 describes the procedure for setting the test conditions for the vertical vibration test using the same figure. For safety reasons, the vibration amplitude in the vertical vibration test should be set considering the maximum OCL relative displacement amplitude that can occur in the OCL. Previous research [3] has reported that "increase in train speed" and "decrease in OCL tension" were conditions that increase the OCL relative displacement amplitude. The simulation conditions in Fig. 6 consider the maximum train speed in

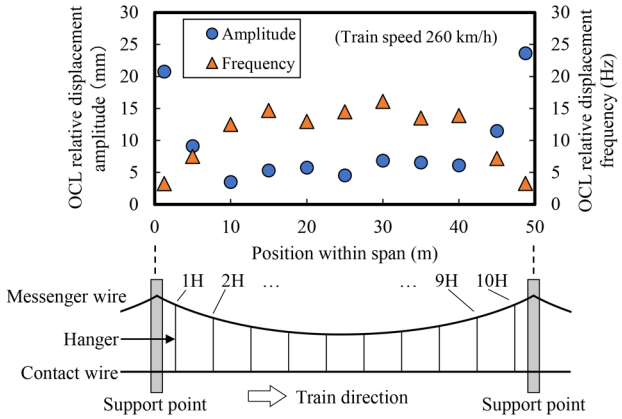

Fig. 5 Relationship between position within span and OCL relative displacement amplitude and frequency

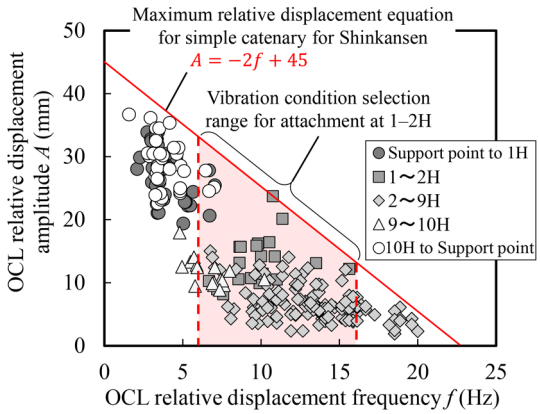

Fig. 6 Relationship between OCL relative displacement frequency and amplitude

operation, and the tension reduction (−10%) that can occur due to temperature changes and other factors. As previously mentioned, the figure shows a tendency of a low frequency and large amplitude near the support point, and a high frequency and small amplitude in the center of the span, as well as the distribution of the graph as a whole to be downward sloping to the right. Table 1 shows the frequency range of the OCL relative displacement for each connector installation position extracted from Fig. 6.

3.2 Horizontal OCL vibration

In this section, the authors analyze the OCL vibration in a section of a simple catenary and viaduct for Shinkansen, where fatigue-failure of connector conducting wires due to resonance has been reported [4].

Previous research [5] has shown that the vibration frequency input to the viaduct is dominated by "running speed (m/s) / car length (m)", and that the vibration of this viaduct is input to utility poles and metal fittings. The vibration frequency range of the OCL to be considered in the horizontal vibration test ("OCL frequency range") can be calculated to be 1.1 – 4.0 Hz when the running speed is 100 – 360 km/h and the car length is 25 m.

The OCL horizontal vibration amplitude was calculated using a structural analysis program. Figure 7 shows the constructed OCL model. This analysis involves the calculation of the OCL horizontal vibration displacement by inputting the pole vibration displacement at the support point of the model. The validity of the analysis results was confirmed by conducting a pole vibration test on the OCL equipment at RTRI (Fig. 8). The analytical results tended to produce slightly larger displacements, but the analytical values and the measured values were generally consistent with each other, so the analysis was judged as valid. Figure 9 shows an example of an analysis of the OCL horizontal vibration for a simple catenary for Shinkansen on an elevated section. The pole vibration displacement to be input to the OCL model was calculated using a structural analysis method [5] using a coupled model of the viaduct and the pole. The dashed lines in each graph in Fig. 9 indicate the maximum amplitude at each connector installation position. Figure 9 shows that the OCL horizontal vibration has a peak frequency near the pole's natural frequency (2.5 Hz), and many other peaks due to the OCL's natural vibration mode according to the span length were also confirmed.

Taking all these peaks into consideration, the horizontal vibration amplitudes were set within the OCL frequency range according to each speed uniformly at the maximum amplitude (Table 2).

Table 1 OCL relative displacement frequency range (simple catenary for Shinkansen)

Connector installation position	Frequency range (Hz)
Support point – 1H	2 – 7
1 – 2H	6 – 16
2 – 9H	7 – 20
9 – 10H	4 – 11
10H – Support point	1 – 7

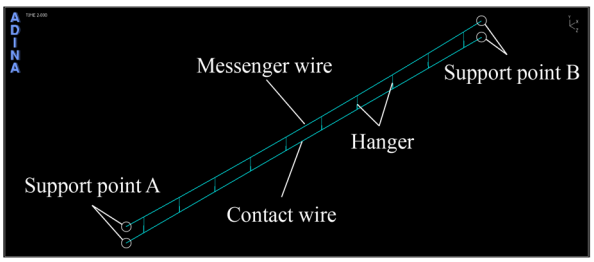

Fig. 7 OCL structural analysis model

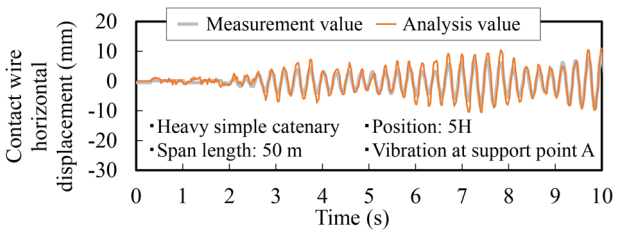

Fig. 8 Validation of OCL structural analysis

4. Connector strain frequency characteristics

The conventional JIS vibration test does not specify the height of the connector to be installed. However, differences in frequency characteristics that depend on the height of the connector need to be considered. Figure 10 shows the results of structural analysis of the

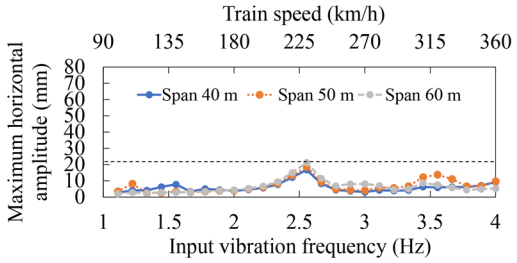

(a) Support point to 1H

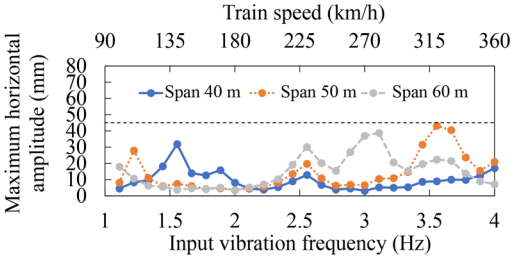

(b) 1 – 2H

Fig. 9 Example of OCL horizontal vibration analysis

Table 2 Vibration amplitude for horizontal vibration test

Maximum train speed (km/h)	Frequency range (Hz)	Vibration amplitude (mm)				
		Support point – 1H	1H – 2H	2H – 3H	3H – 4H	4H – 5H
260	1.1 – 2.9	25	35	60	80	90
320	1.1 – 3.6		45			
360	1.1 – 4.0					

relationship between the conducting wire strain and frequency when vibration is applied by pushing up the contact wire to connectors of different heights. The figure shows that the strain peak frequency and magnitude change depending on the connector height. This is because the frequency at which the connector is likely to deform changes depending on the length and inclination of the conducting wire. Therefore, conducting a safe evaluation in the vibration test requires setting a vibration frequency that causes the largest strain for the expected connector height.

5. Test condition setting procedure

Figure 11 shows the proposed implementation flow for the vertical vibration test and horizontal vibration test. A sample description is provided here, namely the procedure for setting the test conditions for both tests, where the assumption is that the connector for the Shinkansen is installed between 1H and 2H. The connector height selection range is 825–1475 mm when the connector is installed between 1H and 2H (including the overlapping area).

5.1 Vertical vibration test

The test conditions are set using the relationship between the frequency and amplitude of the OCL relative displacement shown in Fig. 6. The procedure is shown below. To obtain a vibration amplitude that is safe and in line with the actual usage situation, it is

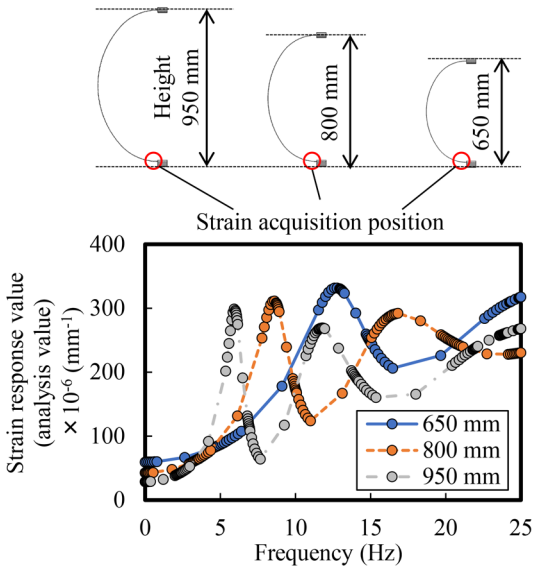

Fig. 10 Connector height and strain frequency characteristics

considered that the value should be set on the line that passes through the maximum amplitude of the same frequency (red solid line in Fig. 6). Henceforth, the equation for this line is referred to as the maximum relative displacement equation.

The frequency range of OCL relative displacement at the target connector attachment position (1H–2H) is 6–16 Hz according to Table 1. As mentioned in Section 4, the frequency characteristics of the conducting wire strain vary depending on the connector height. Therefore, conducting the test on the safe side requires selecting the connector height at which the strain is greatest in the above frequency range, and the frequency at that time. Figure. 12 shows the analysis results of the frequency characteristics of the maximum strain for the selected connector height range. In this case, the connector with a height of 1225 mm (frequency 7.1 Hz) has the maximum strain at 6–16 Hz. Therefore, the test connector height was selected to be 1225 mm, and the vibration frequency was selected to be 7.1 Hz. Then, using the maximum relative displacement equation, the vibration amplitude was determined to be 30.8 mm (=−2×7.1 +45).

The number of vibrations in this test was set to at least 2×10^6 times, which is the same as in the conventional JIS test. A value of at least 2×10^6 times was considered to exceed the number of pantographs that pass during the replacement cycle of a typical connector (approximately 8–15 years).

5.2 Horizontal vibration test

The horizontal vibration test requires a vibration of the messenger wire side and the contact wire side of the connector in the horizontal direction at the same time as in the field, so a new vibration test machine was created (Fig. 13).

The vibration amplitude at the target connector attachment position (1H–2H) is 35 mm (assuming 260 km/h) according to Table 2. As in the vertical vibration test, ensuring a safe test requires selecting the connector height and vibration frequency at which the strain is maximum. Figure. 14 shows the analysis results of the frequency characteristics of the maximum strain when vibration that simulates a horizontal vibration test was input to the connector model. The connector with a height of 1425 mm (frequency of 1.8 Hz) showed the maximum strain in the OCL frequency range of 1.1–2.9 Hz (see

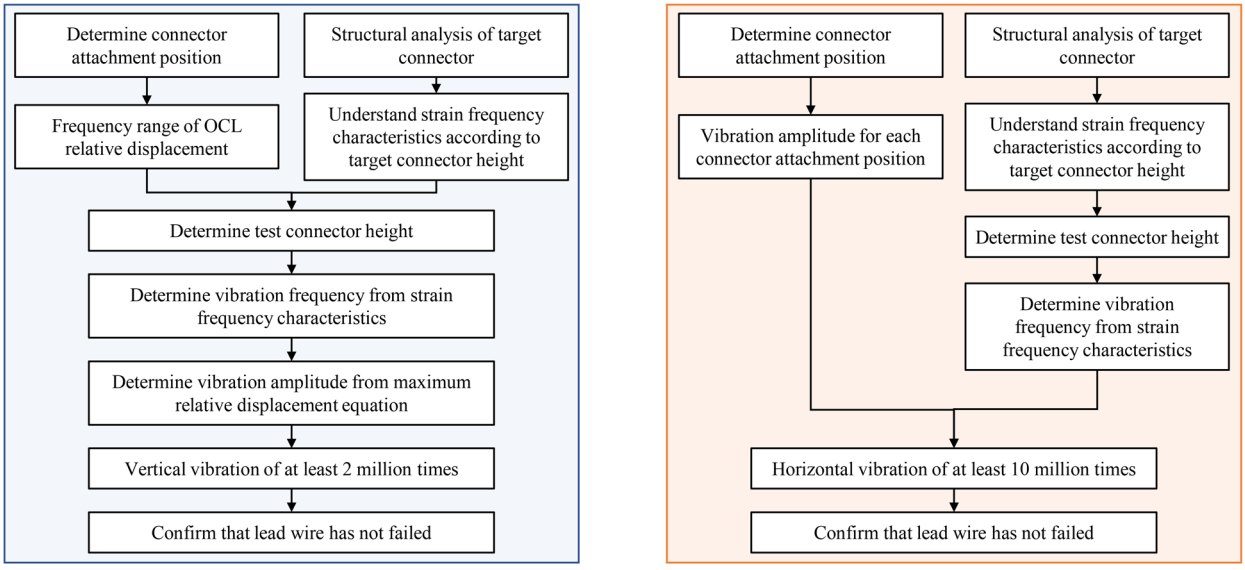

(a) Vertical vibration test (b) Horizontal vibration test

Fig. 11 Test implementation flow

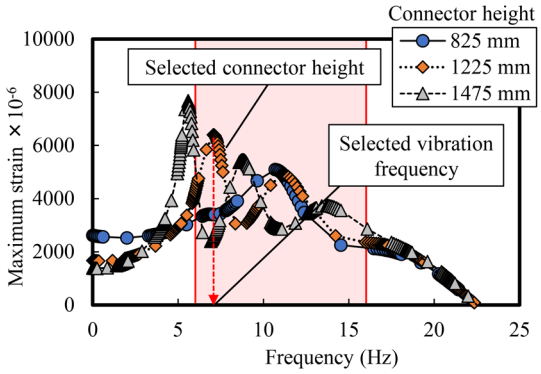

Fig. 12 Selection of test conditions (vertical vibration test)

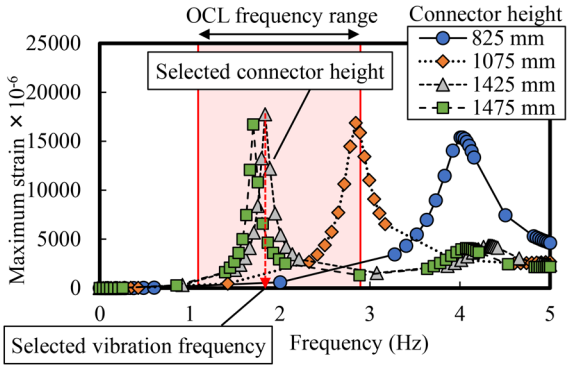

Fig. 14 Selection of test conditions (horizontal vibration test)

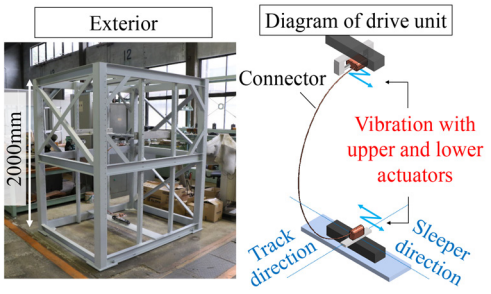

Fig. 13 Connector horizontal vibration tester

Table 2). Therefore, a test connector height of 1425 mm and vibration frequency of 1.8 Hz were selected.

OCL horizontal vibration continues for a certain amount of time with the passage of one train, and the number of vibrations varies depending on the OCL conditions and train speed. Therefore, using this as a basis to determine the number of vibrations is difficult. As a result, the number of vibrations in the horizontal vibration test was set to at least 10^7, which is considered to be the upper limit sufficient for practical use in general vibration tests.

6. Confirmation of proposed test method using actual connector

In this section, the authors conduct the above-mentioned test on a real connector and confirm whether the test results matched the connector's on-site disconnection status. As in the previous section, the authors assumed that the connector for Shinkansen would be installed between 1H and 2H, and performed the vibration test according to the test implementation flow in Fig. 11. Table 3 shows the test conditions defined in the previous section. Note that in both tests, one connector was used.

First, the results of the vertical vibration test are described. Figure 15 (a) shows the connector installed on the tester, and Fig. 15 (b) shows the test results. Results after 2×10^6 vibrations showed that no wire failure occurred. These results suggest that OCL relative displacement-induced fatigue-failure will not occur for cases where the target connector is attached between 1H and 2H. No previous research has reported cases of the target connector breaking at the OCL relative displacement, and the test results are consistent with this.

Next, the results of the horizontal vibration test are described. Figure 16(a) shows the connector attached to the tester, and Fig. 16(b) shows the test results. The horizontal vibration test results

Table 3 Test conditions

Fatigue factor	OCL relative displacement	Resonance
Damage to actual equipment	Failure cases absent	Failure cases present
Corresponding test	Vertical vibration test	Horizontal vibration test
Vibration frequency	6.3 Hz	1.8 Hz
Vibration amplitude	32.4 mm	35 mm
Connector height at maximum strain	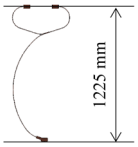	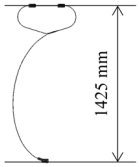

showed that the conducting wires of the target connector failed completely prior to reaching 10^7 vibrations (687,000 times). These results suggest that attaching the target connector between 1H and 2H may result in fatigue-failure when the train speed and connector height conditions are met. This is consistent with the reported case in which the target connector failed due to resonance.

The above results confirmed that the results of this test were consistent with the damage to connectors in the field. Therefore, the results suggest that conducting this test allows for the evaluation of the practical fatigue durability of connectors.

7. Conclusion

The authors sought to appropriately evaluate the fatigue durability of connectors by focusing on two connector fatigue factors of connectors, namely OCL relative displacement and resonance. The authors then proposed a vibration test method consisting of a vertical vibration test and a horizontal vibration test corresponding to each of those fatigue factors. The main results were as follows.

- An OCL/pantograph simulation was used for the vertical vibration test in order to understand the relationship between the amplitude and frequency of OCL relative displacement according to the connector installation position. A relational equation was also proposed for setting the vibration conditions.
- For the horizontal vibration test, the horizontal OCL vibration waveform was determined by OCL structural analysis. The vibration amplitude and OCL frequency range were then proposed according to the position within the span.
- The connector's strain frequency characteristics and OCL frequency range were used to propose a method for selecting the test connector height at which the strain for OCL vibration is maximized.
- An implementation flow was created for the above test method. The same test was also conducted on an actual connector, which confirmed that the test results were consistent with the disconnection conditions of the connector reported at academic conferences and other venues.

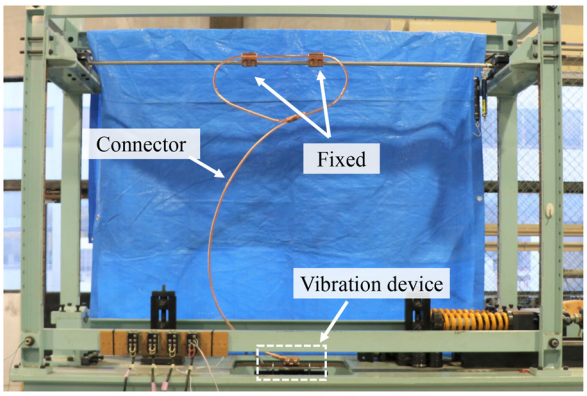

(a) Connector attached to the tester

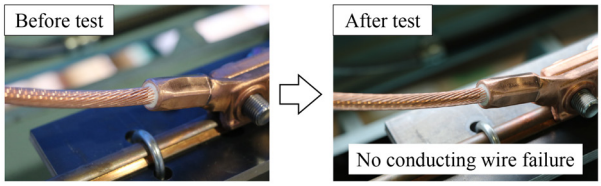

(b) Test result

Fig. 15 Vertical vibration test

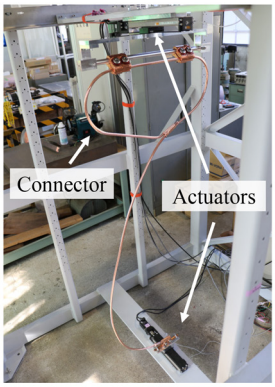

(a) Connector attached to the tester

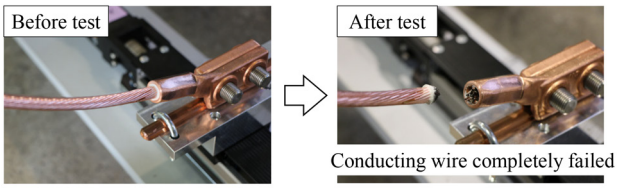

(b) Test result

Fig. 16 Horizontal vibration test

References

[1] Japanese Industrial Standards, JIS E 2002 "Electric traction overhead lines-Fittings-Test methods," 2020 (in Japanese).
[2] Japanese Industrial Standards, JIS E 2201 "Electric traction overhead lines-Fittings," 2013 (in Japanese).
[3] Yamashita, C., Ohara, T., Kobayashi, S., "Measures for Fatigue Damage Reduction in Electrical OCL Connections," *Quarterly Report of RTRI*, Vol. 60, No. 1, pp. 22-27, 2019.
[4] Ohara, T., Yamashita, C., "Study of Vertical Vibration Test of the Connector," *Proceedings of 2022 IEEJ Annual Meeting*, pp.

238-239, 2022 (in Japanese).
[5] Tsunemoto, M., Matsuoka, K., Goto, K., Susuki, H., Ikura, K., "Measures for Reducing Damage to Overhead Contact Line System due to Bridge Oscillations Caused by Passing Trains," *RTRI Report*, Vol. 34, No. 9, pp. 35-40, 2020 (in Japanese).

Authors

Takuya OHARA
Senior Researcher, Current Collection Maintenance Laboratory, Power Supply Technology Division
Research Areas: Fatigue of Overhead Contact Line, Vibration Engineering

Chikara YAMASHITA, Ph.D.Eng.
Senior Chief Researcher, Head of Current Collection Maintenance Laboratory, Power Supply Technology Division (Former)
Research Areas: Tribology under Current Flowing Condition, Fatigue of Overhead Contact Line

Development of Low-cost Train Patrol Support Method Using Smartphone

Hirofumi TANAKA
Track Geometry & Maintenance Laboratory, Track Technology Division

Boyu ZHAO
SMARTCITY RESEARCH INSTITUTE Co., Ltd.

Di SU **Tomonori NAGAYAMA**
The University of Tokyo

Regional railway companies are facing difficult business conditions. However, railway facilities and rolling stock inspections and maintenance are still required to ensure safe and stable train operations. This study introduces the development of a smartphone-based train patrol support application as a low-cost track condition management method that can be introduced even by regional railway companies. Test measurements were made using the application on a commercial line. We also investigated possible uses of the measurement data. Results showed that acceleration data are effective for train vibration management, and forward view video data are effective for understanding track conditions during desktop reviews.

***Key words*:** *train patrol, smartphone, train vibration, forward view video, regional railway, DX*

1. Introduction

Railway operators are facing a tough business environment as the number of railway users and railway employees decreases due to the declining birthrate and an aging population. This trend is particularly noticeable for regional railway operators, with approximately 90% of regional railway operators having current account deficits [1]. Furthermore, many regional railway operators also face the deterioration of their railway vehicles and facilities [1]. Notwithstanding, railway operators still need to inspect and maintain railway facilities and railway vehicles to operate railway vehicles safely and reliably.

To support operators, railway digital transformation (DX), a business transformation in the railway industry using digital technology, has been promoted over the past few years. Measures include, for example, the use of mobile information terminals such as smartphones (hereinafter referred to as "smartphones"). Smartphones are equipped with many built-in sensors and general-purpose products. They are also easy to procure and relatively low-cost compared to dedicated devices. Finding a way to use these devices to support railway maintenance and management, could lead to lower maintenance costs. Making full use of digital technology could also help save labor and provide tools to facilitate maintenance and management work that has traditionally relied on visual inspections and experience. Smartphones for maintenance and management of public infrastructure is already actively being promoted in the road sector. For example, they are already used by road patrols and for road surface condition management [2].

In the railway industry, several studies have been conducted on the use of smartphones for track maintenance and management [3, 4]. However, there are no examples yet of widespread implementation to support train patrols. This study addresses this gap. Using train patrol requirements set out in the Maintenance Standards for Railway Structures (Track Part) [5], we investigated a method designed to support train patrols using various sensors on smartphones, developed a dedicated train patrol support application software, and report in this paper the results of trials on an actual railway line.

2. Train patrol method using smartphone

2.1 Roles and issues of train patrols in the Maintenance Standards for Railway Structures (Track Part)

The "Maintenance Standards for Railway Structures (Track Part) [5]" (hereinafter referred to as the "Maintenance Standards") issued by the Director-General of the Railway Bureau of the Ministry of Land, Infrastructure, Transport and Tourism (MLIT) in January 2007, states that track patrols should "gather an overall understanding of the condition of the tracks." It also states that track patrols should conduct this work "on foot, by train, or by track motor car, etc."

Furthermore, the "Guidance of Maintenance Standards for Railway Structures (Track Part) [6]" (hereinafter referred to as the "Guidance of the Maintenance Standards") published by the Railway Technical Research Institute in March 2007 gives examples of what train patrols should look for. For example, "the presence or absence of abnormal train vibrations, the presence or absence of creaking noises, and the presence or absence of disruption to train operations."

In most cases, actual train patrols are conducted by railway staff who ride at the front of a commercial train, visually and physically checking a wide range of items, including the examples mentioned above, and record them in a field notebook. In addition, some railway operators conduct train patrols during extremely hot periods to detect signs of significant track irregularity, which is labor intensive. In this context, there is a need to consider ways to save labor and improve train patrol efficiency.

2.2 Overview of developed train patrol support application software

We set out to develop a low-cost method of supporting train patrols that can be introduced in regional railways, taking into account the roles of train patrols as defined in the aforementioned Maintenance Standards and the Guidance of the Maintenance Standards as well as their actual working conditions and status. Specifi-

cally, the method uses a smartphone installed with a dedicated application software (hereinafter referred to as the "app") developed for supporting train patrols. Digital data is used to facilitate the work of train patrols. For example, videos or images are used for the wide range of items that require visual checking, and acceleration data is used to check train vibrations traditionally checked by body sensory information.

Figure 1 shows the measurement screen of the train patrol support app (Train Patroller) [7]. This app runs on a smartphone equipped with Apple's iOS and is designed for easy operation. Currently, railway staff install the smartphone on board the railway vehicle during train patrols and start and stop measurements.

Table 1 shows the main measurement items of this app. A GPS receiver built into the smartphone enables measurement of moving speed, latitude, and longitude; motion sensors allow measurement of three-axis acceleration and angular velocity, a rear camera can be used to record video, and audio is recorded through a microphone. There are three measurement modes: "Vibration," "Vibration & Video," and "Video," and measurement items can be selected depending on the purpose. For video, the highest setting allows measurement at 60 fps/4K resolution. To reduce blurring in video measurement mode, iPhone 14 or later is recommended.

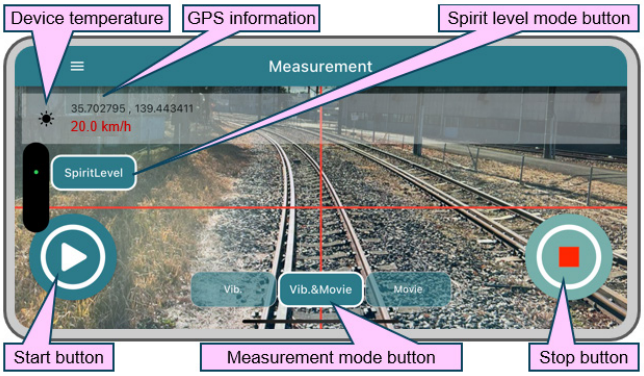

Fig. 1 Measurement screen of train patrol support app

Table 1 Main measurement items of train patrol support app

Sensor	Measurement item	Measurement mode			Sampling, etc. (file format)
		Vibration	Vibration & video	Video	
GPS receiver	Moving speed	Yes	Yes	Yes	1 Hz (text format)
	Latitude/ Longitude	Yes	Yes	Yes	
Motion sensor	Three-axis acceleration	Yes	Yes	–	100 Hz (text format)
	Three-axis angular velocity	Yes	Yes	–	
Camera (rear camera)	Video	–	Yes	Yes	10/20/30/60 fps VGA/HD/ FullHD/4K (mp4 format)
Microphone	Sound	Yes	Yes	Yes	16 kHz (m4a format)

2.3 Method for installation on railway vehicles

Figure 2 shows how to install the smartphone on a railway vehicle. Figure 2 (a) illustrates measurement of vehicle acceleration for managing train vibration. The Guidance of the Maintenance Standards [6] states that "measurement should be taken on the floor on the front bogie at the very front of the train or the rear bogie at the very rear of the train. To ensure accurate measurement, the accelerometer should be placed on a horizontal surface and straight in the train direction." However, in practice this position is not suitable for making measurements because the GPS reception sensitivity is low, and in commercial trains, the area directly above the bogie is the passenger compartment.

Figure 2 (b) illustrates the proposed alternative. The smartphone is installed on the windshield surface inside the driver's cab at the front of the vehicle. By installing it this way, the GPS increases in reception sensitivity and the smartphone is able to capture the forward view video as well. It has been confirmed that the acceleration when the smartphone is installed at this position is about 5 to 15% higher than when it is installed directly above the bogie, although there is variation depending on the vehicle type [8]. In addition, by using a fixture, it is possible to set the smartphone with an angle of dip, making it possible to adjust the field of view of the forward view video depending on the purpose of inspection. Since the installation angle of the smartphone, including angle of dip, affects not only the field of view of the forward view video but also the evaluation of train vibration, it can be checked using the "spirit level" function shown in Fig. 1 when installing the smartphone, and is automatically recorded when measurement starts, and can be used to correct train vibration, which will be described later. Furthermore, the "device temperature" display makes it possible to monitor

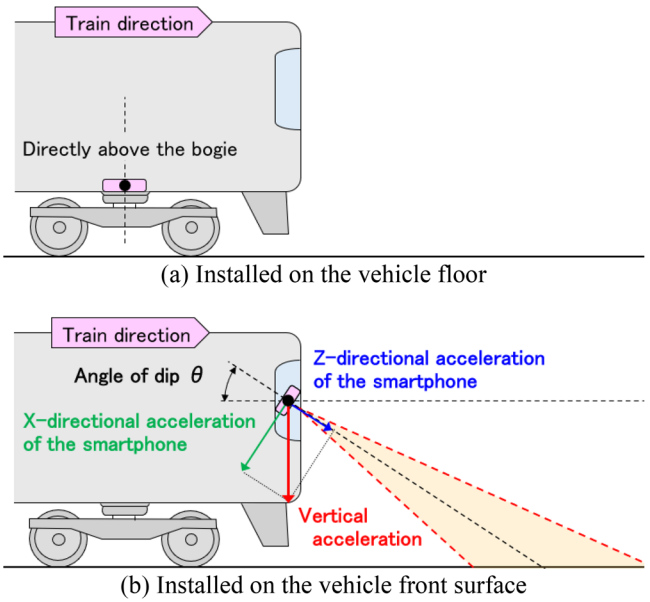

Fig. 2 Example of smartphone installation on railway vehicle

the internal temperature of the smartphone and prevent measurement abnormalities caused by thermal runaway.

2.4 Method for processing measurement data

The data acquired by the developed train patrol support app is saved in a common file format as shown in Table 1, so it can be displayed and processed by various software. Figure 3 shows an example of data processing procedure. First, the measurement data is imported into a PC using Apple's media player "iTunes" in a Windows OS environment. Next, since it is known that there are minute sampling fluctuations in the acceleration and angular velocity data, and GPS-related data recorded by the smartphone, the data is converted into intermediate data using dedicated software "Train Patroller Resampler" to correct these fluctuations [8]. Then, the track maintenance management database system "LABOCS "[9] is used to perform filtering, time/distance conversion, kilometer distance assignment, and creation of a significant value list. This makes it possible to display charts in the LABOCS waveform viewer. LABOCS is a signal processing software developed by the Railway Technical Research Institute that specializes in processing track-related data, and has been adopted by many railway operators. On the other hand, the video data can be viewed as is in a general-purpose video viewer, or it can be viewed by overlaying subtitle information created in LABOCS and assigning kilometer distances. In addition, it is possible to create a bird's-eye image by projective transformation processing [10] and view it with a general-purpose image viewer.

3. Test implementation on commercial line

3.1 Overview of railway line and measurement method

The developed train patrol support app was installed on an Apple smartphone, iPhone 14 Pro, and test measurements were performed on an actual railway line. The test line was a single-track, electrified line with mostly ballast track. The annual passing tonnage on the test section was approximately 7 million tons, and the maximum operating speed on the line was 130 km/h.

Figure 4 shows the installation of a smartphone on a commercial train (express train). In this example, three smartphones were used for comparison and verification. Smartphones A and B were installed on the glass surface of the vehicle front door, and smartphone C was installed on the floor of the vehicle front area. Smartphone A was fixed directly to the glass surface with double-sided tape at an angle of dip 0° to check the situation of the track and its surrounding wide area. Smartphone B was fixed at an angle of dip 28° using a commercially available suction cup with sufficient rigidity to check the situation of the track. The forward view video was acquired with a resolution of 4K (3840 × 2160) and a frame rate of 30 fps. Smartphone C was also fixed directly to the floor with double-sided tape for comparison. It should be noted that since the test vehicle area directly above the bogie was inside the passenger compartment, measurement with the smartphone fixed on the bogie was not performed.

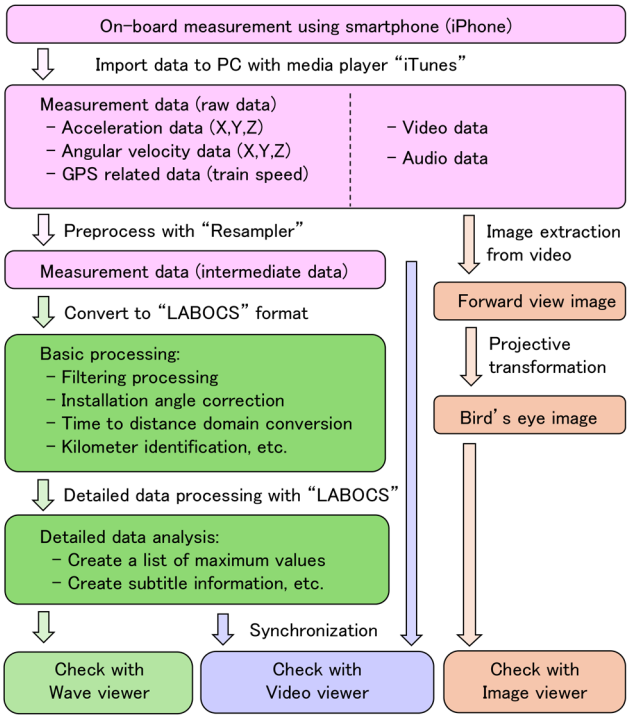

Fig. 3 Example of how measurement data is processed

3.2 Example of using acceleration to manage train vibration

Acceleration data acquired by the train patrol support app can be used to manage train vibration. Figure 5 shows an example of track irregularity waveforms measured in the same section as the train vibration measurement under the conditions shown in Fig. 4 at a similar time. The acceleration is shown as a waveform processed with an 8 Hz low-pass filter based on the Guidance of the Maintenance Standards [5]. It can be seen from the figure that vertical acceleration tends to be large in areas with large longitudinal level, and lateral acceleration tends to be large in areas with large alignment. Moreover, comparing the waveforms of smartphones A, B, and C, it can be seen that there is no clear difference in the waveforms depending on the installation position, installation method, and angle of dip of the smartphone. In addition to the horizontal alignment, the figure also shows the yaw angular velocity measured simultaneously by the smartphone for reference. The phase of the horizontal alignment and the yaw angular velocity are well matched, which shows that the time-distance conversion and kilometer-distance calculation method shown in Fig. 3 have sufficient kilometer-distance calculation accuracy for practical use.

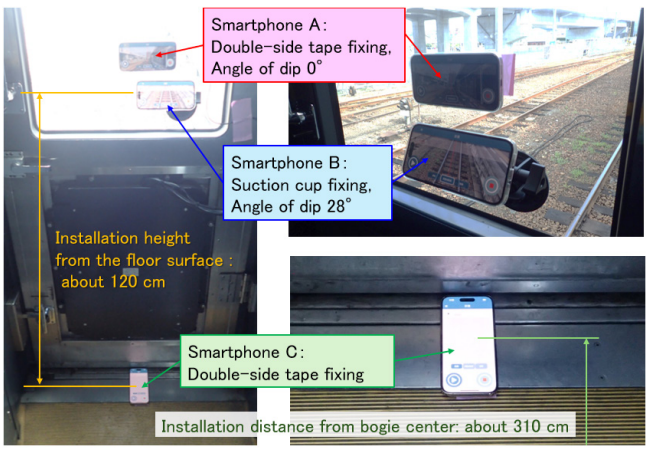

Fig. 4 Example of smartphone installation on a commercial train

Figure 6 shows an example of the power spectral density (PSD) of acceleration calculated using the data of the train section shown in Fig. 5. The average speed of the train in the analyzed section is approximately 100 km/h. Figure 6 (a) shows that the PSD of the vertical acceleration is almost the same for smartphone A and smartphone C, so the influence of the installation position is considered to be small. On the other hand, when comparing smartphone A and smartphone B, the PSD of smartphone B is smaller overall. We infer that this is due to the fact that the observation axis of the acceleration of the smartphone was shifted from the vertical direction because smartphone B was fixed with an angle of dip as shown in Fig. 4. Next, Fig. 6 (b) shows that the PSD of the horizontal acceleration is almost the same for smartphone A and smartphone B, so the influence of the angle of dip is considered to be small. On the other hand, when comparing smartphone A and smartphone C, some differences are seen. This is thought to be due to the influence of the difference in the installation position as shown in Fig.4.

Figure 7 shows an example of a comparison of the total amplitude of acceleration calculated using data including the section

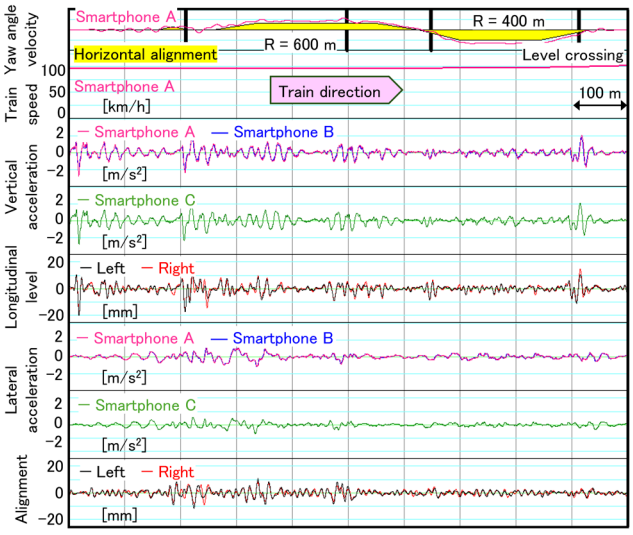

Fig. 5 Example of waveforms for acceleration and track irregularity

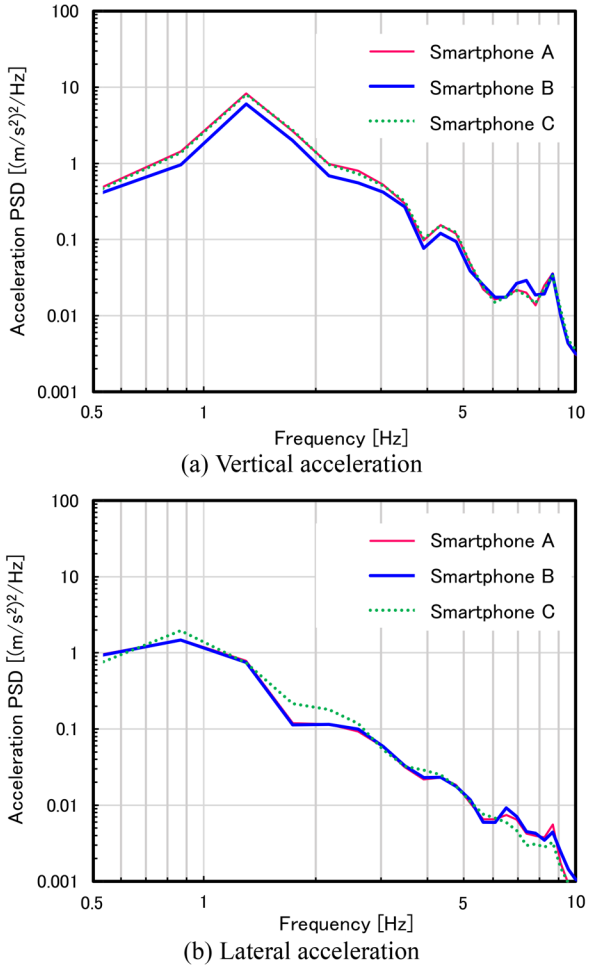

Fig. 6 Comparison of acceleration PSDs (for section with speed of about 100 km/h)

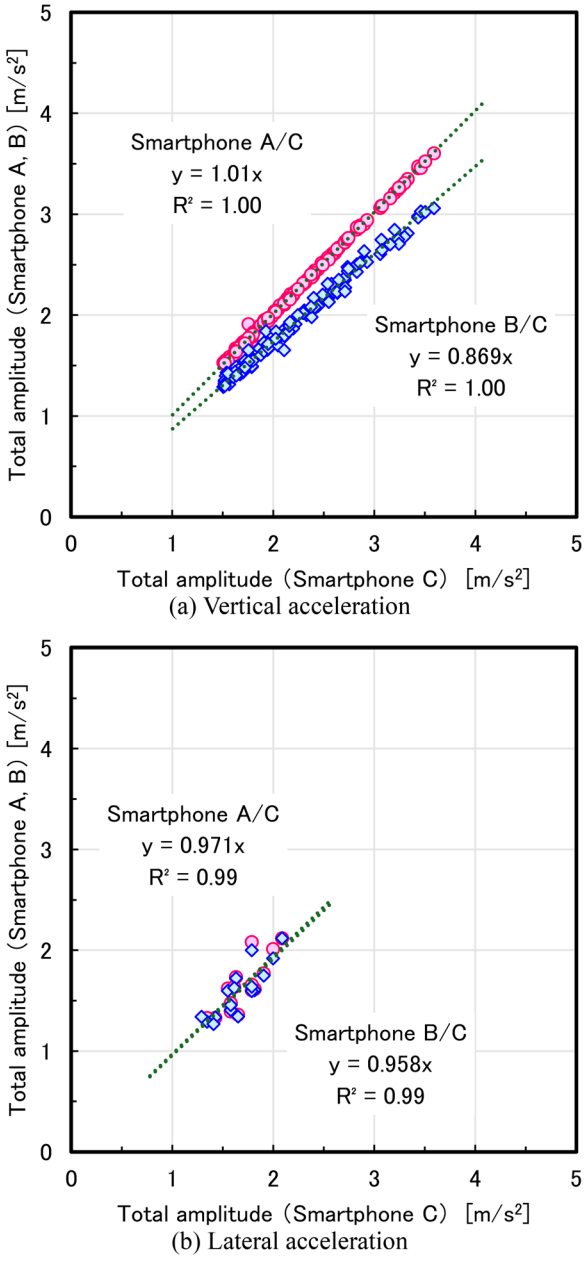

Fig. 7 Comparison of total acceleration amplitudes

shown in Fig. 5. In this figure, the peaks of the total amplitude of smartphone C with 1.5 m/s^2 or more are extracted and plotted for both vertical and lateral acceleration. Figure 7 (a) shows that the total amplitude of vertical acceleration is roughly the same for smartphone C and smartphone A. Comparing smartphone C and smartphone B, the total amplitude of smartphone B tends to be about 15% smaller than that of smartphone C. We infer that this is due to the influence of the angle of dip of smartphone B. Next, Fig. 7 (b) shows that the total amplitude of lateral acceleration is generally smaller and has a large variation compared to vertical acceleration, but smartphone A and smartphone B tend to be about 3 to 4% smaller than smartphone C. We infer that this is due to the characteristics of the vehicle structure and the influence of the smartphone installation position.

Therefore, for the vertical acceleration of smartphone B, which differed significantly from smartphone C, we considered correcting the vertical acceleration by vector synthesis of X-axis acceleration and Z-axis acceleration using the angle of dip of smartphone B. Figure 8 shows a comparison between the vertical acceleration of smartphone C and the vertical acceleration corrected by vector synthesis of the acceleration of smartphone B. As can be seen from the figure, the difference between the two is almost eliminated, and it was found that, even if a smartphone is installed with an angle of dip, it can be used to manage vertical vibration. In addition, when using the acceleration data obtained by this method for train vibration inspection, we consider that it is possible to correct the difference between the acceleration measured at the front of the train and directly above the bogie by performing a comparative measurement when introducing this method.

3.3 Example of using forward view video to check track conditions

The forward view video data acquired by the train patrol support app can be used for desktop track patrols. For example, it can be used to check the track condition at points where train vibration exceeds the standard value. Figure 9 shows an example of a forward view image of a mud pumping area extracted from a forward view video acquired under the conditions shown in Fig. 4. The upper part of the image in Fig. 9 (a) shows the kilometer distance, train speed, and total amplitude of vertical and horizontal vibrations as subtitle information. It can be seen that the train was traveling at about 98 km/h in the relevant section. The yellow trapezoidal dashed line in each figure is the approximate region of projective transformation. The forward view image of Smartphone A installed with an angle of dip 0° shown in Fig. 9 (a) is suitable for checking the overall track conditions. On the other hand, the forward view image of smartphone B installed with an angle of dip 28° shown in Fig. 9 (b) has a field of view too narrow to check the entire track, but the area around the track is magnified making it possible to check the track condition in more detail than in Fig. 9 (a).

Figure 10 shows the results of projective transformation of each of the forward view images shown in Fig. 9 to create a bird's-eye image. Each figure also shows an enlarged image focusing on the same rail fastening system. The overhead image of Smartphone A shown in Fig. 10 (a) includes the track periphery, and the area of the track occupies a small portion of the entire image. On the other hand, the bird's eye image of smartphone B shown in Fig. 10 (b) has a wide area of the entire image occupied by the track, and the image distortion is smaller than that of Fig. 10 (a), so the details of the track, such as the rail fastening system, can be inspected.

It is recommended to set the angle of dip of the smartphone appropriately depending on the range and object to be checked. Forward view videos, forward view images extracted from them, and bird's-eye images obtained by projective transformation of these videos have the potential to be used not only to support train patrols, but also to complement or replace foot patrols.

The analysis time required to extract a forward view image from a forward view video and obtain a bird's-eye image by projec-

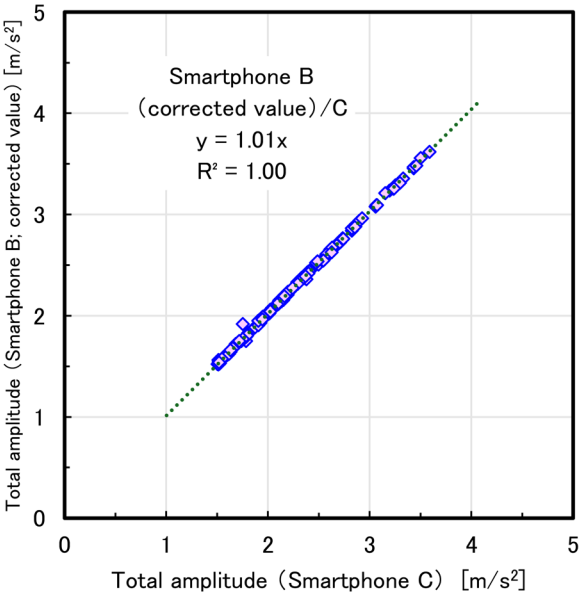

Fig. 8 Vertical acceleration corrected by vector synthesis

(a) Smartphone A (angle of dip 0°)

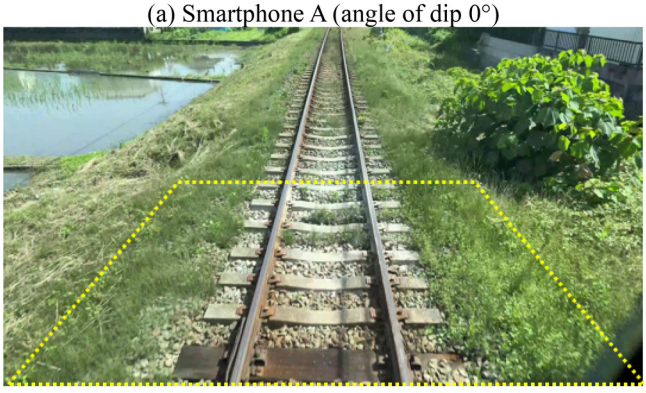

(b) Smartphone B (angle of dip 28°)

Fig. 9 Example of forward view video of mud pumping area

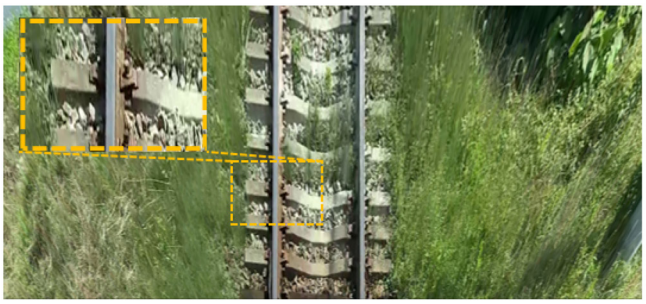

(a) Smartphone A (angle of dip 0°)

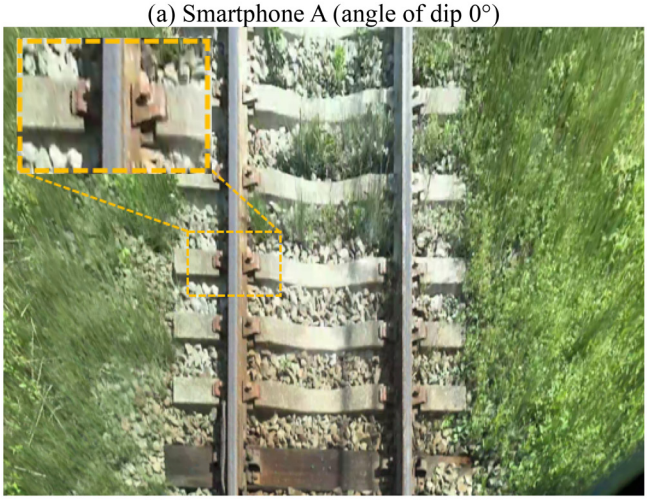

(b) Smartphone B (angle of dip 28°)

Fig. 10 Example of bird's-eye image created by projective transformation of forward view image

tive transformation depends on the specifications of the PC used. In this study, we used a general-purpose PC to extract images of all frames of the video, which took approximately three times the video playback time.

4. Conclusions

In this study, we developed a train patrol app that utilizes various sensors of a smartphone and investigated a method of using this app to support train patrols, and conducted trials on an actual railway line. The findings are as follows:

- Considering the requirements for train patrols stipulated in the Maintenance Standards (Track Part), we developed a train patrol support app that runs on a smartphone. The developed train patrol support app is easy to operate and can measure train speed, acceleration, angular velocity, forward view video, etc. by utilizing various sensors and cameras built into the smartphone. At the highest setting, the video can record the measurement results at 60 fps/4K resolution.
- Using the developed app, we carried out test measurements during train patrols on a commercial line, and examined possible uses of the obtained data. We found that acceleration data can be used to manage train vibrations by correcting acceleration, even when the smartphone is fixed with an angle of dip. Similarly, for forward view video data, we developed a method to add kilometer distance, acceleration values, etc. to forward view videos as subtitle information, and carried out projective transformation of the forward-facing images extracted from the video to create a bird's-eye image, demonstrating that images of the track as seen from directly above can be reproduced. These results are expected to make it easier to carry out desktop checks of track conditions.

Finally, although the technology described in this paper has reached a certain level of practical application as a train patrol support tool, there is still room for further research, such as automatic measurement functions, automatic track anomaly detection technology, and the development of a server system for data processing and viewing. We are currently working on developing these technologies and plan to report on them in due course.

Acknowledgment

We would like to express our gratitude to all the railway operators who offered their cooperation in the trial of the train patrol support method proposed in this study on commercial lines.

References

[1] Railway Bureau of Ministry of Land, Infrastructure, Transport and Tourism, "地域鉄道の現状," https://www.mlit.go.jp/tetudo/content/001573729.pdf (Reference data: July 1, 2025) (in Japanese).

[2] Zhao, B., Nagayama, T. and Xue, K., "Road profile estimation, and its numerical and experimental validation, by smartphone measurement of the dynamic responses of an ordinary vehicle," *Journal of Sound and Vibration*, Vol. 457, pp. 92-117, 2019.

[3] Shinoda, N., Tsunashima, H., Matsumoto, A., Sato, Y. and Ogata, S., "Railway track management based on vibration data of in-service train measured by a mobile device," *Transactions of the JSME (in Japanese)*, Vol. 88, No. 911, No. 21-00375, 2022 (in Japanese).

[4] Ikeuchi, M. and Tanaka, K., "Development of track maintenance system using smartphones," *Japanese Railway Engineering*, Vol. 63, No. 2, pp. 8-10, 2023.

[5] Ministry of Land, Infrastructure, Transport and Tourism, "*Maintenance Standards for Railway Structures (Tracks Part)* ," 2007 (in Japanese).

[6] Railway Technical Research Institute, "*Guidance of Maintenance Standards for Railway Structures (Tracks Part)* ," 2007 (in Japanese).

[7] Tanaka, H., Zhao, B., Su, D. and Nagayama, T., "Study on practical application of low-cost train patrol support method for railway track maintenance using a smartphone," *Journal of AI data science, JSCE*, Vol. 5, No. 1, pp. 56-65, 2024 (in Japanese).

[8] Tanaka, H., Su, D. and Nagayama, T., "Fundamental study of low-cost track condition monitoring by using smartphones and tablets," *Journal of railway engineering, JSCE*, No. 22, pp. 39-46, 2018 (in Japanese).

[9] Yoshimura, A., Yoshida, Y. and Kamiyama, M., "Development of database system for railway track maintenance management, micro LABOCS for Windows and its features," *QR (Quarterly Report of RTRI)*, Vol. 38, No. 2, pp. 102-106, 1997.

[10] Nagamine, N., Goda W., Maeda, R., Tsubokawa, Y., Kato, S. and Itoi, K., "Inspection method of track facilities using image analysis taken from front of trains," *QR (Quarterly Report of RTRI)*, Vol. 64, No. 3, pp. 205-210, 2023.

Authors

Hirofumi TANAKA, Dr.Eng.
Manager, Track Geometry & Maintenance Laboratory, Track Technology Division
Research Areas: Track Condition monitoring, On-board Measurement, Track Maintenance

Boyu ZHAO, Ph.D.
CEO, SMARTCITY RESEARCH INSTITUTE Co., Ltd.
Research Areas: Track Monitoring, Inverse Analysis, Structural Dynamics

Di SU, Ph.D.
Associate Professor, Department of Civil Engineering, The University of Tokyo
Research Areas: Structural Simulation, Dynamics of Transportation Infrastructures, Reliability Design and Risk Analysis

Tomonori NAGAYAMA, Ph.D.
Professor, Department of Civil Engineering, The University of Tokyo
Research Areas: Bridge and Vehicle Dynamics, Inverse Analysis, Infrastructure Monitoring

Evaluation of the Effect of Loose Bridge Bearing on Onboard Measured Track Geometry Using Numerical Analysis

Koji HATTORI
Structural Mechanics Laboratory, Railway Dynamics Division

Kodai MATSUOKA
Data Analytics Laboratory, Information and Communication Technology Division

Hirofumi TANAKA
Track Geometry & Maintenance Laboratory, Track Technology Division

Detection of loose bridge bearings with an uplift gap in steel bridges requires visual in situ inspection, which is labor-intensive. This study investigated the effect of loose bearings on track geometry using numerical calculation, as part of a fundamental investigation into detecting loose bearings using track geometry. A non-linear spring representing the loose bearing was introduced into the existing calculation tool, identifying the loaded track geometry considering the structural deformation. Results of a simulation using this tool clarified that the displacement of loose bearings appears in track geometry as a local fluctuation with a half wavelength of about 5 m, regardless of the size of the uplift gap at the loose bearing.

Key words**:** *drive-by measurement, steel bridge, loose bearing, track geometry, track inspection vehicle*

1. Introduction

An important inspection item in the maintenance and management of steel railway bridges is the detection of loose bearings [1]. A loose bearing refers to a phenomenon in which gaps that have formed between the sole plate and the lower bearing, or between the lower bearing and the bearing seat—due to damage to the bearing seat mortar, settlement of the bearing, or corrosion and wear—are compressed and uplifted when a train passes over. Loose bearings are a concern since they can increase stress in the bearing parts and surrounding components, which leads to fatigue cracks and loose bolts. Therefore, the occurrence and condition of loose bearings need to be correctly detected and monitored, and measures should be taken as needed [2].

Loose bearings are detected by visual inspection from under the girder, but this requires considerable time and expenditure [3]. In addition, inspection on lines with little traffic is even more time consuming because of the need to wait for a passing train to detect loose bearings based on their movement when a train passes. Therefore, detection methods using sensors installed under girders have been developed to reduce the labor and cost intensity of such inspections [4] [5]. However, there was a period when steel railway bridges on conventional lines were built with standard girders, many such bridges are still standing today [6]. Installing equipment under girders on these bridges still requires massive costs and effort.

Meanwhile, progress has been made in recent years in research that uses data measured by onboard sensors to evaluate bridge performance as they pass over them [7]. An issue in previous research has been the elimination of track geometries measured under unloaded conditions such as rail irregularities and distortions, as well as the extraction of structural deformation components. Some of these issues were solved using Matsuoka et al.'s theory [8] based on the use of multiple data from onboard measurements. This has resulted in the development of a method for estimating bridge resonance conditions and girder deflection from onboard measured track geometries, which has been used in practical applications [9] [10] [11]. These methods were mainly aimed at high-speed railways, but onboard measurement data for conventional railways has also been examined in recent years. Hattori et al. [12] [13] [14] developed a girder deflection-track geometry conversion program that calculates loaded track geometry from bridge deformation in order to establish a girder deflection estimation method using two track geometries obtained by a two-bogie track inspection vehicle used for track inspection on many conventional railways (henceforth, "two-bogie inspection vehicle"). This program also allowed for the evaluation of the influence of adjacent bridges, which was an issue when estimating girder deflection using a two-bogie inspection vehicle.

Improving the above-mentioned method for estimating girder deflection using track geometry and detecting loose bearings on bridges using onboard-measured track geometry can significantly reduce the labor needed for inspections from below the girder. However, the detection of loose bearings using onboard measurement data such as track geometry has hardly been examined to date, and to begin with, the effect of loose bearings on track geometry has not even been clarified. Therefore, the effects and characteristics of loose bearing behavior and track geometry need to be clarified, and a method for detecting loose bearings using those characteristics needs to be developed.

Based on these considerations, we conducted fundamental research to develop a method for detecting loose bearings from track geometry obtained with a two-bogie inspection vehicle. To this end, we first extended the existing girder deflection-track geometry conversion program to consider a nonlinear spring representing loose bearings. Next, we used the extended conversion program in order to conduct a numerical analysis of a steel railway bridge with a span length of 12.3 m. We clarified the loose bearing behavior and its effect on track geometry when a train passes. Specifically, we analyzed the bearing spring displacement, obtained track geometry and its wavelength characteristics.

2. Numerical method

2.1 Existing analysis method

In this section we explain the existing girder deflection-track

geometry conversion program [12], which can calculate structure deformation from track geometry.

Figure 1 shows the calculation flow of the girder deflection-track geometry conversion program, and Fig. 2 shows the track geometry measurement using a two-bogie inspection vehicle. This program focuses on the two-track geometries measured onboard the two-bogie inspection vehicle shown in Fig. 2, namely the asymmetrical chord offset track geometry (ACTG) measured at axles 124 ("124 ACTG") and the ACTG measured at axles 134 ("134 ACTG"), which are measured under different load conditions. The difference between these two track geometries is then taken to estimate the girder deflection [12].

The program consists of a structural analysis module that uses a two-dimensional finite element method (2D FEM) and a signal processing module that uses the track maintenance management database system LABOCS [15], which is used in the track maintenance field. The entire program is controlled by the numerical analysis software MATLAB.

The structural analysis models the structure using 2D elements such as springs and beams, as in normal FEM, and calculates the structure response when a loading sequence with the same axle arrangement and axle load as the two-bogie inspection vehicle runs through it. Because the effect of the dynamic response of the structure can be neglected, the structural analysis module calculates the static response of the structure repeatedly when a train passes through it using a simulation in which the loading sequence is gradually moved. It should also be noted that the "dynamic" and "static" terms differ from the "loaded" and "unloaded" track geometry terms used later in this text.

As a result, the loaded track geometries 124 and 134 ACTG, are calculated from the four axle position rail displacements obtained from the two-bogie inspection vehicle. There is a phase difference between the 124 ACTG and 134 ACTG, so these values were converted by filter processing into the 10 m symmetrical chord offset track geometry (124) and 10 m SCTG (134), which have no phase difference. Hereafter, the 10 m symmetrical chord offset track geometry (124) and (134) are referred to as 10 m SCTG (124) and 10 m SCTG (134), respectively.

Figure 3 shows the characteristics of the filter for converting from ACTG to 10 m SCTG. Although not subject to calculations in this study, the system has a function for calculating the difference between the 10 m SCTG (124) and 10 m SCTG (134), called the loaded track geometry difference, which has a linear relationship with the girder deflection.

Meanwhile, preliminary analysis showed slight differences in loose bearing behavior between each axle pass. Hence, the influence on the difference in the loaded track geometry was also small. Therefore, this paper focuses on the 10 m SCTG. In this case, the unloaded track geometry, which is removed by the difference in the loaded track geometry difference, must be removed separately from the 10 m SCTG. This will be described in detail in Section 3.

2.2 Expansion for loose bearings

The nonlinear spring was introduced into the structural analysis module of the existing girder deflection-track geometry conversion program. This expansion allows for the expression of loose bearings. In this paper, the gaps in the loose bearing are collectively referred to as "uplift gap" and modeled. Cases where the uplift gap is present result in a low bearing stiffness, but when the uplift gap is closed by the train load, the stiffness is thought to return to the same value as in the bearing without the looseness (uplift gap). Therefore,

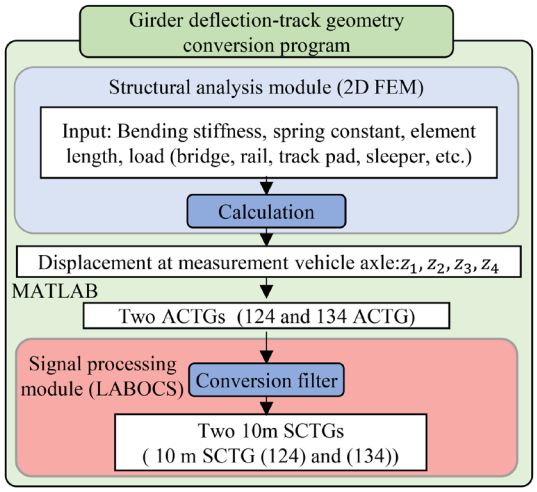

Fig. 1 Calculation flow of girder deflection-track geometry conversion program

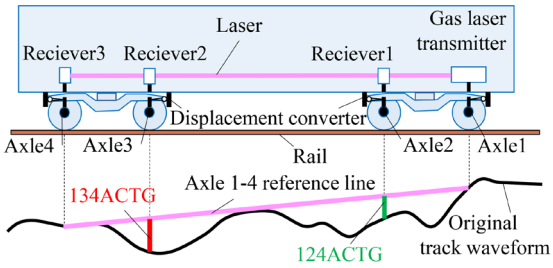

Fig. 2 Track geometry measurement using two-bogie inspection vehicle

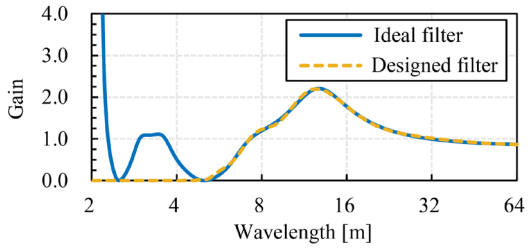

Fig. 3 Characteristics of filter for converting ACTG to 10 m SCTG

this is modeled as a bilinear nonlinear spring with one break point. We sought to reduce the computational load in the inverse analysis that we plan to develop in the future by using the following method, which does not require convergent computations, in order to solve the stiffness equation, including the nonlinear spring. It should be noted that the load and displacement are considered only in the vertical direction below.

First, we create a stiffness matrix $\boldsymbol{K}_1$ that considers only the primary stiffness k_1 of a bilinear nonlinear spring defined by primary stiffness k_1 and secondary stiffness k_2. We then calculate the provisional displacement $\boldsymbol{x}^*$ of all nodes when the external force vector $\boldsymbol{F}$ acts from the stiffness equation using Eq. (1):

$$\boldsymbol{x}^* = \boldsymbol{K}_1^{-1}\boldsymbol{F} \tag{1}$$

The relative displacement of the two ends of the nonlinear

spring in $\boldsymbol{x}^*$ gives the provisional displacement δ^* of the nonlinear spring (displacement when the nonlinear spring is linear with a primary stiffness k_1). The break-point displacement of the nonlinear spring is set as δ_1, and the ratio r of the break-point displacement δ^* of the nonlinear spring is defined as Eq. (2):

$$r=\frac{\delta^*}{\delta_1} \tag{2}$$

When $r<1$, the nonlinear spring does not reach the secondary stiffness region, and the displacement $\boldsymbol{x}^*$ obtained by Eq. (1) is the solution. We show the calculation method when $r\geq 1$ below.

The calculations up to this point are for linear systems, so the external force vector $\boldsymbol{F}_1$ required for the nonlinear spring to reach the break point can be calculated as Eq. (3) using the displacement ratio r:

$$\boldsymbol{F}_1=\frac{\boldsymbol{F}}{r} \tag{3}$$

When this external force vector $\boldsymbol{F}_1$ acts, the nonlinear spring has a displacement that just reaches the break point. The displacement vector $\boldsymbol{x}_1$ of all nodes at this time can be calculated from Eq. (4):

$$\boldsymbol{x}_1=\boldsymbol{K}_1^{-1}\boldsymbol{F}_1 \tag{4}$$

Since $r\geq 1$, the load $\boldsymbol{F}_1$ is a part of $\boldsymbol{F}$. Therefore, we additionally calculate the deformation corresponding to the remaining load $\boldsymbol{F}_2$, which is obtained by subtracting $\boldsymbol{F}_1$ from the external force vector $\boldsymbol{F}$. The load $\boldsymbol{F}_2$ is given by Eq. (5):

$$\boldsymbol{F}_2=\boldsymbol{F}-\boldsymbol{F}_1=\boldsymbol{F}-\frac{\boldsymbol{F}}{r}=\frac{r-1}{r}\boldsymbol{F} \tag{5}$$

The displacement of the nonlinear spring is the break point displacement δ_1 at the time of loading $\boldsymbol{F}_1$, so only the secondary stiffness of the nonlinear spring is effective when $\boldsymbol{F}_2$ acts. Therefore, the displacement $\boldsymbol{x}_2$ of all nodes after the nonlinear spring reaches δ_1 can be calculated as follows, using the stiffness matrix $\boldsymbol{K}_2$, in which the primary stiffness k_1 in the stiffness matrix $\boldsymbol{K}_1$ is changed to the secondary stiffness k_2:

$$\boldsymbol{x}_2=\boldsymbol{K}_2^{-1}\boldsymbol{F}_2 \tag{6}$$

Adding this to $\boldsymbol{x}_1$ allows for the final displacement $\boldsymbol{x}'$ of all nodes to be calculated using Eq. (7):

$$\boldsymbol{x}'=\boldsymbol{x}_1+\boldsymbol{x}_2=\boldsymbol{K}_1^{-1}\frac{\boldsymbol{F}}{r}+\boldsymbol{K}_2^{-1}\frac{r-1}{r}\boldsymbol{F} \tag{7}$$

Figure 4 shows the load-displacement relationship of the bilinear nonlinear spring to be modeled, where P and P_1 in the Fig. 4 represent the load acting on the spring when the loading sequence is $\boldsymbol{F}$ and $\boldsymbol{F}_1$, respectively, and δ represents the final spring displacement considering the secondary stiffness of the spring.

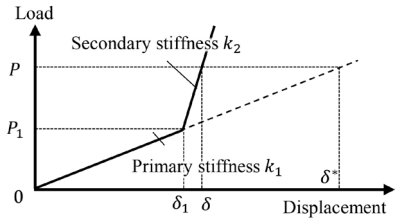

Fig. 4 Load-displacement relationship of bilinear springs to be modeled

2.3 Analysis target

The span length and bending stiffness can be set as parameters when analyzing the effect of loose bearings on track geometry. However, in this study, we have already assumed an actual bridge section to which the detection method is to be applied, so we decided to conduct a study using a model for that section [6].

Figure 5 shows the FEM model of the bridge section targeted in this study. We assumed an actual section with a continuous simple girder (steel bridge) with a bridge length of 13.1 m and a span length of 12.3 m, and we modeled a seven-girder bridge. From the left, the bridges were called B1, B2, …, B7. The nonlinear spring representing the loose bearing was placed on the train entrance or exit side of B4 at the center. The track inspection vehicle is assumed to be a two-car train running on the relevant section, with the first car being a two-bogie inspection vehicle and the second car being a diesel railcar accompanying the track inspection vehicle in the running direction. Only one side of the rail and bridge was modeled, and the loading sequence was the static wheel load of the track inspection vehicle converted to that of one rail. The bridge and rail were modeled using beam elements, and the track pad and bridge bearings were modeled using spring elements. FEM only modeled the vertical component, so the horizontal displacement of the bearing was not modeled.

Table 1 shows the specifications of the bridge and rail used. The girder and rail specifications were taken from drawings, and the stiffness of the track pad was set from material test results [16].

The leading axle's initial position was approximately 25 m from the left end of the leftmost bridge B1. The vehicle moved 0.1 m to the right in the Fig. 5, and the quasi-static calculation was repeated until the rearmost load left the rightmost bridge B7. We recorded the bridge displacement and axle position, rail displacement at each load position, and calculated the 124 and 134 ACTG. We also calculated the 10 m SCTG (124) and 10 m SCTG (134) using a

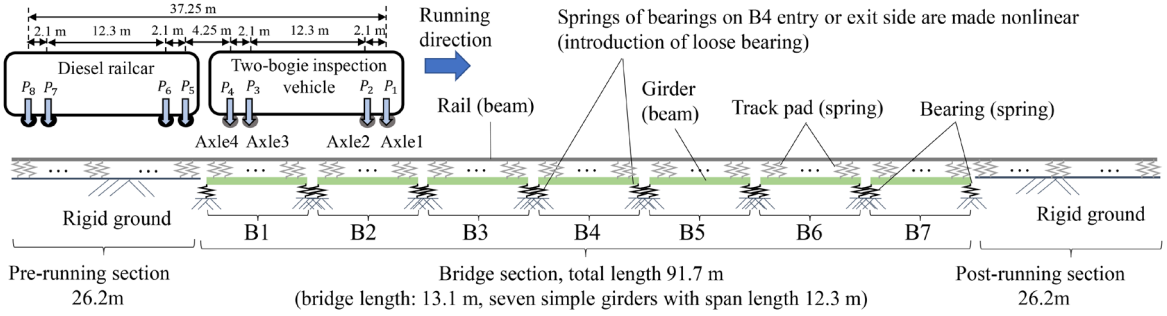

Fig. 5 FEM model of bridge section analyzed in this study

Table 1 Specifications of bridge and rail used in analysis

Rail bending stiffness	6.47×10^{6} (N·m^2)
Track pad stiffness	4.00×10^{7} (N/m)
Girder bending stiffness	1.41×10^{9} (N·m^2)
Normal bearing stiffness	1.00×10^{11} (N/m)

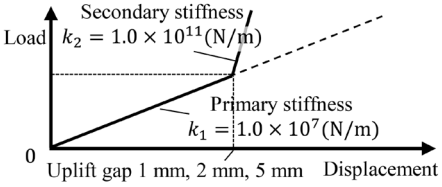

Fig. 6 Load-displacement relationship of nonlinear spring used in analysis

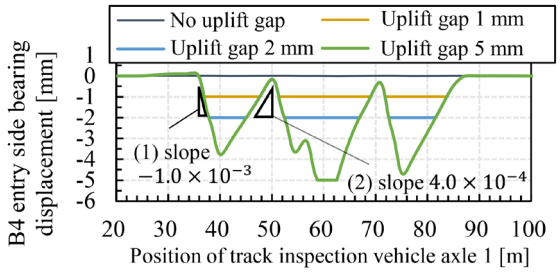

Fig. 7 B4 entry side bearing displacement for B4 entry side bearing uplift gap of 1 mm, 2 mm, and 5 mm, and for no uplift gap

conversion filter from the two ACTGs.

2.4 Analysis case

We sought to understand the loose bearing behavior and its effect on track geometry in the section by analyzing the central bridge B4, changing the uplift gap amount in the bearing expressed by the break point displacement, and the entry and exit sides. Specifically, we considered not only a "no uplift gap" case but also 1, 2, and 5 mm uplift gap cases for the entry and exit sides, for a total of 7 cases.

Figure 6 shows the load-displacement relationship of the nonlinear spring representing the loose bearing. The secondary stiffness was set to 1.0×10^{11} (N/m), the same stiffness as a bearing without an uplift gap. The actual state of the primary stiffness was unclear, so this was set to 1.0×10^{7} (N/m) in order to ensure that the stiffness was sufficiently smaller than the support stiffness of a normal bearing.

According to the Maintenance Standards for Railway Structures [1], the uplift amount is judged as AA if it impairs running safety, but there is no description of the uplift amount. The Design Standards and Commentary for Railway Structures [17] summarized running safety with respect to bearing displacement in terms of a vertical misalignment on the track surface, and set a design limit value for girder and misalignment under multiple-coupled conditions on conventional lines of 4 mm. It should be noted that the uplift gap amount did not directly become the amount of girder end misalignment. Given the above, we set the uplift gap at 5 mm as the amount that exceeds the design limit value of the girder end misalignment and that needs to be reliably detected, and set 2 mm and 1 mm, which are 1/2 and 1/4 of the design limit value, as realistic values.

3. Result of numerical analysis

3.1 Spring displacement of the bearing part

Figure 7 shows the spring displacement of the B4 entry side bearing with 1 mm, 2 mm, and 5 mm uplift gap cases, as well as a no uplift gap case. The no uplift gap case had only a slight spring displacement of ≤0.1 mm when a train passes, whereas the uplift gap cases exhibited a total of three downward displacement peaks occurring when a train passes. These three displacement peaks correspond to the front bogie of the first car (two-bogie inspection vehicle), rear bogie of the first car (two-bogie inspection vehicle), front bogie of the second car (diesel railcar), and rear bogie of the second car (diesel railcar), which each passed through the loose bearing points. The 1-mm and 2-mm uplift gap cases exhibited a bearing spring displacement that remained almost constant after reaching the set uplift gap. The 5-mm uplift gap case exhibited a peak spring displacement of less than 4 mm at the first peak, and the gap remained in this case. Additionally, at the second peak, the rear bogie of the first car (two-bogie inspection vehicle) and the front bogie of the second car (diesel railcar) were simultaneously positioned on bridge B4, which caused the spring displacement to reach an uplift gap amount of 5 mm, transitioning to secondary stiffness.

Next, we look at the slope of the spring displacement. In Fig. 7 (1) slope, where the spring displacement increases in the direction in which the bearing uplift gap is crushed, the slope was -1.0×10^{-3}. However, in Fig. 7 (2) slope, where the spring displacement decreases in the direction of the loose bearing, the slope is 4.0×10^{-4}, thereby exhibiting a different slope value. This case has a loose bearing on the entry side of the bridge, and the load acting on the bearing increased sharply when transferring from the exit side of the adjacent bridge to the entry side of the bridge, so the absolute value of the slope when the spring displacement increased was thought to be large.

Figure 8 shows the displacement distribution of the rail, bridge, and loose bearing when the leading axle passes through the loose bearing part in the analysis result with a 2-mm uplift gap. We can confirm from the results that the spring displacement of the bearing increased sharply immediately after the leading axle entered the bridge. Cases where the bearing spring displacement decreased (e.g., Fig. 7 (2) slope) were due to a decrease in the load sharing rate of the entry side bearing as the load moved from the entry side to the exit side of the bridge, and thus had a smaller slope than in cases where the bearing spring displacement increased. The above discussion is also supported by the fact that the axle movement distance at the peak decreases when the uplift gap was 5 mm roughly corresponded to the span length. Given the above, we assumed that different structural elements were involved in the loose bearing behavior when a train passes, depending on whether the spring displacement increased (uplift gap is crushed) or decreased (uplift gap occurs). The increase in spring displacement occurred when the train moved over between bridges, suggesting that the load sharing by the rails between the bridges played an important role. Figure 8 also showed that large local deformation occurred in the rail at the loose bearing location. Meanwhile, the decrease in spring displacement was due to the load sharing of the bearings within the bridge, suggesting that this was mainly dependent on the bridge span length and axle arrangement.

Figure 9 shows the bearing spring displacement when there was a loose bearing on the exit side. Because of the loose bearing on the exit side, the magnitude of the slope when the bearing spring displacement increases (Fig. 9 (3) slope) or decreases (Fig. 9 (4) slope), is roughly the opposite of the entry side case in Fig. 7. Additionally, the 5-mm uplift gap case exhibited a somewhat larger dis-

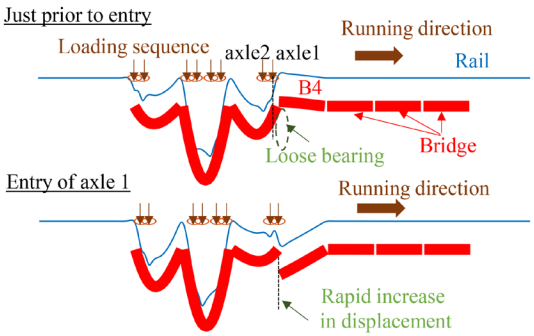

Fig. 8 Loose bearing behavior during bridge transfer (B4 entry side bearing uplift gap 2 mm)

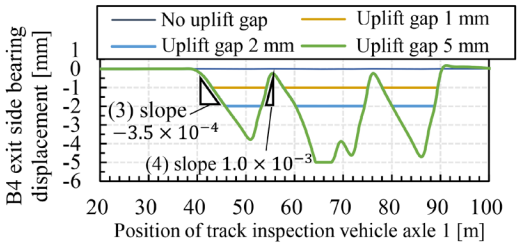

Fig. 9 B4 exit side bearing displacement for B4 exit side bearing uplift gap of 1 mm, 2 mm, and 5 mm, and for no uplift gap

placement at the axle 1 position of 70 m onward at the peak of the second downward displacement compared to Fig. 6. This was the effect of the second diesel railcar being loaded at the same time.

In this paper, we differentiated the bearings between the entry side and exit side, but if the front and rear of a two-car track inspection vehicle runs in reverse, then the bearing spring displacements for the entry and exit sides will be obtained since this is a static analysis. In other words, what governs the phenomenon is not whether it is on the entry side or exit side, but the vehicle's axle arrangement and the magnitude of the wheel load. In this paper, we used the terms "entry" and "exit" only for convenience, and it should be noted that the analysis was based on an example in which the two-bogie inspection vehicle is the leading car of a two-car track inspection vehicle.

3.2 Track geometry

Figures 10 and 11 show the 10 m SCTG (124) and 10 m SCTG (134) in the loose bearing on the entry side of B4, respectively. The 10 m SCTG (124) in the no-uplift gap case corresponded to a girder deflection shape, with a maximum at the bearing part, a minimum near the center of the span, and a waveform with a wavelength roughly equal to the span length. Cases where there is a loose bearing exhibit fluctuations in track geometry around the uplift gap location. Specifically, the upward peak position of the loose bearing location moved toward the train entry side, and the maximum value also increased. Furthermore, an increasing uplift gap amount resulted in the downward peak position at the center of the B4 span shifting toward the entry side, and the peak value also increasing.

The 10 m SCTG (134) shown in Fig. 11 showed the same tendency as the 10 m SCTG (124) in that the fluctuation in the peak position around the loose bearing location tended to shift to the entry side as the uplift gap amount increased, but unlike the 10 m SCTG (124), the peak value did not change considerably. This is because the 10 m SCTG (134) calculated the displacement of the axle 3 position relative to those of axles 1 and 4, but since axle 2 was still on the bridge when axle 3 passed through the loose bearing, the change due to loose bearing in the axle 3 position relative to the axles 1 and 4 was small.

Figure 12 shows the 10 m SCTG (124) when loose bearings were introduced on the exit side of B4. As with the entry side, fluctuations in peak position and peak value occurred around the loose bearing location. An increasing uplift gap resulted in an upward peak at the loose bearing location moving to the exit side, in the opposite direction to that of the entry side. The maximum value did not change when there was a 1 mm uplift gap, but increased when there was a 2 mm or 5 mm uplift gap. The same trend as on the entry side generally occurred in the direction opposite to the running direction.

In summary, although tendencies differed somewhat depending on the size of the uplift gap on the loose bearing, both the track geometry corresponding to the girder deflection, and the phase shift and amplitude fluctuations of the loose bearing location, were superimposed at the 10 m SCTG obtained at the loose bearing location. The phase shift and increase in amplitude of this fluctuation differed depending on the size of uplift gap at the loose bearing location. Specifically, in the target range, the phase shift was only approximately 2 m when the uplift gap was 1 mm. However, in addition to the phase shift, there was also an amplitude increase of approximately 0.4 mm when the uplift gap was 2 mm or 5 mm. Therefore, loose bearings could be detected from this feature of the track geometry.

3.3 Analysis of loose bearings and wavelength of track geometry

In this numerical analysis, we evaluated not only the effect of loose bearings but also the track geometry, including the component of girder deflection. Previous research [12] showed that the component due to girder deflection could be evaluated from the loaded track geometry difference. Therefore, being able to separately estimate the component of the track geometry due to girder deflection and subtracting it from the loaded track geometry is thought to enable the extraction of only the loose bearing component with high accuracy. Therefore, further analysis was conducted only on the effects of loose bearings with the girder deflection component removed.

Figure 13 shows the loose bearing component of the track geometry calculated by subtracting the analysis result without a loose bearing from the analysis result of the 10 m SCTG at the loose bearing location. For each case, the fluctuation component at the loose bearing location was extracted, and its half wavelength (distance for one peak) was approximately 5 m regardless of the extent of the uplift gap. The two factors that caused this were thought to be the filter characteristics of the 10 m SCTG and the load dispersion effect of the rail. First, for the filter characteristics, the 10 m SCTG that was used as an index in this study had a large gain near a half wavelength of 5 m, as shown in Fig. 3, and a gain of 0 at half-wavelengths of 2.5 m or less. Therefore, even in the case of a rapid change in rail displacement at the bearing location due to loose bearings, evaluating this as a 10 m SCTG is thought to remove the short-wavelength components with no gain of 2.5 m or less, and the components near a half-wavelength of 5 m could be extracted. In addition to the filter characteristics of the 10 m SCTG, the load dispersion effect of the rail may have also affected the components with a half-wavelength of approximately 5 m. This is presumed to be due

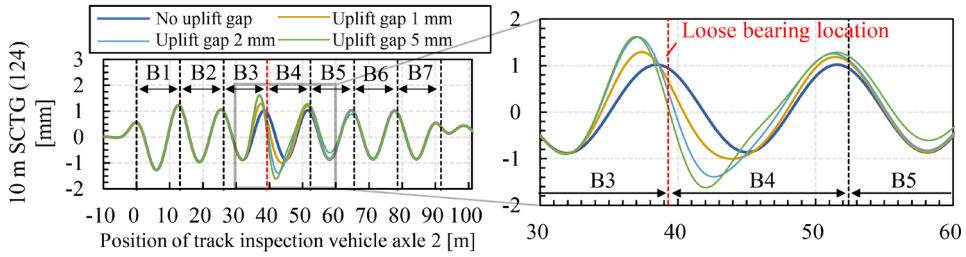

Fig. 10 10 m SCTG (124) for B4 entry side bearing uplift gap of 1 mm, 2 mm, and 5 mm, and for no uplift gap

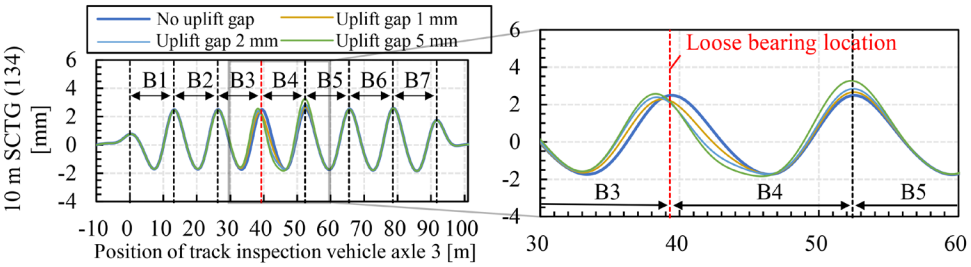

Fig. 11 10 m SCTG (134) for B4 entry side bearing uplift gap of 1 mm, 2 mm, and 5 mm, and for no uplift gap

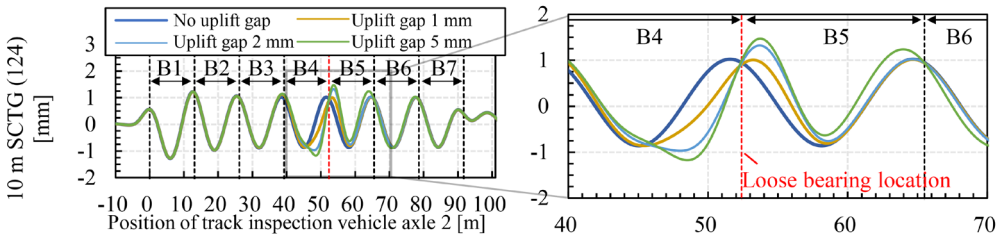

Fig. 12 10 m SCTG (124) for B4 exit side bearing uplift gap of 1 mm, 2 mm, and 5 mm, and for no uplift gap

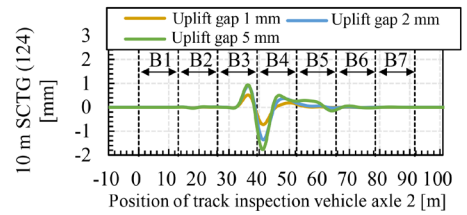

(a) B4 entry side loose bearing: 10 m SCTG (124)

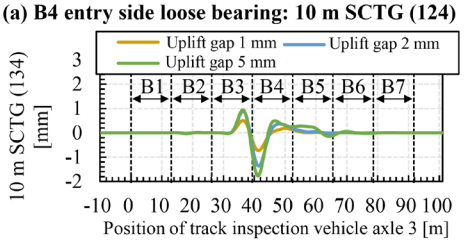

(b) B4 entry side loose bearing: 10 m SCTG (134)

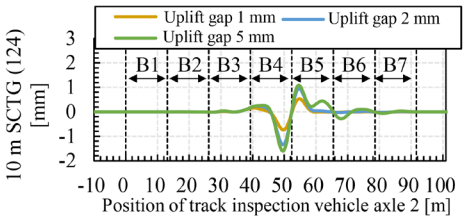

(c) B4 exit side loose bearing: 10 m SCTG (124)

Fig 13 Loose bearing component of 10 m SCTG calculated excluding girder deflection component

to the concentrated load of the train being dispersed by the rail, which makes the displacement change of the bearing spring more gradual, and due to the measured track geometry having a smooth waveform without discontinuities.

4. Conclusion

The results of this study are summarized below.

- A bilinear nonlinear spring representing a loose bearing was introduced into the existing loaded track geometry calculation program (girder deflection-track geometry conversion program) in order to expand the program so that the loaded track geometry at loose bearing locations could be calculated.
- We targeted a seven-girder bridge with a span length of 12.3 m, and calculated the 10 m SCTG on loose bearing using the above-mentioned program. Results showed that loose bearings occurred as a half-wavelength of approximately 5 m at the girder ends of the bridge in question and adjacent bridges.
- For the bridge targeted in this study, the fluctuation wavelength of the 10 m SCTG occurring at the loose bearing locations had a half-wavelength of approximately 5 m, regardless of the bearing uplift gap amount. This was thought to be due to the filter characteristics of and the load distribution of the rail.

Additionally, this analysis only covered bridges with a specific span length that are assumed to be the actual target of application, so the findings obtained in this study still need to be generalized. Furthermore, this analysis did not consider unloaded track geometry

which is superimposed in actual track geometry under loaded conditions in addition to the deformation components of the structure examined in this analysis[8]. Unloaded track geometry causes an error in loose bearing detection, so it needs to be removed. For example, measuring the unloaded track geometry separately from the track inspection vehicle and subtracting it from the loaded track geometry enables the extraction of only the deformation components of the structure from the loaded track geometry.

For future study, we plan to apply the proposed method in order to track geometries measured on actual tracks to detect loose bearings and verify this by comparing it with the measurement results of the uplift gap of loose bearings under the girder.

References

[1] Railway Technical Research Institute, *Maintenance Standards for Railway Structures and Commentary (Steel and Composite Structures) -2017 Supplementary Revision-*, Maruzen Publishing Inc., 2017 (in Japanese).

[2] Kawada, S., Tsukahara, T., Kubota, T. and Matsuda, Y., "Measures for Deterioration of Railway Bridge Bearings in JR East," *Journal of Practical Studies on Infrastructure Maintenance,* Vol. 1, No. 1, pp. 445-451, 2022 (in Japanese).

[3] Yano, T., Iwamoto, H., Uno, M., Tachibana, T. and Matsuoka, H., "A survey and perspective for improving maintenance efficiency of railway infrastructure," *Railway Engineering,* Vol. 28, No. 1, pp. 124-127, 2024 (in Japanese).

[4] Ishizawa, T., Imai, T., Takizawa, A., "Development of the monitoring device for clattering at the support of railway steel bridges," *JR EAST Technical Review,* No. 71, pp. 39-46, 2024 (in Japanese).

[5] Morii, H., Kuribayashi, K. and Konishi, T., "Development of steel bridge clattering-detecting device utilizing vibration-powered generator," *JR EAST Technical Review,* No. 55, pp. 31-32, 2016 (in Japanese).

[6] Kushiya, T., Matsuoka, K., Kajiwara, K., Narita, K., Watanabe, T., Tanaka, H. and Mori, T., "Identification of high-order local vibration modes using multi-point excitation and dynamic behavior of I-shaped girder steel railway bridge, *Journal of JSCE, A1 (Structural Engineering/Earthquake Engineering),* Vol. 78, No. 2, pp. 269-286, 2022 (in Japanese).

[7] Nagayama, T., Reksowardojo, A. P., Su, D. and Mizutani, T., "Bridge natural frequency estimation by extracting the common vibration component from the responses of two vehicles," *Engineering Structures,* Vol. 150, pp. 821-829, 2017.

[8] Matsuoka K. and Tanaka H., "Drive-by deflection estimation method for simple support bridges based on track irregularities measured on a traveling train," *Mechanical Systems and Signal Processing,* Vol. 182, 109549, 2023.

[9] Matsuoka, K., Tokunaga, M. and Kaito, K., "Bayesian estimation of instantaneous frequency reduction on cracked concrete railway bridges under high-speed train passage," *Mechanical Systems and Signal Processing,* Vol. 161, 107944, 2021.

[10] Matsuoka, K., Tanaka, H., Kawasaki, K., Somaschini, C. and Collina, A., "Drive-by methodology to identify resonant bridges using track irregularity measured by high-speed trains," *Mechanical Systems and Signal Processing,* Vol. 158, 107667, 2021.

[11] Matsuoka, K., Tsunemoto, M., Kawasaki, K., and Tanaka, H., "Extraction of potential damage points in overhead contact line systems on high-speed railway bridges using drive-by measured track irregularities," *AI and Data Science,* Vol. 4, Issue 3, pp. 125-134, 2023 (in Japanese).

[12] Hattori, K., Matsuoka, H. and Tanaka, H., "Development of the bridge deflection-track irregularity conversion program for the deflection estimation method based on track irregularities," *Journal of JSCE,* Vol. 80, No. 15, 23-15047, 2024 (in Japanese).

[13] Hattori, K., Matsuoka, K., Tanaka, H., "Batch estimation method of deflections for multi-bridge section based on the difference of track geometries measured by 2 bogies-type track inspection vehicles," *Journal of JSCE,* Vol. 81, No. 5, 24-00262, 2025 (in Japanese).

[14] Hattori, K., Matsuoka, K., Tanaka, H., "Numerical sensitivity analysis for detection of bridge loose bearing based on on-board measured track geometries," *Railway Engineering,* Vol. 28, No. 1, pp. 84-91, 2024 (in Japanese).

[15] Yoshimura, A., Yoshida, Y. and Kamiyama, M., "Development of Database System for Railway Track Maintenance Management, Micro LABOCS for Windows and its Features," *Quarterly Report of RTRI,* Vol. 38, No. 2, pp. 102-106, 1997.

[16] Matsuoka, K., Kajihara, K. and Tanaka, H., "Identification of vibration modes and wave propagation of operational rails by multipoint hammering and reciprocity theorem," *Materials,* Vol. 15, No. 3, pp. 811, 2022.

[17] Railway Technical Research Institute, *Design Standards for Railway Structures and Commentary (Concrete Structures) Part II: Bridges,* Maruzen Publishing Inc., 2023 (in Japanese).

Authors

Koji HATTORI
Researcher, Structural Mechanics Laboratory, Railway Dynamics Division
Research Areas: Drive-by Measurement, Structural Health Monitoring, Track Geometry

Kodai MATSUOKA, Dr.Eng.
Senior Researcher, Data Analytics Laboratory, Information and Communication Technology Division
Research Areas: Bridge Dynamics, Vehicle and Bridge Interaction, Damage Detection

Hirofumi TANAKA, Dr.Eng.
Manager, Track Geometry & Maintenance Laboratory, Track Technology Division
Research Areas: Track Geometry Maintenance, On-board Monitoring, Signal Processing

Relationship between Shear Strength and Snow Properties at the Base of Snowpack

Ryota SATO **Daisuke TAKAHASHI**
Meteorological Disaster Prevention Laboratory, Disaster Prevention Technology Division

Katsuhisa KAWASHIMA **Takane MATSUMOTO**
Research Institute for Natural Hazards and Disaster Recovery, Niigata University

This study investigates how snow properties affect the shear strength at the base of snowpack. Field measurements of the shear strengths showed values ranging from 0.3 to 3.8 kN/m², with an average value of 1.5 kN/m². Despite the variation, it was confirmed that shear strength was positively correlated with dry snow density and snow hardness, and negatively correlated with liquid water content. Additionally, to understand the shear strength of snowpack under rainfall or rapid snowmelt, we measured the shear strength of an area of snowpack sprayed with water.

***Key words*:** *avalanche, shear strengths, snow property*

1. Introduction

Snow avalanches can occur on slopes along railway lines. Therefore, railway companies operating in areas with heavy snowfall face the risk of serious operational disruptions such as derailments caused by avalanches. To prevent such disruptions, railway companies send out patrols when certain indicators are reached for each line section, such as specified temperatures and precipitation levels. However, these criteria are based on empirical based on observation and experience rather than on deduction from theoretical principles. In some cases, patrols are conducted even during periods or in areas where the risk of avalanches is low, using up significant labor resources. Therefore, establishing a method for evaluating avalanche risk based on theoretical principles would enable more accurate assessment of periods and locations where there is increased risk of avalanches, and ensure more effective and efficient deployment of patrols.

Avalanches can be classified into surface avalanches and full-depth avalanches. In surface avalanches the sliding surface is within the snow layer (Fig. 1, left). In full-depth avalanches, the sliding surface is at the base of the snowpack (Fig. 1, right, and Fig. 2) [1]. Both occur when the driving force exceeds the resisting force, so that the snow becomes unstable. It should be noted that driving force is the force that causes the avalanche to slide, and the resisting force opposes the slide. The stability of surface avalanches can be evaluated examining the relationship between the driving force and resisting force within the snow layer.

On the other hand, the stability of full-depth avalanches can be evaluated by examining the relationship between the snowpack base and the ground surface. An increase in driving force is caused by an increase in overburden load due to the addition of water to the snowpack during snowfall or rainfall associated with sudden temperature increases in the winter. On the other hand, a decrease in supporting force is caused by a reduction in shear strength due to the infiltration of rainwater or meltwater into the snowpack or the snowpack base. This results in the presence of water in the sliding surface.

Previous study [2] have reported relationships between shear strength and snow properties, such as snow density and water content within the snowpack, in surface avalanches. On the other hand, the shear strength of the snowpack base is difficult to evaluate because it is affected by soil properties, microtopography, and vegetation, all of which are important factors in full-depth avalanches. Therefore, this study focuses on full-depth avalanches.

Similar to the shear strength in the snowpack, the shear strength of the snowpack base is also thought to be influenced by snow properties such as snow density and water content. Previous studies [3, 4] have reported that the shear strength of the snowpack base tends to decrease as the water content increases in indoor tests. However, since there are no field observation results, the relationship between other snow properties such as density, hardness, and shear strength remains unclear. Therefore, the authors carried out field observations to investigate the relationship between the shear strength of the snowpack base and the snow properties. Additionally, to simulate

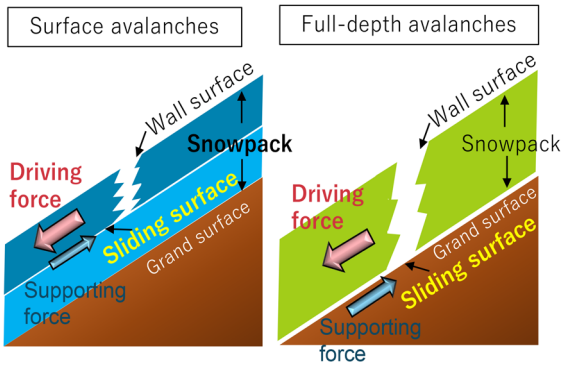

Fig. 1 Conceptual diagram of surface avalanches (left) and full-depth avalanches (right)

Fig. 2 Example of full-depth avalanche

sudden rainfall or meltwater arriving at the snowpack base, the changes in the shear strength were examined when natural snow was watered.

2. Measurement method

2.1 Method for measuring shear strength at the base of snowpack

In the flat ground and the embankment (southeast slope and northwest slope, slope angle 35°) the Shiozawa Snow Testing Station (Minamiuonuma City, Niigata Prefecture: Fig 3), a total of 47 snow profile observations were conducted during the winter seasons of 2014, 2016, 2020, and 2021. The snow profile observations revealed the characteristics of the snow at the snowpack base (2 cm above ground level), such as density, water content, and hardness.

The shear strength (kN) at the boundary between the snowpack and the ground was measured using a shear frame and a digital load cell. As shown in Fig. 4, approximately 10 cm of snow on the ground surface was left after digging it out, and a shear frame was inserted from above. After removing the surrounding snow, the digital load cell was pulled to break the boundary between the ground surface and the snow. Then, the shear strength was measured. The pulling time was approximately 1 second. The average value obtained from 1 to 3 measurements per observation was divided by the effective cross-sectional area of the shear frame (0.025 m^2) to obtain the shear strength per unit area (kN/m^2). Note that the vegetation on the failure surface was either bare ground or grassland, and the type

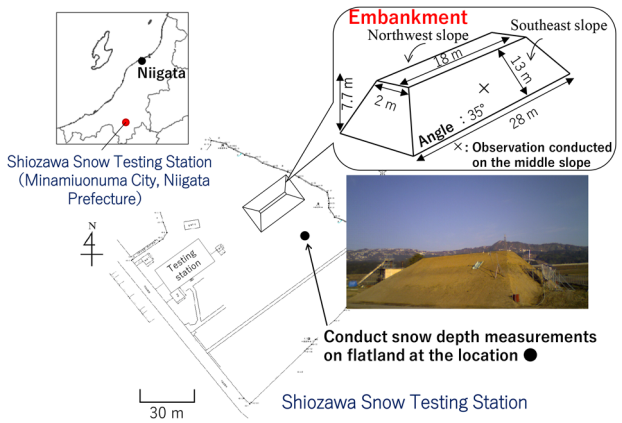

Fig. 3 Map of Shiozawa Snow Testing Station and observation locations

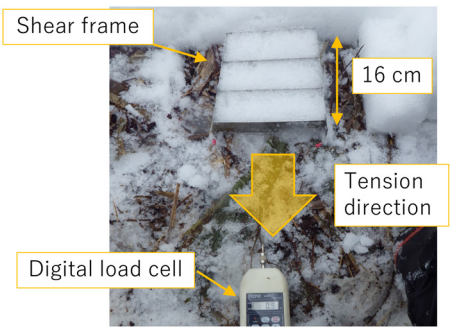

Fig. 4 Situation of shear strength measurement in the field

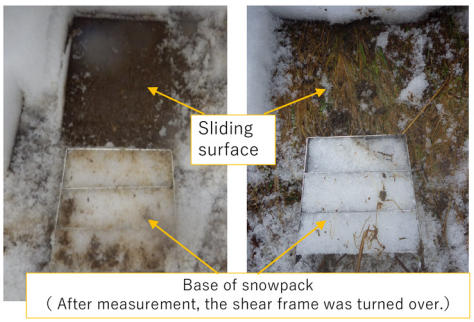

Fig. 5 Examples of bare ground and grassland (Left: bare ground, right: grassland)

of vegetation on most of the failure surface after measurement was recorded (Fig. 5).

2.2 Method for conducting water sprinkling test

Assuming that sudden rainfall or snowmelt water reaches the base of the snowpack, we conducted tests focusing on changes in shear strength over time after sprinkling (Fig. 6).

The test procedure is described below.

(1) Approximately 10 cm of snow is left at the base of an area measuring approximately 1.5 m × 1.7 m. The site is prepared to allow a shear frame to be set up.
(2) Measure the shear strength, density, moisture content, and hardness of the soil before watering.
(3) Using a watering can, approximately 8 L of tap water (approximately 3°C) is sprinkled over the excavated area for approximately 3 minutes. The amount of sprinkled water per converted unit area is 3.1 mm, equivalent to a rainfall intensity of 62.6 mm/h.
(4) Shear strength, density, moisture content, and hardness are measured 30 minutes, 1 hour, 3 hours, and 5 hours, after sprinkling the water. 2 to 4 shear strength measurements were taken at each time interval, and the average value was calculated.

3. Measurement results and discussion

3.1 Measurement results of shear strength in the field

Figure 7 shows the snow conditions (the daily average temperature and the snow depth) and the dates on which the shear strength was measured over the course of four winters (2014, 2016, 2020, and 2021). Figure 7 shows that the 2016 winter had slightly shorter snow periods and slightly shallower maximum snow depths than other winters. However, snow conditions were generally normal for all four winters.

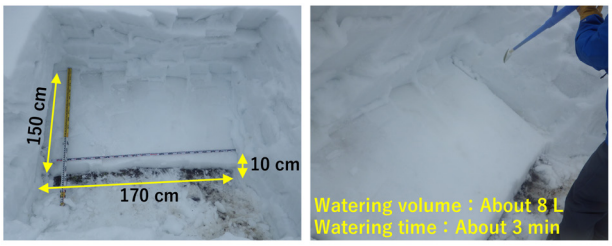

Fig. 6 Watering status

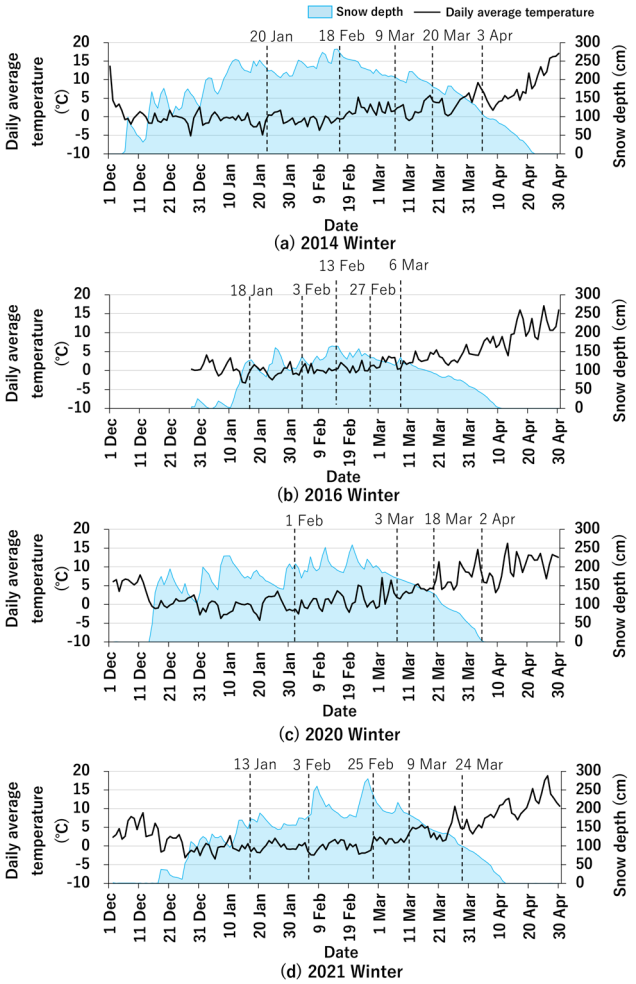

Fig. 7 Snow conditions and observation dates for each winter

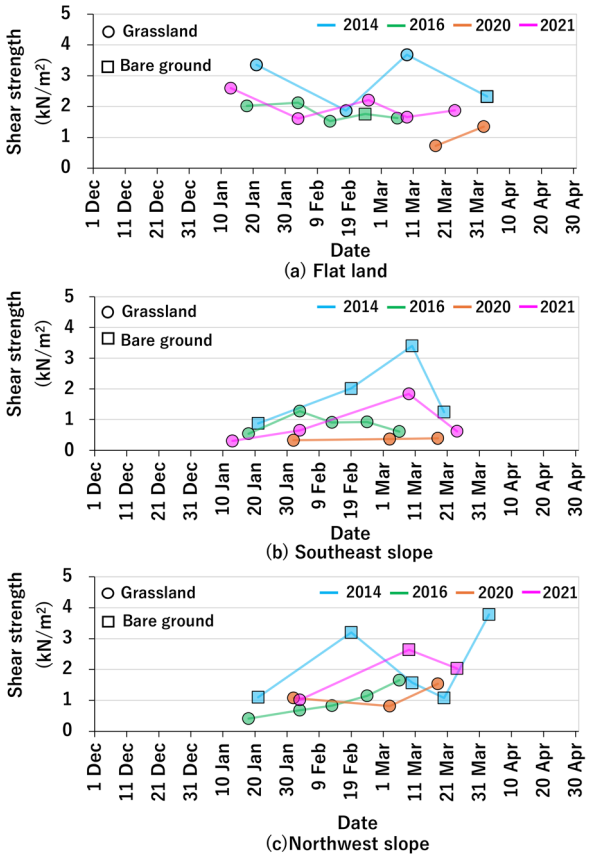

Fig. 8 Measurement results of shear strength at each observation location

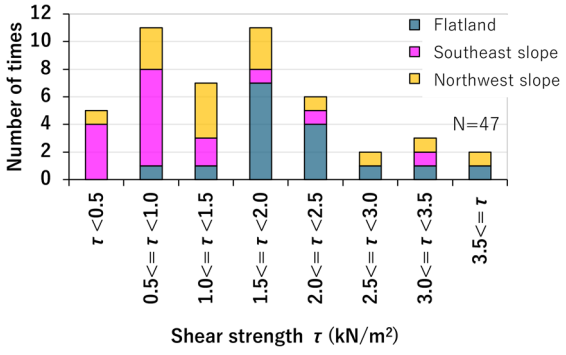

Fig. 9 Histogram of shear strength measurement results (τ : shear strength, classified into classes of 0.5 kN/m²)

Shear strength measurements were conducted at intervals of approximately 10 to 30 days from the coldest winter period through to snowmelt. The quality of snow at the base of the snowpack for all measurements was granular.

Figure 8 shows the results of shear strength measurements for each winter season. The results indicate that shear strength varies over time at each location and that there is no clear temporal trend.

When comparing the shear strength measurement results on flat areas with those on slopes, the values on flat areas tend to remain around 2.0 kN/m². On the other hand, the values on the southeast slope tend to remain around 1.0 kN/m², which is lower than the value on flat areas. The shear strength values on the northwest slope were intermediate between those on the flat area and the southeast slope (1.5 kN/m²). Therefore, when the shear strength of snow on the flat area and slopes during the same period are compared, it shows that the values on the flat area tended to have greater values. The total of 47 measured shear strength values ranged from 0.3 to 3.8 kN/m², with an average value of 1.5 kN/m² (Fig. 9). When the measured values were classified into 0.5 kN/m² intervals, the most frequent occurrences were in the 0.5−1.0 kN/m² and 1.5−2.0 kN/m² ranges, followed by 1.0−1.5 kN/m² range. Therefore, most of the measurements in this study fell within the range of 0.5−2.0 kN/m², which was comparable to the values obtained in indoor tests by Kamiishi et al. and Takahashi et al. Furthermore, this paper presents the measured shear strength at the sliding surface within the snow layer during surface avalanches (0.1−10 kN/m², with an average of 1.0 kN/m²) [5]. Additionally, the results were similar in magnitude to those obtained from shear strength measurements within the snow layer during surface avalanches (ranging from 0.1 kN/m² to 10 kN/m², with an average of 1.0 kN/m²).

Next, Fig. 10 shows the relationship between shear strength, dry density, moisture content, and hardness.

Examining the relationship between shear strength and dry density, as shown in the top of Fig. 10, reveals a positive correlation regardless of the measurement location (flat area: 0.43, southeast slope: 0.60, northwest slope: 0.50). Comparing the correlation coefficients, it is clear that the correlation is stronger on slopes than on

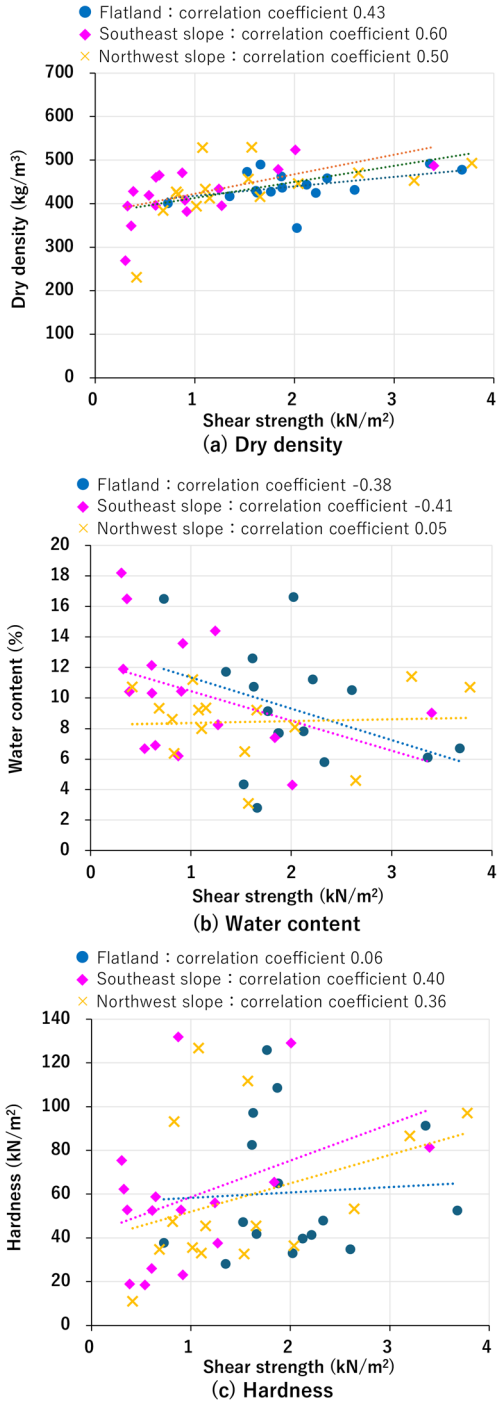

Fig. 10 Relationship between shear strength and dry density, water content, and hardness

flat areas. Additionally, the dry density is particularly low on the southeast and northwest slopes when the shear strength is 1 kN/m² or lower.

Next, examination of the relationship between shear strength and water content, as shown in the middle row of Fig. 10, reveals that although the correlation coefficients are small, it has a negative correlation on flat areas and on southeast slopes (flat areas: −0.38, southeast slopes: −0.41). This indicates that as shear strength decreases, moisture content tends to increase. There was little correlation among the measured values overall on northwest slopes. However, a trend of larger shear strength associated with lower moisture content was observed when focusing on shear strength of 3.0 kN/m² or less. Nevertheless, even when the moisture content was high, at around 10%, the shear strength was large, reaching 3.0 kN/m² or more in some cases. Similar values were observed on the southeast slope, but these values were based on only one data point, and the variation in shear strength of 2.0 kN/m² or less is relatively small. Therefore, the impact on the entire data set is considered to be small. In cases where the value is greater than 3.0 kN/m², the number of data points is small, so it is necessary to continue accumulating measurement data and quantitatively evaluate the influence of moisture content on shear strength. In summary, although there is some variation, shear strength increases with higher dry density and hardness and decreases with higher water content.

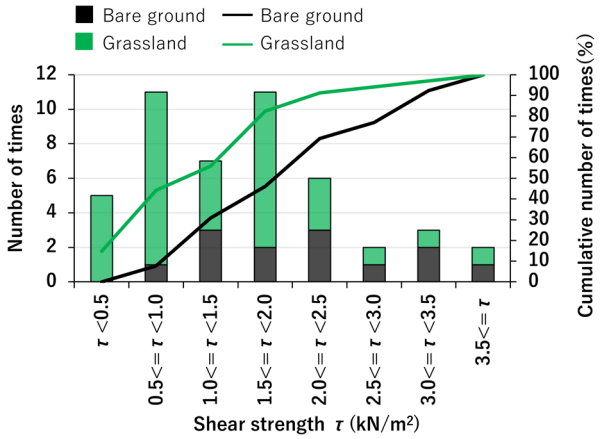

Fig. 11 Histogram of shear strength in grassland and bare ground (τ : shear strength, classified into classes of 0.5 kN/m²)

To confirm the differences in shear strength based on ground vegetation conditions, the shear strength histograms in Fig. 8 were classified into two categories: bare ground and grassland categories as shown in Fig. 11. As a result, with the exception of one case, all shear strengths below 1.0 kN/m² were measured in grassland. Shear strength tended to be lower in grassland, with lower strength classes occurring more frequently. In the case of tall, soft grasses, such as those measured in this study (Fig. 5), the grass does not get caught in the snow. Instead, it acts as an intermediate layer between the snow and the ground surface. In such cases, the grasses facilitate snow sliding, resulting in lower shear strength.

3.2 Watering test results

Figure 12 shows the time-dependent changes in shear strength after watering. Figure 13 shows the time-dependent changes in dry density, moisture content, and hardness of the snow after watering. The measured shear strength before watering was 2.8 kN/m²; dry density, 442 kg/m³; moisture content, 13.5%; and hardness, 94.4 kN/m². The shear strength decreased by approximately 60% 30 minutes after watering and remained largely constant thereafter. Similar to shear strength, hardness decreased by approximately 30% after watering and subsequently fluctuated slightly remaining at a similar level. The dry density and moisture content varied slightly but remained nearly constant from immediately after watering.

According to Izumi [6], wetting snow causes changes to its structure, leading to a rapid decrease in snow hardness. It is thought that this is due to the infiltrated water weakening the bonds between

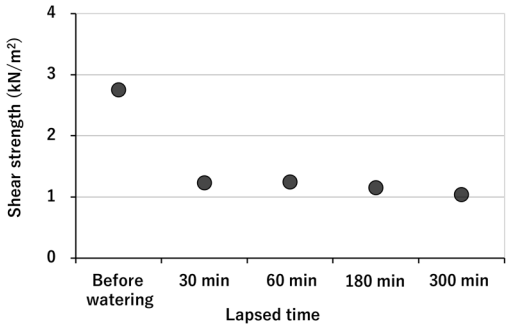

Fig. 12 Shear strength measurement results in water spray test

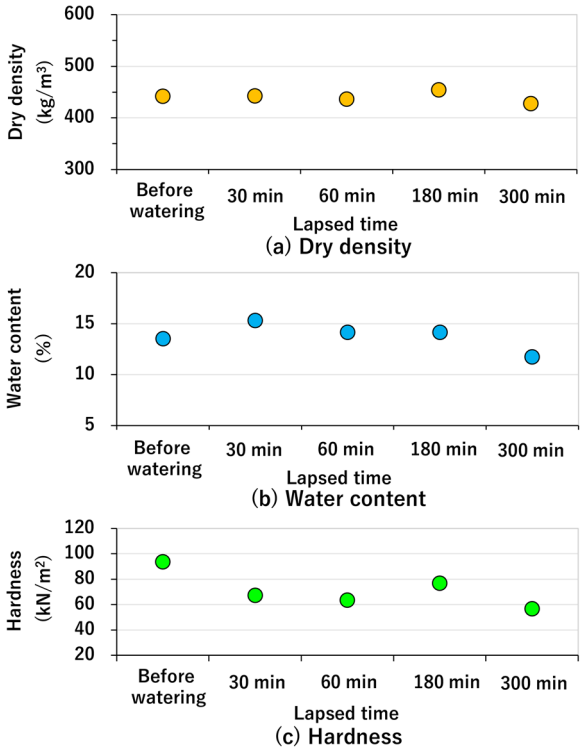

Fig. 13 Measurement results of dry density, water content, and hardness in the watering test

ice particles. The decrease in hardness after watering is also thought to be due to this effect. Although there was some variability, results from shear strength measurements in field observations revealed a positive correlation between shear strength and hardness. Therefore, the decrease in hardness due to watering is considered to be one of the factors that contribute to the reduction in shear strength at the base of the snowpack. Additionally, although it is generally expected that watering snow increases its moisture content, rapid watering in this case caused the snow to exceed its water-holding capacity, leading to swift drainage within the snow layer. This is considered a factor that contributed to the small change in moisture content. As a result, the dry density remained nearly constant. However, water may have been present between the snow surface and the ground surface, which could have potentially contributed to the decrease in shear strength.

Based on the above results, it was found that rapid rainfall and snowmelt can significantly affect the shear strength of the snowpack base. The presence or absence of such water infiltration history may also influence the variability of measurement values in field observations. It is expected that further verification will be conducted in the future to determine if rainfall or snowmelt history can effectively evaluate shear strength. Additionally, collecting measurement data under different conditions, such as changes in surface permeability coefficients, is expected to improve our understanding of the phenomenon.

4. Summary and future challenges

In this study, we investigated the relationship between shear strength at the base of snow cover and snow properties. These properties are important for assessing the risk of full-depth avalanches. Our findings are based on field observations of bare ground and grassland in flat areas and embankments and field sprinkling tests. The results revealed the following:

(1) The range of measured shear strength values at the base of the snowpack was between 0.3 and 3.8 kN/m². The average values for flat terrain, southeastern slopes, and northwestern slopes were 2.0 kN/m², 1.0 kN/m², and 1.5 kN/m², respectively.
(2) The temporal variation in shear strength was unclear, and it fluctuated throughout the winter season.
(3) During the same period, shear strength was generally lower on slopes than on flat ground.
(4) A positive correlation was confirmed between shear strength and dry density at all measurement points.
(5) A negative correlation was confirmed between shear strength and moisture content on flat ground and on the southeast slope. However, on the northwest slope, this relationship could not be confirmed due to the influence of cases with high shear strength despite high moisture content.
(6) No correlation was confirmed between shear strength and hardness on flat ground. However, a positive correlation was confirmed on slopes.
(7) When examining shear strength measurements by grassland and bare ground, all cases with shear strength values of 1.0 kN/m² or less were from grassland, except for one case.
(8) The results of the watering test showed that hardness decreases immediately after heavy rainfall or snowmelt. This increase in hardness may reduce the shear strength at the base of the snowpack.

In this study, we examined the relationship between shear strength measurements and snow conditions during snow accumulation. However, changes in the applied load and particle size after snow accumulation may also influence shear strength. We also plan to conduct more detailed measurements and analyses to investigate the effects more precisely by factor, such as ground conditions (e.g., vegetation types), on shear strength.

This paper is based on the content of a presentation delivered at the 38th Cold Region Technology Symposium [7].

References

[1] Tremper, B., *Wet snow, Staying alive in avalanche terrain*, The Mountaineers Books, Seattle, WA, USA, pp. 143-147, 2008.
[2] Yamanoi, K., Endo Y., "Dependence of shear strength of snow cover on density and water content," *Seppyo*, Vol. 64, pp. 443-451, July 2002 (in Japanese).
[3] Kamiishi, I. et al., "The occurrence and measurement of the

shearing-strength for the prediction of slope face avalanche," *Preprints of 2007 conference Japanese Society of Snow and Ice*, p. 76, 2007 (in Japanese).
[4] Takahashi, D. et al., "Basic tests for the shear strength of snow-ground boundary," *Summaries of JSSI & JSSE Joint Conference on Snow and Ice Research – 2013 in Kitami*, p. 227, 2013 (in Japanese).
[5] Maeno, K., Fukuda, M., *Snow Ice Water Phenomenon, Basic Lecture of Glaciology III*, Kokon-Shoin, pp. 13-81, 2000 (in Japanese).
[6] Izumi, K., "Hardness of Wet Snow III. Decrease in Snow Hardness due to Water Saturation and/or Solar Radiation," *Low Temperature Science, Ser*, Vol. 44, pp. 37-48, 1986 (in Japanese).
[7] Sato, R. et al., "Relationship between shear strength and snow properties at the bottom of snowpack," *ABSTRACTS 2022 COLD REGION TECHNOLOGY SYMPOSIUM,* Vol. 38, pp. 34-37, 2022 (in Japanese).

Authors

Ryota SATO
Senior Researcher, Meteorological Disaster Prevention Laboratory, Disaster Prevention Technology Division
Research Areas: Glaciology

Daisuke TAKAHASHI
Researcher, Meteorological Disaster Prevention Laboratory, Disaster Prevention Technology Division
Research Areas: Glaciology

Katsuhisa KAWASHIMA, Ph.D.
Professor, Research Institute for Natural Hazards and Disaster Recovery, Niigata University
Research Areas: Glaciology

Takane MATSUMOTO, Ph.D.
Project Associate Professor, Research Institute for Natural Hazards and Disaster Recovery, Niigata University
Research Areas: Glaciology

Scheduling Algorithm to Minimize Required Crew Size

Satoshi KATO
Transport Operation Systems Laboratory, Signalling and Operation Systems Technology Division

Taichi NAKAHIGASHI
Transport Operation Systems Laboratory, Signalling and Operation Systems Technology Division (Former)

Railway companies produce crew schedules when they revise their train timetables. Currently, these schedules are produced manually by experts. However, this manual task is time-consuming. It is therefore necessary to develop a system that supports crew scheduling using an automated generation algorithm. We propose an automated crew scheduling algorithm based on mathematical optimization to minimize the number of crew required. The results of a computational experiment using real data from a Japanese railway line confirm that the proposed algorithm can quickly generate efficient crew schedules that optimize crew size.

Key words**:** *crew scheduling, duty, roster, number of crew required, mathematical optimization*

1. Introduction

When revising their timetables, railway companies must produce not only train timetables but also several related schedules. One of these is a crew schedule, which determines the schedules of drivers and conductors. From the viewpoint of effective utilization of available resources, railway companies produce schedules that require as small a crew as possible. However, crew scheduling has to take into many aspects related to the planning of work for crews such as regulatory requirements, and must therefore satisfy numerous constraints [1].

In most railway companies in Japan, crew schedules are currently planned manually by experts. Since the preparation of these plans requires a great deal of knowledge and experience, even experts spend several days to several weeks on a single line. Therefore, an automatic generation algorithm is required in order to save time and reduce the skill required for schedule planning. In addition, the automatic generation algorithm should be able to take into account the differences between drivers and conductors, and be applicable to several railway lines regardless of the number of trains or crew bases.

In this paper, we propose a versatile method for automatically generating crew schedules for train timetable revisions. The proposed method uses mathematical optimization to devise a two-stage process that divides the problem into two parts. This enables a crew schedule plan to be generated that minimizes the number of crew required in a short time. In addition, the performance of the proposed method is confirmed by using real Japanese railway line data.

2. Crew scheduling

2.1 Duty and roster

A crew schedule plan is produced using train timetables and rolling stock schedules for a train timetable revision. A crew schedule ensures that all trains in the given train timetable are adequately staffed and that crew members' work schedules are determined. Crew management consists of two schedules, "duty" and "roster."

A duty consists of multiple train operations and accompanying tasks such as shunting at stations, as well as breaks taken in between. There are two types of duties: a "one-day duty" where the start and end dates are the same, and an "overnight duty" where the duty ends the next day. Each duty must start and end at the same crew base located on the railway line. In addition, each duty must satisfy a number of constraints, such as upper limits on working hours and paid working hours based on laws and company regulations.

A roster is a circulation schedule that includes rest days between duties as necessary, and is the basis for the crew's work shift of each month. A schedule planner generates a roster for each crew base. There are many constraints on a roster, such as ensuring rest time between two duties according to the previous duty (called "home rest time") and granting the required number of rest days. The details of the constraints of a duty and a roster are described in the next section.

As crew members include drivers and conductors, there are some differences between the two roles. Drivers must be assigned to shunting work at stations or rolling stock depots, while conductors may be required to confirm all passengers have alighted at the terminal station. In some cases, the conductor may be exempt from being assigned to an out-of-service train. On the other hand, multiple conductors may be required for an express train. Thus, the number of crew members assigned to each train differs depending on whether they are drivers or conductors.

Figure 1 shows an example of a train timetable and a rolling stock schedule for 14 trains. Crew bases are located at Stations A and B, which we refer to as crew bases A and B, respectively. The circles in the figure indicate trains exiting from the rolling stock depot, the triangles indicate trains entering the rolling stock depot. The lines connecting two trains in a different direction at Station A or C indicate that the train is turning back. Figure 2 shows the set of duties based on Fig. 1, including two duties (Duty 1 and 2) for crew base A and four duties (Duty 3 to 6) for crew base B. Duties 1, 3, and 4 are one-day duties, while Duties 2, 5, and 6 are overnight duties. The dotted lines in Duties 2 and 3 are "crew deadheading," which means crew travelling as a passenger to reach the start of a journey or to return home after a journey. Crew deadheading is inefficient and should be minimized.

Figure 3 shows an example of a roster corresponding to the set of duties in Fig. 2. The number at the top indicates the number of days elapsed. A roster determines the order of duties and rest days.

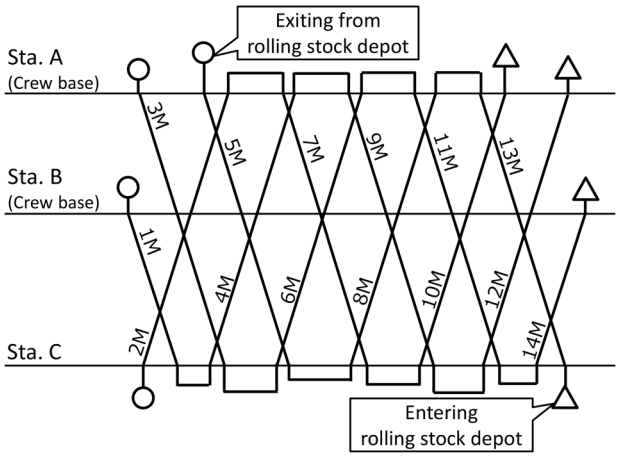

Fig. 1 Example of train timetable and rolling stock schedule

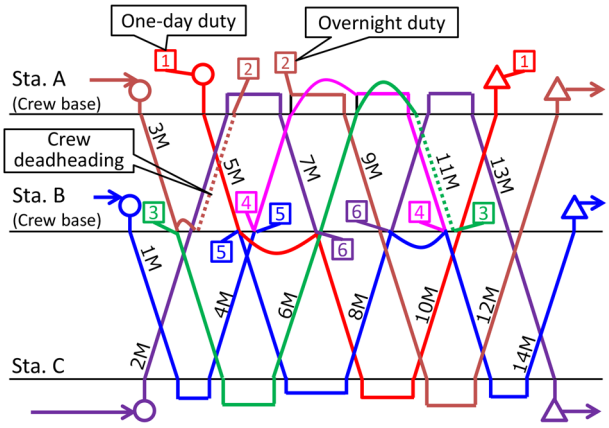

Fig. 2 Example of crew duties

Day	1	2	3	4	5	6	7	8	9
Work	Duty 4 One-day	Duty 3 One-day	Rest day	Duty 6 Overnight		Duty 5 Overnight		Rest day	Rest day
Start time	9:30	8:00		14:00	—	9:00	—		
End time	17:00	16:30		—	12:00	—	9:30		

Fig. 3 Example of crew roster

This roster shows a nine-day circulation schedule, meaning that a crew member assigned to work on the ninth day will be assigned to work on the first day of the following cycle. The number of days in the roster is equal to the number of crew members required to carry out the roster. In this paper, two consecutive rest days, are referred to as "double rest days."

2.2 Constraints

When generating a set of duties and rosters, constraints based on company regulations must be considered. The details of these constraints are listed next.

2.2.1 Constraints for duty generation

a) Ensure each duty on every train and every route section on the train timetable is assigned a crew member.
b) The average paid working hours per a day for each crew base must be within a given limit. This is calculated by dividing the total number of paid working hours on the roster by the "number of working days." The number of working days is defined as the total number of days worked, with a one-day duty counted as 1 and an overnight duty counted as 2.
c) Each overnight facility has a maximum number of overnight duties it can accommodate.
d) The number of working days for each crew base has an upper limit.
e) Each duty starts at one of the crew bases and ends at the same crew base.
f) The working hours of a duty have an upper limit. This value depends on whether the duty is a one-day duty or overnight duty. The working hours refers to the time from the start time to the end time of the duty.
g) Paid working hours for a duty have an upper limit. Paid working hours include the time taken on each train, as well as the preparation time required before and after each train.
h) The rest period for a duty has a lower limit. The rest period is defined as the working hours for a duty minus the paid working hours.
i) Each duty must include mealtimes (breakfast, lunch, and dinner). This constraint is defined that each duty takes the required break time within a specific time period.
j) The start and end times of each duty must be within specific time periods. These time periods are different for one-day and overnight duties.
k) The area covered by each crew base is limited.
l) Sleep time in an overnight duty has a lower limit.
m) Continuous working time has an upper limit. Continuous working time is defined as the time during which the crew is considered to be working without breaks.
n) Interval time between two consecutive continuous working times shall be above and below a set value.

2.2.2 Constraints for roster generation

o) All duties must be incorporated into a roster.
p) The required number of rest days must be included in a roster.
q) The home rest time has a lower limit. The value is different for the case without rest days, with a rest day, and with double rest days.
r) The end time of a duty before a rest day must be before a set time.
s) The start time of a duty after a rest day must be after a set time.
t) The consecutive working days without a rest day have an upper limit. Several constraints of this type may be set.

2.3 Literature review

Many studies have been conducted on crew scheduling algorithms for train timetable revisions. Heil et al. [2] classify the problems, modeling, and solutions from previous studies. Although there have been many studies overseas to generate both duty and roster schedules, labor constraints are specific to the laws and regulations of each country. Therefore, it is difficult to apply methods proposed overseas directly to Japanese railways. In Japan, several studies

have focused on the generation of duty schedules including those by Miura et al. [3] and Nishi et al. [4], and most of these studies apply mathematical optimization. On the other hand, only a few studies focus on crew rostering algorithms, namely Sakaguchi and Nozue [5] and Sugiyama et al. [6].

In addition, only a limited number of studies deal with duty and roster generation simultaneously. In Japan, Sakaguchi et al. [7] have dealt with duty and roster generation. However, their work does not take into account the home rest time with double rest days. Consequently, the required number of crew is an approximate figure.

3. Crew scheduling algorithm

3.1 Outline of proposed algorithm

Since the main objective of this research is to minimize the number of crew required, and mathematical optimization has been widely used in previous studies on crew scheduling, we use it for automatic generation.

As mentioned in Section 2.1, it is necessary to generate both duties and rosters in order to calculate the number of crew required. Therefore, to minimize crew sizes a "simultaneous method" could be adopted to generate both duty schedules and roster schedules simultaneously. However, previous studies have shown that each solution is a large-scale combinatorial optimization problem, so it is very difficult to solve the problem using the simultaneous method. Therefore, we adopt a "two-stage method," whereby first a duty schedule is generated, and then this is used to generate a roster schedule.

The procedure of the proposed algorithm is shown below.

Step 1: Generation of trips

Using input data including the train timetable and rolling stock schedule, as well as the trains and the stations where crew can change, we generate the minimum unit of train service, which is called "trip." Details of trip generation are described in Section 3.2.

Step 2: Application of duty generation algorithm

We generate a set of duties for each crew base. The duty generation problem is modeled as a "Set Covering Problem (SCP)," which is a type of mathematical optimization problem. In addition, we use the "column generation method" [8] as a solution. Details of the duty generation algorithm are described in Section 3.3.

Step 3: Application of roster generation algorithm

We generate a roster for each crew base using the duty schedule obtained in Step 2. The roster generation problem is modeled as a "Travelling Salesman Problem (TSP)," which is also a type of mathematical optimization problem. Details of the roster generation algorithm are described in Section 3.4.

The main objective is to minimize the required crew size. In addition, we aim to obtain a practical crew scheduling plan that takes into account the crew's workload as much as possible. Then, we define the objective functions of Step 2 and Step 3 as follows.

- In Step 2, the number of working days is minimized. In addition, deadheading is minimized.
- In Step 3, the smallest buffer time from the required home rest time with a holiday or double rest days is maximized, because it is desirable to ensure sufficient home rest time with rest days to reduce the crew's workload.

3.2 Generation of trips (Step 1)

As a pre-processing step for the duty generation algorithm, a set of trips is generated. The rolling stock schedule is divided into parts at stations where crews can change, and each part is treated as a trip.

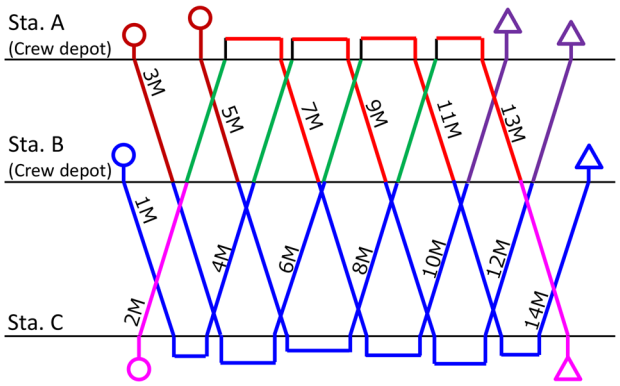

Fig. 4 Example of trips

Figure 4 shows an example of the set of trips. The train timetable and the rolling stock schedule are the same as in Fig. 1. In this example, each crew can change at Stations A and B, but not at Station C, so the rolling stock schedule is not divided at Station C. In case of 3M or 5M at Station A, exit work from the depot is necessary before driving. So exit or entry work at the depot may appear in the driver scheduling. On the other hand, since conductors do not perform this type of work, they do not appear in the conductor scheduling. This change to the definition of a trip allows drivers and conductors to be distinguished.

In addition, the problem size increases as the number of trips increases. The number of trips is thus kept to a minimum by counting a return journey with the same driver as a single trip in driver scheduling, instead of dividing it into two trips.

3.3 Application of duty generation algorithm (Step 2)

3.3.1 Overview of SCP and column generation method

A duty is produced by connecting several trips generated in Section 3.2. As previously mentioned, the duty generation problem is modeled as a SCP that is a mathematical optimization model. The set of columns, the cost of each column, and its covering rows are given in SCP, and we determine a set of columns with the lowest total cost that cover all rows in the original set. When a duty generation problem is modeled as a SCP, the rows correspond to trips and the columns correspond to duties.

Figure 5 shows an example of the coefficient matrix when a duty generation problem is modeled as a SCP. In this example, there are eight trips and seven duties satisfying the constraints (called "candidate duties"). The yellow areas indicate the trips covered by each duty. For example, Trips 1 and 3 are covered by Duty 1 with a coefficient of 1. The cost of each duty is shown in blue. After selecting duties which together cover all eight trips, where each duty covers at least one trip (which explains why the right-hand column shows greater than or equal to 1), the set of candidate duties which together have the lowest cost is found. In this example, the set with the minimum cost of five that covers all trips is achieved by selecting duties 2, 4, and 5.

In order to obtain the set of duties with the minimum cost, it is necessary to list all the duties (columns) that satisfy the constraints mentioned in Section 2.2. However, the number of duties satisfying the constraints is several million or more in reality. Therefore, the

	Duty 1	Duty 2	Duty 3	Duty 4	Duty 5	Duty 6	Duty 7		
Cost	1	1	2	2	2	2	2		
Trip 1	1			1		1		≥	1
Trip 2		1	1		1			≥	1
Trip 3	1				1		1	≥	1
Trip 4		1	1			1	1	≥	1
Trip 5				1		1		≥	1
Trip 6			1	1				≥	1
Trip 7					1		1	≥	1
Trip 8			1		1	1		≥	1

Fig. 5 Example of coefficient of SCP model

number of columns is enormous, which makes solving the problem in a short time difficult. Therefore, we use a column generation method (see Ref. [8]) that will only extract efficient columns. The following procedure outlines how to apply the column generation method to the duty generation problem.

Step 2-1: The algorithm prepares a set of initial columns and adds them to Restricted Linear Programming Master problem (RLPM).

Step 2-2: The algorithm solves the RLPM using the current set of generated columns.

Step 2-3: Based on the best solution of the RLPM in Step 2-2, the algorithm solves the column generation sub-problem to generate new columns with negative reduced costs. If a column with a negative reduced cost is found, it is added to the RLPM, and the process returns to Step 2-2. Otherwise, column generation is terminated, and the process goes to Step 2-4.

Step 2-4: The algorithm obtains a feasible solution using the set of generated columns so far.

3.3.2 Restricted linear programing master problem (Step 2-1 and Step 2-2)

RLPM refers to a mathematical optimization problem in which only certain columns are included, and the variables are linearly relaxed. The formulation of RLPM is given below. Table 1 shows the definitions of the notations used.

$$\text{Min.} \quad \sum_{k\in K}\sum_{j\in J^k} c_j^k x_j^k + \sum_{i\in M} d_i y_i \tag{1}$$

$$\text{s.t.} \quad \sum_{k\in K}\sum_{j\in J^k} a_{ij}^k x_j^k - y_i = m_i, \quad \forall i\in I \tag{2}$$

$$\sum_{k\in K}\sum_{j\in J^k} \left(e_j^k - c_j^k f^k\right) x_j^k \le 0, \quad \forall k\in K \tag{3}$$

$$\sum_{k\in K}\sum_{j\in J^k} g_j^{kl} x_j^k \le q^l, \quad \forall l\in L \tag{4}$$

$$\sum_{k\in K}\sum_{j\in J^k} c_j^k x_j^k \le r^k, \quad \forall k\in K \tag{5}$$

$$x_j^k \ge 0, \quad \forall j\in J^k, \forall k\in K \tag{6}$$

$$y_i \ge 0, \quad \forall i\in I \tag{7}$$

Equation (1) is the objective function, where the first term refers to the number of working days and the second term refers to the cost of crew deadheading. Equation (2) to (7) represent the constraints. Equation (2) to (5) imply constraints a) to d) described in Section 2.2. Equations (6) and (7) imply the possible values of the variables. Compared with the example in Fig. 5, the following points are different: in equation (2), the difference between the right and left sides (excess allocation) is obtained as y_i, which is reflected in the second term of the objective function equation (1); in equation (2), the right-hand side is not uniformly 1 but m_i; equation (3) to (5) has been added; and variable x_j^k is a real number.

Table 1 Notations for formulation of RLPM

Notation	Definition
K	Set of crew bases
I	Set of trips
J^k	Set of candidate duties of crew base k
L	Set of crew accommodations
a_{ij}^k	1 if candidate duty j of crew base k is assigned to trip i, 0 otherwise
c_j^k	Workday of candidate duty j of crew base k
d_i	Weight (Cost) for deadheading of trip i
m_i	Number of crew required for trip i
e_j^k	Paid working hours of candidate duty j of crew base k
g_j^{kl}	1 if candidate duty j of crew base k uses accommodation l, 0 otherwise
f^k	Upper limit of average paid working hours for crew base k
q^l	Upper limit of crew accommodation l
r^k	Upper limit of the number of workdays of crew base k
x_j^k	1 if candidate duty j of crew base k is selected, otherwise 0
y_i	Number of crew deadheading in trip i

3.3.3 Column generation sub-problem (Step 2-3)

A column generation sub-problem involves finding a new column (duty) to be added using the optimal solution of RLPM. Here, we seek columns for which the following reduced cost is negative.

$$c_j^k - \sum_{k\in K}\sum_{j\in J^k} a_{ij}^k \pi_i + \left(e_j^k - c_j^k f^k\right)\theta^k + g_j^{kl}\mu^l + c_j^k \rho^k \tag{8}$$

where π_i, θ^k, μ^l and ρ^k are the dual variables of equations (2) to (5), respectively, obtained by solving the RLPM. Since a column implies a duty, the generating column must satisfy the constraints e) to n) described in Section 2.2.

This problem can be modeled as a constrained shortest path problem on a network, with trips represented by nodes and connectivity between trips represented by arcs. By applying a labeling method to solve this problem, the optimal solution can be obtained in a short time (see Ref. [9] for details).

3.3.4 Obtaining a feasible solution (Step 2-4)

In the process of the column generation method, x_j^k is linearly relaxed, so a feasible solution (a solution where x_j^k is an integer) cannot be obtained. Therefore, it is necessary to calculate a feasible

solution after the column generation method has converged. Then, we apply a heuristic algorithm based on Nishi et al. [5] to obtain a feasible solution. At the stage of convergence of column generation, some x_j^k are fixed to 1. Here, variable fixing is based on the following ideas.

- When the objective function values of the RLPM converge, all values of x_j^k are fixed to 1 if x_j^k is equal to 1 in the RLPM.
- If there is no x_j^k whose value is equal to 1, only one x_j^k closest to 1 is fixed to 1.

After fixing some x_j^k, return to Step 2-2 in Section 3.3.1 and column generation is applied again. In this way, the number of x_j^k to be fixed is increased by repeating column generation. Finally, column generation is terminated when all trips are covered by the set of columns corresponding to the fixed variables.

3.4 Application of roster generation algorithm (Step 3)

3.4.1 Modelling as TSP

Give the set of duties generated by the above algorithm, roster generation algorithm gives a set of rosters that satisfy the constraints o) to t) in Section 2.2.

We model the crew rostering problem as a TSP by representing the generated duties as nodes and the connections between duties as arcs. The cyclic paths of the TSP solution pass through all nodes and correspond to the roster. That is, the constraint o) in Section 2.2 can be satisfied.

Since there are three cases between two sequence duties on a roster: no rest day between two duties, a rest day between two duties, and double rest day between two duties, three types of arcs are defined: a “normal arc” with no rest day, a “rest day arc” with a rest day, and a “double rest days arc” with double rest days. Therefore, up to three types of arcs can be drawn between two nodes. However, if any of the constraints q) to s) mentioned in Section 2.2 are not satisfied, the arc is not drawn. As described in section 3.1, the smallest buffer time from the required home rest time with a rest day or double rest day is maximized. Therefore, the cost of each arc is set to zero for a normal arc and the smallest buffer time from the required home rest time for a rest day arc and a double rest days arc.

Figure 6 shows an example of a TSP network. In this example, the duties of crew base B in Fig. 2 are given. Duties 3 to 6 correspond to nodes 3 to 6, respectively. Arcs are drawn only when all three types of arcs satisfy the constraints. In this network, we find a cyclic path that passes through any of these four nodes only once with the lowest cost.

3.4.2 Formulation as TSP

The following is an outline of the formulation as a mathematical optimization problem (see Ref. [9] for details).

<Objective function>

Maximization of the smallest buffer time in the required home rest time with a rest day or double rest days

<Constraints>

- Assignment of each duty to one of the rosters
- Subtour elimination constraints
- Constraints for consecutive working days
- Ensuring the required number of rest days
- Constraints on possible values of each variable

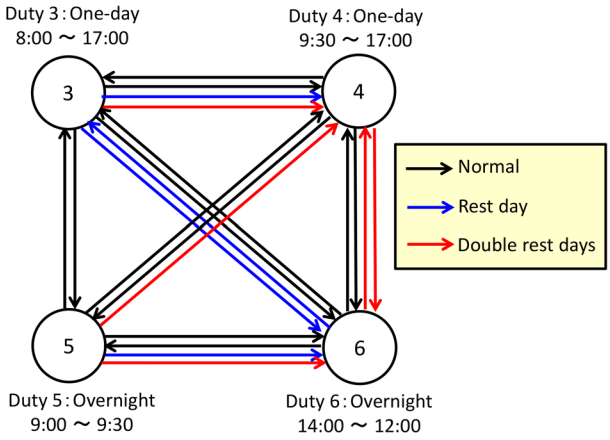

Fig. 6 Example of network based on TSP model

4. Case study

4.1 Lines and settings

In order to evaluate the effectiveness of the proposed method, we show the results of a case study with real Japanese railway data. The outline of each line is shown in Fig. 7. We generate a conductor schedule in Line I, where there are two crew bases adjacent to Stations B and E, and seven accommodation stations including these two stations. On the other hand, we generate a driver schedule in Line II, where there is one crew base adjacent to Station J and seven accommodation stations including Station J.

Table 2 also shows the number of crew bases, number of trains, and number of trips for each line as information on the size of the two Lines. All of these lines are relatively large with more than 400 trains each. Although the number of crew bases and the number of trains on Line I are both larger than Line II, the trains on Line I include many trains of out-of-service. Since a train which is out-of-service does not require a conductor, the scale of the study of Line II is bigger than that of Line I. In addition, the covering area of the two crew bases on Line I are different.

The performance of the proposed method is evaluated using criteria such as the number of working days and computational time. Here, we compare the evaluation criteria for the schedule generated by the proposed method with those for the actual schedule produced by experts. We use a PC with a Windows 10 Professional OS, Core i7-8700K CPU and 64 GB memory for the calculation and Gurobi Optimizer 10.0.1 [10] to solve the mathematical optimization problem.

4.2 Results of computational experiments

The results of the proposed method are shown in Tables 3 and 4. Table 3 compares the crew duties generated by the duty generation algorithm with the actual schedules for Lines I and II. The table shows the number of working days, the average paid working hours per a day, the average working hours (counted only for overnight duties), and the computational time (in seconds). The number of working days is lower than the actual schedule for both Lines I and II, indicating that the duty generation algorithm can produce an efficient schedule. On the other hand, the average paid working hours are slightly lower than that of the actual schedule for Line I, but higher for Line II. The average working hours increase significantly in both Line I and II. Although there is no problem with the results

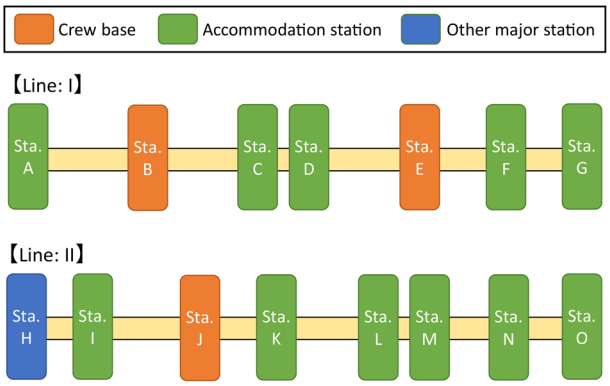

Fig. 7 Outline of each Line

Table 2 Characteristics of each Line using case

Line	Crew type	No. of crew bases	No. of trains	No. of trips
I	Conductor	2	483	430
II	Driver	1	402	403

because both the paid working hours and working hours satisfy the constraints, in practice it is suggested that greater consideration is given to crew workload, not just in terms of crew size but also based on indicators such as paid working hours and working hours.

Table 4 compares crew rosters generated by the roster generation algorithm with the actual schedule. The table shows the number of crew required, the minimum buffer time from the required home rest time with a rest day or double rest days, and the computational time (in seconds). It is understood that the larger the buffer time, the lower the workload and the better the scheduling. The proposed required crew sizes are smaller than that in the actual schedule for both Lines I and II. The minimum buffer times are also larger than that in the actual schedule. Therefore, we can produce a plan that is more efficient than the actual schedule in terms of both crew size and workload.

The computational time for both Line I and II is less than 30 minutes for the generation of the duty and the roster. Considering that the current manual work takes several days to several weeks, the proposed algorithm can generate a crew schedule plan in a sufficiently short time.

5. Conclusion and future work

This paper discusses the generation of crew scheduling plans for train timetable revisions and proposed a crew scheduling algorithm to minimize required crew sizes. The proposed algorithm uses mathematical optimization and is based on a two-stage process: first, a set of duties is generated, and this is used to generate a set of rosters, in sequence. We also presented case studies using data from several Japanese railway lines, including both drivers and conductors. We confirmed that the proposed algorithm can automatically generate a schedule plan with smaller crew sizes than required by the actual schedule within 30 minutes. On the other hand, the working hours and paid working hours are longer than in actual schedules, indicating that experts produce scheduling plans that consider the crew's workload.

In the future, we will develop a more practical method for automatically generating crew schedule plans by incorporating a new perspective on crew workload.

References

[1] Abbink, E., Huisman, D. and Kroon, L., "Railway crew management," In Borndorfer, R., Klug, T., Lamorgese, L., Mannino, C., Reuther, M., Schlechte, T. (Eds.), *Handbook of optimization in the railway industry*, pp. 243-264, Springer International Publishing, 2018.

[2] Heil, J., Hoffmann, K. and Buscher, U., "Railway crew scheduling: models, methods and applications," *European Journal of Operational Research*, Vol. 283, No. 2, pp. 405-425, 2020.

[3] Miura, R., Imaizumi, J., Fukumura, N. and Morito, S., "An application of Wedelin's method to railway crew scheduling

Table 3 Results of duty generation

Line	Method	No. of working days	Average paid working hours	Average working hours	Computational time (sec.)
I	Proposed	72	6h57m	23h40m	125.7
	Actual	73	7h05m	20h48m	—
II	Proposed	80	6h48m	20h43m	237.2
	Actual	82	6h12m	19h17m	—

Table 4 Results of roster generation

Line	Method	No. of crew required	Minimum buffer time	Computational time (sec.)
I	Proposed	104	7h43m	32.4
	Actual	105	2h48m	—
II	Proposed	116	9h12m	1010.7
	Actual	119	0h32m	—

problem," *IEEJ Transactions on Electronics, Information and Systems*, Vol. 129, No. 10, pp. 1958-1967, 2009 (in Japanese).
[4] Nishi, T., Muroi, Y. and Inuiguchi, M., "Column generation with dual inequalities for railway crew scheduling problems," *Public Trasport*, Vol. 3, No. 1, pp. 25-42, 2011.
[5] Sakaguchi, T. and Nozue, N., "Crew Roster Scheduling Based on Constraint Logic," *RTRI Report*, Vol. 10, No. 4, pp. 29-34, 1996 (in Japanese).
[6] Nishi, T., Sugiyama, T. and Inuiguchi, M., "Two-level decomposition algorithm for crew rostering problems with fair working condition," *European Journal of Operational Research*, Vol. 237, No. 2, pp. 465-473, 2014.
[7] Sakaguchi, T., Kato, S. and Fukumura, N., "An Algorithm for Crew Route Scheduling Focusing on Manpower Efficiency," *Quarterly Report of RTRI*, Vol. 54, No. 4, pp. 197-201, 2013.
[8] Desaulniers, G., Desrosiers, J. and Solomon, M. M., *Column generation*, Springer Publishing Inc., New York, U.S.A., 2005.
[9] Kato, S., Nakahigashi, T. and Kokubo, T., "Crew scheduling algorithm for minimizing the required number of crew members," *IEEJ Transactions on Industry and Applications*, Vol. 144, No. 5, pp. 342-352, 2024 (in Japanese).
[10] Gurobi Optimizer, https://www.gurobi.com/jp/products/gurobi/ (Accessed: August 6, 2025)

Authors

Satoshi KATO
Senior Researcher, Transport Operation Systems Laboratory, Signalling and Operation Systems Technology Division
Research Areas: Transportation Planning, Mathematical Optimization

Taichi NAKAHIGASHI
Researcher, Transport Operation Systems Laboratory, Signalling and Operation Systems Technology Division (Former)
Research Areas: Transportation Planning, Train Rescheduling

Generation Mechanism of Localized Wear of Cu-impregnated Metalized Carbon Contact Strip

Yoshitaka KUBOTA
Frictional Materials Laboratory, Materials Technology Division

Takamasa HAYASAKA
Research and Development Promotion Division

Shinichiro KOGA
West Japan Railway Company

Hidehiko NOZAKI
Toyo Tanso

Localized wear on pantograph contact strips is a serious issue that needs to be addressed urgently, as it can cause the pantograph head to fuse and the overhead contact wire to break. However, the exact causes of localized wear are still unclear, and effective solutions have not yet been developed. This study aims to identify the causes of localized wear in copper-impregnated metalized carbon contact strips. To achieve this, worn strips were analyzed using a micro-Raman spectrometer and the sliding wear behavior of contact strips with different levels of carbon graphitization was examined using a block-on-ring wear tester.

***Key words*:** *pantograph contact strip, abnormal wear, metalized carbon contact strip, stepped wear, grooved wear, graphitization, Raman spectroscopy*

1. Introduction

The most commonly used current collection system for electric railways is the overhead contact line system. In this system electric rolling stock collects power from a contact wire via a pantograph. A sliding contact component, known as the pantograph contact strip (hereinafter referred to as the contact strip), is mounted at the top of the pantograph and makes direct contact with the contact wire (Fig. 1(a)).

Contact strips are worn due to friction with the contact wire. Wear profiles of contract strips usually correspond to the lateral deviation of the contact wire (Fig. 1(b)), as shown in Fig. 1(c). However, in rare cases, wear can develop locally, leading to uneven wear such as stepped wear or grooved wear (Fig. 1(c)). Figure 2 shows an example of actual localized wear. Even when detected at an early stage, localized wear can cause train delays due to the need for unscheduled replacement of the contact strip. If detection is delayed, it may result in fusion of the pantograph head and, in severe cases, damage to the overhead contact wire, both of which pose serious operational risks. Therefore, resolving this issue is critically important.

Nevertheless, the mechanisms underlying the initiation and progression of localized wear, particularly in metallized carbon contact strips, are still not well understood, and no systematic countermeasures have been established. Although methods to detect localized wear using sensors installed on the contact wire have been proposed [1], a fundamental solution requires a deeper understanding of its causes and formation mechanisms.

When investigating the mechanism of the localized wear, it is important to distinguish between initial formation of localized wear and rapid progression of wear in regions where wear has already begun. This study focuses on the early-stage formation of localized wear in copper-impregnated metallized carbon contact strips.

2. Current understanding on localized wear of contact strips

2.1 Localized wear with identified causes

Localized wear with already identified causes can be broadly categorized into the following three types:

(1) Wear caused by contact loss due to frost or ice on the overhead wire;
(2) Wear caused by contact loss resulting from insufficient followability of the overhead contact line–pantograph system.
(3) Wear occurring at the boundary between the principal and

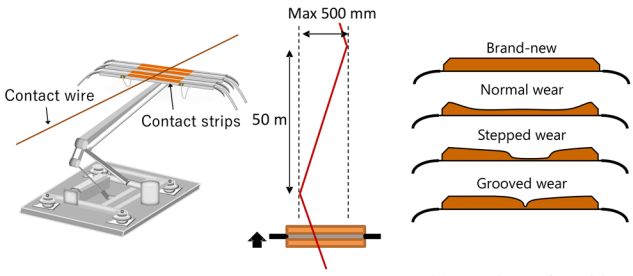

(a) Pantograph and contact wire (b) Stagger (zigzag) of contact wire (c) Schematic side view of worn contact strip

Fig. 1 Schematic drawings of pantograph and contact strip

Fig. 2 Example of localized wear of contact strip

auxiliary contact strips.

Type (1) is commonly observed with copper-based sintered alloy contact strips. When the pantograph passes over sections of the contact wire with frost or ice, continuous arc discharges are generated, leading to the melting and wear of the contact strip. Notable characteristics of this type include its frequent occurrence during winter and arc discharge damage on the side surfaces of the pantograph head. Countermeasures have included the use of arc-resistant contact strip materials and the removal of the ice coatings using dedicated pantographs for de-icing.

Type (2) occurs when the followability of the overhead contact line–pantograph system is poor, resulting in repeated contact loss. For example, localized wear has been reported in cases where the pantograph uplift force was reduced due to a low contact wire height [2], and in areas with corrugated wear on the contact wire. In cases where ground equipment-related factors are responsible, contact loss occurs repeatedly at the same location on the contact strip, resulting in consistent localized wear at the same position across different trains.

Type (3) refers to wear that occurs on the auxiliary contact strip at the boundary with the principal contact strip, typically on the auxiliary strip made of aluminum. This type of localized wear is attributed to significant differences in electrical resistivity and wear characteristics between the principal and auxiliary contact strips. Using auxiliary contact strips made of the same material as the principal contact strip has proven to be an effective countermeasure.

2.2 Influence of arc discharge on the wear of metallized carbon contact strips

The indent at the beginning of this section should be 15 milli As discussed in the previous section, many cases of localized wear are believed to result from arc discharges during contact loss events. This wear is more common in metal-based contact strips, which can melt or soften due to such discharges. However, localized wear is also found in carbon-based strips, which do not melt under atmospheric pressure, and this remains a significant concern.

Previous studies have shown that wear on copper-impregnated carbon strips increases with arc discharge energy [3], and arc exposure causes the copper to melt out, reducing the strip's hardness. These findings suggest that localized wear results from arc energy concentrating on specific areas of the strip surface.

However, in experiments conducted using a contact force of 55 N, comparable to the standard uplift force of pantographs, no clear correlation was found between arc energy distribution and the resulting wear profile [4]. Further tests investigating whether arc-damaged areas initiate localized wear revealed similar wear rates in damaged and undamaged areas. In contrast, experiments with roughly double the normal contact force showed a strong correlation between electric charge of arc discharge and contact strip wear. These findings suggest that both arc discharge and high contact force contribute to increased wear of the contact strip. Nevertheless, the precise mechanism behind this phenomenon remains unclear.

Building on the previous research, this study aims to perform detailed observation and analysis of localized wear on the metallized carbon contact strips. We also conducted experiments using contact strip specimens that simulated degradation caused by arc discharge, such as copper ejection or graphitization, to investigate the effects of contact force and the surface roughness of the contact wire on the wear of the strip.

3. Investigation of localized wear occurrence and observation/analysis of contact strips with localized wear

3.1 Contact strip material

The contact strip studied is the PC78A, a copper-impregnated metallized carbon strip manufactured by Toyo Tanso. Its microstructure is shown in Fig. 3, and its chemical composition and physical properties are listed in Table 1. Typically, the carbon substrate in such strips is non-graphitic carbon fired at 1,000–1,500°C, which also applies to PC78A. When exposed to temperatures above 2,000°C, this carbon undergoes a structural transformation into graphitic carbon, a process known as graphitization.

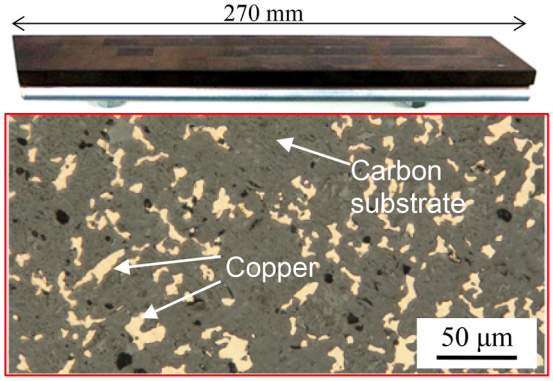

Fig. 3 Appearance and microstructure of Cu-impregnated carbon contact strip

Table 1 Chemical composition and physical properties of contact strip

Chemical composition (mass %)	
C	52
Cu	48
Physical properties	
Density (10^3 kg/m^3)	3.0
Shore Hardness (HSD)	90
Electric resistivity (µΩm)	1.8
Flexural strength (MPa)	120
Charpy impact value (kJ/m^2)	4.2

3.2 Investigation of localized wear occurrence

3.2.1 Overview of the investigation

Localized wear on PC78A was investigated in Areas A and B from December 2009 to March 2012. The investigation focused on two aspects: the date of discovery and the displacement (distance from the center of the pantograph head) of the wear location. The trains operating in these areas were either 115 or 117 series electric trains, typically in a four-car formation with two motor cars and two trailers. A single pantograph (Type PS16) equipped with two rows of 40 mm-wide contact strips. The maximum current per strip was estimated from the traction motor ratings: about 520 A for the 115 series and 450 A for the 117 series.

3.2.2 Results and discussion

Figure 4 shows the monthly distribution of localized wear occurrences. If icing or frost on the contact wire were the main cause, a higher frequency would be expected in winter. However, no such seasonality was observed in the investigated areas, as shown in Fig. 4.

Figures 5 and 6 show the location distribution where localized wear occurred. The data indicate that wear tends to occur near the center of the pantograph head and around ±200 mm from the center—positions that correspond to the endpoints of the contact wire's zigzag pattern. The central area of the contact strip has lower pantograph followability, making contact loss and arc discharges more likely. Similarly, at ±200 mm from the center, the contact wire is supported by fittings and has greater inertia, which also increases the likelihood of contact loss. The high frequency of localized wear occurrence in these displacements suggests that arc discharges during contact loss, as previously considered, may be the cause of localized wear on metallized carbon contact strips.

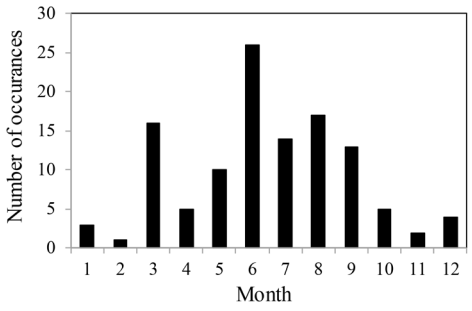

Fig. 4 Monthly distribution of localized wear detection

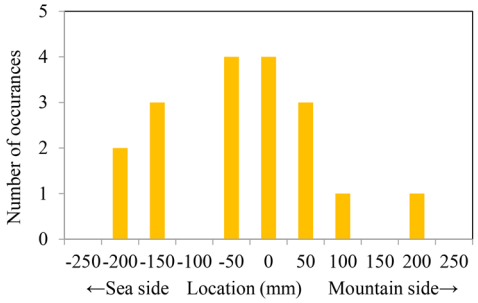

Fig. 5 Localized wear location distribution (Area A)

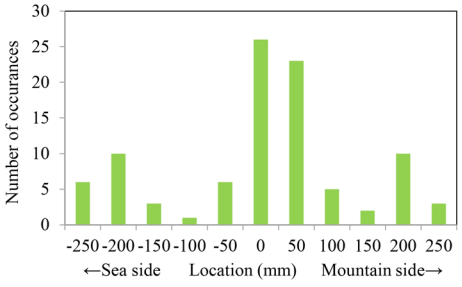

Fig. 6 Localized wear location distribution (Area B)

3.3 Cross-sectional microstructural observation and Raman spectroscopic analysis of localized wear regions on contact strip

The cross-sectional microstructure of localized wear regions on the contact strip was examined using a digital microscope. Figure 7 shows a representative result. In the figure, slightly darkened areas indicate regions where copper has melted and been ejected. The depth of the copper-ejected region reached approximately 1,500 µm at the flat surface of the localized wear region, but only around 10 µm on its sloped surfaces. In contrast, in normally worn regions—areas without localized wear—the depth ranged from 10 to 100 µm. These findings suggest that the flat surface of the localized wear region experienced more intense thermal effects than other areas.

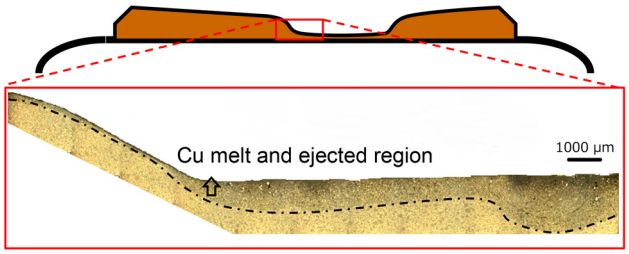

Fig. 7 Example of microstructure around localized worn part

3.3.1 Raman spectroscopic analysis

To evaluate the degree of graphitization of the carbon substrate at the bottom of the localized wear area, Raman spectroscopy was conducted. Raman spectroscopy assesses the crystallinity and structural properties of carbon materials by analyzing the spectrum of light scattered by laser irradiation.

Figure 8 shows a Raman spectrum of PC78A (black line). Carbon materials typically display two characteristic peaks: the G band (~1,580 cm^{-1}), associated with graphite structures, and the D band (~1,360 cm^{-1}), related to structural disorder and defects.

By deconvoluting the spectrum (red and blue curves in Fig. 8), the intensities of the G and D bands, denoted as I_G and I_D, are obtained. As graphitization progresses, the G band becomes sharper, the intensity ratio $R=I_G/I_D$ (also known as the R-value [5]) increases, and the full width at half maximum (FWHM) of the G band decreases. These indicators are commonly used to evaluate the degree of graphitization.

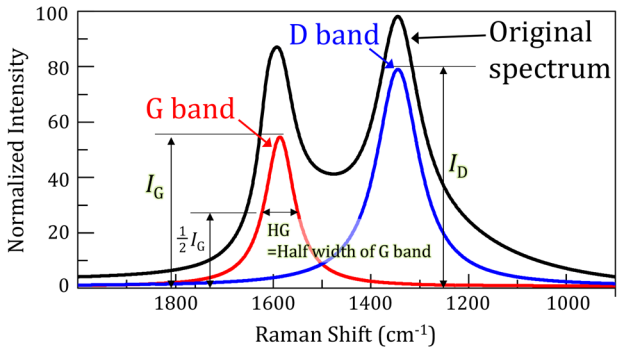

Fig. 8 Example of Raman spectrum of PC78A

(1) Analytical method and graphitization degree evaluation indicator

The analysis was performed using an Almega Laser Raman Spectrometer (Thermo Nicolet). Although the R-value is commonly used to evaluate graphitization, this study used the full width at half maximum (FWHM) of the G band instead, based on preliminary findings showing a strong correlation with firing temperature.

(2) Analysis of standard samples

Before analyzing the actual contact strips, Raman spectroscopy was performed on standard samples prepared by varying the firing temperature of the carbon substrate to investigate the relationship between graphitization and temperature. Rockwell hardness was also measured to assess how firing temperature affected substrate hardness.

(3) Results and discussion of standard sample analysis

Figure 9 shows the relationships between firing temperature and both the FWHM of the G band and hardness. The FWHM, denoted as HG (cm^{-1}), exhibited a strong negative correlation with the firing temperature T (°C), as shown in Eq (1).

$$HG = -0.024\,T + 113 \quad (1)$$

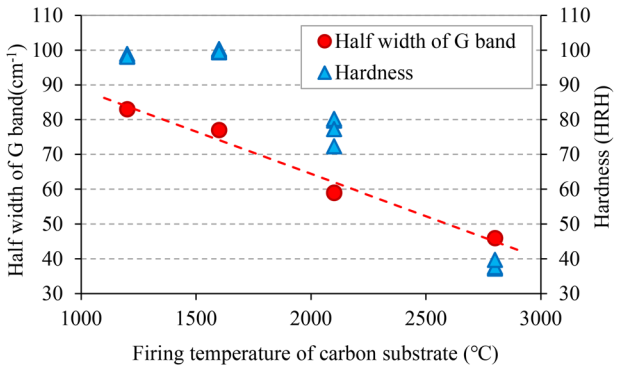

Fig. 9 Relationship between firing temperature of carbon substrate and half width of G band and Rockwell hardness of contact strip

Based on Eq. (1), the equivalent firing temperature experienced by a contact strip can be estimated from the FWHM of the G-band in its Raman spectrum. In the following sections, thermal history is evaluated using this estimated temperature rather than the FWHM directly.

According to Fig. 9, the Rockwell hardness of the carbon substrate, initially about 100 HRH at manufacturing, drops to around 80 HRH when the firing temperature exceeds 2,000°C, and further declines to approximately 40 HRH at 2,800°C. In this study, 2,000°C —the point at which hardness begins to decrease—is defined as the graphitization temperature. When the estimated temperature exceeds this threshold, graphitization is considered to have progressed.

(4) Analysis of the actual contact strip

Raman spectra were measured at three locations (Fig. 10) on both locally and normally worn areas of the contact strip. In total, six points were measured on locally worn areas (two samples) and twelve on normally worn areas (four samples). After surface measurements, the strip was sectioned, and similar measurements were taken on cross-sections 0.2–0.3 mm below the surface.

(5) Analysis and discussion of localized wear on the contact strip

Figure 11 presents the estimated thermal history derived from the measured Raman spectra. Of the 12 points measured in normally worn areas, 10 had estimated peak temperatures at the contact surface below 2,000°C (ranging from 1,400°C to 1,750°C). The two points exceeding 2,000°C were located at the edges of the contact strip, where arc discharges are more likely to occur.

Fig. 10 Points of Raman spectroscopic analysis for actual contact strip

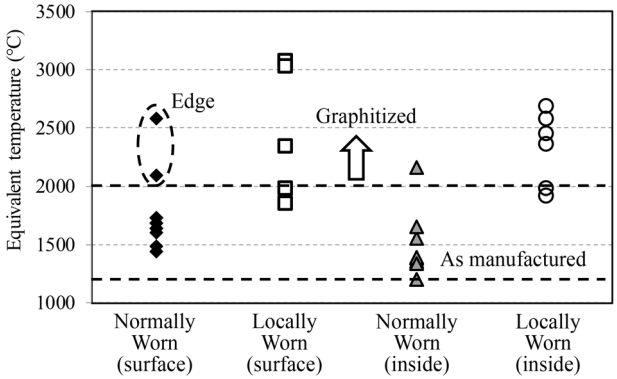

Fig. 11 Estimated maximum temperature on surface and inside of contact strip

By contrast, in locally worn areas, four out of six points showed peak temperatures above 2,000°C (ranging from 2,300°C to 3,100°C), with significant graphitization observed even in the central region of the strip.

Measurements taken at a depth of 0.2–0.3 mm from the sliding surface showed similar trends. In normally worn areas, 11 of 12 points had peak temperatures below 2,000°C. In locally worn areas, four of six points exceeded 2,000°C (ranging from 2,300°C to 2,700°C), indicating that graphitization extended to these subsurface regions.

4. Arc discharge experiment

This chapter describes an experiment conducted to investigate the influence of heat generated by arc discharge on the graphitization of the carbon substrate of the contact strip.

4.1 Experimental method

First, a current of 500 A was applied between a hard copper contact wire (anode) and a PC78A contact strip (cathode) in contact. The voltage of the power supply was 70 V DC. An arc discharge was then generated by moving the contact strip vertically downward at 10 mm/s. The arc duration was controlled by turning off the arc using a thyristor to short-circuit the electrodes after ignition. Since the arc duration in actual operation is at most on the order of 100 ms, it was set between 0.2 ms and 500 ms in this experiment. Afterward, Raman spectra were measured on the arc-damaged surface and on a cross-section 0.2–0.3 mm below the surface.

4.2 Experimental results and discussion

Figure 12 shows the estimated peak temperatures on the surface of the arc-damaged trace and at a depth of 0.2–0.3 mm below the surface. Even with an arc duration of just 0.2 ms, the surface temperature exceeded 2,500°C, indicating that graphitization occurred within this short duration. At the 0.2–0.3 mm depth, when the arc duration ranged from 0.2 to 10 ms, peak temperatures remained below 1,200°C and no structural changes in the carbon substrate were observed. However, when the arc duration exceeded 50 ms, peak temperatures rose above 2,000°C, and graphitization was observed.

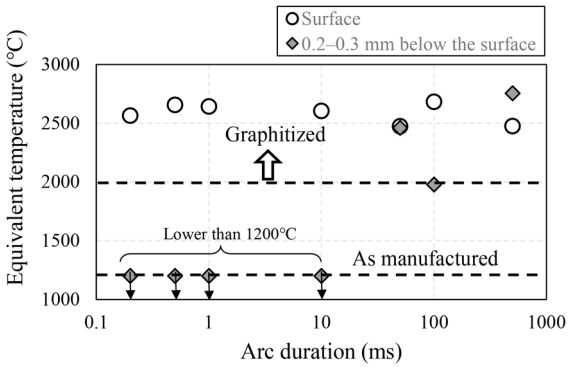

Fig. 12 Estimated equivalent temperature of arc-damaged region

5. Wear experiments under electric current

Wear experiments under electric current were conducted to:
(1) examine the effect of copper ejection on contact strip wear;
(2) identify factors promoting graphitization of the carbon substrate; and
(3) clarify how graphitization of the carbon substrate affects wear.

5.1 Experimental method

The experiments were conducted using the wear tester developed by the Railway Technical Research Institute. This tester simulates actual operating conditions by pressing a contact strip specimen (25 mm × 60 mm × 9 mm) against a pure copper ring (material: JIS C1020P-1/2H; contact width: 5 mm) representing the contact wire and sliding it while an electric current is applied. The zigzag motion of the contact wire is simulated by laterally oscillating the contact strip.

During the experiments, electric current, voltage between the contact strip and contact wire, contact force, and frictional force were measured. Arc discharge was defined as occurring when the voltage exceeded 10 V. To quantify the effects of arc discharge, the amount of charge of arc discharge Q(C) was calculated as the cumulative sum of the product of current and arc duration during arc events.

5.2 Effects of copper ejection on wear and factors promoting graphitization

Previous research suggested that the increased wear of PC78A from arc discharge was caused by oxidation of the carbon substrate, promoted by copper ejection. However, as discussed in Section 3.3, both copper ejection and graphitization occur during arc discharge. To isolate the effect of graphitization, we conducted experiments comparing wear on specimens with copper ejected from the surface to those without. The cross-sectional microstructure near the surface of the copper-ejected specimens is shown in Fig. 13. Additionally, to determine whether graphitization occurs due to Joule heating independent of arc discharge, Raman spectroscopy was performed on the sliding surface of the contact strip after the experiments.

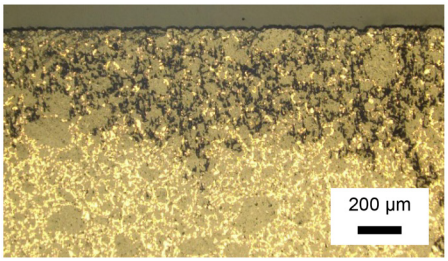

Fig. 13 Microstructure of Cu ejected contact strip specimen

5.2.1 Experimental conditions

The experimental conditions are summarized in Table 2. To investigate whether the carbon substrate undergoes graphitization due to Joule heating induced by electric current, the maximum current was set to 500 A, which corresponds to the maximum current collected per contact strip in actual vehicles.

Table 2 Experimental conditions (effect of Cu ejection from surface)

Items	Condition
Sliding speed	100 km/h
Current	DC100, 300, 500 A
Contact load	54 N
Sliding distance	25 km
Test piece	1,200°C fired Normal and Cu ejected
Sliding surface of simulated contact wire	Smooth※

※Surface roughness: 0.05~0.15μm (Ra), 0.1~1.0μm (Rz_{JIS})

5.2.2 Experimental results and discussion

Figure 14 shows the specific wear rate of the contact strip (i.e., wear volume per unit normal load and per unit sliding distance) as a function of the average current during the experiments. There was no observable trend indicating an increase in specific wear rate for specimens simulating copper ejection from the surface.

To examine the effect of arc discharges on wear, Fig. 15 plots the arc discharge charge per unit sliding distance on the horizontal axis.

For all strips, the specific wear rate increased with the amount of arc discharge, while copper ejection had no significant effect.

Since copper ejection also occurred in normally worn areas, it is suggested that copper ejection alone is unlikely to cause localized wear of the contact strip.

Figure 16 shows the estimated maximum surface temperature of the contact strip specimen based on the Raman spectra. Under

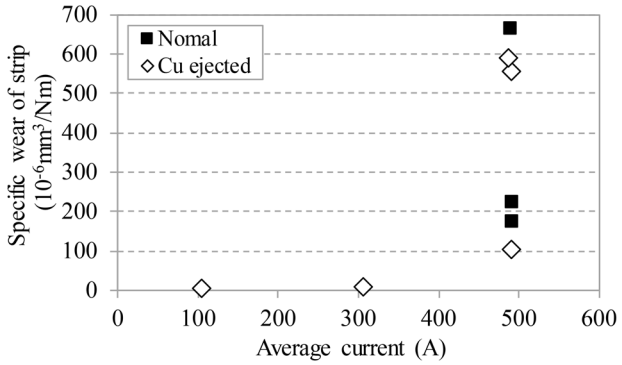

Fig. 14 Result of wear experiment (effect of current)

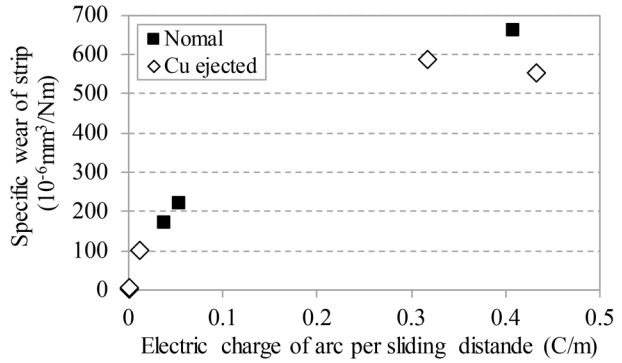

Fig. 15 Result of wear experiment (effect of arc-discharge)

conditions where the arc discharge rate was 0% or 0.1%, no estimated peak temperature exceeded the graphitization threshold of 2,000°C, regardless of the applied current. As a result, no graphitization of the carbon substrate was observed.

In contrast, at an arc discharge rate of 2.5%, the estimated peak temperature exceeded 2,700°C at the specimen edge, where arc discharge was more likely. While it cannot be ruled out that graphitization may occur without arc discharge under even larger electric current conditions, the results confirmed that arc discharge is a major factor promoting graphitization.

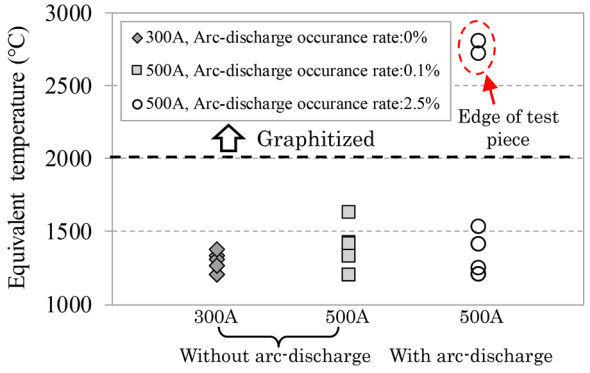

Fig. 16 Estimated maximum temperature of surface of contact strip specimen

5.3 Influence of contact force and surface roughness of the contact wire on localized wear of graphitized regions of contact strip

5.3.1 Experimental conditions

This section examines the effects of contact force and wire roughness on the wear of contact strips with different graphitization levels. The strips were made from materials fired at different temperatures. Experimental conditions are shown in Table 3.

Table 3 Experimental conditions (effect of graphitization on wear of contact strip)

Items	Condition1	Condition2	Condition3
Sliding speed, km/h	100		
Current, A	0–DC500		
Contact load, N	54	54	98
Sliding distance, km	25		
Contact strip test piece	1,200, 1,600, 2,100(or 2,200), 2,800°C fired		
Sliding surface of simulated contact wire	Smooth*1	Rough*1	Smooth*2

*1 Surface roughness: 0.05–0.15 μm (Ra), 0.1–1.0 μm (Rz_{JIS})
*2 Surface roughness: 1.5–2.5 μm (Ra), 5–15 μm (Rz_{JIS})

To investigate the effects of contact force and the surface roughness of the contact wire on wear, wear experiments were conducted under the following three conditions: (1) a typical pantograph contact force of 54 N with a smooth contact wire surface, (2) a contact force of 54 N with a rough contact wire surface simulating surfaces severely damaged by arc discharge, and (3) an increased contact force of 98 N with a smooth contact wire surface. In service lines using PC78A contact strips, surface roughness in undamaged areas (without contact loss or arcing) is approximately Ra 0.1–0.6 μm and Rz_{JIS} around 2 μm, whereas in areas severely damaged by arc discharge, it reaches Ra 2–18 μm and Rz_{JIS} 8–30 μm.

5.3.2 Experimental results and discussion

(1) Condition 1 (contact force: 54 N, smooth contact wire surface)

Figure 17 shows the experimental results under these conditions. Since no arc discharge occurred, the specific wear rate of the contact strip was plotted against the applied current. Across all cur-

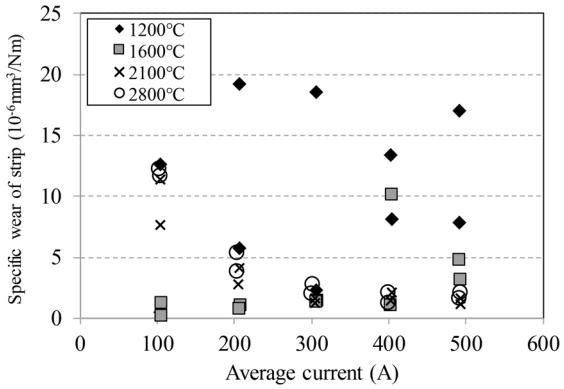

Fig. 17 Result of wear experiment under condition1

rent levels, strips fired at 2,100°C or 2,800°C showed no clear tendency to wear more than those fired at 1,200°C or 1,600°C. These results suggest that, under standard contact force and with a smooth contact wire surface, even highly graphitized contact strips did not show increased wear.

(2) Condition 2 (contact force: 54 N, rough contact wire surface)

The experimental results are shown in Fig. 18. Under these conditions, arc discharges occurred, so the specific wear rate of the contact strip was plotted against the arc charge. Since the arc charge in actual service is typically around 10^{-3} C/m, the comparison in Fig. 18 focuses on the range of 0–0.01 C/m. The results show that the specific wear rate of the strip made from carbon substrate fired at 2,100°C was about five times higher, and that of the strip fired at 2,800°C was about nine times higher than the average wear rate (40 × 10^{-6} mm³/Nm) of the strips fired at 1,200°C and 1,600°C.

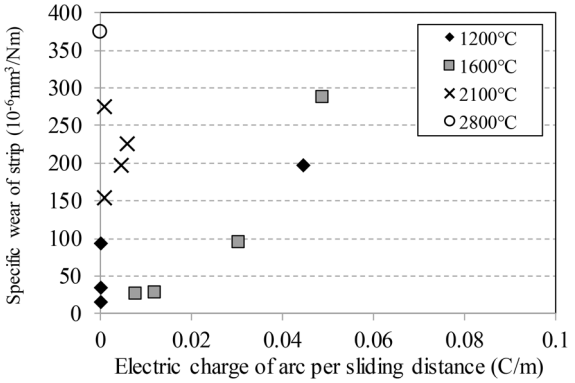

Fig. 18 Result of wear experiment under condition 2

(3) Condition 3 (contact force: 98 N, smooth contact wire surface)

The experimental results are shown in Fig. 19. As in Condition 2, the comparison focuses on the region where the arc discharge ranges from 0 to 0.01 C/m. The specific wear rate of the contact strip specimen fired at 2,200°C was about 20 times higher than the average of the 1,200°C- and 1,600°C-fired strips (54 × 10^{-6} mm³/Nm). The strip fired at 2,800°C showed severe wear under the 100 A current, and the experiment was discontinued. As a result, its data is not shown in the figure. However, its specific wear rate at the time of discontinuation was 4,232 × 10^{-6} mm³/Nm—roughly 80 times higher than the average of the 1,200°C- and 1,600°C-fired strips.

Notably, field measurements on actual vehicles have shown

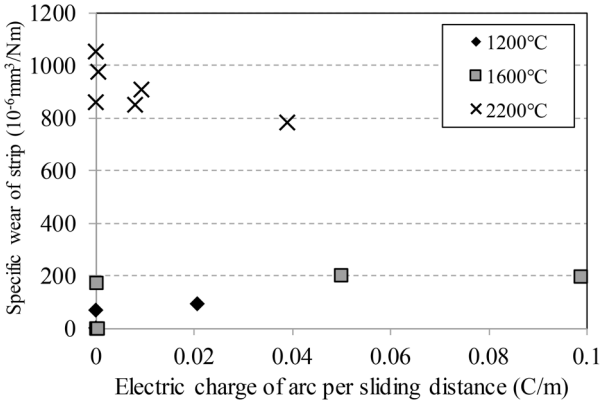

Fig. 19 Result of wear experiment under condition 3

that contact forces exceeding 98 N occur approximately 20% of the time. This suggests that the high contact force used in the experiment can also occur in actual environments.

5.3.3 Summary

The results suggest that the wear rate of the contact strip increases significantly when the carbon substrate is graphitized and contacts a rough wire surface, or when the contact force is higher than usual. This increase is likely caused by abrasive wear from a cutting action. Abrasive wear occurs when two solid surfaces slide against each other and the harder, rougher surface cuts into the softer one. As shown in Fig. 20, after graphitization, the carbon substrate becomes softer than the simulated contact wire, reversing their original hardness relationship. This reversal likely led to abrasive wear.

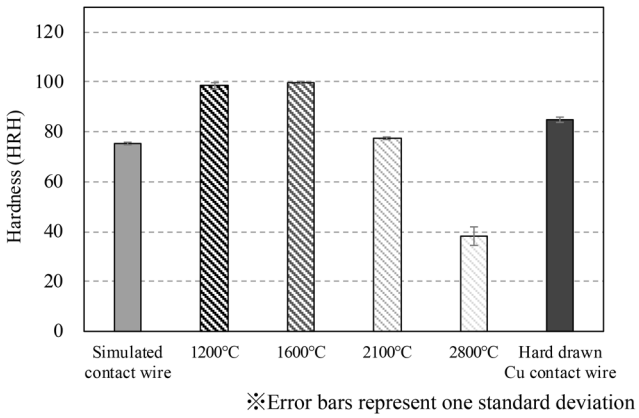

Fig. 20 Comparison of hardness

6. Localized wear mechanism and countermeasures

6.1 Mechanism

Based on the above results, the localized wear mechanism in copper-impregnated metallized carbon contact strips can be described as follows:

(1) Arc discharge due to contact loss promotes graphitization of the carbon substrate, leading to arc-damaged regions with reduced hardness.

(2) When these softened regions interact with a rough contact wire surface or experience high contact force, a cutting action occurs, significantly increasing the wear rate and resulting in localized wear.

6.2 Countermeasures

Since localized wear in the copper-impregnated metallized carbon contact strips is presumed to be caused by arc discharge, a fundamental countermeasure is to reduce arc discharge caused by contact loss. Arc discharge can also occur when an oxide film on the contact wire surface hinders electrical contact, not just during contact loss. In such cases, removing the oxide film effectively suppresses localized wear.

As noted in Section 6.1, localized wear tends to occur in graphitized regions of the carbon substrate, which appear glossy and are visually identifiable. Field maintenance has confirmed that early

replacement of contact strips with such glossy areas reduces the incidence of localized wear.

7. Conclusion

To clarify the mechanism of localized wear in copper-impregnated metallized carbon contact strips, we conducted a field survey, observations of worn strips, and wear experiments. The following findings were obtained:

1) Localized wear tends to occur at the center of the contact strip or at the edges of the contact wire deviation.
2) At locations with localized wear, the carbon substrate of the contact strip is graphitized.
3) Graphitization of the carbon substrate in the contact strip progresses even with very short duration of arc discharges, and the graphitized area expands internally with longer duration of arc discharge.
4) The hardness of the graphitized contact strip is lower than that of the contact wire. When the contact wire surface is rough or the contact force is high, the wear rate increases by approximately 5 to 20 times compared to non-graphitized strips.

It should be noted that this paper is a partially revised version of the article published in IEEJ Transactions on Industry Applications, Vol. 141 [6]. The copyright of the original paper is held by the Institute of Electrical Engineers of Japan.

References

[1] Koyama, T., Usuda, T., Kawasaki, K., Nakamura, K., Kawamura, T., "Methods for Detecting Pantograph Defects Using Sensors Installed on Contact Lines," *QR of RTRI*, Vol. 57, No. 3, 2016.

[2] LIU Guo-liang, "Analysis of pantograph carbon contact strip abnormal wear on Guangzhou Metro Line 2 train," *Electric Locomotives & Mass Transit Vehicles*, No. 2, 2008.

[3] Kubo, S., Kato, K., "Effect of arc discharge on wear rate of Cu-impregnated carbon strip in unlubricated sliding against Cu trolley under electric current," *Wear*, Vol. 216, Issue 2, pp. 172-178, 1998.

[4] Kubota, Y., Hayasaka, T., Miyauchi, T., "Effect of Arc Discharge on the Wear Profile of Cu Impregnated Carbon Based Pantograph Contact Strip," presented at *ICEC 2014 (The 27th International Conference on Electrical Contacts)*, Dresden, Germany, June 22-26, 2014.

[5] Tuinstra, F., Koenig, J. L., "Raman spectrum of graphite," *J. Chem. Phys*., 53, 1126-1130, 1970.

[6] Kubota, Y, Hayasaka, T., Koga, S, Nozaki, H, "Generation Mechanism of Localized Wear of Cu-impregnated Metalized Carbon Contact Strip," IEEJ Transactions on Industry Applications, Vol. 141.

Authors

Yoshitaka KUBOTA
Senior Researcher, Frictional Materials Laboratory, Materials Technology Division
Research Areas: Tribology, Sliding Contact, Current Collecting Materials

Takamasa HAYASAKA, Ph.D.
General Manager, Head of R&D Planning, Research and Development Promotion Division
Research Areas: Arc Discharge Plasma, Contact Line Structures, Current Collection

Shinichiro KOGA
Senior Engineer, West Japan Railway Company
Research Areas: Vehicle Maintenance

Hidehiko NOZAKI
Technical Manager, Toyo Tanso Co,Ltd
Research Areas: Carbon Materials

Stability Analysis of Pantograph Under Sliding Condition Based on Frequency Response Function Measurement

Shigeyuki KOBAYASHI **Yuki AMANO** **Yoshitaka YAMASHITA**
Current Collection Laboratory, Railway Dynamics Division

Unstable pantograph vibrations can occur at low train speeds due to high friction. To reduce the cost of contact strip maintenance, this study proposes a stability analysis method that incorporates friction effects without requiring a complex analytical model. Instead of a complex analytical model, the method estimates the frequency response function (FRF) in the sliding state by measuring the FRF while a vehicle is stationary and applying an assumed friction coefficient. Modal characteristics are extracted from the estimated FRF, and stability is evaluated using damping ratios. The validity of this approach was confirmed by comparing its results with those from low-speed sliding tests.

***Key words*:** *pantograph, overhead contact line, friction-induced vibration, instability*

1. Introduction

A pantograph is a current collection device mounted on the roof of railway vehicles. It supplies the vehicle with electric power by maintaining contact between the contact strip at the top of the pantograph and the contact wire. During operation, the contact strip slides along the contact wire, so it needs to be highly resistant to wear. To improve lubricity, metallic contact strips are typically impregnated with lubricating components [1]. Bench tests using contact wire and contact strip specimens have revealed that the friction coefficient tends to increase as sliding speed decreases [2]. Moreover, the friction coefficient can be further elevated by surface roughening of the contact strip due to wear or arc-induced melting. Under such conditions, particularly during low-speed operation in areas such as stations, the pantograph may occasionally experience large-amplitude vibrations, known as unstable vibrations [3]. Since these vibrations have been identified as a factor contributing to increased contact wire wear [4], the development of effective countermeasures is essential.

To elucidate the mechanism of unstable vibrations, the authors previously conducted analytical investigations using two models: a simplified two-degree-of-freedom model representing the coupling between the pitching and vertical motions of the contact strip [5], and a flexible multibody dynamics (FMBD) model of the pantograph that incorporates elastic deformations of the pantograph head and articulated frame [6]. These model-based analyses offer various advantages in that they allow both the evaluation of unstable vibration occurrence under arbitrary friction coefficients and the proposal of structural modifications to mitigate such vibrations. However, in order to predict unstable vibrations with high accuracy using these models, it is necessary to identify model parameters such as mass, stiffness, and damping coefficients based on excitation tests of actual pantographs, which involves considerable effort. An alternative approach is to evaluate the stability of real pantographs under stationary conditions. For example, low-speed sliding tests can be performed using the Railway Technical Research Institute's high-speed test facility for pantograph/OCL systems (HiPaC) [7]. However, it is difficult to evaluate stability under arbitrary friction conditions using such sliding tests, as they do not allow control of the friction coefficient between the contact strip and the contact wire.

As described above, each of the previously proposed methods for stability analysis has its own advantages and limitations. This study proposes a practical method for analyzing stability under arbitrary friction coefficients. The method replaces the conventional approach, which requires considerable effort to identify mass, stiffness, and damping coefficients, with the use of modal damping ratios that are easier to determine. Furthermore, the validity of the proposed method is verified by comparing its evaluation results with those obtained from low-speed sliding tests of the pantograph. This approach allows railway operators and pantograph manufacturers to carry out practical stability analysis of pantographs under sliding friction conditions.

2. Overview of unstable vibrations induced by sliding friction

Before introducing the proposed method, this section provides an overview of unstable vibrations. Section 2.1 describes the phenomenon of unstable vibrations observed in pantographs. Section 2.2 presents the results of an investigation into the friction coefficient at which unstable vibrations occur. This investigation was based on low-speed sliding tests conducted using HiPaC.

2.1 Unstable vibrations of the pantograph

The unstable vibrations addressed in this study are explained using the conceptual diagram of the pantograph, with a focus on the pitching degree of freedom of the contact strip, as illustrated in Fig. 1. When a torque induced by the frictional force acts on the contact strip, it oscillates pitching vibrations. These pitching vibrations couple with vertical vibrations of the contact strip, leading to the occurrence of unstable vibrations [5]. When stability is analyzed using a mechanical model, it can be assessed using the sign of the

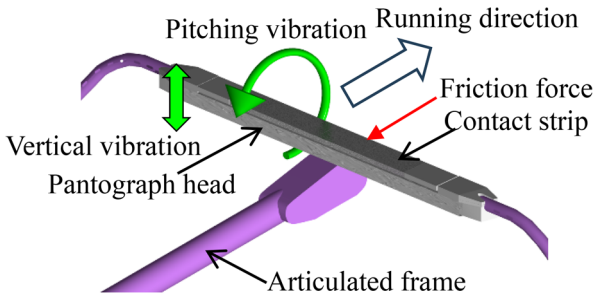

Fig. 1 Conceptual diagram of the pantograph

real part of the complex eigenvalues obtained from an eigenvalue analysis. The real part of an eigenvalue corresponds to the negative of the modal damping ratio; thus, a positive value indicates an absence of energy dissipation, leading to energy accumulation in the system. In the proposed method described in Section 3, the presence or absence of unstable vibrations is determined from the modal damping ratios of the system.

2.2 Reproduction of the phenomenon through low-speed sliding tests

In order to show the conditions under which unstable vibrations occur in real pantographs, and to provide reference data for comparison with the evaluation results obtained using the proposed method described in Section 4, reproduction tests were conducted while measuring the friction coefficient simultaneously. These tests were performed using HiPaC. As shown in Fig. 2, a rigid disk equipped with an actual contact wire mounted along its lower outer circumference was rotated to allow the contact strip positioned beneath the disk to slide against the wire. The contact wire used in this test was GT110, and the contact strip was an iron-based sintered alloy strip.

When the intermediate hinge of the pantograph is positioned counterclockwise from the contact point between the pantograph and the contact wire (when viewed from above), this configuration is referred to as the "knuckle-forward condition." Conversely, the configuration where the hinge is located on the clockwise side is referred to as the "knuckle-backward condition."

The friction coefficient was measured using two-component load cells (manufactured by Toyo Sokki, rated capacity: 250 N, model: 2D-250N-250N, hereinafter referred to as the two-component force sensor) installed between the pantograph head and the pantograph head support, as shown in Fig. 3. These sensors were sensitive to forces along two orthogonal axes: the train running direction and the vertical direction. Contact and friction forces acting on the contact strip were measured using this setup. Since these measured forces include the inertial forces of the contact strip and the pantograph head, measurement accuracy decreases at high frequencies where inertial effects dominate. However, for quasi-static phenomena up to approximately 1 Hz, sufficient accuracy can be achieved [8].

First, ten low-speed sliding tests were carried out under the knuckle-forward condition by rotating the disk at a peripheral speed of 5 km/h. To ensure consistent initial conditions for each test, a preconditioning run was performed before each test, which consisted of one minute sliding at a peripheral speed of 300 km/h. As a result of the low-speed sliding tests under the knuckle-forward condition, no unstable vibrations were observed. The maximum friction coefficient had an average value of 1.1 with a standard deviation of 0.12 across the ten measurements.

Secondly, seven low-speed tests were conducted under the knuckle-backward condition, and unstable vibrations occurred in all cases. As these unstable vibrations occurred immediately after the start of the preconditioning run, it was not possible to increase the peripheral speed further, and therefore the preconditioning run was not applied in these tests. Under the knuckle-backward condition, the friction coefficient immediately prior to the occurrence of unstable vibrations had an average value of 0.79 with a standard deviation of 0.17 for the seven measurements.

3. Stability analysis method based on frequency response function measurement

This section proposes a stability analysis method that does not require the identification of the mass, stiffness, and damping coefficients of the pantograph model. This method uses the frequency response function (FRF) obtained from excitation test data.

3.1 Overview

In the proposed method, the FRF of the pantograph at the contact point with the contact wire and at other relevant locations is first obtained from excitation test data. By specifying the contact position with the contact wire and assigning a friction coefficient, the FRF of the entire system, which represents the sliding contact condition between the contact wire and the pantograph, is estimated. Secondly, the modal characteristics of the entire system are identified from the estimated FRF, and the modal damping ratios are determined. Finally, the stability of the system is evaluated by examining the sign of the identified modal damping ratios.

3.2 Estimation method of FRF under sliding contact conditions

As shown in Fig. 4, the entire system is modeled as a system in which a contact element, consisting of a contact spring and dashpot, is attached to the top surface of the contact strip. It is assumed that a friction force acts in the y-direction. The FRF representing the input-output relationship at point i of the entire system is estimated, and used for the subsequent stability analysis.

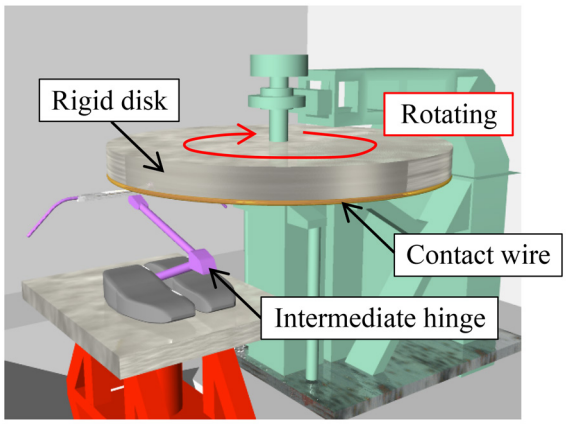

Fig. 2 Conceptual diagram of HiPaC

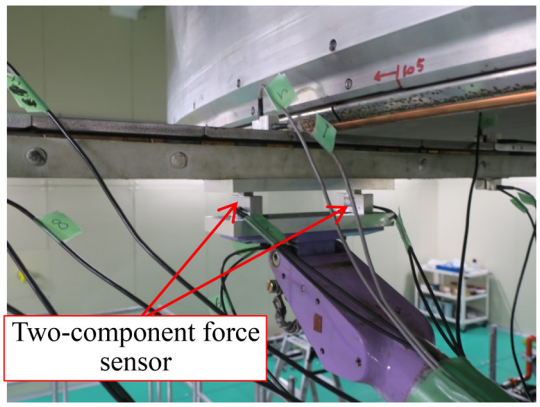

Fig. 3 Measurement of friction coefficient using two-component force sensors

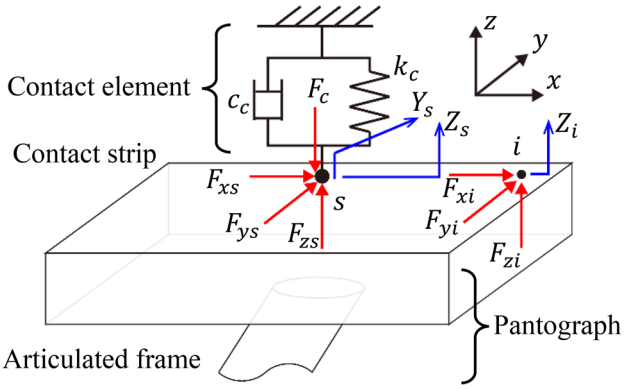

Fig. 4 Entire system composed of the pantograph and the contact element

As shown in Fig. 4, the equilibrium of displacement and force at points i and s is considered. The z-direction displacement Z_i at point i on the top surface of the contact strip, the z-direction displacement Z_s and y-direction displacement Y_s at point s, which is the contact point with the contact element, are expressed using the FRFs and external forces as follows.

$$Z_i = G_{zi}F_{zi} + G_{zizs}F_{zs} + G_{ziys}F_{ys} \tag{1}$$

$$Z_s = G_{zszi}F_{zi} + G_{zs}F_{zs} + G_{zsys}F_{ys} \tag{2}$$

$$Y_s = G_{yszi}F_{zi} + G_{yszs}F_{zs} + G_{ysyi}F_{yi} \tag{3}$$

Here, F_{zi} denotes the force acting in the z-direction at point i, G_{zi} represents the auto-FRF in the z-direction at point i, and G_{zszi} denotes the cross-FRF from the z-direction input at point i to the z-direction response at point s. When Maxwell's reciprocity theorem holds, the input-output relationship remains unchanged if the input and response points are interchanged, and thus $G_{zizs} = G_{zszi}$ is satisfied [9].

The contact force F_c and the friction force F_{ys} acting at point s in the entire system are expressed by the following equations.

$$F_c = -F_{zs} = (k_c + j\omega c_c)(G_{zszi}F_{zi} + G_{zs}F_{zs} + G_{zsys}F_{ys}) \tag{4}$$

$$F_{ys} = -\mu(k_c + j\omega c_c)(G_{zszi}F_{zi} + G_{zs}F_{zs} + G_{zsys}F_{ys}) \tag{5}$$

The equations (1) through (5) can be collectively expressed in matrix form as follows.

$$\begin{bmatrix} \mathbf{I} & \mathbf{A} \\ \mathbf{0} & \mathbf{B} \end{bmatrix} \begin{Bmatrix} Z_i \\ Z_s \\ Y_s \\ F_{zs} \\ F_{ys} \end{Bmatrix} = \begin{Bmatrix} G_{zi} \\ G_{zszi} \\ G_{yszi} \\ -(k_c + j\omega c_c)G_{zszi} \\ -\mu(k_c + j\omega c_c)G_{zszi} \end{Bmatrix} F_{zi} \tag{6}$$

$$\mathbf{A} \equiv \begin{bmatrix} -G_{zizs} & -G_{ziys} \\ -G_{zs} & -G_{zsys} \\ -G_{yszs} & -G_{ysyi} \end{bmatrix} \tag{7}$$

$$\mathbf{B} \equiv \begin{bmatrix} 1+(k_c + j\omega c_c)G_{zs} & (k_c + j\omega c_c)G_{zsys} \\ \mu(k_c + j\omega c_c)G_{zs} & \mu(k_c + j\omega c_c)G_{zsys}+1 \end{bmatrix} \tag{8}$$

Here, ω denotes the angular frequency, and j represents the imaginary unit. By solving the vector on the left-hand side of equation (6), the FRF of the entire system can be estimated. To estimate the FRF using this method, various FRFs of the pantograph are required, as indicated in the coefficient matrices **A**, **B**, and the vector on the right-hand side of equation (6). When applying this method to a real pantograph, the necessary FRFs are measured through excitation tests, and the FRF of the entire system is estimated using equation (6).

3.3 Stability analysis method based on FRF

In the next chapter, excitation tests using a real pantograph are carried out to estimate $\hat{G}_{zi}$, the z-direction FRF at point i of the entire system. Here, $\hat{}$ indicates that the FRF corresponds to the entire system. Using the estimated FRF, modal identification is performed, and the stability of the system is evaluated according to the sign of the identified modal damping ratios. Specifically, the system is considered stable if all the modal damping ratios are positive, and unstable if any of them are negative.

4. Verification of the proposed method based on excitation tests

4.1 Test method

Impulse excitation tests were carried out to measure the various FRFs of a real pantograph, which are required for estimating the FRF of the entire system. The pantograph was placed on a surface plate and raised statically with an uplift force of 54 N. Impulse excitation was applied in the free state without contact between the contact strip and the contact wire.

As shown in Fig. 5, two aluminum blocks were bonded to the top surface of the contact strip to facilitate excitation and acceleration measurement. Accelerometers were attached to the aluminum blocks, and impulse forces were applied to either the top or front surface of the blocks using an impulse hammer. The use of aluminum blocks enabled excitation and acceleration measurements to be taken in the y-direction, which would otherwise be difficult to perform directly on the top surface of the contact strip, as required for the estimation based on equation (6).

Depending on the type of FRF to be measured, the accelerometer was mounted either on the top surface (Fig. 5(a)) or the front surface (Fig. 5(b)) of the aluminum block. The installation positions were as follows:

Point s : the virtual contact point with the contact wire. This was located at the center in the lateral direction and at the edge in the longitudinal direction of the contact strip.

Point i : the target location for FRF estimation. This was set 100 mm from point s in the x-direction. In many of the test cases, Maxwell's reciprocity theorem was applied to obtain various translational FRFs. When needed, the accelerometer mounting point was treated as the excitation point, and the impulse excitation point was treated as the acceleration measurement point.

4.2 Stability analysis results

In this study, the modal characteristics were identified by applying a modal identification method to the FRF estimated using a contact stiffness of $k_c = 10^7$ N/m and a contact damping coefficient of $c_c = 10^3$ Ns/m. The differential iteration method [10], a frequency-domain identification technique assuming a general viscous

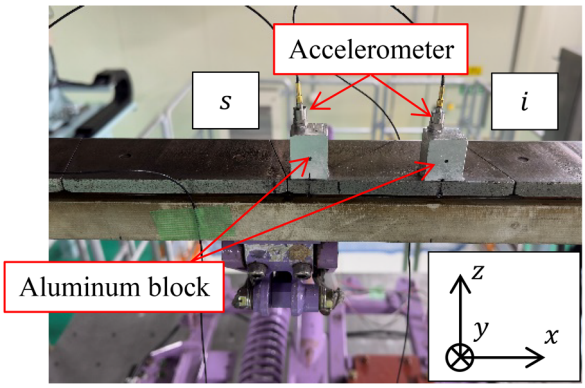

(a) Accelerometer setup 1 (measurement of z-direction FRF)

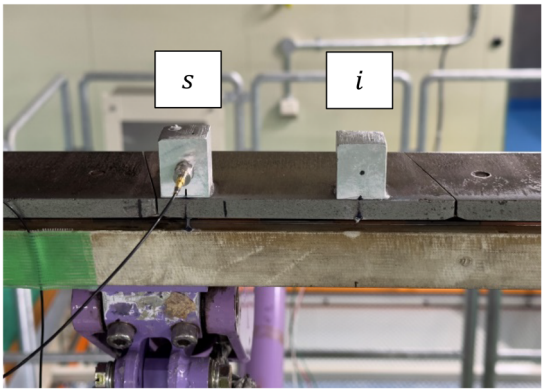

(b) Accelerometer setup 2 (measurement of y-direction FRF)

Fig. 5 Excitation and acceleration measurement by attaching two aluminum blocks to the top surface of the contact strip

damping system, was employed for the modal identification. The theoretical value of the FRF, $G(\omega)$, is given by equation (9).

$$G(\omega)=\sum_{r=1}^{n}\left\{\frac{U_r+jV_r}{j(\omega-\omega_{dr})+\sigma_r}+\frac{U_r-jV_r}{j(\omega+\omega_{dr})+\sigma_r}\right\} \tag{9}$$

The above equation represents the theoretical compliance formulation, in which force is the input and displacement is the output. The nonlinear parameters include the damped natural angular frequency ω_{dr} and the modal damping ratio σ_r, while the linear parameters U_r and V_r correspond to the real and imaginary parts of the mode shape vector, respectively. These parameters are identified in the analysis. In the differential iteration method, initial values for the modal parameters are provided, and the nonlinear terms are linearized by performing a Taylor expansion of the FRF around these initial values. The update to the modal parameters is then computed.

In this study, the initial value of ω_{dr} was determined using the mode indicator function [11], which represents the ratio between the power of the FRF and the power of its real part. The initial value of σ_r was set assuming a modal damping ratio of 1%. The initial values for the linear terms were determined by applying the least squares method to the initial nonlinear parameters. Using these initial values, the differential iteration method estimates the linear terms using

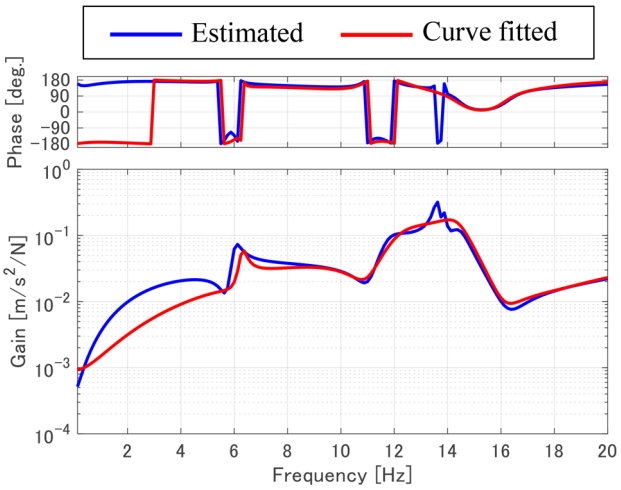

(a) Knuckle-forward direction

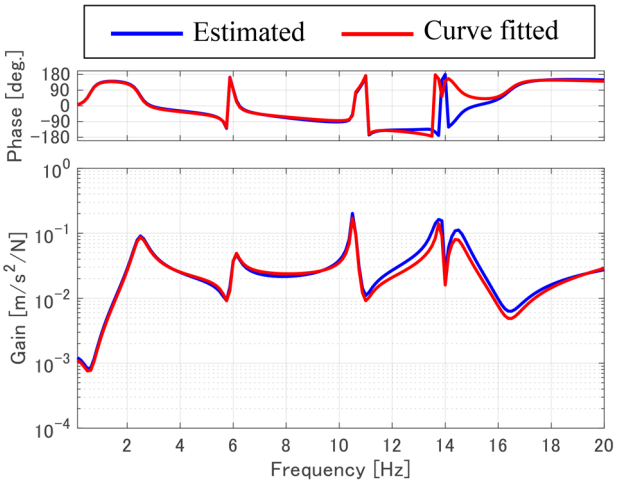

(b) Knuckle-backward direction

Fig. 6 Comparison between estimated FRF and curve fitting result (friction coefficient = 1)

least squares, and then iteratively updates the nonlinear terms to minimize the error between the estimated FRF and the theoretical FRF $G(\omega)$ as given by equation (9). Hereafter, the process of identifying mode characteristics that minimizes the error between estimated and theoretical FRFs is referred to as 'curve fitting.' According to Reference [6], unstable vibrations occur at a frequency of approximately 8 Hz. Therefore, curve fitting was performed for a frequency range up to 20 Hz in this study.

Figure 6 shows a comparison between the estimated FRF and the fitted curve for a friction coefficient of 1. Table 1 summarizes the identified natural frequencies and corresponding modal damping ratios for the modes in which unstable vibrations were observed. Table 1 shows that under the knuckle-forward condition, the system remains stable even with a friction coefficient of 1. In contrast, under the knuckle-backward condition, unstable vibrations occur when the friction coefficient exceeds 0.89, and the corresponding frequency is approximately 10.6 Hz. Although the fitting accuracy is low in some frequency ranges shown in Fig. 6, it is relatively high near 10.6 Hz, where unstable vibrations occur. Therefore, it is considered that fitting errors at other frequencies have a negligible effect on the stability analysis.

Table 1 Modal identification results for each friction coefficient

	Friction coefficient [−]	Natural frequency [Hz]	Modal Damping ratio [%]
Knuckle-forward	0.80	12.07	48.69
	0.90	12.54	36.17
	1.00	11.80	49.00
Knuckle-backward	0.80	10.65	0.25
	0.85	10.62	0.09
	0.88	10.61	0.01
	0.89	10.60	−0.005
	0.90	10.60	−0.03
	0.95	10.57	−0.13
	1.00	10.55	−0.27

As mentioned in Section 2.2, the average friction coefficient just before unstable vibrations occurred under the knuckle-backward condition in the low-speed sliding tests was 0.79. However, due to large variability, unstable vibrations also occurred at lower friction coefficients, such as 0.6. The stability analysis results obtained using the proposed method differ from the test results by approximately 0.1 in terms of the average friction coefficient. Nevertheless, considering the measurement variability, the analysis is considered to be generally valid. On the other hand, in the proposed method, aluminum blocks were attached to the top surface of the contact strip to facilitate excitation and acceleration measurements. This setup may introduce error factors such as moment inputs. Therefore, improvements in excitation and measurement methods are planned to enhance accuracy in future studies.

5. Conclusions

This study proposed a method for analyzing pantograph stability using the FRF obtained from excitation tests of the pantograph. This method involves estimating the FRF in the sliding state and identifying the sign of the resulting modal damping ratios. This method was applied to analyze the stability of a real pantograph, revealing that unstable vibrations occur when the friction coefficient exceeds 0.89 under the knuckle-backward condition. In contrast, no unstable vibrations were observed under the knuckle-forward condition even when the friction coefficient was 1.0. These results are generally consistent with the findings from reproduction tests of unstable vibrations conducted using a high-speed pantograph testing device, thereby supporting the validity of the proposed method. Future work will focus on improving the methods used to excite and measure acceleration on the top surface of the contact strip, with the aim of enhancing the accuracy of the evaluation.

References

[1] Matsuyama, S., "Contact strips of pantographs and contact wires," *METALS & TECHNOLOGY KINZOKU*, Vol. 70, No. 2, pp. 42-50, 2000 (in Japanese).

[2] Nemoto, K. and Kubota, Y., "Effect of sliding speed on friction and wear between copper alloy contact wire and iron-based sintered alloy contact strip," presented at the *J-RAIL2019*, Tokyo, Japan, December 4-6, 2019, Paper S7-4-2 (in Japanese).

[3] Sakamoto, M., Kaku, H. et al., "Pitching suppression measures for the ED76-Type pantograph," *R&m*, 2012. 5, pp. 55-59, 2012 (in Japanese).

[4] Arimoto, H. and Iwase, M., "Current collection of overhead contact line [III]," *Electric Railways*, Vol. 28, pp. 35-39, 1974 (in Japanese).

[5] Amano, Y. and Kobayashi, S., "Analytical Study on the Influence of Friction on Unstable Oscillation of Pantograph," *Quarterly Report of RTRI*, Vol. 64, No. 2, pp. 109-114, 2023.

[6] Amano, Y., Kobayashi, S. et al., "Mechanism and suppression of friction-induced vibration in catenary-pantograph system," *Nonlinear Dynamics*, Vol. 112, pp. 14959-14980, https://doi.org/10.1007/s11071-024-09802-6, 2024.

[7] Koyama, T., "Development of High-speed Test Facility for Pantograph/OCL Systems," *Quarterly Report of RTRI*, Vol. 63, No. 2, pp. 128-132, 2022.

[8] Kobayashi, S., Amano, Y. et al., "Measurement of Friction Coefficient between Contact Wire and Pantograph Using High-Speed Test Facility for Pantograph/OCL Systems," presented at the *J-RAIL2023*, Tokyo, Japan, December 12-14, 2023, Paper S7-2-5 (in Japanese).

[9] Japan Society of Mechanical Engineers, "reciprocal theorem," *Mechanical Engineering Dictionary*, Available: https://www.jsme.or.jp/jsme-medwiki/07:1007360, accessed: Sep. 25, 2024.

[10] Nagamatsu, A., Modal Analysis. Baifukan, pp. 124-126, 1990 (in Japanese).

[11] Rades, M., "Performance of various mode indicator functions," *Shock and Vibration* 17, pp. 473-482, 2010.

Authors

Shigeyuki KOBAYASHI, Ph.D.
Senior Researcher, Current Collection Laboratory, Railway Dynamics Division Research
Areas: Catenary-Pantograph Interaction

Yuki AMANO, Ph.D.
Researcher, Current Collection Laboratory, Railway Dynamics Division
Research Areas: Catenary-Pantograph Interaction, Dynamics of Machinery, Vibration Control

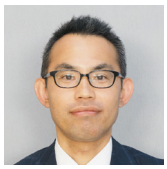

Yoshitaka YAMASHITA, Ph.D.
Senior Chief Researcher, Head of Current Collection Laboratory, Railway Dynamics Division
Research Areas: Catenary-Pantograph Interaction, Dynamics of Machinery, Vibration Control

Summaries of Papers in RTRI REPORT (in Japanese)

Countermeasures of Low-Frequency and Aerodynamic Noise Emitted from Shinkansen Train

Mariko AKUTSU, Toki UDA
(Vol.39, No.8, 1-7, 2025.8)

When a Shinkansen train runs at high speeds in an open section, low-frequency noise and audible noise are emitted from the bogies. It is essential to reduce these aerodynamic noises in order to achieve further speed increases in the future. To understand the generation mechanisms of low-frequency and audible noise, field tests and low-noise wind tunnel tests were carried out. This paper describes the measurement method used in the wind tunnel testing and the development of countermeasures against low-frequency and audible noise.

Development of Tie Plate with Elastic Support Structure for Rigid Crossings Fixed Directly to Composite Sleepers

Saki SHIMIZU, Ryosuke OTAKA, Shingo TAMAGAWA, Tadashi DESHIMARU, Shingo MATSUTANI
(Vol.39, No.8, 9-16, 2025.8)

Turnouts fixed directly to composite sleepers for the Shinkansen trains have large dents on the nose rails, compared to those of ballasted turnouts. To solve this issue, focusing on the difference in the dynamic load depending on the support condition, the authors newly developed a tie plate for rigid crossings with elastic support. The developed tie plate can make depth of dents on nose rails of turnout fixed directly to composite sleepers equal to that for a ballast turnout. In addition, it is compatible and replaceable with the conventional tie plates.

Development of a Method for Diagnosing Deterioration of Railside Facilities using Train Forward Images

Riho MAEDA, Hiroki MUKOJIMA, Nozomi NAGAMINE
(Vol.39, No.8, 17-24, 2025.8)

Railside facilities are installed at stations and at various locations between them. Therefore, facility management operations, such as identifying locations and types and carrying out individual inspections, are labor-intensive and require labor savings. To reduce the labor required for facility management, we have developed a system that enables the facility inspector to check the condition of the rail side facilities remotely using a video camera to capture images in front of the train. The developed system can estimate kilometers travelled, recognize equipment automatically, and estimate the degree of deterioration of the signal equipment boxes. This paper describes an overview of the system, evaluates its accuracy, and outlines the prospects for monitoring the deterioration of facilities.

Influences of Sun Position and Subject Blur on Contact Wire Wear Measurement Using Light Section Method

Hiromu SUSUKI, Itaru MATSUMURA, Yusuke HEIRA
(Vol.39, No.8, 25-32, 2025.8)

Current methods of measuring contact wire wear are unable to accurately measure the diameter of unevenly worn contact wires. To address this issue, we have developed a wear measurement method using a light section method for contact wires. We have also conducted basic studies on the fundamental configuration of cameras and laser light sources, as well as performance verification in limited environments. In order to apply this method to real vehicles, it is necessary to investigate how disturbances caused by the sun's position and subject blur due to high-speed running affect measurement performance in real-world environments. We have verified their performance of these factors in this study and report that the proposed measurement method has sufficient performance.

Evaluation of Cytotoxicity by Exposure to 60 GHz Millimeter Wave in *In Vitro*

Masateru IKEHATA, Sachiko YOSHIE, Yukihisa SUZUKI, Hiroshi SASAKI
(Vol.39, No.8, 33-40, 2025.8)

Recent advances in information processing technology have led to the improvements of wireless data communication technology in various areas including railway systems. This study investigated the possible health effects of millimeter waves (60 GHz), which are used in next-generation communication technology, on the human body. Using a three-dimensional tissue model constructed from normal human cells, the authors conducted experiments for the aim of this study. The results of the experiments showed that the threshold for cell damage is incident power density of approximately 200 mW/cm^2 under exposure conditions of 6 minutes, which is the evaluation time required for compliance with the current regulations. In addition, it was also shown that, the threshold for cytotoxicity decreases to approximately 130 mW/cm^2 under high-temperature and high-humidity conditions (42.5℃, 80% humidity). This mechanism is attributed to thermal factors, and it was found that cell surface temperatures exceeding 50℃ can be a condition that causes damage.

Development of Obstruction Warning Signal Detection Device

Shoji KOMURO, Hiroki MUKOJIMA, Nozomi NAGAMINE
(Vol.39, No.8, 41-48, 2025.8)

Obstruction warning signals indicate a stop signal to the driver when a situation occurs that disturbs train operation, such as at a level crossing. On many railway lines, drivers check the flashing of obstruction warning signals visually, which may cause a risk of missing the signal. For this reason, a support device was developed that detects flashing lights from images taken by a front camera and alerts the driver to pay attention to the train ahead. This paper describes the detection methods and the device used to detect flashing, and report on the verification results in commercial train operations.

Extracting "Tour Themes" from Railway Usage Data of Foreign Visitors to Japan and Its Application to Policy Measures

Wataru INABA, Shingo NAKAGAWA, Takuya WATANABE, Noriko FUKASAWA
(Vol.39, No.8, 49-54, 2025.8)

This study aims to obtain knowledge that can be used for railway operators' policy measures to improve convenience of foreign visitors' travel within Japan. Using station boarding and alighting data, we analyzed day-by-day use of railways by foreign visitors touring major cities in Japan. We assumed "tour themes" associated with combinations of stations, and attempted to extract various tour themes from a large data set using topic model. Given the characteristics of the station boarding and alighting data, we applied BTM (Biterm Topic Model), an effective topic model for short texts, to the actual data and extracted 30 tour themes. Moreover, we proposed possible policy measures by interpreting these 30 tour themes, as a case study. The results demonstrate that, based on the data, railway operators can consider policy measures to promote foreign visitors' tour within

Japan and improve transportation planning.

The Effect of Weak Layers Intersecting Diagonally with Tunnel on Tunnel Floor Heaves

Kazuhide YASHIRO, Keisuke SHIMAMOTO, Takeshi KAWAGOE
(Vol.39, No.8, 55-62, 2025.8)

It is well known that floor of tunnels often heaves at the intersection with a weak layer. Therefore, we conducted a study focusing on the effect of the angle and position in which the weak layer intersects with the tunnel on floor heave. A case study was conducted on tunnels that had recently experienced floor heave. The results showed that the amount of vertical displacement of the invert excavation surface during tunnel construction is large in areas with fractured strata and a high slaking index. This is particularly the case in areas where such strata extend below the invert at a gradual gradient. Laboratory tests showed that rocks taken from strata with many fractures are more susceptible to deterioration due to water absorption and are more likely to deform. Furthermore, we were able to reproduce the above tendency using numerical analysis. In order to suppress floor heave in the tunnels, it was found that it is important to select the structure of the invert taking into account the angle and position at which the tunnel intersects with the weak layer.

Estimation of Wheel/Rail Contact Conditions Based on State Space Model Using Acquired Data by Instrumented Wheelset

Shoya KUNIYUKI, Takatoshi HONDO, Mitsugi SUZUKI, Takefumi MIYAMOTO, Kimihiko NAKANO
(Vol.39, No.9, 1-8, 2025.9)

This paper describes a practical method of estimating wheel/rail contact conditions using the measurement data from an instrumented wheelset. The aim is to improve the accuracy of running safety evaluation without significantly increasing measurement costs. This method uses state-space theory and a Kalman filter-based state estimator to calculate contact conditions of a wheelset, including the angle of attack, contact positions and friction coefficients. Estimation results obtained through vehicle dynamics simulations demonstrate that the proposed approach reliably estimates contact conditions in curved track sections with radii under 600 m. The feasibility of the method was validated using running test data, which demonstrated that it provides an efficient solution for estimating contact conditions.

Development of a Tri-axial Magneto-optical Probe for Measuring Magnetic Fields in the Low-frequency Bands

Yoshihito KATO, Masateru IKEHATA
(Vol.39, No.9, 9-15, 2025.9)

When measuring low-frequency magnetic fields related to rolling stock, multiple sensors are needed. Therefore, we developed a system that uses a tri-axial magneto-optical probe to measure magnetic fields. This probe is capable of wideband measurement, which enables measurement with a single device. A mechanism was constructed by incorporating optical elements, etc. to detect magnetic fields in a direction 90 degrees that is different from that of conventional single-axial magneto-optical probes. These were then combined to create a tri-axial probe. We confirmed through performance verification tests that using a low noise laser in the low-frequency band as the light source significantly improves the noise characteristics below 100 Hz.

Application of Liquefied Stabilized Soil in Construction of Railway Earth Structures

Susumu NAKAJIMA, Yuki KURAKAMI, Keisuke OTA
(Vol.39, No.9, 17-23, 2025.9)

The authors propose a specification of the Liquefied Stabilized Soil (LSS) for use in parts of earth structures affected by repeated train loads on the basis of FEM analysis. This study also clarifies the required strength and deformation characteristics of LSS for railway embankments, having conducted a series of laboratory tests and test construction. The study found that LSS can be made stable under repeated train loads if sufficient density and stress ratio are achieved. Laboratory tests and long-term monitoring of the test constructed LSS also show that constructing a protective layer above the LSS layer is highly effective in maintaining the LSS in wet conditions and reducing the vertical stress acting on its surface in accordance with the proposed specification.

Basic Study on Crack Detection Method for PC Sleepers Using Deep Learning Model

Shintaro MINOURA, Tsutomu WATANABE
(Vol.39, No.9, 25-32, 2025.9)

PC sleepers are an important component of railway tracks, contributing to the speed and safety of trains. In recent years, cracks have appeared in the longitudinal direction of some PC sleepers due to alkali–silica reactions, raising concerns about the efficiency of maintenance of these PC sleepers. Therefore, this study proposes using a deep learning model to estimate the position and length of cracks from top surface images of PC sleepers taken by a camera mounted on a maintenance vehicle. Examining the applicability of this method confirmed that this method can estimate the position and length of cracks on PC sleepers while preventing false detection of ballast and fastening devices. In addition, it was shown that this method can be employed to identify areas with a high concentration of cracks, as well as analyse crack patterns on commercial lines.

Experimental Analysis of Mechanism of Steady State Caused by Huge Earthquakes and Development of an Effective Stress Analysis Method for Sandy Soil

Tomoya ONODERA, Ryuichi IBUKI, Jun IZAWA, Kiyoshi FUKUTAKE, Takatoshi KIRIYAMA, Souichi MABUCHI, Tsuyoshi KODAMA
(Vol.39, No.9, 33-42, 2025.9)

When designing railway structures to withstand huge earthquake motions, it is necessary to evaluate the response of ground using effective stress analysis. It is known that the “steady state” occurs during large soil deformation. In this steady state, shear strain increases while stress remains constant. Currently, there have been few researches on the steady state mechanism under actual ground conditions. This study examined the behavior of sandy soil under large deformation conditions using elemental tests with Toyoura sand. Then, an effective stress analysis method which can reproduce the steady state behavior was proposed.

Validation of Natural Frequency Identification Method for Individual Bridges and Viaducts, Excluding the Effects of Adjacent Structures

Kazunori WADA, Kimitoshi SAKAI
(Vol.39, No.9, 43-49, 2025.9)

The natural frequency of railway bridges and viaduct groups is used as an integrity assessment index for substructures. However, this may include the effects of vibrations of adjacent structures, and there is a possibility that the vibration characteristics cannot always be evaluated clearly. From this reason, the authors theoretically derived a method for identifying the natural frequency of individual bridges and viaducts, using the natural frequency

and natural mode of the entire structure evaluated by microtremor observation. In this paper, we verified the applicability of the proposed method to railway bridges and viaducts by conducting a 3D dynamic analysis based on real structures and measurements. The result showed that the natural frequency of the substructure could be identified with an error of about 10%. Therefore, by identifying the natural frequency of the substructure using the proposed method, it is possible to improve the integrity assessment of structures after an earthquake.

Support System for Preventing a Decline of Train Driver's Alertness Levels

Ayako SUZUKI, Kei HOSHINO, Masahiro HONDA, Takeshi HARA
(Vol.39, No.9, 51-57, 2025.9)

We developed a system to estimate train drivers' alertness levels from facial images and issue alerts. A laboratory experiment with general participants showed an accuracy of 80.1% for the eye region and 87.0% for the mouth region. Testing on operational trains confirmed accurate image capture and real-time alertness estimation under various lighting conditions. Using data from 13 operators, the model trained on 10 operators achieved 85.7% accuracy for the eye region and 71.9% for the mouth region when evaluated on the remaining 3. The alert sound received a high effectiveness rating of 5.3 out of 6, and device usability was rated 4.4 out of 5, demonstrating strong positive evaluations.

Design Methodology for Railway RC Viaducts Using BIM/CIM Models

Ryota KONISHI, Ken WATANABE
(Vol.39, No.9, 59-65, 2025.9)

BIM/CIM can prevent rework in the construction process by allowing more time for the design process to be considered, and it can also shorten the total time taken for the design and construction processes compared to work that uses conventional two-dimensional drawings. This paper presents a new approach to design that links BIM/CIM models with design calculations. It proposes a program that automatically generates a three-dimensional frame analysis model from BIM/CIM models, and improves upon the conventional design and construction process.

Dynamic Compression Tests of Aluminum-alloy Structure for Railway Vehicles Considering Buckling and Shear Fracture

Keisuke NAGATA, Tomohiro OKINO, Jun-ichi TAKANO
(Vol.39, No.10, 1-12, 2025.10)

Two types of impact compression tests were conducted to investigate the crushing characteristics of a double-skinned aluminum-alloy carbody structure used in a conventional railway vehicle. One of the two tests is an overall compression test in which the overall specimen's end face is compressed. Another one is a local compression test in which part of its end face is compressed. As a result of the tests, buckling was the main cause of failure in the overall compression test, whereas shear crushing was the main cause of failure in the local compression test. Finite element analyses were conducted in which several material rupture laws were used to compare with the test results. According to the comparison of the analyses and the tests, the results of the analyses applying the ESI-Wilkins-Kamoulakos model agree with those of the tests.

Evaluation Method for Flange-Climb Derailment Focusing on Contact Position and Transverse Creepage Between Wheel and Rail

Shoya KUNIYUKI, Kimihiko NAKANO
(Vol.39, No.10, 13-22, 2025.10)

This paper proposes a new method for evaluating the running safety of railway vehicles against flange-climb derailment, focusing on the contact conditions between wheel and rail. The method uses two key variables: lateral contact position and normalized transverse creepage, defined as the ratio of transverse creepage to the wheelset angle of attack. Through vehicle dynamics simulations under various running conditions, the relationship between these variables and the running safety was investigated. The results show that the transit domains for the loci of these variables differ significantly between derailment and non-derailment cases. This paper provides fundamental insights into the development of advanced safety assessment techniques for railway operations, taking into account the detailed wheel-rail contact dynamics.

Development of Grouted Ballasted Track for Existing Shinkansen Asphalt Roadbed

Kazuki ITO, Narita TAKAHASHI, Takatada TAKAHASHI
(Vol.39, No.10, 23-33, 2025.10)

One way to reduce maintenance costs for ballasted track is to replace existing lines with grouted ballasted track. When forming the grouted ballasted track, the voids in the ballast bed are filled with a cement-based grout material to create what is known as a pre-packed concrete bed. In this study, we proposed a design method for laying a grouted ballasted track on an existing 40-year-old asphalt roadbed and confirmed that the safety requirements regarding the destruction and fatigue failure of asphalt roadbeds and pre-packed concrete beds were satisfied.

A Study of Infrared Coating Thickness Measurement Method when Repainting of Coated Steel Bridge

Tatsuro SAKAMOTO, Sho YAMANAKA
(Vol.39, No.10, 34-43, 2025.10)

Repainting of coated steel bridges is performed manually, and construction management is required to prevent variations in film thickness. However, the coating thickness measurement equipment used on site measures film thickness locally, which makes it difficult to measure a large number of points over a wide area. The purpose of this paper is to determine the applicability of a film thickness measurement method using an infrared camera. To this end, we report the results of the evaluation of the optical properties of coatings applied to steel plates with various surface profiles and the results of a study on the material composition of coatings suitable for this film thickness measurement.

A Method of Predicting Rail Creeping and Track Buckling Using Wide-area 2-D FEM of Railway Tracks Based on GIS Data

Fumihiro URAKAWA, Tsutomu WATANABE
(Vol.39, No.10, 44-55, 2025.10)

This study developed a horizontal two-dimensional static elasto-plastic FEM analysis program for rail track. The validity of the developed program was confirmed by comparing it with an existing one-dimensional analysis model. Additionally, it was found that the developed program was able to analyze the behavior prior to track buckling and the buckling temperature T_A with the same level of accuracy as the existing buckling analysis model. Furthermore, corner breakage in curves was a problem in the analysis using GIS line data of railway. Therefore, we proposed a smoothing method in which corner breakage was replaced with a circular arc of radius R and then moving average was performed, and confirmed its effectiveness.

A Method for Estimating Bridge Girder Deflections Under Resonant Condition Based on Drive-by Measured Track Geometries

Kodai MATSUOKA, Koji HATTORI
(Vol.39, No.10, 56-65, 2025.10)

In some high-speed railways, considerable cost and labor are invested in-situ bridge deflection measurements to appropriately manage resonant bridges during train passage. In this study, we propose a method for estimating girder deflection of resonant railway bridges using drive-by measured track geometries. Analyzing the dynamic response of resonant bridges could show that the deflection is estimated from three peak values in the difference of track geometries between the first and last cars. Numerical simulations and field verification on a high-speed railway showed that the proposed method can accurately estimate maximum girder deflection, with an error margin of less than 0.5 mm.

QUARTERLY REPORT of RTRI

第 66 巻　第 4 号
2025 年 11 月 1 日　発行
監修・発行所：公益財団法人鉄道総合技術研究所
〒 185-8540　東京都国分寺市光町 2-8-38
発行人：芦谷公稔
問い合わせ：鉄道総研広報

Vol. 66, No. 4
Published date: 1 November 2025
Supervision/Publisher: Railway Technical Research Institute
Address: 2-8-38 Hikari-cho, Kokubunji-shi, Tokyo 185-8540, Japan
Issuer: Dr. Kimitoshi ASHIYA
Contact us: Public Relations, Railway Technical Research Institute
Mail Address: rtripr@rtri.or.jp

QUARTERLY REPORT of RTRI

RAILWAY TECHNICAL RESEARCH INSTITUTE

Printed in Japan